Alumina forming alloys (steels, high entropy materials) for the mitigation of compatibility issues with liquid metals and steam in energy related, high-temperature applications

Zur Erlangung des akademischen Grades

Doktor der Ingenieurwissenschaften

von der KIT-Fakultät für Maschinenbau des

Karlsruher Instituts für Technologie (KIT)

genehmigte

Dissertation

von

Hao Shi

aus Ningxia, China

Tag der mündlichen Prüfung: 15.01.2020

Hauptreferent: Prof. Dr.-Ing. Robert Stieglitz

Korreferent: Prof. Dr.-Ing. Georg Müller

Abstract

Energy-related applications with aggressive environments at high temperatures require the development of advanced structural materials. Alumina forming alloys (e.g. Ni-based, Fe-based) have received a great attention for high temperature applications because of their excellent oxidation resistance and adequate mechanical properties. By adding appropriate amounts of Al and Cr, these alloys are able to form protective alumina-rich oxide scales when exposed to the oxygen-containing extreme conditions (e.g. high temperature, corrosivity). Ferritic FeCrAl alloys have been successfully developed for use in liquid Pb environment. However, ferritic steels as well as ferritic FeCrAl alloys suffer from liquid metal embrittlement in liquid Pb. Alumina-forming austenitic alloys (AFA) have the potential to mitigate the corrosion issues in molten Pb and to avoid liquid metal embrittlement at the same time, due to the austenitic structure. Another promising material type is high entropy alloys (HEA). Typically, they have five or more principle elements with the atomic fraction of each element in the range of 5-35 at.%. By alloying passive layer forming elements like Al and Cr, the alloys are able to withstand oxidizing conditions at temperatures above 1000 °C by the formation of a protective alumina-rich scale.

In this dissertation, AFA and HEA model alloys, based on the backbone composition of Fe-Ni-Cr-Al are designed in order to search for the composition map of target materials that are compatible with the selected aggressive environments (molten Pb and steam). AFA model alloys based on Fe-(20-29)Ni-(12-16)Cr-(2-4)Al (in wt.%) have been designed based on equilibrium phase calculations (Thermo-Calc) and the Schaeffler diagram. All the annealed alloys are single FCC phase with specific heat capacity, thermal conductivity and thermal expansion comparable with SS316. Nine alumina-forming HEA alloys have been designed based on the empirical parameters, including enthalpy of mixing ($\Delta Hmix$), atomic size difference (δr), parameter Ω ($(\Sigma c_i T_{m,i})\Delta Smix/|\Delta Hmix|$) and valance electron concentration (*VEC*). The designed alloys include four quaternary alloys with dual phase ($Al_{8.91\text{-}11.7}Cr_{22.40\text{-}30.28}Fe_{32.62\text{-}34.50}Ni_{26.91\text{-}34.28}$, FCC+B2 or BCC), two quaternary alloys with single FCC phase ($Al_{6.02\text{-}7.96}Cr_{23.23\text{-}25.01}Fe_{33.99\text{-}34.06}Ni_{34.75\text{-}34.98}$), and three quinary alloys alloyed with Nb/Ti/Cu ($Al_{7.90\text{-}8.24}Cr_{21.37\text{-}22.04}Fe_{30.29\text{-}31.96}Ni_{33.01\text{-}35.02}Nb_{5.08}/Ti_{5.01}/Cu_{5.00}$, FCC+Laves or γ' phase and single FCC). The thermo-physical properties of as-cast HEA alloys have comparable thermal physical properties like SS 316 at temperatures below 800 °C.

Compatibility tests have been performed in 10^{-6} wt.% oxygen containing molten Pb at 550 °C and 600 °C for 1000 h and 2000 h. The excellent corrosion resistance of the AFA alloys observed in these tests is due to the formation of a protective oxide scale (<200 nm) based on an outer layer of

Cr_2O_3 and an inner layer of Cr_2O_3-Al_2O_3 solid solutions. The passivated alloys also preserve their austenitic matrix. By adding yttrium, the uniformity in scale thickness and in Al and Cr distribution has been improved. In case of Nb containing samples, TEM evaluation of the alloy matrix indicates the formation of B2-NiAl and Laves (Fe_2Nb) phases in addition to the austenite phase. The mechanism of the oxide layer passivation on HEA alloys is almost identical to that of the AFA alloys. A continuous oxide scale is formed based on Cr_2O_3 or $(Fe,Cr)_3O_4$ (in case of BCC phase) or TiO_2 (HEA alloyed with Ti), which acts as a first corrosion barrier. Then, alloys with sufficient Al addition form a protective oxide scale underneath the first corrosion barrier, based on Cr_2O_3-Al_2O_3 solid solution or α-Al_2O_3. Four HEA model alloys have shown their microstructure stabilities during exposure in low-oxygen containing molten Pb at 550-600 °C. Three HEA alloys show precipitations of B2-NiAl phases at the grain boundaries. Sample with Ti addition exhibits phase transformations, namely FCC$\rightarrow$sigma and $\gamma' \rightarrow \eta$ phase.

For the tests in steam at 1200 °C three AFA alloys based on the compositions with Y or Nb addition and four HEA alloys, two with Nb and Ti have been selected. The AFA alloys containing Y (Fe-15Cr-2.5Al-20Ni-0.5Y, Fe-16Cr-2.5Al-22Ni-0.5Y) and the three HEA alloys not containing Ti have formed protective α-Al_2O_3 scales on the alloy surface.

Considering both test environments, a general formula of AFA alloys that are compatible with oxygen containing Pb at 550-600 °C and steam at 1200 °C is derived: Fe-(20-29)Ni-(15.2-16.5)Cr-(2.3-4.3)Al (wt.%). A formula of HEA alloys based on the backbone composition of Fe-Ni-Cr-Al that are compatible with oxygen containing molten Pb at 550-600 °C and steam at 1200 °C, and maintaining the FCC structure in the matrix, is defined as: (30.29-34.50)Fe-(33.15-35.02)Ni-(21.37-25.01)Cr-(6.02-11.69)Al (at.%). In addition, elements like Nb or Y used either as principle element (Nb in HEA) or as minor additions (AFA) have an additional positive effect on the alumina scale formation in aggressive environments. The addition of Nb foster in addition the mechanical strength at high temperatures.

Zusammenfassung

Aggressive Umgebungsbedingungen bei gleichzeitig hohen Temperaturen, wie sie in vielen Anwendungen im Energiebereich herrschen, benötigen die Entwicklung neuartiger Strukturmaterialien. Aluminiumoxid bildende Legierungen (z.B. auf Ni-basis, bzw. Fe-basis) haben wegen ihrer herausragenden Oxidationsbeständigkeit bei ausreichenden mechanischen Eigenschaften für Hochtemperaturanwendungen große Beachtung erfahren. Durch Zulegieren geeigneter Mengen von Al und Cr sind solche Legierungen in der Lage in sauerstoffhaltigen extremen Umgebungsbedingungen stabile schützende aluminiumreiche Oxidschichten zu bilden. Ferritische FeCrAl-Legierungen wurden erfolgreich für die Verwendung in flüssigem Pb optimiert. Jedoch ist Flüssigmetallversprödung nicht nur für ferritische Stähle sondern auch für ferittische FeCrAl-Legierungen ein Anwendungshindernis. Aluminiumoxid bildende austenitische Stähle (AFA) haben das Potential korrosionsbeständig und immun gegen Flüssigmetallversprödung in flüssigem Blei zu sein. Eine andere vielversprechende Materialgruppe sind Hochentropiematerialien (HEA). Diese haben typischerweise fünf oder mehr Basiselemente mit einem Anteil von jedem der Elemente zwischen 5 und 35 at.%. Durch das Zulegieren von Elementen, die die Bildung von Schutzschichten fördern, wie Al und Cr, können HEA-Legierungen oxidativen Umgebungsbedingungen bei Temperaturen von größer 1000 °C durch die Bildung von aluminiumreichen Oxidschichten widerstehen.

In dieser Doktorarbeit, werden AFA und HEA Modellegierungen basierend auf den Grundelementen Fe-Ni-Cr-Al entwickelt, um Elementzusammensetzungen von neuartigen Legierungen zu finden, die mit den ausgewählten aggressiven Medien (flüssiges Blei und Dampf) kompatibel sind. Die AFA-Modellegierungen basierend auf Fe-(20-29)Ni-(12-16)Cr-(2-4)Al (in gew.%) wurden unter Verwendung von thermodynamischen Gleichgewichtsberechnungen (Thermo-Calc) und des Schaeffler-Diagramms entwickelt. Alle wärmebehandelten Legierungen sind einphasige austenitisch (FCC) mit einer Wärmekapazität, einer Wärmeleitfähigkeit und einem thermischen Ausdehnungskoeffizienten vergleichbar dem des austenitischen Stahls SS316. Neun aluminiumoxidbildende HEA-Legierungen wurden Mithilfe empirischer Parameter wie Mischungsenthalpie (ΔHmix), Atomgrößendifferenz (δr), Parameter Ω ((ΣciTm, i) ΔSmix /|ΔHmix|) und Valenzelektronenkonzentration (VEC) entworfen. Die Legierungen umfassen vier quaternäre Legierungen mit zweiphasigem Gefüge ($Al_{8,91-11,7}Cr_{22,40-30,28}Fe_{32,62-34,50}Ni_{26,91-34,28}$, FCC + B2 oder BCC), zwei quaternäre Legierungen mit einer einzelnen FCC-Phase ($Al_{6,02-7,96}Cr_{23,23-25,01}Fe_{33,99-34,06}Ni_{34,75-34,98}$) und drei Quinärlegierungen, legiert mit Nb / Ti / Cu ($Al_{7,90-8,24}Cr_{21,37-22,04}Fe_{30,29-31,96}Ni_{33,01-35,02}Nb_{5,08}$/

$Ti_{5,01}/Cu_{5,00}$, FCC + Laves oder γ'-Phase und Einzel-FCC). Die thermophysikalischen Eigenschaften von HEA-Legierungen, die nicht wärmebehandelt wurden, haben vergleichbare thermophysikalische Eigenschaften wie SS316 bei Temperaturen unter 800 °C.

Korrosionstests wurden in geschmolzenem Pb mit einem Sauerstoffgehalt von 10^{-6} gew.% bei 550 °C und 600 °C für 1000 h und 2000 h durchgeführt. Die in diesen Tests beobachtete hervorragende Korrosionsbeständigkeit der AFA-Legierungen beruht auf der Bildung einer schützenden Oxidschicht (<200 nm) bestehend aus einer äußeren Schicht aus Cr_2O_3 und einer inneren Schicht aus einem Cr_2O_3 -Al_2O_3 Mischkristall. Die passivierten Legierungen bewahren zudem ihre austenitische Matrix. Durch die Zugabe von Yttrium wurde die Gleichmäßigkeit der Oxidschichtdicke sowie der Al- und Cr-Verteilung verbessert. Bei Nb-haltigen Proben zeigt die TEM-Auswertung der Legierungsmatrix die Bildung von B2-NiAl- und Laves-Phasen (Fe_2Nb) zusätzlich zur Austenitphase. Der Mechanismus der Oxidschichtpassivierung auf HEA-Legierungen ist nahezu identisch mit dem der AFA-Legierungen. Es bildet sich eine durchgehende Oxidschicht auf Basis von Cr_2O_3 oder $(Fe, Cr)_3O_4$ (im Falle der BCC-Phase) oder TiO_2 (mit Ti legiertes HEA), die als erste Korrosionsbarriere wirkt. Legierungen mit ausreichendem Al-Zusatz bilden danach eine schützende Oxidschicht unterhalb der ersten Korrosionsbarriere, bestehend aus einem Cr_2O_3-Al_2O_3 Mischkristall oder α-Al_2O_3. Vier HEA-Modelllegierungen zeigten ihre Mikrostrukturstabilität während der Auslagerung in sauerstoffhaltigem geschmolzenem Pb bei 550-600 °C. Drei HEA-Legierungen zeigen Ausscheidungen von B2-NiAl-Phasen an den Korngrenzen. Probe mit Ti-Zusatz zeigt Phasenumwandlungen, nämlich FCC$\rightarrow$sigma- und γ'$\rightarrow\eta$-Phase.

Für die Tests in Wasserdampf bei 1200 °C wurden drei AFA-Legierungen mit Y- oder Nb-Zusatz und vier HEA-Legierungen, zwei mit Nb und Ti ausgewählt. Die AFA-Legierungen, die Y enthalten (Fe-15Cr-2,5Al-20Ni-0,5Y, Fe-16Cr-2,5Al-22Ni-0,5Y) und die drei HEA-Legierungen, die kein Ti enthalten, haben schützende α-Al_2O_3-Schichten auf der Legierungsoberfläche gebildet.

Für beide Testumgebungen wird eine allgemeine Formel für AFA-Legierungen abgeleitet, die mit Pb bei 550–600 °C und Dampf bei 1200 °C kompatibel sind: Fe-(20–29)Ni-(15,2–16,5)Cr-(2,3-4,3) Al (gew .-%). HEA-Legierungen auf Basis der Grundelemente Fe-Ni-Cr-Al, die mit sauerstoffhaltigem geschmolzenem Pb bei 550 bis 600 °C und Dampf bei 1200 °C verträglich sind und ihre FCC-Struktur in der Matrix beibehalten, sind kompatibel in folgender Zusammensetzung: (30.29-34.50)Fe-(33.15-35.02)Ni-(21.37-25.01)Cr-(6.02-11.69)Al (at.%). Darüber hinaus wirken sich Elemente wie Nb oder Y, die entweder als Hauptelement (Nb in HEA) oder als geringfügige Zusätze (Nb und Y in AFA) verwendet werden, zusätzlich positiv auf die Bildung von Aluminiumoxidschichten

in aggressiven Umgebungen aus. Die Zugabe von Nb trägt zudem zur Steigerung der mechanischen Festigkeit bei hohen Temperaturen bei.

Table of Contents

List of abbreviations

AFA	Alumina forming austenitic
AM	Amorphous
at.%	Atomic percent
ATF	Accident tolerant nuclear fuel
BCC	Body-centered cubic
BF	Bright field
BSE	Backscattered electrons
CSP	Concentrated solar power
COSTA	COrrosion in STAgnant lead alloys
D	Dendrite
DP-HEA	Dual-phase HEA
DTA	Differential thermal analysis
EBSD	Electron Backscatter Diffraction
EDS	Energy-dispersive X-ray spectroscopy
FCC	Face-centered cubic
FeCrAl	Alumina forming ferritic
FFT	Fast fourier transformation
F/M	Ferritic/martensitic
FIB	Focused ion beam
FWHM	Full width at half maximum
HCP	Hexagonal close-packed
HEA	High entropy alloy
HLM	Heavy liquid metal
HTF	Heat transfer fluid
ID	Inter-dendrite
IM	Intermetallic
LBE	PbBi eutectic
LCOE	Levelized cost of electricity
LFA	Laser flash analysis
LME	Liquid metal embrittlement
PV	Photovoltaics
SAED	Selected area electron diffraction

SCWR	Super-critical water-cooled reactor
SE	Secondary electron
SEM	Scanning electron microscopy
SS	Solid solution
S/TEM	(Scanning) Transmission electron microscopy
TES	Thermal energy storage
TL	Transitional layer
VEC	Valance electron concentration
VHTR	Very high-temperature gas reactor
wt.%	Weight percent
XRD	X-ray diffraction pattern

List of symbols

a	Thermal diffusivity (m^2/s)
σa	Neutron absorption cross section area (barn)
B2	NiAl Phase
C_O	Oxygen concentration (wt.%)
$C_{S,O}$	Oxygen solubility in Pb (wt.%)
C_p	Specific heat capacity (kJ/kg ·K)
d	Thickness of the plate (m)
ΔG_{mix}	Gibbs free energy of mixing (kJ/mol)
$\Delta_f G^0$ (Fe_3O_4)	Standard Gibbs free energy of formation of Fe_3O_4 (J/mol)
$\Delta_f G^0$ (H_2O)	Standard Gibbs free energy of formation of H_2O (J/mol)
$\Delta_f G^0$ (PbO)	Standard Gibbs free energy of formation of PbO (J/mol)
$\Delta Hmix$	Enthalpy of mixing (kJ/mol)
l	Thickness of the plate sample (m)
K	Equilibrium constant
K_2	Equilibrium constant
L	Original length of the test material (m)
ΔL	Length change (m)
P_{O2}	Oxygen partial pressure (bar)
γ'-phase	$Ni_3(AlTi)$ phase with FCC $L1_2$ structure
σ-phase	FeCr phase with tetragonal crystal structure
η-phase	Ni_3Ti compound with close-packed structure
β-phase	NiAl-B2 phase
r_i	Atomic radius of element i
δr	Atomic size difference
R	Gas constant (8.314 J/mol)
ΔS_{mix}	Entropy of mixing (kJ/K)
$t_{1/2}$	The time value at half signal height (s)
T	Temperature (K)
ΔT	Change in temperature (K)
T_m	Melting point
$T_{m,i}$	Melting temperature of element i (K)
VEC_i	Valence electron concentration of the i-th element

α	Ferrite with BCC structure
α	Coefficient of liner thermal expansion ($°C^{-1}$)
γ	Austenite with FCC structure
ε	Martensite with BCC structure
ρ	Material density (kg/m^3)
θ	Angle (°)
λ	Thermal conductivity (W/(m·K))
$\delta\chi$	Electronegativity
Ω	The ratio of entropy of mixing multiplying temperature to enthalpy of mixing

List of tables

List of figures

1. Introduction

1.1 Motivation

Since the industrial revolution, the supply and demand in energy, especially in terms of electricity, increases worldwide. According to the global energy statistical yearbook 2018, the global electricity consumption has increased by a factor of two over the last three decades (Fig. 1-1), and will continue to increase in the future [1-3]. At the same time, air pollution and global warming caused by burning fossil fuels force humans to shift to "Eco-Friendly Energy Sources" and highly efficient energy production solutions [4-6]. Renewable energy sources like wind, solar, biomass, hydroelectric energy and geothermal power represent such technological solution options [7-11]. According to the BP statistical analysis of world energy data in 2018 [1-2], the consumption of renewable energy grew by 14.5% compare with the previous year while coal's share of world energy continues to decrease [3].

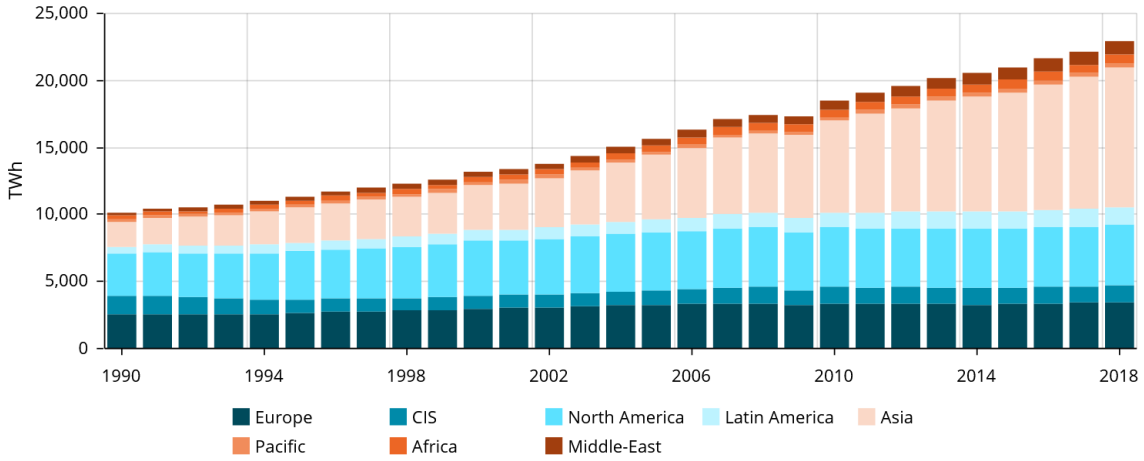

Fig. 1-1 Global electricity consumption from year 1990-2018 [1].

Among these energy sources, the share of solar (mainly Photovoltaics, PV) and wind energy reaches 7.5% of world energy production, and power generation accounts for more than 30% of total additional power production in 2018 [2]. However, a long term planning of electrical power supply with the help of wind power is a great challenge due to the fluctuating provision on all time scales, which requires the availability of considerable storage technologies. Concentrated solar power (CSP) generates the electricity by converting the sunlight into high temperature heat using mirrors or lenses [12-14]. Recently, advanced CSP power stations are combined with a thermal energy storage (TES) aiming to provide low-cost and dis-patchable power from the sunlight [15-17]. According to the SunShot initiative launched by US DOE, the levelized cost of electricity (LCOE) from sunlight will be reduced to $50–60 per MWh by 2020 [11, 18]. This will make the CSP solar energy

competitive at large scale with other forms of energy supply. Regarding CSP, temperatures higher than 600 °C in the heat transfer fluid must be reached to achieve this goal [11].

To slow down and limit the global warming, a transition to low-carbon economy by reducing the CO_2 footprint of electricity production is required, demanding a substantial reduction of fossil fuel utilization to the lowest achievable level. However, most of the renewable energy sources have no base-load capability and are intermittent, like wind and PV. One option of a base load capable energy source with a low CO_2 footprint, nuclear energy, which contributes 11% of the world's energy supply today is considered in many countries as part of the future energy mix [1-2]. However, in the last few decades, the severe accidents at Three Mile Island (1979), Chernobyl (1986), and Fukushima (2011) put the focus on the operational safety of nuclear fission reactors [19-20]. The safety concerns have triggered two main research directions; the development of accident tolerant nuclear fuel (ATF) for the running reactor fleet, and the design of improved sustainable fission reactors, the so-called Gen IV reactors. The development of accident tolerant nuclear fuel (ATF) aims to withstand the severe accident scenarios for current reactors [20-22]. The research and design of the new nuclear reactor generation ("Generation IV International Forum" [23]) targets highly improved safety standards (any consequence of a severe accident has to be limited to the reactor side) in combination with higher temperatures and advanced heat transfer fluids. According to the "Generation IV International Forum", six new types of reactors, including gas-cooled fast reactor, lead cooled fast reactor, molten salts reactor, sodium-cooled fast reactor, super-critical water-cooled reactor (SCWR), and very high-temperature gas reactor (VHTR) are selected as the next generation reactor designs [23-24]. Moreover, operation at high temperature (>700 °C) will allow the reactors to produce not only electricity but also hydrogen [25-26].

Advanced energy generation technologies are proposed as replaceable solutions for future energy supply. These systems often involve high temperature, mechanical loads and high irradiation doses (in case of nuclear applications) [27-44], for instance, concentrated solar power (>600 °C), methane cracking (~850 °C), hydrogen production (700-1000 °C), liquid metal batteries (<450 °C), and Gen IV nuclear fission reactors (500-1000 °C, neutron dose: 10-150 dpa) [33]. Therefore, advanced heat transfer fluids (HTF) with excellent thermo-physical properties are proposed [45-46]. Table 1 lists the thermo-physical properties of different heat transfer media. Compared to currently used media such as air/helium/oil/organics/molten salts, the heavy liquid metals lead (Pb) and lead-bismuth eutectic (LBE-$Pb_{45}Bi_{55}$) show the widest working temperature ranges at a still relatively high thermal conductivity vital to reduce component size. Compared with the liquid metal Na, they have a significantly lower reactivity to oxygen and water. These specific properties are ideal for heat transfer fluid applications such as advanced lead cooled fast reactors, spallation particle sources, and CSP [13, 17, 28, 47, 48]. Moreover, the systems using Pb/LBE as coolant can be operated at

temperatures above 500 °C [28, 29, 49]. The thermal energy harvested by the working fluids will be directly or indirectly transferred to a steam generator or an advanced gas turbine for electricity production. Using water/steam as heat transfer media will simplify the system design and reduce the costs of electricity [45-46]. Moreover, high temperature steam can be applied for gasification and pyrolysis systems that are recently being developed due to their high efficiency and low environment impact in energy conversion and production [50, 54].

Table 1-1 Thermo-physical properties of candidate heat transfer mediums.

Heat transfer fluids	Temperature, °C	Specific heat capacity (C_p), kJ/kg ·K	Thermal conductivity (λ), W/m·K	Density (ρ), kg/m^3	Reference
Air	~700	1.05 (600 °C)	0.06 (600 °C)	1.225	[55-56]
He	850-950	5.19 (25 °C)	0.33 (600 °C, 1 bar)	0.055 (600 °C, 1 bar)	[57-58]
Steam	600-950	2.42 (steam, 600 °C)	0.08 (600 °C)	0.6 (100 °C, 1 MPa)	[45, 59, 60]
Thermal Oil - (shell heat transfer Oil S2)	<340	1.8-3.0 (0-300 °C)	0.11-0.13 (0-340 °C)	655-876 (0-340 °C)	[61]
Organics (biphenyl/diphenyl oxide)	<400	1.93 (300 °C)	~0.01 (300 °C)	997-1090	[45]
Na	98-1000	1.23	140	900	[62]
Pb/LBE	327-1749 /125-1533	0.14 (600 °C)	18.8 /15.6 (600 °C)	10324/9936	[29, 63, 64]
Solar salts	<565	~1.55 (500 °C)	0.55 (400 °C)	1800	[65-66]

In the context of this work, heavy liquid metal Pb and steam are addressed as the working fluids due to both their attractive physicochemical properties and the potential for large-scale applications [29, 36, 40, 42, 53]. Their compatibility with structural materials (e.g. container, pipes, heat exchanger, cladding materials), in particular the high corrosiveness at elevated temperatures, challenges their commercial application [29, 46, 67, 73]. Therefore, developing advanced materials is essential to improve the high temperature compatibility between structural materials and aggressive heat transfer fluids.

One concept of protecting structural steels from high temperature corrosion is to add appropriate concentrations of Al and Cr into the bulk material to allow the alloys to form protective alumina rich oxide scales in oxygen containing environmental conditions. Alumina forming alloys (e.g. Ni-based, Fe-based) have received a great attention for high temperature applications because of

their excellent oxidation resistance and improved mechanical properties [74-88]. The corrosion behavior of ferritic FeCrAl alloys have been investigated in liquid Pb environment [85]. However, ferritic steels as well as ferritic FeCrAl alloys suffer from liquid metal embrittlement in liquid Pb [89, 91]. Alumina forming austenitic (AFA) steels combine the advantages of corrosion resistance and stable mechanical properties in aggressive environments at high temperatures. Nowadays, commercial steels (ferritic/martensitic and austenitic) are able to withstand exposure to liquid Pb up to 500 °C. As a first step in the development of advanced materials, the search for compatibility with aggressive environments at 550 °C or even 600 °C is very challenging, especially for AFA steels. An alternative approach to structural materials with the required compatibility is the high entropy alloy concept first reported in 2004, which has attracted attention to many research groups [92-99]. These alloys contain five or more principle elements in equal or near-equal atomic ratio to form solid solutions. Some of these combinations show superior mechanical, physical properties in comparison with the traditional materials. High entropy alloys are expected to withstand higher temperatures and to be more resistant to radiation, an important criterion for nuclear applications [96]. Recently, the high entropy alloys are proposed as candidates for high temperature structural materials considering their excellent corrosion resistance, structural stability and mechanical properties [96, 97, 99].

1.2 Aim and objectives

Motivated by the necessity to develop advanced structural materials for energy-related applications targeting high temperatures in aggressive environments, the aim of this thesis is to develop AFA and HEA model alloys compatible with liquid Pb (at 550 °C and 600 °C) and steam (1200 °C). The exposure temperature of 1200 °C in steam corresponds to a loss of coolant accident in water-cooled fission reactors. The criteria for a promising alloy are:

- Thermodynamic stability and metallurgic feasibility of the alloy composition.
- Thermo-physical properties appropriate for the application.
- Corrosion resistance in oxygen containing liquid Pb and steam at high temperature.
- Mechanical properties adequate for use as structural material.
- Microstructural stability during long-term exposure to liquid Pb and steam.

In the approach considered in this thesis for the development of the structural materials for energy applications, the corrosion resistance is considered as the main criterion to start from. Therefore, the principle objective of the work consists in the design, production, aggressive-environments exposure and corrosion behavior characterization of Fe-Cr-Al-Ni model

alloys, which then serve as the basis for future industrial alumina-forming austenitic and high-entropy alloy systems.

In addition, the other criteria of promising alloys mentioned above induce secondary objectives of the current work. To get a first estimation on the suitability of the developed model alloys for energy applications, secondary objectives are (i) to elaborate whether the thermo-physical properties of the model alloys are comparable with those of commercial steels and (ii) to investigate the microstructural stability of the model alloys during short-term exposure.

In the process of material development, starting from the selected promising model alloys as backbone, additions of further alloying elements are required to reach the targeted mechanical properties. Although the final material development is out of the scope of this thesis, it is a further secondary objective to exemplify a first step of this process: to investigate the influence of additional alloying elements, which are known to improve the mechanical properties, on the corrosion behavior.

The development of the final materials with the characterization of their mechanical properties and of their microstructural stability during long-term exposure are beyond the scope of this thesis.

1.3 Organization of the thesis

Based on the formulated goals the submitted thesis is structured along following logics. First, the current state-of-the-art of structural materials in HLM and steam with respect to corrosion behavior and technological means to improve their performance are critically reviewed (chapter 2). Chapter 3 elaborates the fundamentals of material processing, its characterization as well as the experimental corrosion measurement techniques. Based on the major material improvement options outlined in chapter 1, the section 4 describes the model alloy design, its preparation and the experimental observations of its microstructural state. It also scopes evolutionary steps towards more advanced alloys (AFA-2nd generation) and its thermo-physical properties. The experimentally determined corrosion performance of the different alumina forming model alloys (AFA) as a function of time, temperature level forms the core of chapter 5. Therein, the impact of the experimental parameters on the stability of the microstructure is analyzed, a comparative summary of different alloys is provided and finally, suggestions to improve AFA alloys based on the experiments are elaborated. Chapter 6 replicates the AFA studies for High Entropy Alloys (HEA). Further, chapter 7 investigates both AFA and HEA alloys with respect to their oxidation performance in steam, with a closer look to in-situ hydrogen release and surface analysis. Finally, chapter 8 condenses the major results, identifies still open aspects and formulates options to overcome them.

2. Materials challenges in aggressive environments - state of the art

2.1 Material degradation at extreme conditions

2.1.1 Corrosion and corrosion mitigation in heavy liquid metals (HLM)

The corrosion of metallic materials in heavy liquid metals (e.g. Pb, LBE) is mainly driven by physical dissolution of alloying elements [29, 69, 100]. The dissolution of alloy elements like Ni, Fe and Cr in Pb/LBE results in materials loss and phase transition [101-103]. Fig. 2-1 displays the solubility of Fe, Cr, Ni and Al in molten Pb or PbBi eutectic (LBE) as a function of temperature [29, 104]. The solubility of alloying elements in molten Pb are ordered as follows: Ni>Al>Cr>Fe. Increasing the temperature significantly increases the solubility of the structural material constituents in the liquid. On the other hand, large temperature differences within a cooling system leads to dissolution attack occurring close to the heat source while in the vicinity of the heat sink the solubility in the coolant can be undercut yielding to deposition of corrosion products there even plug the pipes [100]. Moreover, the liquid metals can penetrate into the steel matrix through cracks and grain boundaries affecting their performance. In particular, when the liquid metal reaches a crack tip, it will significantly accelerate the crack growth rate under mechanical load [68, 105]. The corrosion process in static condition may stop after a certain period when the concentration of the dissolved elements in the molten metal reach the saturation values. However, when the flowing condition (velocity > 2 m/s) is introduced at above 500 °C, corrosion can even be accelerated due to the shear and frictional stress acting on the surface, changing oxygen conditions, mass transport between the hot and cold part. This causes an erosion attack of the passive oxide layer protecting the structural material [69, 106, 109].

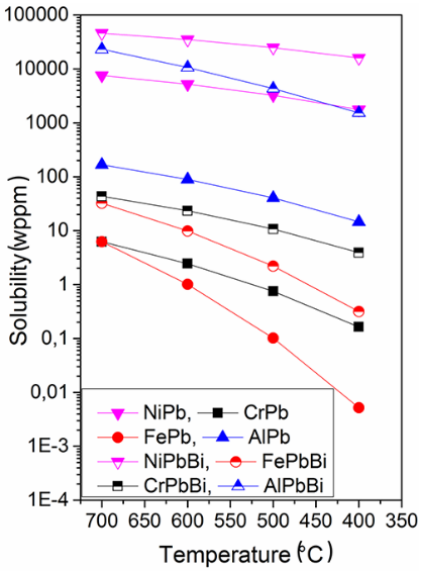

Fig. 2-1 Solubility of Ni, Cr, Fe and Al in liquid metals Pb, PbBi eutectic as a function of temperature [29, 104].

The addition of an appropriate quantity of oxygen is widely considered as an effective strategy to mitigate the corrosion in HLM due to in-situ growth of the protective oxide scales on the bulk material [110-111]. According to the Ellingham-diagram depicted in Fig. 2-2, some alloying elements like Fe, Cr and Al exhibit a stronger chemical affinity to oxygen than Pb and Bi. When the dissolved oxygen concentration is higher than the respective decomposition oxygen partial pressure of M_xO_y (M: alloying element) and lower than that of PbO and BiO, these alloying elements, instead of the HLM, are selectively oxidized. In case of temperatures lower than 500 °C, both austenitic and ferritic/martensitic (F/M) steels are expected to be protected by the Fe- and Cr- oxide scales when exposed to oxygen containing (10^{-8}-10^{-6} wt.%) molten Pb or LBE environments [109, 112, 113]. Results from different exposure tests indicate that the oxide scales formed at such conditions consist of an outer magnetite and an inner spinel layer [112, 114, 115]. However, above 500 °C, austenitic steels do not form any protective oxide scale; even at oxygen conditions that are sufficient for magnetite formation [29, 116, 117]. Exposure of austenitic steels to Pb at temperatures above 500 °C will result in dissolution attack, in particular targeting Ni, and phase transformation triggered accordingly [29, 69, 116]. Regarding F/M steels, the thick oxide scales formed on surfaces at temperatures above 500 °C lead to a thinning of the bulk material reducing admissible stresses but also unfavorable since the low thermal conductivity of the oxide scale reduces efficiency [109, 114]. For instance, the mean oxidation rate of T91 in oxygen containing LBE can reach 0.13 mm/year at 550 °C [118]. When the temperature is higher than 550 °C, the risk to local dissolution attacks and oxide scale spallation are likely to occur [69, 114]. Therefore, for high temperature operations (>500 °C), mitigation strategies considering advanced alloys are significantly important to alleviate the corrosion issues.

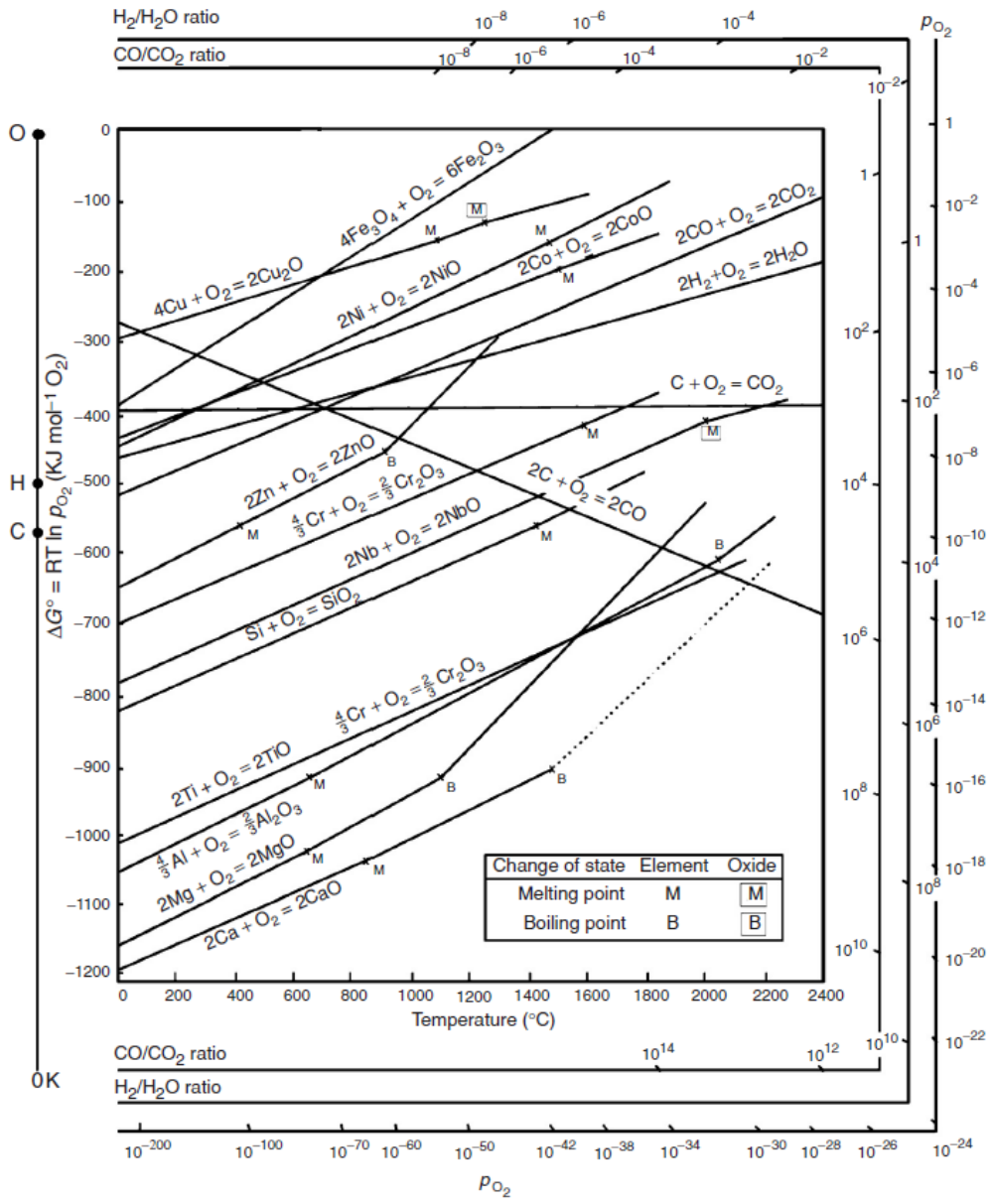

Fig. 2-2 Ellingham-diagram for the selected oxide formation as a function of temperature and oxygen partial pressure [119].

2.1.2 Corrosion investigation in steam

The severe degradation of structural materials, particularly in terms of corrosion and mechanical failure, pose a challenge for high temperature steam applications [22, 54, 120, 121]. At temperatures below 750 °C, the corrosion investigations of different materials (e.g. ferritic/martensitic, austenitic steels, Ni-based alloys) in steam environments have been reported [54, 121, 125]. Quadakkers et al. [122] tested the 9–12% Cr steels in steam environment at the temperature range of 550-650 °C. A thick oxide scale, consisting of fast growing magnetite and inner Cr-containing spinel, was observed on the surface of 9Cr–1Mo steel after 1000 hours exposure at 650 °C. During the long time exposure period (>1000 h), cracks and pores present in the oxide scale

and at the scale-matrix interface lead to the scale exfoliation. Austenitic steels (e.g. 304H, 347H) show lower oxidation rates than ferritic steels (e.g. T22, T91) due to the formation of Fe-Cr spinel when exposed to steam at 700-800 °C [121]. The oxidation rates are also temperature dependent. Increasing temperatures lead to formation of thick oxide scales and an increased risk to scale spallation [121, 124]. Fresnillo et al. [126] investigated the oxidation behavior of two Ni-based alloys (alloy 625) at 700-800 °C in Ar-50% H_2O for 3000-10000 h. A thin (1-2 µm) and continuous Cr_2O_3 rich oxide scale together with Mn-rich spinel was obtained on all samples. The oxidation process follows the parabolic law. Reports on the oxidation tests of alloys in steam environments at temperatures beyond 800 °C are limited. Most of these reports are focused on FeCrAl alloys [22, 127, 130]. At temperatures below 1000 °C, the oxide scales formed on Fe-21Cr-5Al-3Mo (APMT) and Fe-12Cr-6Al-2Mo (C26M) consist of an outer Al, Cr and Fe rich layer and an inner Al rich layer [129]. When the temperature is above 1000 °C, only alumina layers have been observed [128, 129, 131]. In addition, Pint et al. [132] and Moon et al. [133] have reported on the high temperature steam oxidation of Fe-Cr-Si alloys. At temperatures beyond 1200 °C, only Fe-20Cr-2Si was found to be protected by a continuous amorphous SiO_2 layer.

2.2 Materials solutions for aggressive environments (HLM, steam)

Conventional steels (e.g ferritic/martensitic, austenitic steels) rely on magnetite and chromia scales for corrosion protection [54, 121, 124]. However, when exposed to aggressive environments (e.g. water/steam, molten chloride salts), chromia and magnetite scales become compromised because of the formation of volatile chromium oxy-hydroxide $CrO_2(OH)_2$, $Fe(OH)_2$ and CrO_4^{2-}[134, 136]. In contrast, alumina shows relatively low oxidation rate and high thermodynamic stability in corrosive environments (e.g. water vapor/steam, supercritical CO_2 conditions, molten sodium sulphate, molten Pb, metal dusting conditions) [81, 128, 137, 140].

Alumina-forming alloys are defined as the alloys containing aluminum which can in-situ form protective alumina-scales during exposure in oxygen-containing environments at elevated temperature. In the last two decades, alumina-forming ferritic FeCrAl alloys and alumina forming austenitic alloys (AFA) have received a lot of attention due to their excellent oxidation resistance and creep resistance (in case of AFA) at elevated temperature [79-88, 141, 145]. By alloying with certain amounts of Al, the ferrite FeCrAl model alloys with a general formula Fe-xCr-yAl (x>5, y>2.5 wt.%) can form an external alumina scale at 800 °C in pure oxygen [146]. In case of austenitic alloys, the model alloys with a formula Fe−(2.5-4)Al−(12-15)Cr−(12-30)Ni are able to form an external alumina scale when exposed to air with 10% water vapor at 650-800 °C [81, 141, 147]. In addition, high entropy alloys (HEA) are being considered as potential high temperature structural materials due to their high strength, hardness and ductility, potential superior oxidation resistance, and structural stability [99, 148, 153]. By alloying passive layer formation elements like Al or Cr, the alloys are

expected to withstand temperatures above 1000 °C via formation of a protective oxide scale in air conditions [154-155].

2.2.1 Alumina forming ferritic alloys (FeCrAl)

Alumina-forming FeCrAl alloys have attracted a lot of attention because of their excellent oxidation and corrosion resistance at elevated temperature [128, 130, 144]. The applications include heating element foils, thin wires in cooking plates, radiation devices, toasters, microwave equipment, washing machine to glow plugs, heat resistance wires and various protection tubes [141, 142, 145, 156, 157].

Considering the oxidation resistance of the Fe-Al alloy system, it was found that the addition of Cr significantly decreases the critical Al-content needed to form protective alumina scales, the so-called “third element effect” [146, 158, 159]. The effects of adding Cr are related to transition from internal to external oxidation, inhibition of the Fe external oxidation, and nucleation of α-Al_2O_3 on the corundum structure of Cr_2O_3 [158, 161]. Zhang et al. [159] exposed the Fe-10Al, Fe-5Cr-10Al and Fe-10Cr-10Al (at.%) alloys in 1 atm oxygen atmosphere at above 900 °C. The oxides formed on the surface of Fe-10Al consisted of mixtures of Fe and Al oxides and large quantities of Fe-rich oxide protrusions. As sufficient Cr is added (from 5 at.% Cr to 10 at.% Cr), the Fe-10Cr-10Al alloy is able to form an external alumina scale with a thickness less than 1 μm after 10 h exposure at 1000 °C.

Moreover, reactive elements (e.g. Y, Zr, Hf) are often added due to their positive effects on improving the oxidation resistance of alumina-forming alloys [162, 165]. The effects of minor addition of reactive elements manifest as (i) an increase of Al and Cr selective oxidation, which either induces the formation of protective scales at lower concentrations or accelerates the development of the protective scale in case of alloys with sufficient concentrations of these elements, (ii) a decrease of the oxidation rate, (iii) a change in the scale growth mechanism and (iv) a drastic improvement of the oxide scale adherence [162-168]. Cueff et al. [166-167] have compared the oxidation behavior of Kanthal A1 (without yttrium) and Kanthal AF (with 0.028 wt.% yttrium) in air at 1173 K. After 30 h oxidation test, the blade-like whiskers and small equiaxed oxide morphologies indicate the formation of both transition alumina (θ-Al_2O_3) and stable α-Al_2O_3 on yttrium-free alloy. In contrast, only α-Al_2O_3 is observed on yttrium-containing alloy Kanthal AF. In addition, the thin oxide layer formed on Kanthal AF (1 μm) compared with that formed on Kanthal A1 (2 μm) indicates that yttrium addition slows down the oxidation rate.

Regarding the aggressive environments related applications, the exposure of FeCrAl alloys in corrosive conditions (e.g. air+10%H_2O, molten Pb, steam, molten salts) has shown their excellent material compatibilities [66, 130, 158, 162, 166, 169, 171]. As an example, the corrosion behavior of

FeCrAl model alloys in molten Pb have been investigated [85, 138, 172]. A series of Fe-(6-16)Cr-(4-8)Al (wt.%) alloys were designed, prepared and exposed to 10^{-6} wt.% containing molten Pb at the temperature range of 400-600 °C [85, 138, 172]. After a certain exposure time (800-1800 h), an Al-rich oxide scale was formed to effectively inhibit corrosion caused by molten Pb on FeCrAl model alloys having the aluminum concentration $C_{Al} = 15.3\text{-}0.81\ (C_{Cr}) + 0.0156\ (C_{Cr})^2$ [wt.%], where C_{Cr} = 10-25 wt.% [138]. The thickness of the alumina scale formed on Fe-16Cr-6Al, measured from TEM cross section image, varies from 60-500 nm when the samples were exposed at 400-600 °C in oxygen containing molten Pb. Unfortunately, alloys (including steels) with body-centered cubic (BCC) structures are susceptible to liquid metal embrittlement (LME) at temperatures below 400 °C [173-174], and therefore the idea of using ferritic alloys in HLM environment was abandoned so far.

2.2.2 Alumina forming austenitic alloys (AFA)

Austenitic steel as structural component has its advantages for high temperature applications because of the excellent formability, weld ability and corrosion resistance [175, 178]. By alloying with low amount of Al (<5 wt.%), austenitic steels have the possibility to form an external alumina scale when exposed to high temperature oxygen containing conditions [81, 143]. However, Al stabilizes the bcc-structure and results in the loss of creep strength of austenitic steels at high temperature [143]. Therefore, the concentrations of Al have to be kept at low level in order to balance the alumina scale formation and high temperature mechanical properties.

Recently, a new alumina-forming austenite alloy (AFA) family Fe−(2.5-4)Al−(12-15)Cr−(12-30)Ni−(0.6-3)Nb (wt.%), which shows excellent oxidation resistance by forming protective alumina-rich scales, has been developed [81, 141]. These alloys have balanced the Al, Cr and Ni content in order to maintain the single austenite structure in the matrix and second strengthening phases mainly Fe_2Nb (Laves), β-NiAl (B2), γ'-Ni_3(Al,Ti) and MC (M=Cr, Nb) are employed to improve the creep resistance at elevated temperature [81, 179, 180].

The scientific community has reported the excellent corrosion resistance and mechanical properties of AFA alloys at high temperatures [81, 137, 143, 181, 184]. Yamamoto et al. [81, 179, 185] and Brady et al. [143, 147, 180, 186, 187] investigated the high temperature corrosion behavior and creep resistance of AFA alloys in air with 10% water vapor, as well as the influence of alloying elements like Nb, Ti, Zr, B, C, Y and Hf. Their results indicate that AFA alloys (Fe-20Ni-14Cr-3Nb-xAl base, wt.%) with a minimum of 2.5 wt.% Al is sufficient to form and maintain an external alumina scale when exposed to air with 10% water vapor at 800 °C [81, 143]. Reactive elements like Y, Hf and Zr have a positive influence on the oxidation performance of AFA alloys [147, 186, 187], as observed on alumina-forming ferritic alloys (FeCrAl). Due to the formation of strengthening phases like Fe_2Nb

(Laves), β-NiAl (B2), γ'-Ni_3(Al,Ti) and MC (M=Cr, Nb), AFA steels show an order of magnitude higher creep resistance than the commercial A286 super alloys at 750 °C and 100 MPa conditions [179, 185, 188].

Ejenstam et al. [181] have exposed two AFA steels (Fe-14Cr-14Ni-2.5Al-base, Fe-14Cr-20Ni-2.5Al-base, wt.%) in 10^{-7} wt.% oxygen containing molten Pb at 550 °C up to one year. Both AFA alloys have formed a thin alumina rich oxide scale (< 100 nm). Only the low Ni-containing AFA alloy (14Ni) did not show Ni dissolution in molten Pb. However, due to the low Ni content (austenite stabilizer), Electron Backscatter Diffraction (EBSD) analysis has indicated the formation of around 17% (volume fraction) ferrite phases in AFA steel after 1 year exposure at 550°C. Guo et al. [189] tested the AFA 316 stainless steels (Fe-16.7Ni-15.9Cr-3.5Al-base, wt.%) in aerated supercritical water (SCW) at 650 °C/25 MPa. AFA 316SS steels show the superior corrosion resistance over 316SS without Al addition due to the formation of protective Al-, Cr-rich oxide scale. He et al. [137] investigated the corrosion behavior of AFA steel (Fe-25Ni-13.8Cr-3.5Al-base, wt.%) in supercritical carbon dioxide at 450-650 °C and 20 MPa. At low temperature (<550 °C, exposure time: 1000 h) and high temperature (>550 °C) with exposure time less than 600 h, the substrates are protected by slowly growing Al_2O_3 and Cr-, Mn-rich oxide scale. While the exposure temperature and time increase, non-protective Fe-, Cr-rich multilayer instead of Al_2O_3 scale was obtained. Brady et al. [186] studied the corrosion behaviors of Fe–(25–45)Ni–(10–25)Cr–(4–5)Al wt.% base alloys in air with 10% water vapor at 1100 °C. The alloy Fe-35Ni-25Cr-4Al-base was protected by an external Al_2O_3 scale, while alloys with 45 Ni or 10 Cr show the internal oxidation behavior. In addition, minor additions of Nb and C seem to have a beneficial effect on the corrosion resistance while Ti and C promote internal oxidation. Kim et al. [140] investigated the steam oxidation behavior of alumina-forming duplex steels Fe-(18-21)Ni-(16-21)Cr-(5-6)Al (wt.%) in steam at 1200 °C. After 8 h exposure, Fe-18.7Ni-16.3Cr-6.14Al wt.% base AFA alloy has the lower mass gain than that of 310S. The layer formed on the surface, based on the XRD and EDS mapping, mainly consists of a thick outer Fe-Ni-Cr rich spinel layer and a continuous inner α-Al_2O_3 layer. Below the oxide scale, a depletion zone of B2-NiAl phase (up to tens of microns) was observed due to the formation of α-Al_2O_3 scale. Corrosion tests of AFA alloys in other conditions have shown the high compatibility of AFA alloys/steels with the extreme environments [184, 190, 192]. For instance, Yan et al. [184] exposed the Fe-25Ni-18Cr-3Al-base steel into molten sodium sulphate at 900 °C, and found the formation of a continuous alumina scale at the early stage. Put et al. [190] tested AFA alloys (Fe-23.6Ni-14.7Cr-7Al-base, wt.%) in metal dusting environments between 550-750 °C. The corrosion test of Fe-25Ni-14Cr-3.5Al-2.5Nb-base (wt.%) AFA steels in 60% $NaNO_3$/40% KNO_3 mixture shows the formation of a thin Al- and Cr-based oxide scale at 390 °C [191]. Brady et al. [192] investigated the corrosion behaviors of Fe-25Ni-13.8Cr-3.5Al-base, Fe-20Ni-13.8Cr-3Al-base and Fe-12Ni-13.9Cr-2.5Al

-base (wt.%) AFA alloys in simulated biomass cook stoves at above 600 °C. The exploration and the development of AFA steels have been focused so far mainly on the replacement of Ni-base alloys or austenitic steels in different environments [81, 143, 184, 190, 194]. However, due to the different physical and chemical interactions between metallic materials and HLMs, the direct transfer of AFA steels to these conditions (e.g. Pb, LBE) is questionable. Therefore, it is necessary to develop dedicated AFA steels, targeted for the HLMs applications, which are able to in-situ form protective alumina scale while maintain the austenitic matrix at the same time.

2.2.3 High entropy alloys (HEA)

High entropy alloy (HEA) is a relatively new concept. The early definition of HEA is based on the entropy of mixing [92]. Alloys can be classified as low entropy (entropy of mixing < 0.69R, R is gas constant), medium entropy (0.69R<entropy of mixing<1.61R), and high entropy (entropy of mixing>1.61R) alloys. According to Boltzmann's hypothesis, the high entropy contributed by the mixing of multi-metallic elements favors the stabilization of a single solid solution [92]. In literature there is an ongoing discussion about the terminology of HEA and similar concepts like multi-component alloys, etc [92, 99, 148, 149, 195]. One requirement for an alloy to form a HEA is to contain five or more principle elements with the concentration of each principle element between 5-35 at.% [194] . Yang and Zhang et al. [196] considered not only the entropy of mixing (ΔS_{mix}) but also the enthalpy of mixing (ΔH_{mix}). They found that HEA may form if the parameter $\Omega=(\Sigma c_i T_{m,i})\Delta S_{mix}/|\Delta H_{mix}|$ is larger than 1. Here, $T_{m,i}$ is melting temperature of element i. This consideration allows alloys with only three or four principle elements to form HEA, which expands the range for searching new HEAs.

In principle, multi-component alloys can exist as solid solution (SS), amorphous phase (AM) and intermetallic compounds (IM), depending on the alloying elements, chemical concentrations and solidification conditions [92, 93, 197, 199]. In order to minimize the number of trial-and-error experiments, some empirical approaches combined with high throughput calculations have been developed to predict the formation of solid solution, as separated from amorphous phase. Generally, these calculations are based on thermodynamic considerations (e.g. the Gibbs free energy of mixing (ΔG_{mix}), the enthalpy of mixing (ΔH_{mix}) and the entropy of mixing (ΔS_{mix})), a geometrical parameter (atomic size difference (δr)) and physical parameters (e.g valance electron concentration (*VEC*), electronegativity ($\delta\chi$)) [92, 196, 200, 203]. By limiting the range of the enthalpy of mixing and atomic radius difference, -15 kJ/mol < ΔH_{mix} < 5 kJ/mol and δr <6.6%, the formation of a solid solution can be predicted in the known HEA family which is based on the 3d transition metal family [197, 200]. However, there is still no effective theoretical method to separate the IM from SS [149, 199]. Moreover, Guo et al. [200] discussed the VEC of as-cast HEA and indicated this parameter can be used to predict the BCC or FCC solid solution formations. However, recent studies indicated that dual

phase (FCC+BCC) HEAs show even better mechanical properties (e.g. tensile, hardness, strength) compared with single solid solutions [98, 204, 208]. Lu et al. [209] have designed the eutectic high entropy alloys $AlCoCrFeNi_{2.1}$ with lamellar FCC/B2 structure. The tensile tests indicated that the as cast alloys show excellent strength and ductility up to 700 °C (at 700 °C: proof stress: 108 MPa, fracture stress: 538 MPa, and elongation: 22.9%). Song et al. [205, 210] reported the higher compressive strength (2279.5 MPa) and hardness (835 HV) value of dual phase (FCC+BCC phases) CrMnFeVTi compared with the single phase HEAs.

High entropy alloys are considered as the next generation structural materials due to their excellent mechanical properties (e.g. hardness, strength and fatigue resistance), oxidation/corrosion resistance and high temperature structural stabilities [99, 148, 152, 211, 213, 214]. Wang W.R. et al. [205, 215] and Wang R. et al. [216] systematically studied the AlxCoCrFeNi (x in mole radio, x=0-2.0) high-entropy alloy, mainly focused on the effect of Al on phase compositions, microstructure, mechanical properties (e.g. hardness, compressive stress), and corrosion resistance. As $x<0.4$ or $x>1.0$, the alloys show the single FCC or BCC solid solutions. When $0.4<x<1.0$, the alloy matrix consists of FCC and BCC dual phase structure. Increasing the Al content, the hardness of the alloys increased at the cost of the reduced ductility. The equiaxed dendrites $Al_{0.9}CoCrFeNi$ (FCC+BCC structure) alloy has reached the maximum hardness (Hv 527) among the as-produced alloys. Compared with AlSI304L stainless steel, the AlCoCrFeNi alloys after aging (at 800 °C, 1000 °C and 1200 °C) have lower corrosion potential and pitting potential in 0.6M NaCl, which means higher susceptibility to corrosion attacks. In addition, influences of adding fifth or sixth elements (e.g. Mn, Nb, Mo, V, Si, Ti, Zr, Y) on either the microstructures or the properties have been widely reported [207, 217-228]. Ma et al. [226] investigated the effect of Nb addition on the microstructure and properties of AlCoCrFeNi high entropy alloy. Both AlCoCrFeNi and $AlCoCrFeNb_{0.1}Ni$ alloys formed a single body-centered-cubic (BCC) solid solution phase. However, increasing the Nb content, for instance $AlCoCrFeNb_{0.25}Ni$, $AlCoCrFeNb_{0.5}Ni$ and $AlCoCrFeNb_{0.75}Ni$ alloys, promotes the formation of (CoCr)Nb type Laves phase. Besides, the compressive yield strength and Vickers hardness show an approximately linear increase as Nb amounts increase. Zhu et al. [227] investigated the effects of Mo addition on microstructure and mechanical properties of AlCoCrFeNi-based HEA alloys. For Mo content between 0.2 and 0.5 (mole ratio), Al and Mo segregate in different phases. The alloy strength was improved significantly by Mo addition. However, the ductility was reduced at the same time.

Regarding the oxidation/corrosion behavior of HEA alloys, Butler et al. [155, 213, 229, 230] investigated the high temperature oxidation behavior and structure stability of $Al_x(NiCoCrFe)_{100-x}$ (where x = 8, 10, 12, 15, 20, and 30 (at.%)). After 100 h isothermal oxidation at 1050 °C in air, all the

samples formed an external Cr_2O_3 scale combined with an internal Al_2O_3 layer. Increasing the Al content was reported to improve the oxidation resistance. Annealing treatment at high temperature (1050 °C for 520 h) and low Al content (<15 at.%) were found coarsening the microstructures. Chang et al. [207] studied the influence of Al and Ti on the microstructure and oxidation properties of $AlxCo_{1.5}CrFeNi_{1.5}Ti_y$. Their results indicate that Al can promote the γ′ phase formation instead of brittle η phase (Ni_3Ti). Moreover, $Al_{02}Ti_{03}$ ($Al_{0.2}Co_{1.5}CrFeNi_{1.5}Ti_{0.3}$) shows oxidation resistance by forming a continuous Cr_2O_3 layer during the isothermal oxidation at 900 °C for 200 h. Kai et al. [228] compared the oxidation behavior of FeCoNiCr-X (X=Al, Si and Mn) in dry air at 700-900 °C. By alloying Al or Si, the alloys show lower oxidation rates. Mn addition degrades the oxidation resistance of FeCoNiCr. The oxidation kinetics of all alloys follow the parabolic law. Another study of the oxidation of $Al_{1.3}CrFeNi$ at 1000 °C in air revealed a duplex structure (BCC/B2) in the matrix and oxide scales mainly consisting of Al_2O_3 and Cr_2O_3 [214]. Liu et al. [231] studied the oxidation behavior of high-entropy alloys AlxCoCrFeNi (*x*=0.15, 0.4) in supercritical water at 550 °C. Both HEAs show the superior oxidation resistance compared with heat resistance steel HR3C (25Cr-20Ni-Nb-N), in terms of forming thin spinel $(Fe,Cr)_3O_4$ oxide scales. The electrochemical tests of oxidized alloys indicate that the polarization resistance of the alloys was improved when the oxide scales passivated on the alloy surface. Cross section analysis indicates the formation of a duplex layer on $Al_{0.15}$ and a single Cr-rich layer on $Al_{0.4}$. As for the oxidation performed at 600 °C, mainly spinel was identified in the oxide scale.

Despite the enormous scientific interest in HEAs, there are no reports regarding the compatibility of HEA alloys with HLM and steam. Since the alumina based oxide scale shows superior stability in oxygen containing aggressive environments (e.g. steam, HLMs), it is essential to add the passive oxide scale forming elements in the potential HEA alloys.

3. Fundamentals and experimental methods

In this chapter, the experimental methods applied within this thesis are presented. First, the alloy production process including heat treatment is clarified. Then the basic principles of oxygen-control for the corrosion test in molten Pb and the oxidation tests in steam conditions are described. After that, various material microstructure characterization methodologies used in this investigation are explained, including X-ray diffraction pattern (XRD), scanning electron microscopy (SEM), focused ion beam (FIB), (scanning) transmission electron microscopy (S/TEM), and energy-dispersive X-ray spectroscopy (EDS). Finally, the details related with measurements of the material thermal-physical properties are given, namely differential thermal analysis (DTA), laser flash analysis (LFA), and thermal expansion coefficient determination.

3.1 Alloy preparation and heat treatment

The model alloys (AFA and HEA) are prepared by arc melting with non-consumable tungsten electrode in argon atmosphere using highly pure elements (purity>99.99%). The alloy ingots were flipped over and re-melted at least 5 times in a water-chilled copper mold in order to promote the homogenization of the compositions. After that, the as-cast AFA alloys were sealed in quartz tubes in Ar atmosphere and annealed at 1250 °C for 2 h, followed by water quenching. The HEA alloys were used in the as produced state without any further heat treatment.

3.1.1 Arc-melting process

The ingots were prepared under argon gas atmosphere in an arc melting system. Fig. 3-1 show a scheme and an image of the arc melting system used in this study. The main part of the system is consisted of a high vacuum chamber (around 1.1 dm^3) and a viewing glass. The water-cooled electrode with tungsten electrode tip is integrated in the support frame of the chamber. At the upper part of the support frame, an independent knob handle is used to move the electrode vertically and horizontally above the copper base plate. The water-cooled copper plate, which incorporates the crucible shape, can be taken off after the removal of the fixing screws. Alloying elements are put inside the crucible and heat-up by the arc between the electrodes and the alloying elements. The arc-melting process can be summarized as following: the chamber is pumped to vacuum conditions ($<5*10^{-2}$ mbar) before starting the melting process. Argon gas is used to sweep the chamber 2-3 times in order to support the pumping process. Then, the chamber is filled with high purity argon gas to a pressure of 1-1.5 bar. When applying the voltage to the system, an arc ignites between the tungsten electrode and the alloying elements placed in the crucible. By moving the electrode and by that the arc across the alloying elements, all metals are molten and alloyed. Before melting the pure elements, small pieces of Zr are molten to remove remaining oxygen in the

chamber. After melting the sample for tens of seconds, the arc can be turned off by gradually decreasing the current. The specimen is flipped over and re-melted at least 5 times to facilitate alloy homogenization.

In this experiment, a mini arc melting system (MAM-1, Serial-No.2426220) with a non-consumable tungsten electrode has been applied to prepare the as-cast alloys. The maximum temperature can reach up to 4000 °C. A scheme and an image of this furnace is shown in Fig. 3-1.

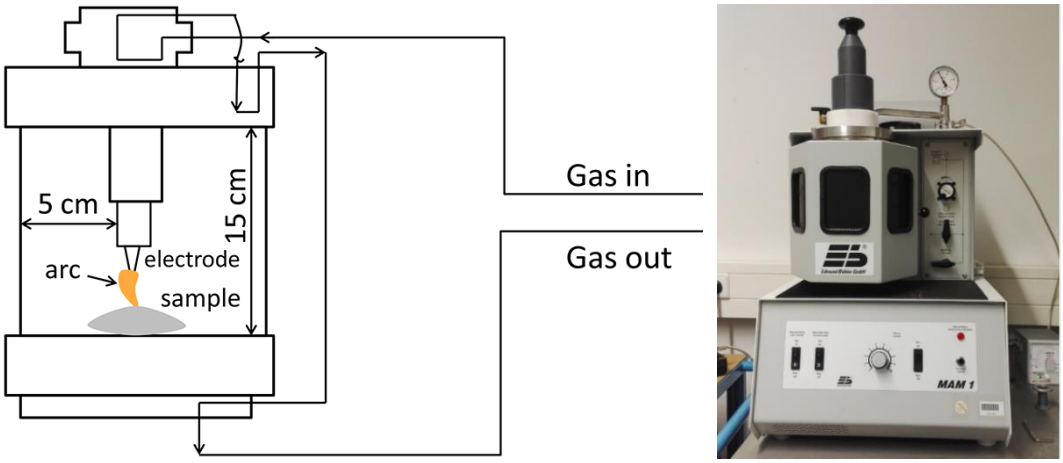

Fig. 3-1 Scheme of arc melting furnace used for as-cast alloy production.

3.2 Corrosion experiments

3.2.1 Corrosion test in oxygen containing molten Pb--COSTA

Since the metallic elements like Ni, Al, Cr, Fe have the dissolutions issues in molten Pb, the idea of in-situ oxidation of the alloy surface has been developed as a mitigation strategy to inhibit the corrosion attack caused by molten Pb [72, 110]. A facility developed for corrosion tests in stagnant liquid metals with controlled oxygen conditions is used in this study. In order to promote formation of oxide scale on alloy surface while avoiding the oxidation of the molten Pb, the oxygen concentration in the liquid Pb has to be controlled in a dedicated range. According to the Gibbs free energy of formation of Fe_3O_4 (structure) and PbO (fluid), the relation is displayed in following equation (3.1)[72]:

$$2\Delta_f G^0(PbO) > RT \ln P_{O2} > 0.5\Delta_f G^0(Fe_3O_4), \quad (3.1)$$

where $\Delta_f G^0$ (J/mol) represents the standard Gibbs energies of formation of PbO and Fe_3O_4; P_{O2} (bar) is the oxygen partial pressure in the atmosphere which is in equilibrium with the molten Pb; R denotes the universal gas constant (8.314 J/mol·K). T (K) is the temperature of molten Pb.

In a Pb pool with oxygen containing cover gas, the PbO formation can be described by the following reaction: $Pb+1/2\ O_2 \leftrightarrow PbO$. The equilibrium constant K is defined by equation (3.2).

$$K = \frac{a_{PbO}}{a_{Pb} a_{O2}^{1/2}} = \frac{c_O / c_{S,O}}{p_{O2}^{1/2}} = \exp(-\frac{\Delta G_{PbO}^0}{RT}) \quad , \tag{3.2}$$

where *K* represents the equilibrium constant; a_{PbO}, a_{Pb} *and* a_{O2} are the activities of PbO, Pb and O_2 in the equilibrium reaction. According to Henry's law for the solute in an ideal dilute solution $a_{PbO} = c_O / c_{S,O}$, where c_O (wt.%) is the oxygen concentration, and $c_{S,O}$ (wt.%) represents the oxygen solubility in Pb.

Based on the reference data, the relation between the oxygen partial pressure in the Pb pool and the temperature is given by the following equation (3.3) [110]:

$$logP_{O2} = 2\log c_o + 8.16 - \frac{16261}{T}. \tag{3.3}$$

The oxygen control system is initially designed for the passivation of Fe-based oxide scales in molten Pb environment. Here, the Fe oxidation reaction is employed to describe the oxygen controlling principle. Based on the Fe oxidation reaction in oxygen, shown in equation (3.4):

$$\frac{3}{4} Fe(s) + \frac{1}{2} O_2(g) = \frac{1}{4} Fe_3O_4(s), \tag{3.4}$$

the equilibrium constant is calculated by equation (3.5):

$$K_2 = \frac{a_{Fe3O4}^{1/4}}{a_{Fe}^{3/4} a_{O2}^{1/2}} = \frac{1}{p_{O2}^{1/2}} = \exp(-\frac{\frac{1}{4}\Delta G_{Fe3O4}^0}{RT}), \tag{3.5}$$

where K_2 is equilibrium constant; a_{Fe3O4}, a_{Fe} *and* a_{O2} are the activity of Fe_3O_4, Fe and O_2 in the equilibrium reactions. Here, the activity of solid Fe_3O_4 and Fe is taken as unit, $a_{Fe3O4} = a_{Fe} = 1$.
By setting the oxygen partial pressure lower than the oxygen partial pressure required to oxidize Pb but higher than that to form Fe_3O_4, the exposed metal Fe will be oxidized/passivated instead of Pb.

Due to the relatively low oxygen partial pressure (<10^{-20} bar) in the cover gas required for Fe_3O_4 formation, it is difficult to control the oxygen concentration directly by an O_2/Ar flow [72, 110]. Therefore, H_2/H_2O couple is here applied to adjust the oxygen content required for the passive oxide scale formation in molten Pb environments. The following equation describes the relation between the oxygen partial pressure and the H_2/H_2O ratio [110]:

$$\frac{P_{H2O}}{P_{H2}} = \frac{1}{(P_{O2})^{1/2}} \exp(\frac{\Delta fG^0(\mathrm{H_2O})}{RT}), \tag{3.6}$$

where P_{H2O}, P_{H2} and P_{O2} denote the partial pressure of H_2O, H_2 and O_2 in the reaction, respectively.
When oxygen and H_2/H_2O mixture exist as cover gas in the system, the relations read to:

$$\frac{P_{H2O}}{P_{H2}} = \frac{c_{o,s}}{c_o (P_{O2})^{1/2}} \exp(\frac{\Delta fG^0(\mathrm{H_2O})}{RT}). \tag{3.7}$$

The boundary conditions are the oxygen concentration for PbO formation (equation 3.8) and the one for Fe_3O_4 formation (equation 3.9):

$$\frac{P_{H_2O}}{P_{H_2}} = \frac{c_{o,s}}{c_o} \exp\left(\frac{\Delta fG^0(H_2O) - \Delta fG^0(PbO)}{RT}\right), \tag{3.8}$$

$$\frac{P_{H_2O}}{P_{H_2}} = \frac{c_{o,s}}{c_o} \exp\left(\frac{\Delta fG^0(H_2O) - \frac{1}{4}\Delta fG^0(Fe_3O_4)}{RT}\right). \tag{3.9}$$

In Fig. 3-2, an Ellingham-Richardson diagram shows the Gibbs free energy (ΔG) of oxide formation of Fe, Cr, Al and Pb as a function of temperature. Additionally, the scale on the right side of the diagram also provides the associated oxygen partial pressure (P_{O2}) and the respective one of the hydrogen/steam couple - H_2/H_2O. The dashed line shows the oxygen concentration in the molten Pb as a function of temperature. Both selected oxide formers, Al and Cr, being studied in this work exhibit a substantial lower Gibbs free energy of oxide scale formation than Fe, and therefore require lower amounts of oxygen partial pressure in the gas atmosphere. However, the dissolution of alloying elements is not considered in this diagram. Therefore, the oxygen concentration has been selected based on experience in the level required for Fe_3O_4 oxidation.

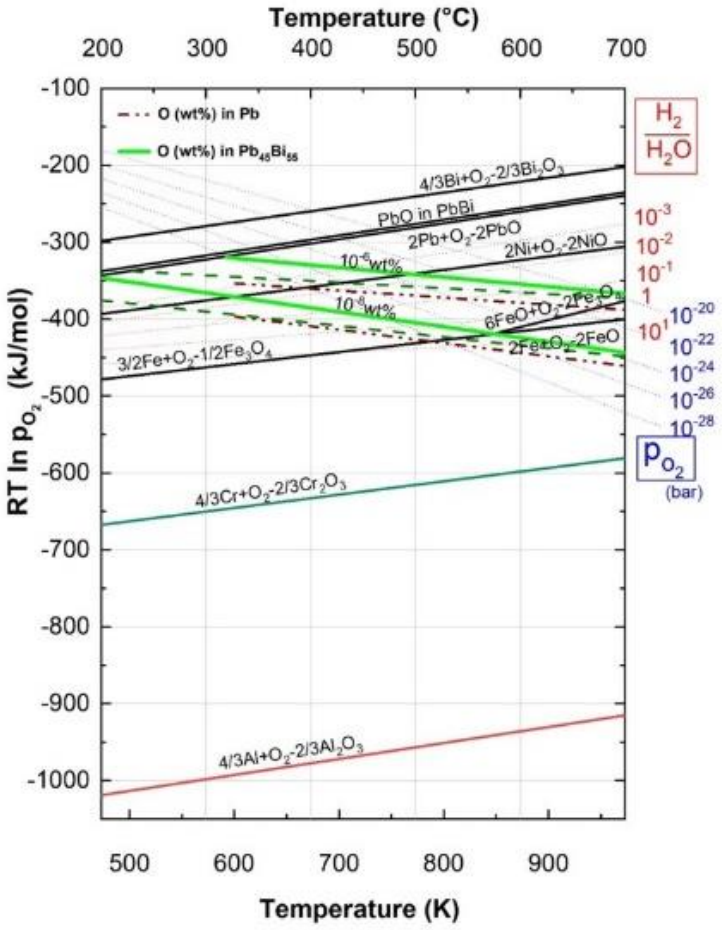

Fig. 3-2 Ellingham–Richardson diagram shows the Gibbs free energy of oxide formation of the alloying elements (Al, Cr, Fe, Ni) and of Pb, Bi respectively. Range of constant oxygen concentrations in Pb and the $Pb_{45}Bi_{55}$ melt indicate the stability regions of Fe, Cr, Al oxides without PbO precipitation in the temperature range.

Fig. 3-3 shows the schematic set-up of the oxygen control system in stagnant heavy liquid metal and its implementation in the COSTA facility [72, 110] illustrated in Fig. 3-3 (right). Gases of Ar and Ar/5%H_2 from separate bottles are mixed to obtain the required hydrogen amount. The mixed gas passes a moisturizer which is kept at controlled temperature by a thermostat to obtain the targeted water content and the specified H_2/H_2O ratio. Then the gas flows into the furnace, where an equilibrium between the oxygen partial pressure in the gas and the oxygen concentration in the molten Pb is achieved.

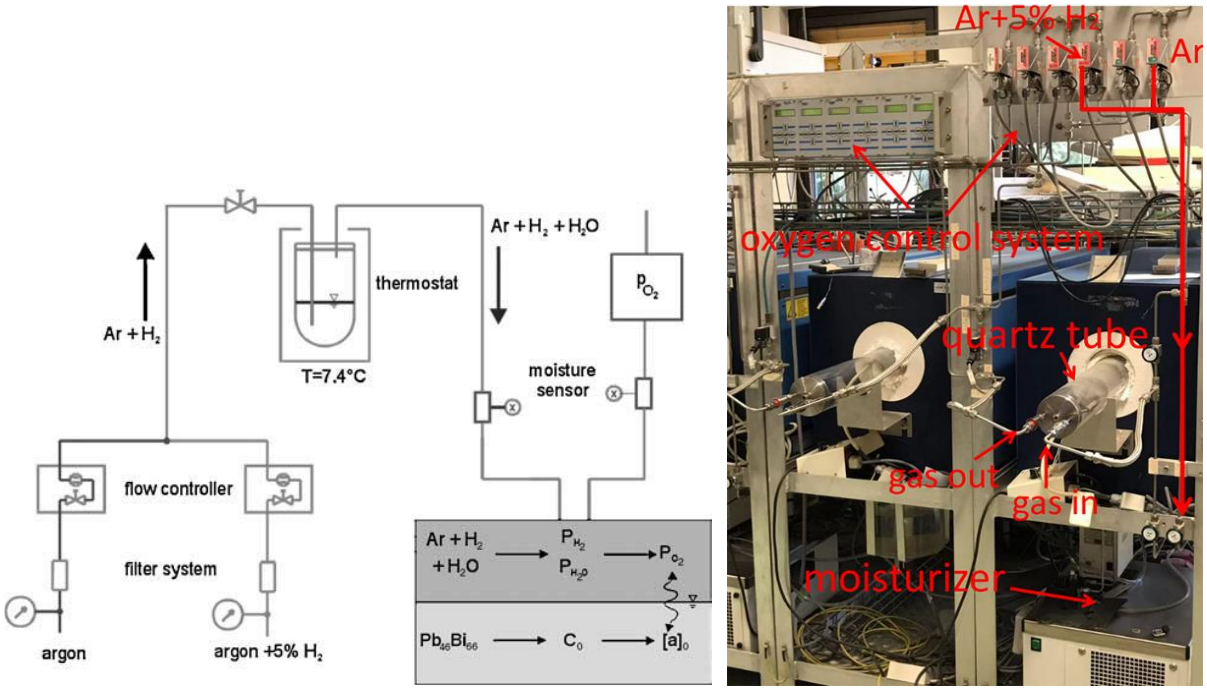

Fig. 3-3 Corrosion test in molten Pb with oxygen control; (a) schematic diagram of oxygen control system; (b) COSTA: stagnant heavy liquid metals corrosion test facility.

Alumina crucibles have been filled with Pb, subsequently placed on a Ni tray in a quartz tube inside the furnace. Further the liquid Pb is exposed to reducing conditions for 3 days, followed by 7 days at the specified exposure conditions. The procedure for exposing the alloys follows the one described in [70]. The prepared alloy ingots are cut into discs of around 10 mm diameter and 1.2 mm thickness. A hole with a diameter of 1.5 mm is drilled on each specimen near the edge. All specimens are grounded to a 1200 grit surface finish. Just before testing, the specimens are successively cleaned with water, acetone and ethanol in an ultrasonic bath, and after that dried. Each specimen is hanged using the hole and fastened to the alumina holders with a Mo-wire to prevent floating. In order to introduce the specimens into the pre-conditioned liquid Pb, a dedicated glove-box is used as air lock, conditioned to a similar oxygen partial pressure as in the quartz-tube. After connecting

the glove-box to the quartz-tube, the Ni-tray with all molten Pb-containing crucibles is transferred into the glove box. All the specimens are placed in the crucibles and fully immersed in the molten Pb. During this loading phase, which takes about 3 minutes, the temperature of the liquid Pb drops to about 450-500 °C. After putting back the Ni-tray with all crucibles and specimens into the quartz-tube, the temperature recovers to the set value within 10 min, while the oxygen partial pressure at the quartz-tube outlet recovers within less than 2 hours. During exposure tests, the oxygen partial pressure is continuously measured and kept constant at the set value.

The specimens are exposed at 550 °C for 1000 h and at 600 °C for 1000 h and 2000 h, respectively. After exposure, the samples are extracted from molten Pb using the same conditioned glove-box as for the loading process. Then, the remaining adherent Pb is cleaned by a mixed solution of acetic acid, hydrogen peroxide and ethanol (1:1:1) after cool down.

3.2.2 Oxidation test in steam--BOX rig

The steam oxidation test is performed in a horizontal tube furnace, called BOX rig, in atmospheric pressure, shown in Fig. 3-4 [130]. The tube is made by alumina, with a diameter of 32 mm and length of 600 mm. Molybdenum is used for the heater, which allows for a maximum temperature of 1700 °C (HTM Reetz GmbH, Berlin). As for the gas supply system, it consists of two gas flow controllers: a liquid flow controller and a controlled evaporator mixer unit (CEM). The CEM here plays the function of evaporator and gas mixer. During the exposure tests, the samples are put vertically. Only the arrow side touches the holder. Then the holder is placed in the center of the furnace. The temperature is controlled by a mantled thermocouple located above the sample. Oxidation tests are performed in flowing argon and steam gas environments. The flow rate is controlled to 20 l/h Ar and 20 g/h H_2O for steam oxidation.

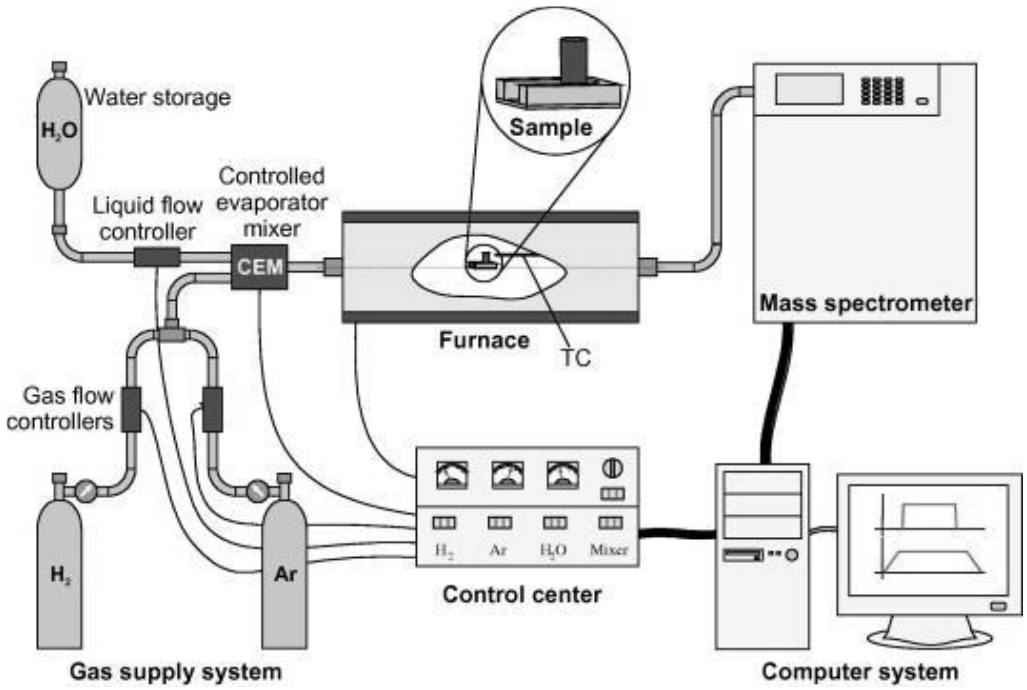

Fig. 3-4 BOX Rig for the high-temperature steam oxidation test.

During the experimental process, the specimens are first heated to 1200 °C in high purity Ar (6N) atmosphere with a gas flow rate of 20 l/h Ar, then the atmosphere is changed to 20 l/h Ar and 20 g/h H_2O (resulting in ~55 vol.% H_2O) for steam oxidation. The specimens are oxidized in a flowing argon and steam atmosphere. Argon is used as the carrier gas and the reference gas for mass spectrometer analysis. Finally, after the 1 hour isothermal exposure, the specimens are cooled down to room temperature by simultaneously changing the atmosphere back to high purity Ar with 20 l/h Ar flow rate. The heating and cooling rates are kept at 10 K/min. The off-gas tube from the furnace to the mass spectrometer is heated to about 150 °C to prevent steam condensation. The mass spectrometer is calibrated for H_2 with certificated Ar-H_2 gas mixtures. The hydrogen release rate is treated as a continuous measurement of the oxidation reaction kinetics.

3.3 Microstructural and thermo-physical properties characterization

3.3.1 Methods for microstructural properties characterization

X-ray diffraction pattern (XRD)

XRD is employed to identify the phase composition of the alloy matrix and that of the oxide scales formed after the corrosion test. The working principle is based on the Bragg's law. When the incident X-rays are diffracted by lattice atoms, they can form constructive interference once the path length difference is a multiple of the wavelength of the beam [232-233]. Usually, the Bragg-Brentano geometry, also called θ/2θ arrangement, is applied for lab test facilities. In this geometry, the sample and the detector are rotated precisely by the angles θ and 2θ respectively, while the X-ray source is kept stationary. Varying the incident angle of X-rays may cause the diffraction occurring on

dedicated crystal planes. Fig. 3-5 illustrates the schematic diagram of θ/2θ X-ray diffraction. The phase compositions of investigated alloys are analyzed by a Seyfert C3000 powder diffractometer (Cu-Kα radiation (λ=1.5406 Å)) with θ-2θ conventional geometry. The range of measurement (θ) varies from 10° to 90°.

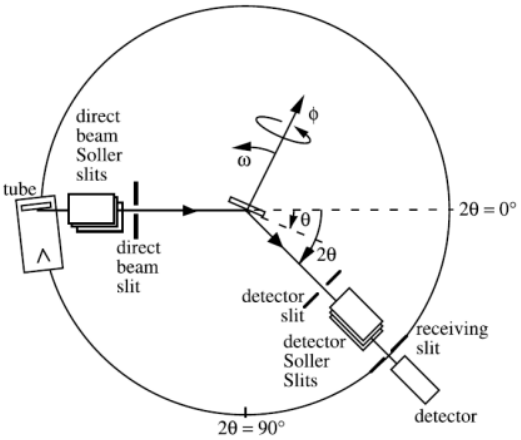

Fig.3-5 Schematic diagram of the functional set-up of θ/2θ X-ray diffraction (XRD) [233] provides to determine crystallographic structure, chemical composition, and physical properties of materials.

Scanning Electron Microscopy (SEM)

SEM is applied for the characterization of surface morphology and microstructure of samples before and after corrosion test. Fig. 3-6 shows the schematic diagram of interactions between the electron beam and matter in SEM. In a SEM system, a focused electron beam with energy ranging from 0.2-40 keV, interacts with the sample in a teardrop-shape (around 0.1-5 μm deep into the sample) [234]. A variety of signals are generated during the interaction, including secondary electrons (SE), backscattered electrons (BSE), diffracted backscattered electrons, and photons (characteristic X-rays) [235]. Secondary electrons yield in high-resolution surface images since they derive from surface near regions. Backscattered electrons come from deeper interaction regions of the sample and carry the information of "mass". In general, BSE images show contrast due to variations in chemical composition of a specimen, whereas SE images reflect mainly its surface topography. The areas of interest for transmission electron microscopy (TEM) investigations were defined by SEM. The SEM used in this study are Philips XL 40 SEM (cathode: LaB_6) with a working distance of 10 mm, and SEM Hitachi S-4800 (cathode: tungsten) with a working distance of 8 mm.

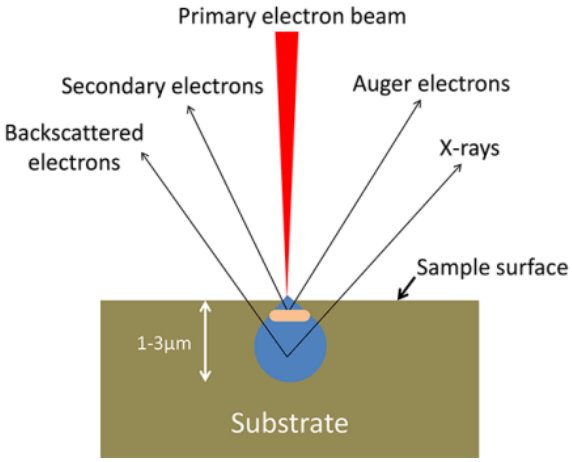

Fig. 3-6 Schematic illustration of interactions between the electron beam and a material sample in a SEM.

Focused ion beam (FIB)

A Dual Beam FIB-SEM system is applied to prepare the electron-transparent specimens for TEM evaluation. The basic idea of sample preparation by FIB is removing the atoms from the material by bombarding the target with accelerated heavy ions [236]. Gallium is the most commonly used ion source because of its low melting point (29.8 °C) and low vapor pressure. The FIBs used in this study are Zeiss Auriga 60 equipped with Omniprobe™ 400 micromanipulator (for AFA54, AFA75) or FEI Strata 400S Dual beam FIB equipped with Omniprobe™ 200 micromanipulator (for HEA1, HEA4).

To protect the target area from ion impacts by milling, a 2-step Pt deposition is applied: 200 nm Pt by e-beam deposition (30keV, 0° tilt), 2 µm Pt by ion-beam deposition (30keV, tilted to ion beam perpendicular, Strata 52°, Auriga 54°). The oxide scales of interest are located directly below the Pt-layer. The milling and later lift-out process at 30keV consist of the following steps. Firstly, 2 trenches are milled before and behind the deposited Pt layer (see Fig. 3-7 left). Then the samples are tilted back to 0° stage (tilt to achieve 52° or 54° with respect to the ion beam) in order to perform the so-called U-cut. In the third step, the micromanipulator is attached. At the end, the lamella is completely cut from the bulk and lifted-out. Then the lamella is attached to a Cu-lift-out grid for later TEM analysis and removed from the micromanipulator.

For the final thinning to electron transparency, the lamella is over-tilted by 1.5°, and the milling continues on alternating sites in a small window at 30 keV. For the final polishing an over-tilting of 3° @ 5 keV and 5° @ 2 keV on alternating sites for 2 min each is used.

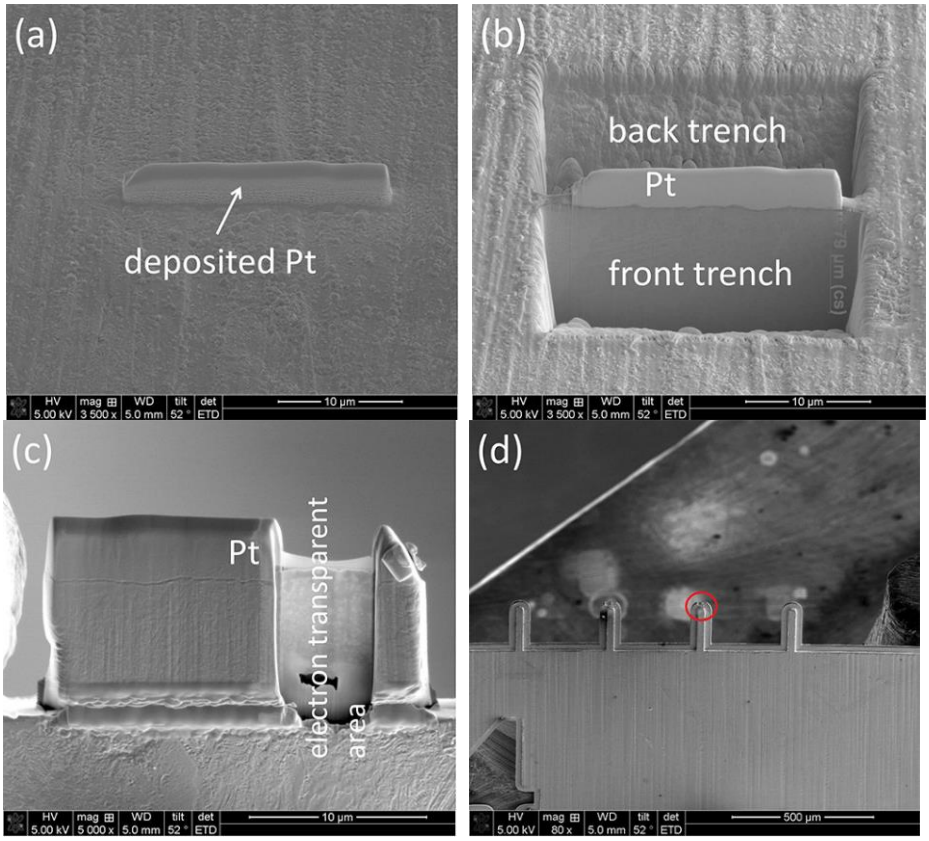

Fig. 3-7 Examples of TEM foil preparation by FIB milling process, (a): Pt deposition on surface; (b): trenches before and behind the target area; (c): final TEM-lamella with electron transparent area, (d): TEM-lamella on a lift-out grid (red circle).

(Scanning) Transmission electron microscopy (S/TEM)

S/TEM comprises a variety of different techniques that provide information on morphology, structure and composition of a sample [237]. In general, the optical setup in a transmission electron microscope is similar to an optical microscope. Instead of light, accelerated electrons (usually 200 to 300 keV) are used as probing beam, and the lenses are electromagnetic lenses. The point resolution of modern S/TEMs without corrector is usually around 0.2 nm or even better.

As the investigated TEM samples are thin (usually <100 nm), the interaction volume of accelerated focused electrons with matter is small compared to SEM (compare with Fig. 3-6), and mostly coherent forward scattering occurs. The electrons go through the sample. Unscattered electrons as well as elastically scattered electrons are used for imaging and diffraction. The region of interest contributing to electron diffraction is selected by the selected area aperture. With the objective aperture centered on the un-scattered central beam a bright-field image results. For high-resolution images, a large objective aperture (100 µm or larger) is centered, also including scattered electrons in the image, and a magnification above 250.000 must be selected. For dark-field imaging, a small objective aperture (20 µm) is centered, and the electron beam is tilted, so that the diffraction spot of interest appears in the center of the aperture. In the scanning transmission mode,

the focused electron beam rasterizes the sample. A High Angle Annular Dark-Field detector (HAADF) detects the transmitted signal.

The instrument used is a FEI Tecnai G² F20 ST, operated at 200 keV with a field emission gun, equipped with an Orius SC600 CCD Camera (Gatan, Pleasantron, California, USA) for image acquisition, a S-UTW EDS Si(Li) Detector (EDAX, Mahwah, New Jersey, USA) for elemental analysis, and a HAADF-detector for STEM-mode.

The samples are mounted in a double-tilt analytical holder that is optimized for EDS analysis.

Energy-Dispersive X-ray Spectroscopy (EDS)

Due to the interaction of accelerated electrons with matter, characteristic X-ray signals are generated in a SEM, as already mentioned before (see Fig. 3-6), and also in a TEM. Therefore, EDS combined with SEM/TEM is used to collect the X-rays for chemical compositions analysis of regions of interest. In addition, to determine the thickness of oxide scales observed in SEM cross sections, the FWHM (Full Width at Half Maximum) of the measured respective EDS signal is used.

During TEM investigations, the EDS-line profiles and elemental mapping are acquired in STEM mode, using drift correction. The samples are tilted 20° towards the detector to improve signal/noise ratio. Data evaluation has been done with TIA™, a proprietary software of FEI.

3.3.2 Methods for thermo-physical properties characterization

Differential thermal analysis (DTA)

DTA is applied in this investigation to define the annealing temperature. In DTA measurement, both the sample and a reference undergo the same procedure of thermal cycle. The temperature difference between sample and reference is recorded as a function of temperature, which allows to determine melting, sublimation and other phase transitions.

Laser flash analysis (LFA)

Thermal conductivity (λ: W/(m·K)) is the ability of material to conduct heat. It is calculated by equation (3.10) [238].

$$\lambda(T) = \rho(T) \cdot c_p(T) \cdot a(T), \tag{3.10}$$

where ρ is the material density (kg/m^3), C_p the specific heat capacity (J/g/K), and α (m^2/s) is the thermal diffusivity. In order to evaluate the thermal conductivity of the prepared alloys, thermal diffusivity, specific heat capacity and density have to be measured.

Thermal diffusivity refers to how fast a material reacts to the temperature change. A LFA is used to measure the diffusivity a. The principle of LFA is applying an energy pulse to heat one surface of

the sample. Then, the temperature change of the opposite surface parallel to the heated one is measured by an infrared detector. Fig. 3-8 describes the temperature change curve during the thermal diffusivity measurement [238].

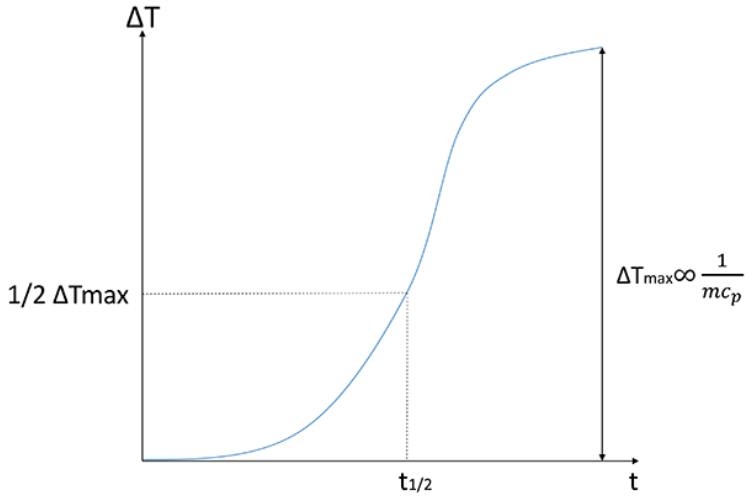

Fig. 3-8 Sketch of the temporal temperature change during the measurement of thermal diffusivity using a LFA.

The thermal diffusivity can be calculated according to equation (3.11) [238]:

$$a = 0.1388\frac{d^2}{t_{1/2}}, \tag{3.11}$$

In which $t_{1/2}$ (s) denotes the time value at half signal height and d (m) the thickness of the plate sample. The specific heat capacity can be calculated by equation (3.12)

$$c_p^{sam} = \frac{T_{max}^{ref}}{T_{max}^{sam}} \cdot \frac{(\rho \cdot l)^{ref}}{(\rho \cdot l)^{sam}} \cdot c_p^{ref}, \tag{3.12}$$

where T (K) is the temperature, ρ (kg/m^3) the material density and l (m) the thickness of the plate sample. The LFA used in this measurement is LFA 457 MicroFlash. The size of plate sample is 10x10x1.5 mm. The measurements are performed in a temperature range of 50-800 °C.

Thermal expansion coefficient

Thermal expansion defines the change of material size due to a temperature change. The linear thermal expansion refers to the material length change due to heating/cooling. The coefficient of thermal expansion α can be calculated by:

$$\alpha = \frac{\Delta L}{L \cdot \Delta T}, \tag{3.13}$$

where L (m) is the original length of the test material, ΔL (m) the length change and ΔT (K) is the change in temperature.

A 10 mm long rod type sample with a diameter of 3 mm is used in this measurement. During the measurement, the sample is inserted into the sample holder with one side being in contact with

a pushrod. The expansion or shrinkage caused by temperature change can be detected by the displacement system connected to the pushrod. The investigated temperature range is 25-1000 °C. The equipment used in this study is DIL 402 (Dilatometer Series).

4. Design, microstructure, and thermo-physical properties of as produced materials

4.1 Model alloy design

Considering the aggressive environment (molten Pb, steam) involved applications, the candidate alumina-forming alloys require to be compatible with extreme conditions like high temperature, corrosion, and radiation in case of nuclear systems. Therefore, the following criteria are defined to help tailor the composition of potential alloys:

(i) High temperature (>550 °C) corrosion resistance by forming alumina-based scale during exposure.

(ii) FCC structure to avoid liquid metal embrittlement.

(iii) Long time structural stability, avoiding phase transitions that may cause degradation during exposure.

(iv) Excellent thermo-physical (specific heat capacity, thermal diffusivity, thermal conductivity, thermal expansion) and high temperature mechanical properties (creep, fatigue resistance, etc.).

(v) Competitive costs and alloying elements (raw materials) availability.

(vi) Alloying elements with low neutron absorption cross section area (σa <10 barns) means low activation materials under radiation, in case of application in nuclear environment.

4.1.1 AFA model alloys design

4.1.1.1 AFA-1st generation

Corrosion resistance is one of the most important requirements for materials in contact with HLM [29]. The design activity is directed towards finding an appropriate set of composition ranges for the quaternary Fe-Cr-Al-Ni system, where Al acts as a ferrite stabilizer and alumina layer former, Cr as a ferrite stabilizer, chromia layer former and provider of the third-element effect, and Ni as an austenite stabilizer. Basically, two requirements are taken into consideration: (i) passivate Al_2O_3 base oxide scale during exposure in oxygen containing conditions (molten Pb, steam) at temperatures above 550 °C (molten Pb: 550-600 °C; steam: 1200 °C) and (ii) maintain the austenitic structure of the matrix during high temperature exposure.

In order to promote the formation of an alumina scale, an Al concentration ranging between 2 and 4 wt.% is chosen to sustain the formation of protective alumina scale and to avoid the excessive ferrite formation and the alloy embrittlement. Four Cr concentrations, namely 12, 14, 15 and 16 wt.%, are selected to ensure a strong third element effect on the alumina formation and, at the same time, to limit the formation of ferrite and Cr-rich phases. Considering the amount of Ni addition, the Ni fraction varies between 20 and 29 wt.%, depending on the equivalent

concentrations of bcc stabilizer (Al, Cr), in order to stabilize the austenite at the exposure temperature range. On the other hand, the Ni content has to be chosen as low as possible due to its high solubility in molten Pb and the high costs.

Based on the introductory notes, the phase-stability diagrams at 550 °C and 600 °C for the Fe-12Cr-xAl-yNi, Fe-14Cr-xAl-yNi, Fe-15Cr-xAl-yNi and Fe-16Cr-xAl-yNi systems are calculated using the commercial software Thermo-Calc (TCFE7 database) [239]. As an example, the superimposed calculated phase diagrams for Fe-(12, 14, 15 and 16)Cr-xAl-yNi systems at 600 °C are shown in Fig. 4-1. The selected alloy compositions (Table 4-1) with the general formula Fe-(12-16)Cr-(2-4)Al-(20-29)Ni, are close to the separation lines between the stability domains of the austenite(γ) and austenite plus ferrite(γ+α). The figure also contains the point corresponding to 316 austenitic stainless steel, which is located very close to the separation lines of γ and γ+α phases.

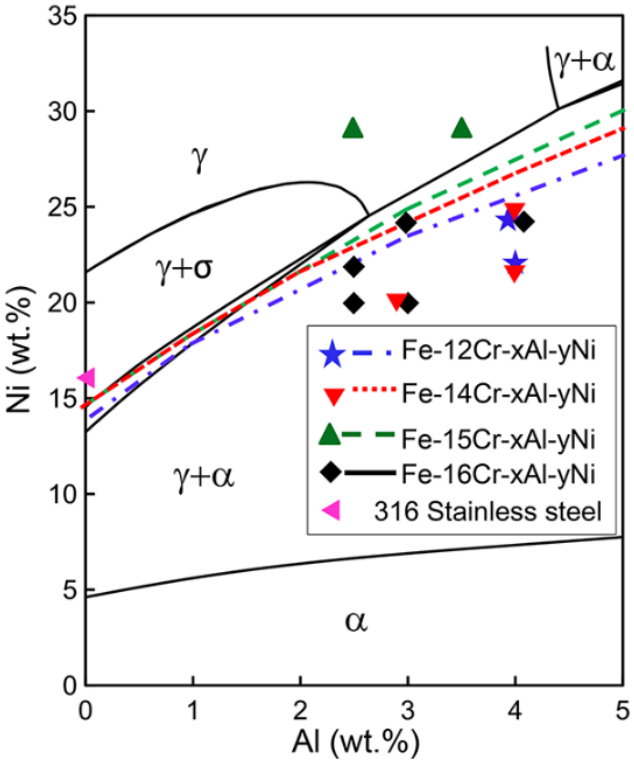

Fig. 4-1 Calculated phase diagrams of Fe-(12, 14, 15, 16)Cr-xAl-yNi model systems at 600 °C, with the coordinates of the selected nominal compositions for this study and the 316 steel indicated: ★ – AFA48, AFA51; ▼ – AFA45, AFA49, AFA52; ▲- AFA55, AFA56; ◆ – AFA46, AFA47, AFA50, AFA53, AFA54; ◀ - 316; [70].

Table 4-1 Nominal compositions of the first generation AFA model alloys designed for this study (wt.%).

Code	Cr	Al	Ni	Fe
AFA45	14	3.0	20	Balance
AFA46	16	2.5	20	Balance
AFA47	16	3.0	20	Balance

AFA48	12	4.0	22	Balance
AFA49	14	4.0	22	Balance
AFA50	16	2.5	22	Balance
AFA51	12	4.0	24	Balance
AFA52	14	4.0	24	Balance
AFA53	16	3.0	24	Balance
AFA54	16	4.0	24	Balance
AFA55	15	2.5	29	Balance
AFA56	15	3.5	29	Balance

In addition, the empirical Schaeffler diagram, which is developed by stainless steel industry, has been employed to estimate the types of structural phases and their amounts as a function of the chemical composition of the steels [240]. With this diagram a rough evaluation of the phase constitution of the stainless steels at ambient temperature, following the water cooling from liquid phase or from austenite domain (>1200 °C) can be made using nickel and chromium equivalents [240-241]. Fig. 4-2 depicts the Schaeffler diagram where the first generation of the AFA model alloys selected for the current corrosion study are implemented. According to this diagram, all model alloys have an austenite structure at room temperature. For comparison, two commercial austenitic stainless steels (AISI 310 and AISI 316) are also marked in the diagram. In the industrial process, in order to stabilize the austenite structure, the final heat treatment of the commercial austenitic stainless steels is made at temperatures around 1100 °C, followed by rapid cooling. In principle, the Schaeffler diagram predicts the microstructural outcome of this process.

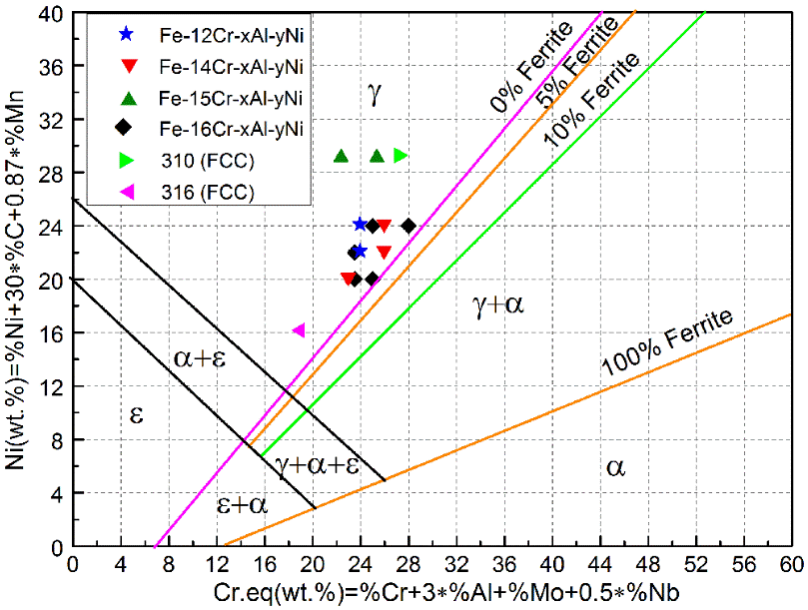

Fig. 4-2 Schaeffler constitution diagram including the coordinates of the Fe-Cr-Al-Ni model alloys and two references: stainless steels AISI 310 and AISI 316 (γ - austenite, α - ferrite, ε - martensite).

Both design tools are of value for the current study since the Schaeffler diagram estimates the initial (before tests) phase constitution, while Thermo-Calc calculations predict the phase equilibrium after the long-term exposure at 550 °C and 600 °C.

4.1.1.2 AFA-2nd generation

The backbone compositions of AFA-2nd generation model alloys are defined based on the corrosion test results of AFA-1st generation alloys. Two elemental additions to the backbone compositions are considered: a reactive element, yttrium (0.5 wt.%), with positive effects on the scale formation and adherence[162, 165], and niobium (1.5 wt.%) to promote the formation of Fe_2Nb Laves phase precipitates, which are beneficial for high-temperature strengthening (creep strengthening) [179, 188].

Three AFA model alloys of 2nd generation containing Y based on the formula Fe-(14-16)Cr-2.5Al-(18-22)Ni-0.5Y, and another three samples containing Y and Nb based on the formula Fe-(15-16)Cr-(2-3)Al-(20-29)Ni-0.5Y-1.5Nb have been considered for preparation and investigation, which are shown in Table 4-2.

Table 4-2 Nominal composition of the second generation AFA model alloys (wt.%).

Code	Cr	Al	Ni	Y	Nb	Fe
AFA70	14	2.5	18	0.5	--	Balance
AFA71	15	2.5	20	0.5	--	Balance
AFA72	16	2.5	22	0.5	--	Balance
AFA73	15	2.0	20	0.5	1.5	Balance
AFA74	15	3.0	29	0.5	1.5	Balance
AFA75	16	3.0	24	0.5	1.5	Balance

The equilibrium phase diagram calculated by the Thermo-Calc (TCFE7 database) and containing the coordinates of the 2nd generation AFA alloys, is depicted in Fig. 4-3. The compositions of AFA-2nd generation alloys are in the same region with the compositions of the 1st generation AFA model alloys, close to the separation lines between the stability domains of the austenite(γ) and austenite plus ferrite(γ+α).

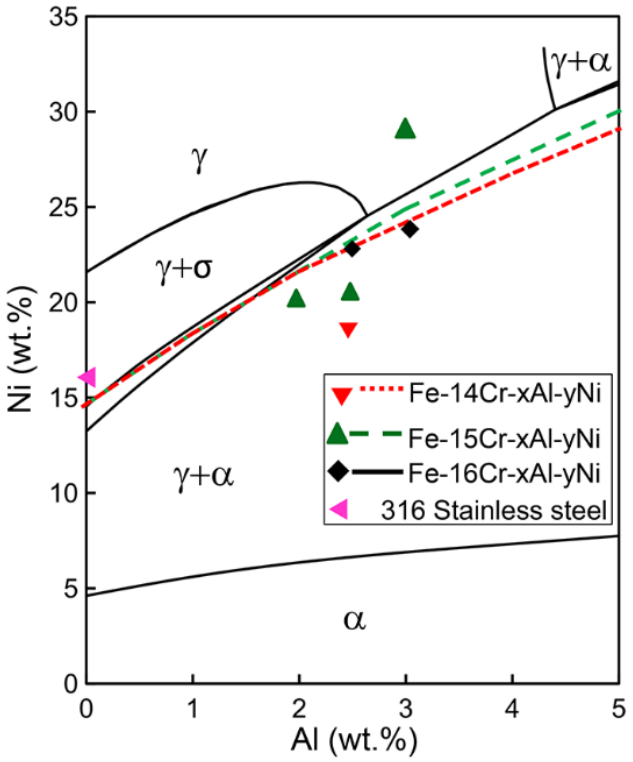

Fig. 4-3 Phase diagram of Fe-(14-16)Cr-(2-3)Al-(18-29)Ni-0.5Y-(1.5Nb)with the coordinates of the 2nd generation AFA model alloys, ▼ – AFA70; ▲– AFA71, AFA73, AFA74; ◆ – AFA72, AFA75; ◀ – 316.

Further confirmation by the Shaeffler diagram shown in Fig. 4-4 indicates that all the 2nd generation compositions fall into the FCC structure at room temperature.

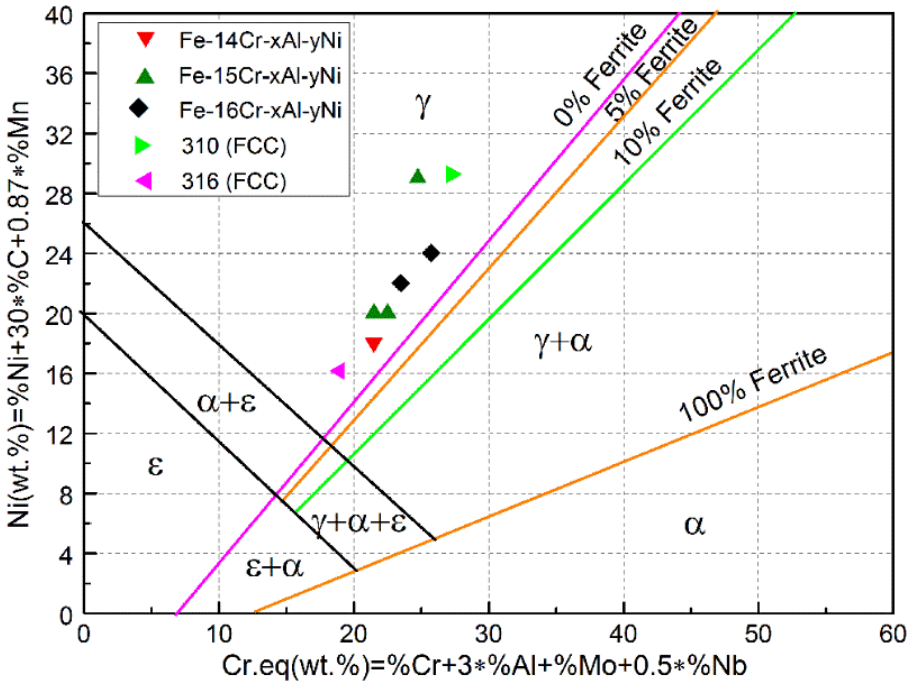

Fig. 4-4 Schaeffler constitution diagram including the coordinates of the Fe-Cr-Al-Ni-Y-Nb model alloys and two references: stainless steels AISI 310 and AISI 316 (γ - austenite, α - ferrite, ε - martensite).

4.1.2 HEA model alloys design

4.1.2.1 Selection of alloying elements

The design of HEA starts from the general premises enumerated in the introduction of this chapter: corrosion resistance in molten Pb and steam, stable FCC structure of the alloy matrix, excellent high-temperature thermo-physical and mechanical properties, competitive costs, raw materials availability and in case of nuclear applications to be made from low activation elements. Moreover, besides the single phase FCC HEA, model alloys from a new category called dual-phase HEA (DP-HEA) [98, 208], in which the solid solution is strengthened by secondary phase precipitations, are considered in this study for applications in HLM and steam environments. The most common intermetallic compounds used are: NiAl (B2 phase), $L1_2$-$Ni_3(AlTi)$ (γ' phase) and Fe_2Nb (Laves phase) [208, 242, 245].

Fig. 4-5 depicts the lattice structure of potential candidate elements [246]. Most elements have either BCC or HCP phases. Transition elements as Mn, Ni and Cu are FCC structural elements. Aluminum also has FCC structure, but stabilizes the BCC phase. Co has HCP phase structure and stabilizes the FCC structure. In order to obtain the target FCC dominated structure, at least one element from Mn, Ni, Cu and Co must be added. However, element Mn is not considered since a high Mn content in HEA alloys degrades the oxidation resistance [207, 228].

H		BCC		FCC		HCP											He
Li	Be											B	C	N	O	F	Ne
Na	Mg											Al	Si	P	S	Cl	Ar
K	Ca	Sc	Ti	V	Cr	Mn	Fe	Co	Ni	Cu	Zn	Ga	Ge	As	Se	Br	Kr
Rb	Sr	Y	Zr	Nb	Mo	Tc	Ru	Rh	Pd	Ag	Cd	In	Sn	Sb	Te	I	Xe
Cs	Ba	Lu	Hf	Ta	W	Re	Os	Ir	Pt	Au	Hg	Tl	Pb	Bi	Po	At	Rn
Fr	Ra	Lr	Rf	Db	Sg	Bh	Hs	Mt	Ds	Rg	Uub		Uuq				

Fig. 4-5 Lattice structure of some elements displayed in periodic table.

Moreover, refractory elements, like Nb, Ta, W, Zr, V, Ti, are also considered due to the capability to improve the high temperature mechanical properties [208, 220, 222, 226, 248]. Mo is not considered due to its susceptibility to σ phase formation [223, 249]. In case of nuclear applications, radiation resistance has to be considered as well. Table 4-3 gives the thermal neutron absorption cross sectional area of some elements, which corresponds to the absorption of thermal neurons with a velocity of 2200 m/s and an energy of 25.3 meV [246]. The elements Si, Zr, Al, Nb, Y, Fe and Cr have neutron absorption cross sections lower than 5 barns. Elements with a relatively large neutron absorption cross section like W, Co and Ta are not considered in this study as candidate elements.

Table 4-3 Neutron absorption cross sectional area of selected elements [246].

Element	atomic number	σa (barn)	Element	atomic number	σa (barn)
Si	14	0.171	Ni	28	4.49
Zr	40	0.184	V	23	5.08
Al	13	0.232	Co	27	37.2
Nb	41	1.15	Hf	72	104
Y	39	1.28	Ta	73	20.6
Ru	44	2.56	W	74	18.3
Fe	26	2.56	Ti	22	6.09
Cr	24	3.1	Cu	29	3.78

Based on the formulated selection pre-requisites, the following seven elements are selected in this study for the HEA design: Al, Cr, Ni, Fe, Nb, Ti, and Cu. Some elements are also the core (Fe, Cr, Ni, Al) or the minor (Nb) constituents of alumina-forming austenitic alloys studied in this work [70].

4.1.2.2 Design rules

Although only seven elements are considered, there are 56 possibilities when combining four or five elements in equal atomic ratio and an infinitely large number of non-equal molar combinations. In order to minimize the number of trial-and-error experiments, some empirical parameters have been applied to predict the formation of solid solution and intermetallic compounds. The parameters considered in the current work are the enthalpy of mixing (ΔH_{mix}), atomic size difference (δr), the parameter Ω calculated from the enthalpy of mixing, the entropy of mixing (ΔS_{mix}), the melting temperature of the alloy (T_m) and the valence electron concentration (*VEC*).

ΔH_{mix} is defined by the following equation (4.1):

$$\Delta H_{mix} = \sum_{j>i}^{n} 4 H_{ij} c_i c_j \,, \tag{4.1}$$

where H_{ij} is the mixing enthalpy of the binary *i-j* alloy system and c_i, c_j are atomic concentrations of elements i, j.

Considering the candidate elements, the mixing enthalpy of binary alloy A-B, calculated with Miedema's method, are given in Table 4-4. The Miedema method providing an estimation of the mixing enthalpies for all binary solutions, is based on a macroscopic atom model in which the electron density at the Wigner-Seitz cell boundary and the chemical potential of electronic charge of pure metals are used as inputs. Having a rather fair accuracy, this method gives a quick access to the enthalpies of mixing [250].

Table 4-4 Mixing Enthalpy ΔH_{mix} (kJ/mol) of binary alloy A-B calculated with Miedema's method [249].

	Al	Cr	Fe	Ni	Nb	Cu	Ti	

Al	0	-10	-11	-22	-18	-1	-30	Al
Cr		0	-1	-7	-7	12	-7	Cr
Fe			0	-2	-16	13	-17	Fe
Ni				0	-30	4	-35	Ni
Nb					0	3	2	Nb
Cu						0	-9	Cu
Ti							0	Ti

Another criterion considered in this investigation for the alloy design is the atomic size difference (δr). The atomic radius is defined as the half of the inter-nuclear distance in the crystal of the elements [252]. Table 4-5 shows the atomic radius of elements used in HEA design [253]. According to the Hume-Rothery's rule, solid solutions are favored when the alloys are made from elements with similar atomic size. The following equation (4.2) defines the δr in a multi-component system [197].

$$\delta_r = \sqrt{\sum_{i=1}^{n} c_i \left(1 - \frac{r_i}{\bar{r}}\right)^2}\ , \tag{4.2}$$

where $\bar{r} = \sum c_i r_i$, r_i represents the atomic radius of element i.

Table 4-5 Atomic radius and valance electron concentrations of elements used in the HEA alloy design [253].

Element	Atomic radius (Å)	VEC
Al	1.432	3
Cr	1.249	6
Fe	1.241	8
Ni	1.246	10
Nb	1.429	5
Cu	1.278	11
Ti	1.462	4

Zhang et al. [197] were the first to propose criteria for the phase formation in the high-entropy alloys based on the atomic size difference (δr), the enthalpy of mixing (ΔH_{mix}) and the entropy of mixing (ΔS_{mix}). By plotting the reported values of (ΔH_{mix}) in HEA versus δr (Fig. 4-6), they obtained a phase formation map displaying the stability domains of the solid solutions, ordered solid solutions, intermediate phases (intermetallic compounds) and bulk metallic glasses. The figure shows that the disordered solid solutions are formed when ΔH_{mix} is in the range from -15 to 5 kJ/mol, while δr is between 1% and 6.6%. In case of the disordered solid solutions, the entropy of mixing reaches a maximum which is higher than that of amorphous phase and intermetallic compounds when the alloying elements are in equiatomic ratio.

The parameter Ω proposed by Yang and Zhang et al. [196] is defined by equation (4.3):

$$\Omega = \frac{Tm \cdot \Delta S_{mix}}{|\Delta H_{mix}|}, \tag{4.3}$$

where $T_m = \Sigma c_i T_{m,i}$, $T_{m,i}$ is the melting point of element i.

This parameter Ω is used to estimate the high-entropy solid-solution formation. It needs to be larger than 1.1 for alloys to form HEA [196].

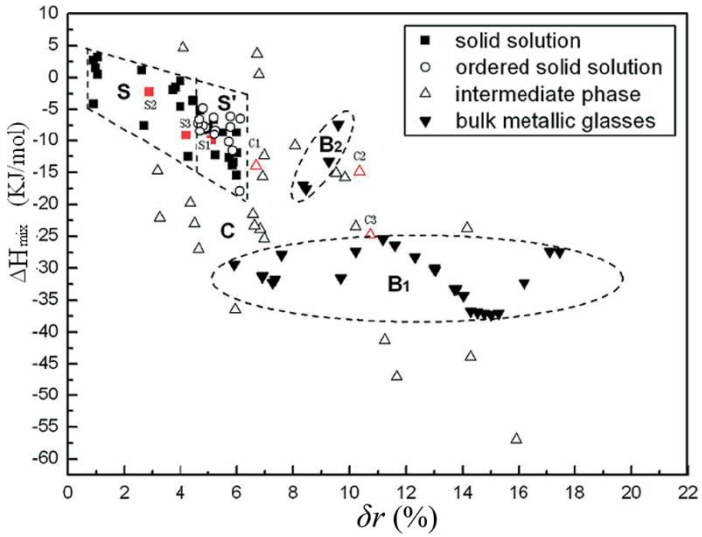

Fig. 4-6 Phase formation map in HEA, based on the enthalpy of mixing (ΔH_{mix}) and atomic size difference (δr): "solid solution" indicates the alloy contains only disordered solid solution, "ordered solid solution" indicates minor ordered precipitates besides solid solution and "intermediate phase" indicates there is precipitation of intermediate phases like the intermetallic compound [196].

Guo et al. [200] proposed the valence electron concentration (*VEC*) as an additional criterion for the prediction of the phase stability in high-entropy alloys. According to the definition, *VEC* of a multi-element system can be expressed as in equation (4.4) [200]:

$$VEC = \sum c_i \cdot VEC_i, \tag{4.4}$$

where c_i and VEC_i are the atomic percentage and valence electron concentration of the *i*-th element (Table 4-5). Moreover, Guo et al. [200] found that *VEC* can be used to quantitatively predict the stability of the solid-solutions with FCC and BCC structures, formed in high-entropy alloys. For BCC-solid solution *VEC* < 6.8, while for FCC, *VEC* ≥ 8. These values were carefully reviewed and adjusted later: the intermetallic compounds are formed when 6.0 < *VEC* < 7.8, the BCC-phase is stable at *VEC* < 6.0 while the FCC-phase at *VEC* > 7.8 [254]. For *VEC* between 7.5 and 7.8, FCC solid solution with precipitates of intermetallic compounds is formed.

4.1.2.3 Predicted results

The high-entropy model alloys design has been performed with respect to the parameters δr, ΔH_{mix} and Ω, which can predict the formation of single solid-solution and of a dual-phase alloy

(solid-solution with intermetallic compound precipitates), and to the parameter *VEC* used for the prediction of the FCC, BCC solid-solutions and the intermetallic compounds.

Six quaternary Al-Cr- Fe-Ni-based and three quinary Al-Cr-Fe-Ni-(Nb, Ti, Cu)-based high-entropy alloys have been prepared by fulfilling the critical values of the following criteria:

- Number of alloy constituents: more than four principal elements.
- Element concentration between 5 and 35 at.%.
- -15 kJ/mol < ΔH_{mix} < 5 kJ/mol.
- 1% < δr < 6.6%.
- $\Omega > 1.1$.
- *VEC* > 7.5.

To preserve the alloys *VEC* value above 7.5, the concentration of Al, which due to a VEC_{Al} = 3 may promote the formation of the BCC solid solution, has been selected between 6 and 12 at.%. The same ratio is also considered in case of Nb (VEC_{Nb} = 5) and Ti (VEC_{Ti} = 4) to select their concentration around 5 at.%. Copper (VEC_{Cu} = 11) stabilizes the FCC structure and shows a positive enthalpy of mixing with the other selected elements, except Al (Table 4-4 which indicates a tendency for Cu segregation [217, 224]. For this reason and in order to compare the influence of the fifth element addition, the concentration of Cu is also selected at 5 at.%. Table 4-6 shows the designed alloy compositions and their parameters values of ΔH_{mix}, δr, *VEC* and Ω.

Table 4-6 Design of candidate HEA and their corresponding ΔH_{mix}, *VEC*, δr, Ω, and predicted phase.

Code	Nominal Composition (at.%)	Δ_{Hmix}	*VEC*	δr	Ω	Predicted Phase
HEA1	$Al_{9.76}Cr_{30.28}Fe_{32.95}Ni_{26.91}$	-8.62	7.56	4.44	2.28	FCC+IM
HEA2	$Al_{9.85}Cr_{22.50}Fe_{34.50}Ni_{33.15}$	-8.29	7.75	4.41	2.31	FCC+IM
HEA3	$Al_{8.91}Cr_{23.13}Fe_{33.68}Ni_{34.28}$	-7.87	7.76	4.22	2.43	FCC+IM
HEA4	$Al_{11.69}Cr_{22.40}Fe_{32.62}Ni_{33.29}$	-8.87	7.62	4.74	2.18	FCC+IM
HEA5	$Al_{6.02}Cr_{25.01}Fe_{33.99}Ni_{34.98}$	-6.84	7.89	3.54	2.76	FCC
HEA6	$Al_{7.96}Cr_{23.23}Fe_{34.06}Ni_{34.75}$	-7.55	7.85	4.02	2.52	FCC
HEA7	$Al_{8.24}Cr_{21.37}Fe_{30.29}Ni_{35.02}Nb_{5.08}$	-10.92	7.71	4.83	1.98	FCC+IM
HEA8	$Al_{7.90}Cr_{22.04}Fe_{31.91}Ni_{33.14}Ti_{5.01}$	-11.18	7.62	5.27	1.89	FCC+IM
HEA9	$Al_{8.01}Cr_{22.01}Fe_{31.96}Ni_{33.01}Cu_{5.00}$	-5.45	7.95	4.02	3.82	FCC

The Fig. 4-7 displays the phase formation maps in a coordinate system, $\Omega - \delta r$, in which the stability domains of the solid solutions, ordered solid solutions, intermediate phases (intermetallic compounds) and bulk metallic glasses are also indicated as defined by Yang and Zhang et al. [196]. On these maps the designed nine HEA alloys are also indicated. As can be observed, two quaternary

alloys (HEA5 and HEA6) and one quinary alloy (HEA9) are positioned in the subdomain related to single-phase solid-solution. The other six alloys are in the subdomain of the solid solution with precipitates of intermetallic compounds.

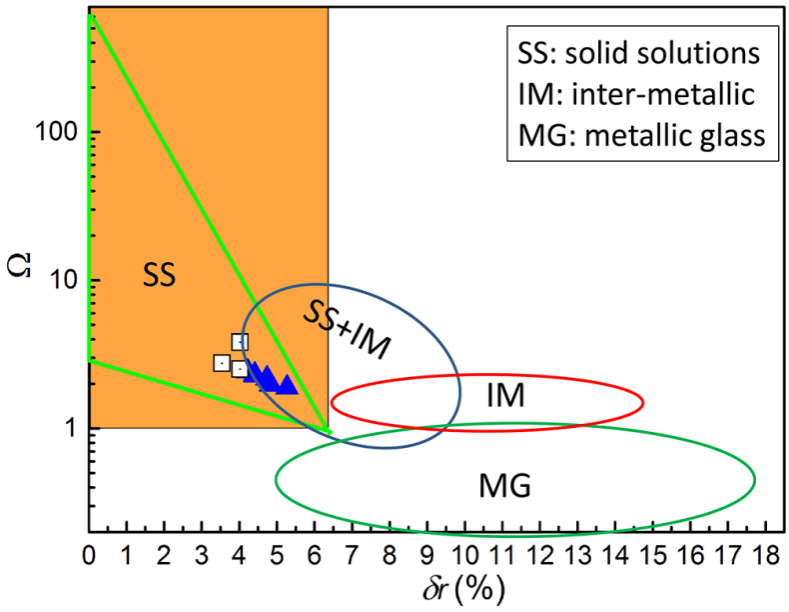

Fig. 4-7 Phase formation map based on Ω and δr, as defined by Yang and Zhang et al. [196], containing the compositions of HEA alloys designed for this study.

Regarding the *VEC* criterion, it can be observed that three compositions (HEA5, HEA6 and HEA9) show values above 7.8, which means that their predicted microstructure is a single-phase FCC solid-solution. The *VEC* values of the other 6 designed alloys (HEA1, HEA2, HEA3, HEA4, HEA7, HEA8) are in the range between 7.62 and 7.76 meaning that their predicted phases are FCC solid-solution containing precipitates of the intermetallic compounds (dual-phase high-entropy alloys).

4.2 Microstructure and thermo-physical properties

In this chapter, the model alloys are analysed with respect to the microstructure and thermo-physical properties. In depth analysis of the relation between the thermo-physical properties and the microstructure properties is not performed, since the objective is to get a first and coarse comparison with commercial steels only.

4.2.1 AFA-1st generation

The microstructure of all the annealed samples consists of large grains with an average size of 300 µm, as illustrated in Fig. 4-8. Some randomly distributed oxide inclusions (Al-rich) with the size $\leqslant$1 µm are observed. Taking into consideration the large dimension of the grains and the very low density of the structural and chemical defects, the general corrosion behavior of the alloys will be mainly influenced by alloys chemical composition and structure.

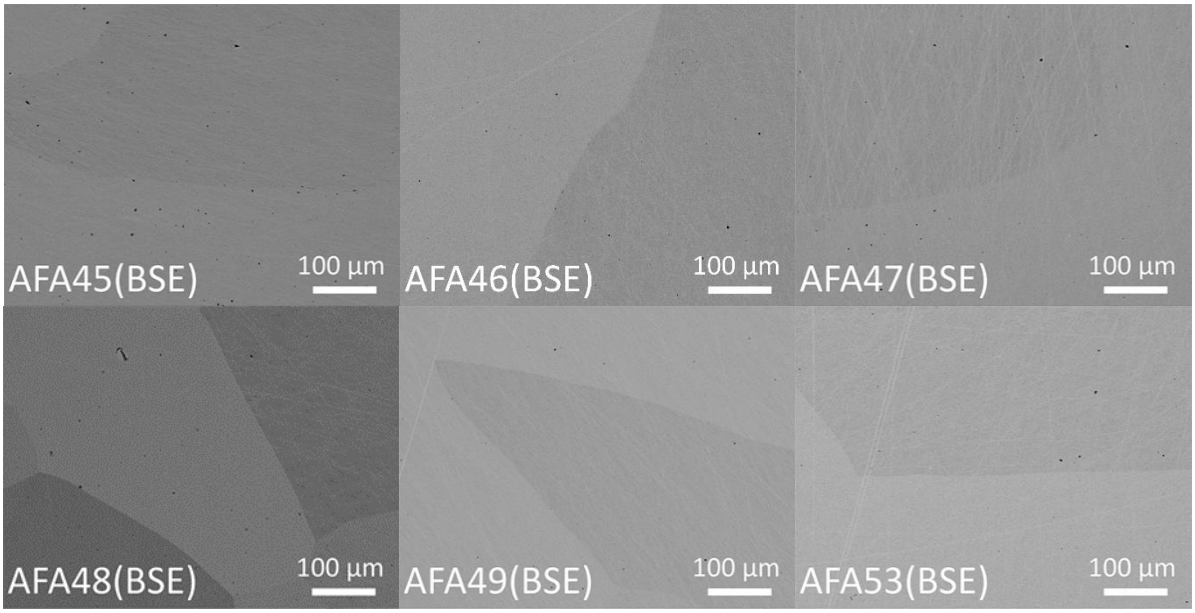

Fig. 4-8 Representative microstructures of AFA-1st generation alloys after annealing at 1250 °C for 2 h, large austenite grains (0.3-2 mm) represent the general feature of the microstructure.

Table 4-7 shows the chemical compositions of AFA-1st generation alloys measured by EDS. The measured composition of all the samples is close to the nominal compositions. The accuracy of the measurement is within 1 wt.%.

Table 4-7 Chemical compositions of AFA-1st generation measured by EDS (wt.%).

Code	Nominal composition	Cr	Al	Ni	Fe
AFA45	Fe-14Cr-3Al-20Ni	14.4	2.8	19.5	Balance
AFA46	Fe-16Cr-2.5Al-20Ni	16.6	2.3	19.6	Balance
AFA47	Fe-16Cr-3Al-20Ni	16.6	2.7	21.7	Balance
AFA48	Fe-12Cr-4Al-22Ni	12.2	4.0	21.3	Balance
AFA49	Fe-14Cr-4Al-22Ni	14.4	4.2	21.2	Balance
AFA50	Fe-16Cr-2.5Al-22Ni	16.5	2.5	21.4	Balance
AFA51	Fe-12Cr-4Al-24Ni	12.3	4.3	23.3	Balance
AFA52	Fe-14Cr-4Al-24Ni	14.3	4.3	23.4	Balance
AFA53	Fe-16Cr-3Al-24Ni	16.5	3.2	23.3	Balance
AFA54	Fe-16Cr-4Al-24Ni	16.3	4.3	23.4	Balance
AFA55	Fe-15Cr-2.5Al-29Ni	15.4	2.5	28.3	Balance
AFA56	Fe-15Cr-3.5Al-29Ni	15.2	3.8	28.5	Balance

XRD analysis of all samples indicates the formation of a single-phase austenitic structure (γ-Fe, face centered cubic–FCC) without any secondary metallic phases as shown in Fig. 4-9. These results confirm the predictions from the Schaeffler diagram.

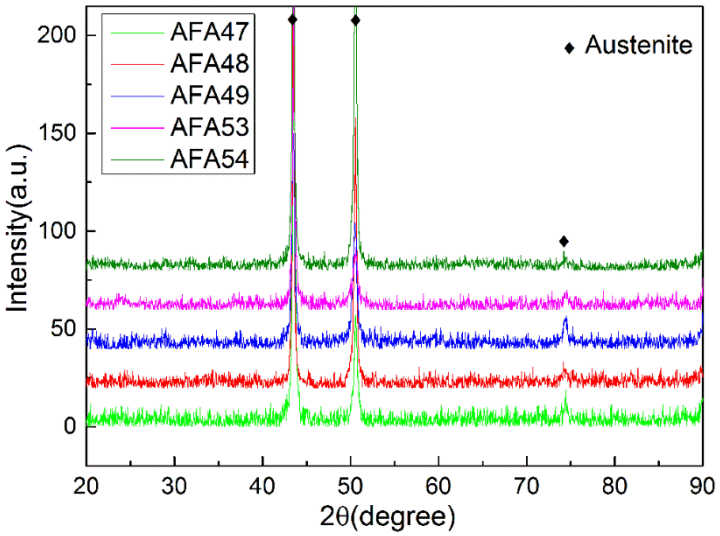

Fig. 4-9 Representative XRD patterns of AFA-1st generation after annealing at 1250 °C for 2 h.

In addition, the thermo-physical properties of six AFA alloys of the 1st generation have been measured. These are AFA46, AFA50, AFA53, AFA54, AFA55 and AFA56. Fig. 4-10 shows the specific heat capacity of AFA alloys and SS316 steel as a function of temperature. The error bar of this measurement is ± 5%. As temperature increases from 50 °C to 800 °C, all the samples show an increase in specific heat capacity. The specific heat capacity of AFA53 and AFA54 is higher than that of SS316 at the temperature range of 150-800 °C, which can be due to the high amount of Al and Cr additions (3.2 Al-16.5 Cr (wt.%) in AFA53, 4.3Al-16.3 Cr (wt.%) in AFA54) [255]. AFA46, AFA50 and AFA56 have similar values of specific heat capacity, which is lower than that of SS316. AFA55 has the lowest value of specific heat capacity among all the tested samples. This can be due to the low Al (2.5 wt.%) but high Ni additions (29 wt.%) [255]. The measured specific heat of AFA samples varies in the range of 0.545-0.755 J/g/K at 600 °C except AFA55 which has a low value of 0.459 J/g/K. In comparison, the specific heat of SS316 is 0.663 J/g/K at 600 °C.

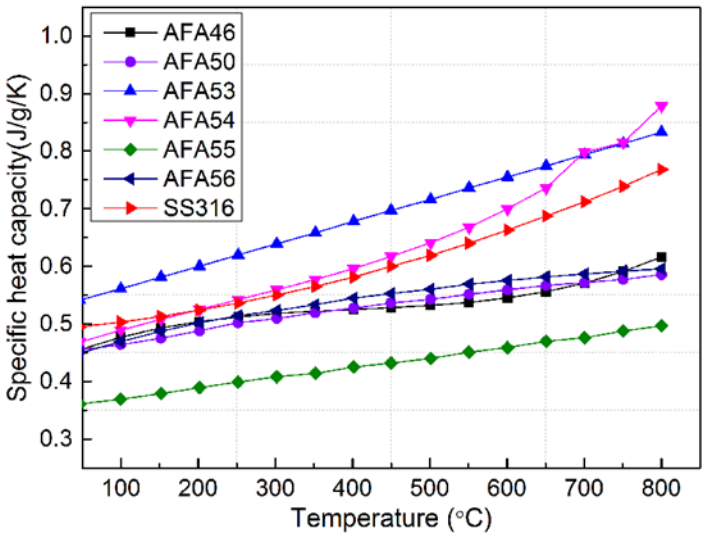

Fig. 4-10 Measured specific heat capacity of AFA samples as a function of temperature.

Fig. 4-11 shows the thermal diffusivity of AFA samples. The error bar of this measurement is ± 3%. At temperatures below 600 °C, AFA46, AFA53 and AFA54 show a value of thermal diffusivity that increases with temperature. In the temperature range of 600 to 750 °C, it starts to decrease and increases again depending on alloy composition between 700 and 750 °C. At 600 °C, the value of thermal diffusivity of AFA samples changes from 4.72 to 5.42 mm^2/s. SS316 shows the same trend of thermal diffusivity as a function of temperature. The measured thermal diffusivity at 600 °C is 5.1 mm^2/s. The decrease in thermal diffusivity might indicate some microstructural changes. AFA50, AFA55 and AFA56 show increasing values of thermal diffusivity as temperature increases in the entire temperature range tested.

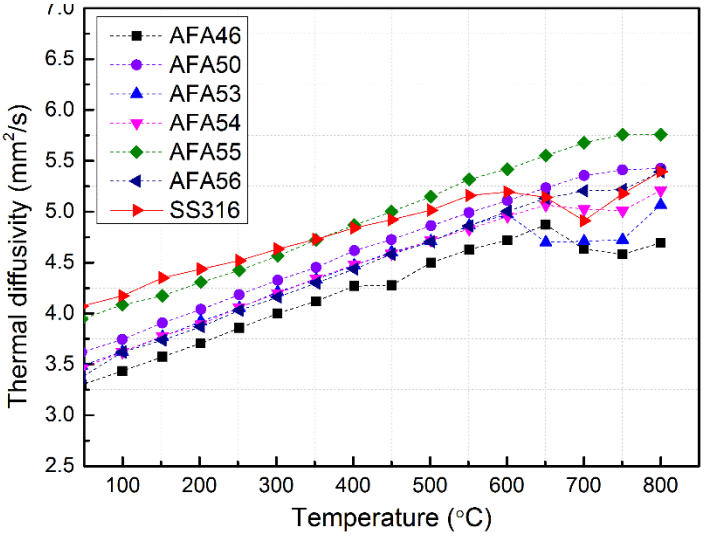

Fig. 4-11 Measured thermal diffusivity of AFA samples as a function of temperature.

Based on the measured alloy density, specific heat capacity and thermal diffusivity, thermal conductivity of AFA samples can be calculated according to the equation (3.10). Fig. 4-12 shows the plot of thermal conductivity of AFA samples as a function of temperature. All the samples show the trend of increasing thermal conductivity with increasing temperature. AFA53 has the closest value of thermal conductivity to SS316, varying from 15-35 W/m/K in the temperature range of 50 °C to 800 °C. AFA54 has a thermal conductivity that is lower than that of SS316 below 600 °C, but higher above 600 °C. AFA46, AFA50, AFA55 and AFA56 have all similar values of thermal conductivity in the range between 10 and 22 W/(mK), which are lower than that of SS316.

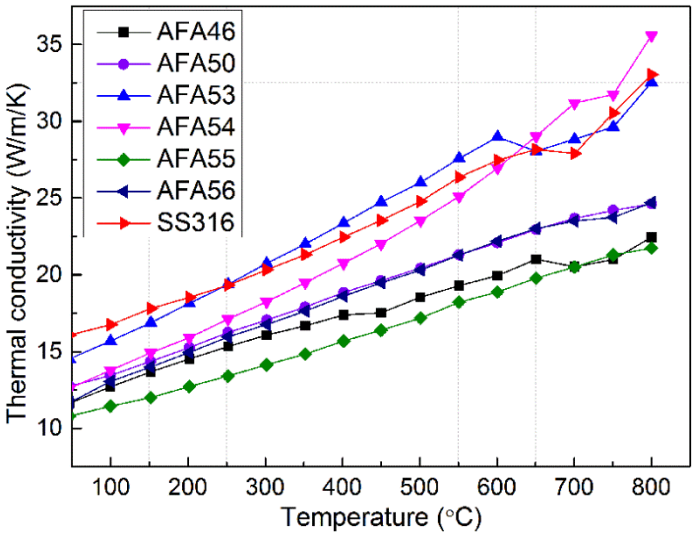

Fig.4-12 Experimentally evaluated thermal conductivity of AFA samples as a function of temperature.

Fig. 4-13 shows the linear thermal expansion of selected AFA alloys of 1st generation and SS316 as a function of temperature. AFA46, AFA50, AFA54, AFA55 and AFA56 exhibit all similar values of thermal expansion, with small differences between the heating and cooling process compared to SS316. In summary, the coefficient of liner thermal expansion measured on AFA alloys varies from 1.83×10^{-5} to 1.97×10^{-5} °C^{-1} at 600 °C, which is close to the value of SS316 which is of 2.05×10^{-5} °C^{-1} at same temperature. In contrast, the thermal expansion of AFA53 (blue color curve, Fig. 4-13 left) shows a difference between the heating and cooling process which might be related to the microstructure changes. Since the thermo-physical properties of AFA model alloys are comparable with the that of commercial steel SS316, it can be concluded that the alumina-forming austenitic steels can replace the SS316 steel without major changes of the equipment engineering design in case of applications at temperature above 500 °C.

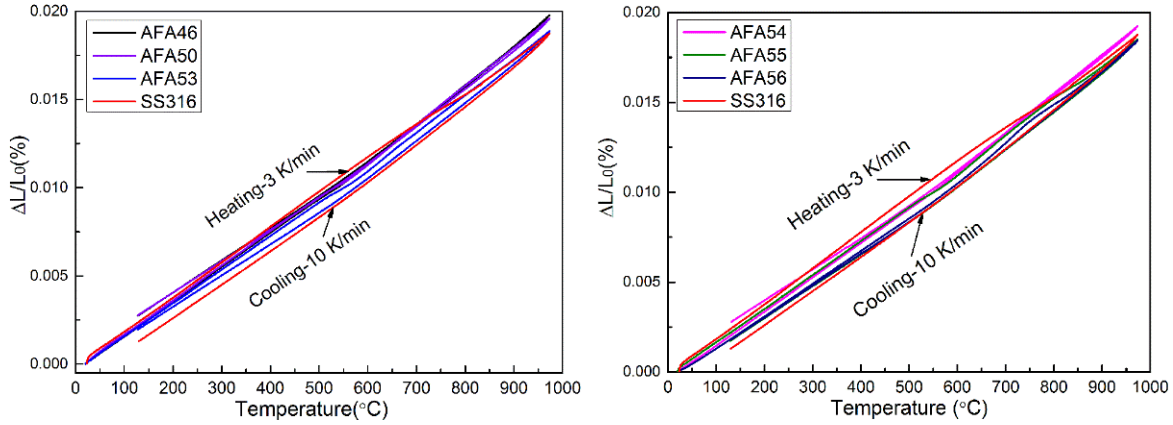

Fig.4-13 Linear thermal expansion of AFA samples as a function of temperature, heating: 21-970 °C; cooling: 970-128 °C.

4.2.2 AFA-2nd generation

Based on the corrosion performances of AFA-1st generation, six AFA model alloys have been designed and prepared for further validation of their corrosion resistance (1000 h and 2000 h) at 600 °C. Microstructure analyses indicate the formation of large grains in all of the annealed samples, as shown in Fig. 4-14. The bright dots/precipitates observed are distributed randomly in the alloy matrix and are rich in Y, Al and Ni. This is due to the over-doping with Y. None of the three Nb containing samples exhibits any Nb rich phase based on the SEM/EDS measurements. Table 4-8 shows the compositions of six AFA-2nd generation alloys measured by EDS.

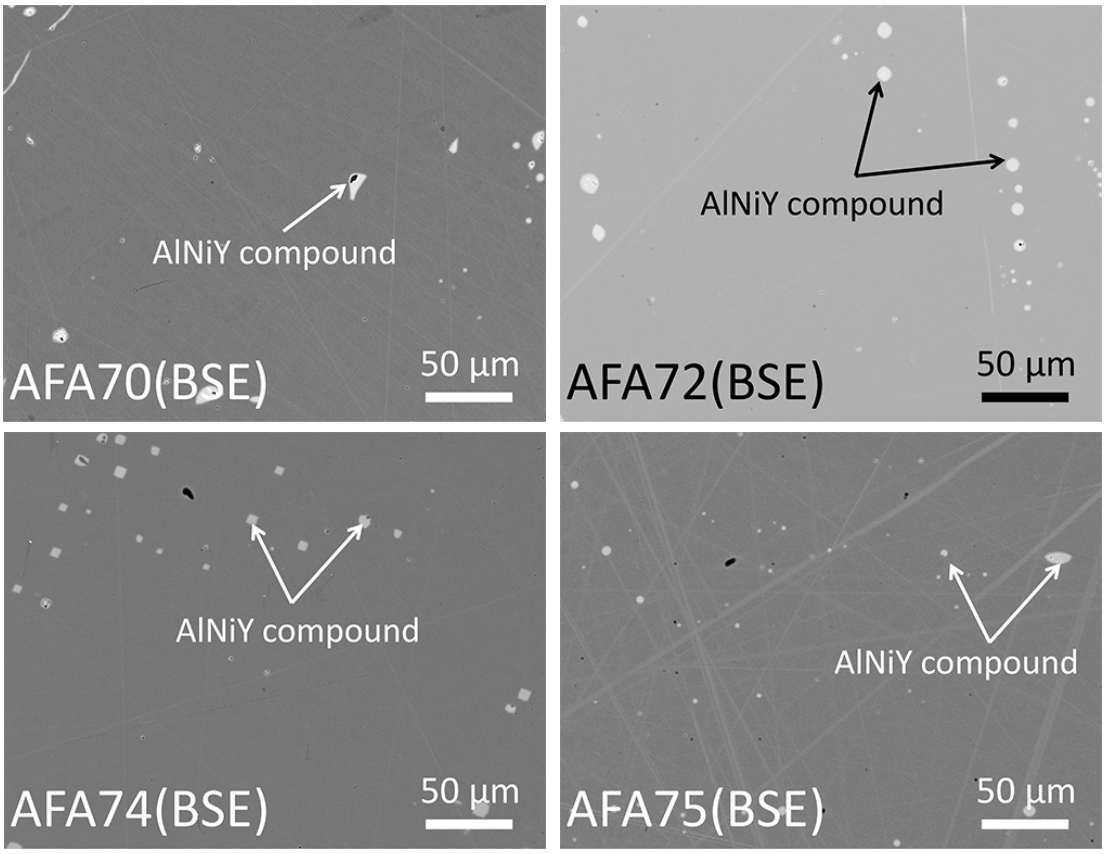

Fig. 4-14 Examples of microstructures of AFA-2nd generation alloys after annealing at 1250 °C for 2 h.

Table 4-8 Chemical compositions of AFA-2nd generation measured by EDS (wt.%).

Code	Nominal compositions	Al	Cr	Ni	Nb	Y	Fe
AFA70	Fe-14Cr-2.5Al-18Ni-0.5Y	2.7	14.7	17.9	--	0.4	Balance
AFA71	Fe-15Cr-2.5Al-20Ni-0.5Y	2.5	15.4	19.9	--	0.5	Balance
AFA72	Fe-16Cr-2.5Al-22Ni-0.5Y	2.5	15.4	21.8	--	0.5	Balance
AFA73	Fe-15Cr-2Al-20Ni-0.5Y-1.5Nb	2.1	15.4	22.0	1.3	0.5	Balance
AFA74	Fe-15Cr-3Al-29Ni-0.5Y-1.5Nb	4.3	15.5	27.9	1.1	0.5	Balance
AFA75	Fe-16Cr-3Al-24Ni-0.5Y-1.5Nb	3.1	15.7	24.1	1.68	0.7	Balance

Characterization of the phases by XRD analysis are displayed in Fig. 4-15. Only austenite is identified in the matrix of all compositions. These results are consistent with the predictions made by the Schaeffler diagram.

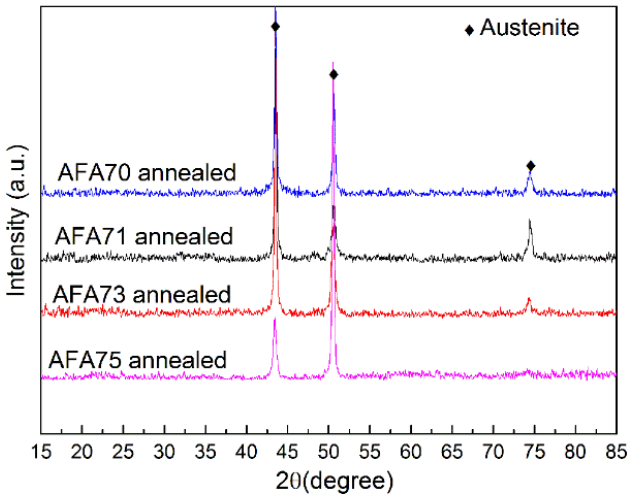

Fig. 4-15 Representative XRD patterns of AFA-2nd generation samples after annealing at 1250 °C for 2 h.

4.2.3 HEA alloys

Fig. 4-16 shows the microstructure of the as-cast quaternary alloy system. The microstructure of HEA1 displays the dendrites of bright contrast phases mixed with dark-gray inter-dendrites. Some regions exhibits the mixture of both structures in nano-size grains. HEA2, HEA3 and HEA4 reveal dendritic structures. Based on the EDS quantitative measurements, the dendrite (D) regions have higher concentrations of Fe and Cr while the inter-dendrite (ID) regions are rich in Al and Ni. In case of HEA5 and HEA6, the microstructures in the matrix are homogenous. No second precipitates are visible.

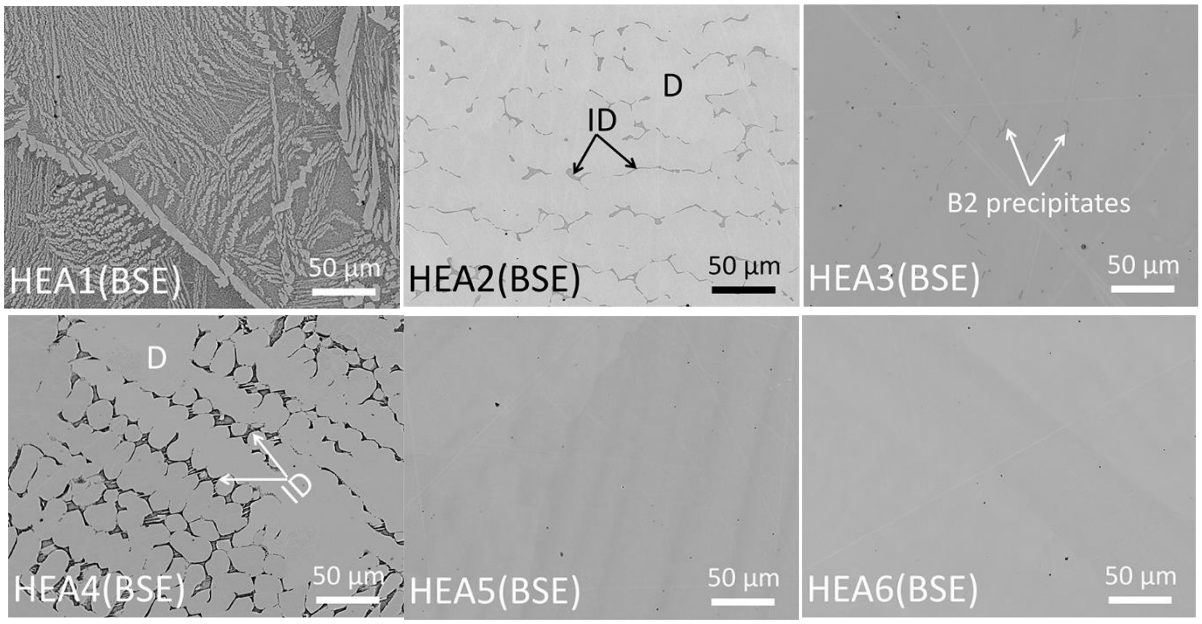

Fig. 4-16 Microstructures of as-cast quaternary FeCrNiAl HEA alloys, prepared by arc melting.

Further characterization of the samples by XRD patterns are shown in Fig. 4-17. The alloy matrix of HEA1, HEA2 and HEA4 show the signals from FCC and B2-NiAl phase, may also include the overlapped signals from BCC phase. In case of HEA3, only FCC is identified. However, the

inter-dendrites shown in the alloy matrix indicate the formation of B2-NiAl precipitates as shown in Fig. 4-16. Only austenite is visible in the matrix of HEA5 and HEA6.

The phase constitutions of all quaternary samples correspond with the predictions supported by the design rules: HEA5 and HEA6 are single-phase FCC solid-solutions, while the microstructure of HEA1, HEA2, HEA3 and HEA4 consists in the FCC solid-solution as alloy matrix with precipitates of the intermetallic compound B2-NiAl.

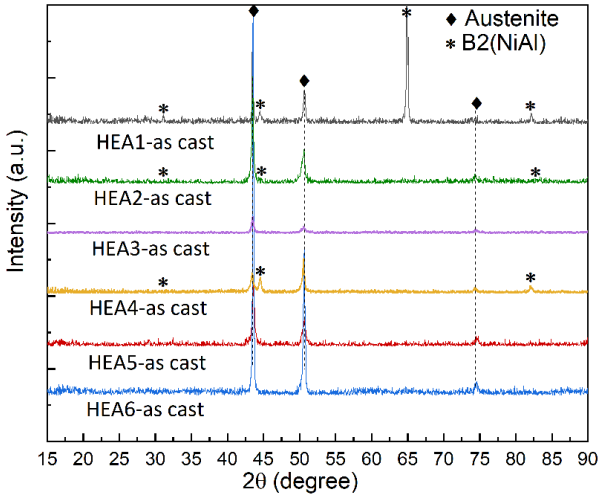

Fig. 4-17 XRD patterns of as-cast quaternary FeCrNiAl HEA alloys.

The microstructure of as-cast quinary HEA alloys is shown in Fig. 4-18. HEA7 and HEA8 form the dendrites structures, while only single solid solution has been observed in the bulk of HEA9. By alloying Nb, HEA7 shows Nb-rich inter-metallic compounds in the inter-dendrite (ID) regions. In case of HEA8, Al, Ni and Ti are enriched in the inter-dendrite (ID) regions.

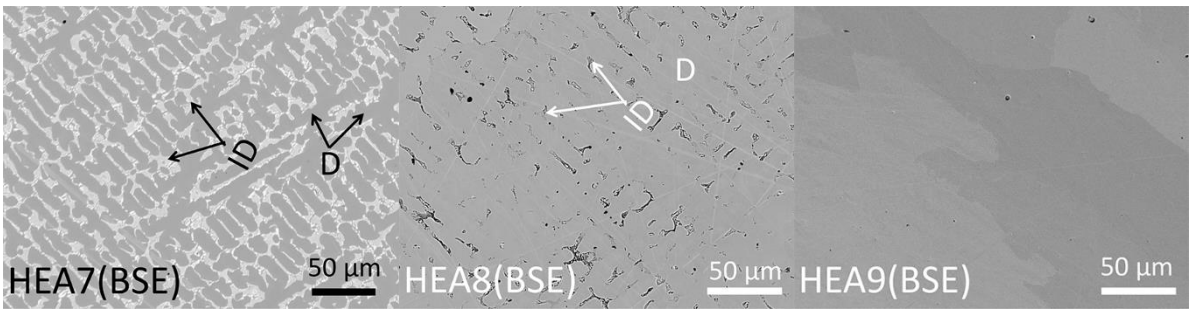

Fig. 4-18 Typical microstructures of as-cast FeCrNiAlX (X=Nb, Cu or Ti) HEA alloys, prepared by arc melting.

Further characterizations of as-cast samples by XRD indicate the formation of FCC and Laves (Fe_2Nb) in the matrix of HEA7 as shown in Fig. 4-19. In the matrix of HEA8, FCC, γ′ phases ($Ni_3(Al,Ti)$) are identified. HEA9 with Cu addition shows the formation of a single FCC phase.

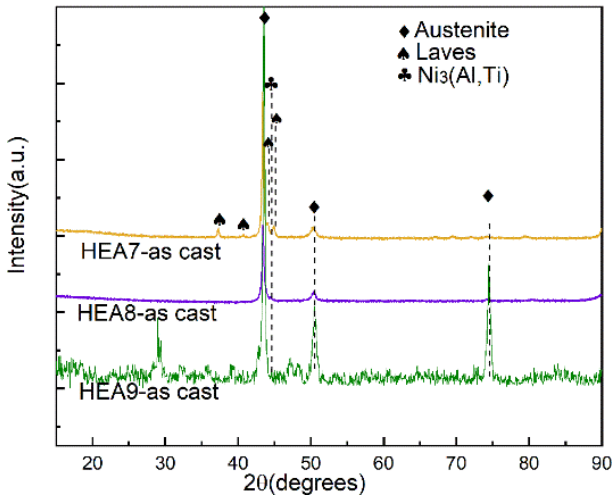

Fig. 4-19 Representative XRD patterns of as-cast quinary FeCrNiAlX (X=Nb, Cu or Ti) HEA alloys.

As in the case of quaternary HEA model alloys, the phase constitutions of quinary alloys predicted by the design rules are confirmed: the matrix of HEA7 and HEA8 is the FCC solid-solution in which intermetallic phases Fe_2Nb and $Ni_3(Al,Ti)$ precipitate respectively, while the HEA9 exhibits a single-phase FCC solid-solution.

Table 4-9 shows the nominal and measured chemical compositions (at.%) of as-cast HEA alloys. The accuracy of the measurement is 1 at.%. The inter-dendrites of HEA1 show lower Al content compared to the nominal Al concentrations, which indicate the formation of BCC phase instead of B2 phase. The small dark grains or precipitates observed in the morphology in Fig. 4-16 are the B2-NiAl phase obtained by XRD, shown in Fig. 4-17. The inter-dendrites of HEA2, HEA3 and HEA4 show the high concentration of Al and Ni, indicating the formation of B2 phases, which are also obtained by XRD in Fig. 4-17.

Table 4-9 Chemical compositions of as-cast HEA alloys, measured by EDS (at.%).

Alloy	Nominal Composition (at.%)	Morphology	Al	Cr	Fe	Ni	Nb	Ti	Cu
HEA1	$Al_{9.76}Cr_{30.28}Fe_{32.95}Ni_{26.91}$ (B2 precipitates are not measured)	D ID	6.33 7.13	28.84 33.19	35.28 34.58	29.55 25.1	--	--	--
HEA2	$Al_{9.85}Cr_{22.50}Fe_{34.50}Ni_{33.15}$	D ID	9.43 20.99	22.95 17.62	34.53 21.85	33.09 39.54	--	--	--
HEA3	$Al_{8.91}Cr_{23.13}Fe_{33.68}Ni_{34.28}$	M P	9.74 11.85	23.81 23.7	33.31 29.26	33.14 35.19	--	--	--
HEA4	$Al_{11.69}Cr_{22.40}Fe_{32.62}Ni_{33.29}$	D ID	9.26 20.17	22.4 14.05	36.9 36.9	30.46 30.46	--	--	--
HEA5	$Al_{6.02}Cr_{25.01}Fe_{33.99}Ni_{34.98}$	SPh	5.79	25.5	34.42	34.29	--	--	--

HEA6	$Al_{7.96}Cr_{23.23}Fe_{34.06}Ni_{34.75}$	SPh	7.9	23.7	34.41	33.99	--	--	--
HEA7	$Al_{8.24}Cr_{21.37}Fe_{30.29}Ni_{35.02}Nb_{5.08}$	D ID	7.05 6.23	23.29 19.58	34.43 26.66	34.07 30.76	1.16 16.77	--	--
HEA8	$Al_{7.90}Cr_{22.04}Fe_{31.91}Ni_{33.14}Ti_{5.01}$	D ID	6.45 14.01	23.94 15.17	35.74 23.48	31.14 38.94	--	2.73 8.4	--
HEA9	$Al_{8.01}Cr_{22.01}Fe_{31.96}Ni_{33.01}Cu_{5.00}$	SPh	8.01	22.01	31.96	33.02	--	--	5

SPh: single phase; M: matrix; P: precipitates; D: dendrite; ID: inter-dendrite.

The thermal physical properties of quaternary (single phase, dendrite) and quinary HEA alloys are measured. The error bar of this measurement is ± 5%. Fig. 4-20 shows the specific heat capacity of HEA1, HEA3, HEA4, HEA5, HEA7 and HEA8 as a function of temperature. Sample HEA1, HEA3, HEA4, HEA5 and HEA8 show a monotonous increase of the specific heat capacity with rising temperature. However, the specific heat capacity of HEA7 increases up to 600 °C to drop in the range from 600 °C and 700 °C, before it rises again which might be caused by the microstructure changes (e.g. phase transformation, precipitation). The measured specific heat of HEA alloys is in the range of 0.52-0.57 J/g/K at 600 °C.

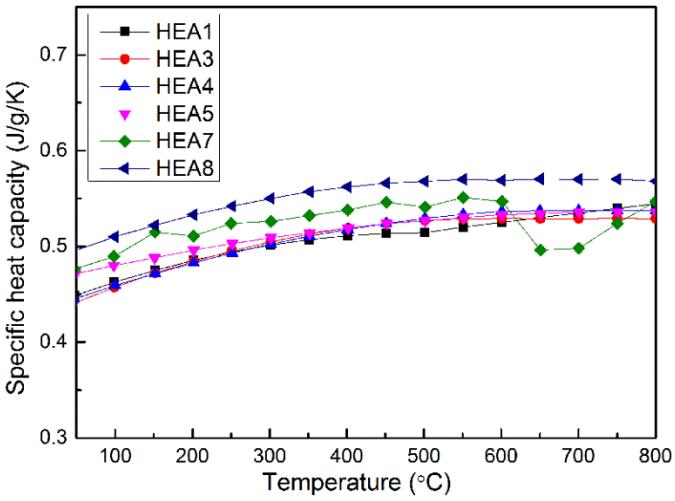

Fig. 4-20 Measured specific heat capacity of HEA samples as a function of temperature.

The thermal diffusivity of sample HEA1, HEA4, HEA5, HEA7 and HEA8 monotonically increase with temperature up to 700 °C, shown in Fig. 4-21. The error bar of this measurement is ± 3%. Then a slight decrease start from 700 °C until the end of the measurement. HEA3 shows the increase of thermal diffusivity from 50 °C to 600 °C. Then it begins to decrease and increases again from 650 °C. The decrease of thermal diffusivity might be related to the dissolution of ordered B2 phase, which leads to the disordering of matrix phase corresponding to the decrease in thermal diffusivity as temperature increases [256]. Except HEA7 which shows a low value of 4.2 mm^2/s, all the other alloys have values in the range of 4.79-5.70 mm^2/s at 600 °C. The slope of HEA7 diffusivity curve shows changes at around 350 °C and 700°C, which might be related to microstructure changes.

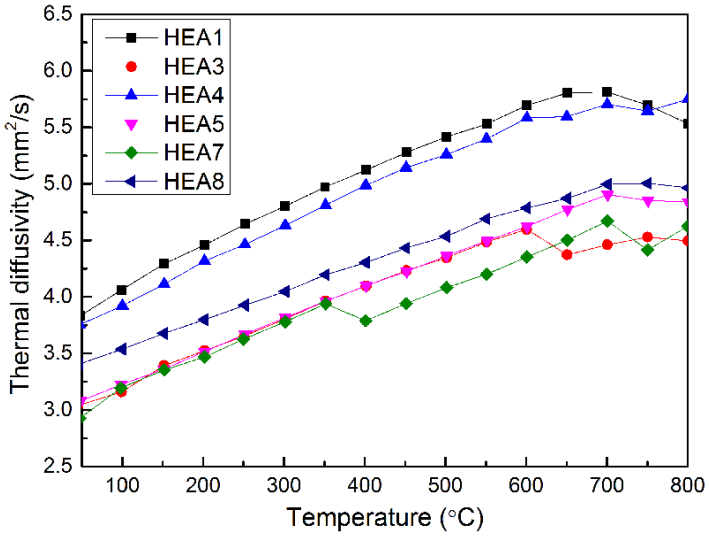

Fig. 4-21 Measured thermal diffusivity of HEA samples as a function of temperature.

The thermal conductivity, calculated from the measured thermal diffusivity, specific heat capacity, and alloy density, of HEA1, HEA4, HEA5 and HEA8 increases in the temperature range 50-700 °C, as shown in Fig. 4-22. The measured thermal conductivity of these four samples varies in 18.4-22.29 W/m/K at 600 °C. Then the thermal conductivity starts to decrease at above 700 °C. HEA1 and HEA4 show the highest thermal conductivity at the measured temperature range due to the relative high fraction of BCC (or B2) phase [257]. HEA3 and HEA7 show an increasing value of thermal conductivity in the temperature range between 50 and 600 °C. At 600 °C, HEA3 and HEA7 have the thermal conductivity with a value of 17.76-18.27 W/m/K. Above, both samples show a decrease of thermal conductivity at 600-650 °C, increasing again exceeding 700 °C. Such variation might be related to microstructural changes.

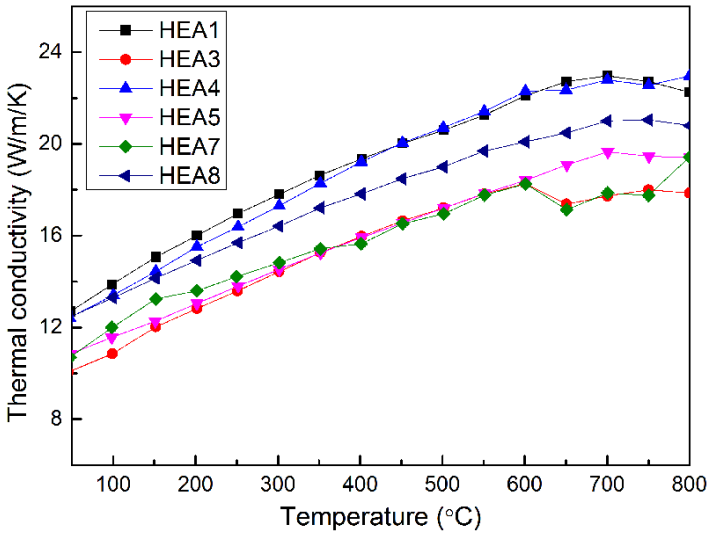

Fig. 4-22 Evaluated experimental thermal conductivity of HEA samples as a function of temperature.

The linear thermal expansion of HEA1 to HEA8 alloys is depicted in Fig. 4-23. HEA1, HEA3, and HEA4 show thermal expansion values with marginal difference between the heating and cooling

process (Fig. 4-23, left). In contrast, HEA5 exhibits a significant difference in thermal expansion between heating and cooling below 750 °C, e.g. 0.0025% at 150 °C during heating vs 0.005% at 150 °C during cooling. The thermal expansion during heating is lower than the value during cooling. HEA7 shows a difference in thermal expansion between heating and cooling below 850 °C (Fig. 4-23, right). Moreover, the curve of thermal expansion shows anomalies at the temperature range of 700-750 °C in both the heating and cooling process. In case of HEA8, the thermal expansion curves show a hysteresis in the temperature range 700-930 °C. The anomalies of the thermal expansion of HEA7 and HEA8 could be attributed to reversible microstructural changes at temperature above 700 °C. However, the range of coefficient of thermal expansion measured at 600 °C is between $1.58x10^{-5}$ and $2.04x10^{-5}$ $°C^{-1}$.

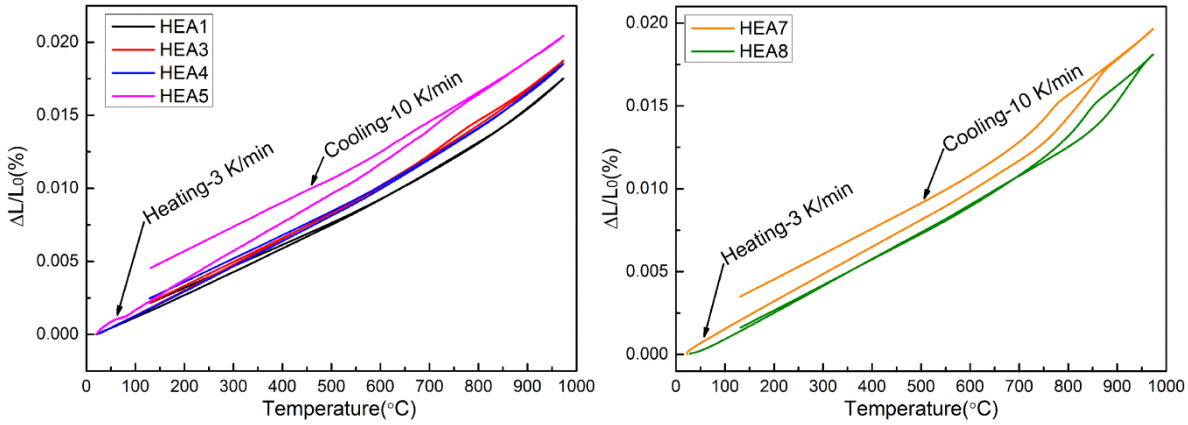

Fig. 4-23 Measured linear thermal expansion of HEA samples as a function of temperature; heating: 21-970 °C; cooling: 970-128 °C.

5. Corrosion behavior of AFA model alloys

5.1 Corrosion behavior of AFA-1st generation at 550 °C and 600 °C for 1000 h

Twelve AFA-1st generation model alloys were exposed to 10^{-6} wt.% oxygen containing molten Pb at 550 °C and 600 °C for 1000 h. Table 5-1 summarizes the corrosion performance of AFA alloys in molten Pb conditions. Eight alloys (AFA45, AFA46, AFA47, AFA50, AFA53, AFA54, AFA55 and AFA56) have formed a protective oxide scale, while four compositions (AFA48, AFA49, AFA51, and AFA52) exhibited corrosion attack during exposure in oxygen containing molten Pb conditions at 550 °C. At 600 °C, six samples (AFA46, AFA50, AFA53, AFA54, AFA55 and AFA56) have been passivated and the remaining seven compositions have shown the evidence of corrosion attacks (Table 5-1).

Table 5-1 Corrosion performance of AFA-1st generation alloys after 1000 h exposure to 10^{-6} wt.% oxygen containing molten Pb at 550 °C and 600 °C.

Code	Chemical composition (wt.%)	550 °C	600 °C
AFA45	Fe-14.4Cr-2.8Al-19.5Ni	🙂	☹
AFA46	Fe-16.6Cr-2.3Al-19.6Ni	🙂	🙂
AFA47	Fe-16.6Cr-2.7Al-21.7Ni	🙂	☹
AFA48	Fe-12.2Cr-4Al-21.3Ni	☹	☹
AFA49	Fe-14.4Cr-4.2Al-21.2Ni	☹	☹
AFA50	Fe-16.5Cr-2.5Al-21.4Ni	🙂	🙂
AFA51	Fe-12.3Cr-4.3Al-23.3Ni	☹	☹
AFA52	Fe-14.3Cr-4.3Al-23.4Ni	☹	☹
AFA53	Fe-16.5Cr-3.2Al-23.3Ni	🙂	🙂
AFA54	Fe-16.3Cr-4.3Al-23.4Ni	🙂	🙂
AFA55	Fe-15.4Cr-2.5Al-28.3Ni	🙂	🙂
AFA56	Fe-15.2Cr-3.8Al-28.5Ni	🙂	🙂

🙂: Corrosion resistance; ☹: Corrosion attack.

5.1.1 Corrosion attack of AFA alloys at 550 °C and 600 °C

After 1000 h corrosion test at 550 °C, AFA48 and AFA51 (with 12 wt.% Cr), AFA49 and AFA52 (with 14 wt.% Cr) have shown dissolution attacks. At 600 °C, the samples with 12 wt.% Cr (AFA48, AFA51) and 14 wt.% Cr (AFA45, AFA49, AFA52), together with another sample containing 16 wt.% Cr (AFA47) show dissolution attack and oxide scale spallation. Fig. 5-1 shows the representative surface view and cross section of AFA48 (12 wt.% Cr, at 550 °C), AFA49 (14 wt.% Cr, at 550 °C) and AFA47 (16 wt.% Cr, at 600 °C) alloys after exposure tests at 550 °C and 600 °C. After exposure to oxygen-containing molten Pb at 550 °C, samples with 12 wt.% Cr show widespread dissolution attack, approximately at 90% of the surface area as show in Fig. 5-1 (AFA48). The cross section

analysis in Fig. 5-1 (AFA48) reveals a thick dark-gray layer (>50 µm at some parts) with Pb penetration and some small precipitates. In case of samples containing 14 wt.% Cr, the alloys have formed an oxide scale with localized dissolution attacks. This corrosion attack covers around 30 to 40% of the surface area (e.g. AFA49, AFA52). According to the cross section analysis (e.g. AFA49), a thick layer shown in dark contrast, of around 15 to 20 µm, is observed on both samples. Moreover, bright Pb penetration are also visible at some spots. When exposed to oxygen-containing molten Pb at 600 °C, the samples containing 12 wt.% Cr display a dissolution attack at around 90% of surface area like the ones exposed at 550 °C. The cross section analysis reveals similar features like the samples exposed at 550 °C, namely a dark-gray layer with Pb penetration, and small precipitates. Samples with 14 wt.% Cr (AFA45, AFA49, AFA52) and 16 wt.% Cr (AFA47) have shown localized dissolution attacks at about 30% to 50% of surface area. The other part of the surface is covered by an oxide scale. The cross section analysis shows the dark-gray layer (10-30 µm) with the Pb penetration and some small precipitates. Cross section mapping of AFA52 (exposed at 600 °C) reveals the signals of O, Al and Cr at the alloy surface, shown in Fig. 5-2. In the dark-gray region, an enrichment of Fe and depletion of Ni is clearly visible. Besides, the dark precipitates are rich in Al and Ni according to the EDS mapping and line scanning, see Fig. 5-3.

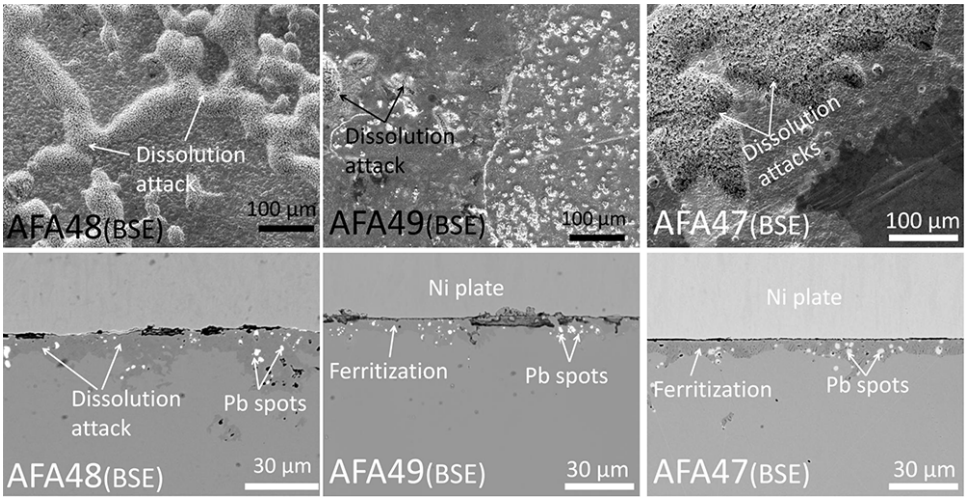

Fig. 5-1 Dissolution attacks observed on the surface and cross section of AFA48 (550 °C), AFA49 (550 °C) and AFA47 (600 °C) after 1000 h exposure to 10^{-6} wt.% oxygen containing molten Pb.

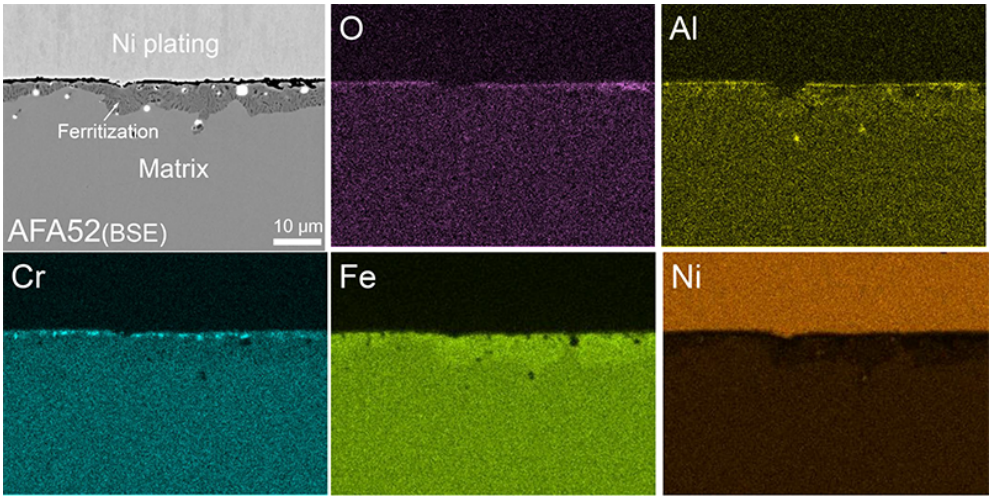

Fig. 5-2 EDS mapping of the cross section of AFA52 after 1000 h exposure to 10^{-6} wt.% oxygen containing molten Pb at 600 °C.

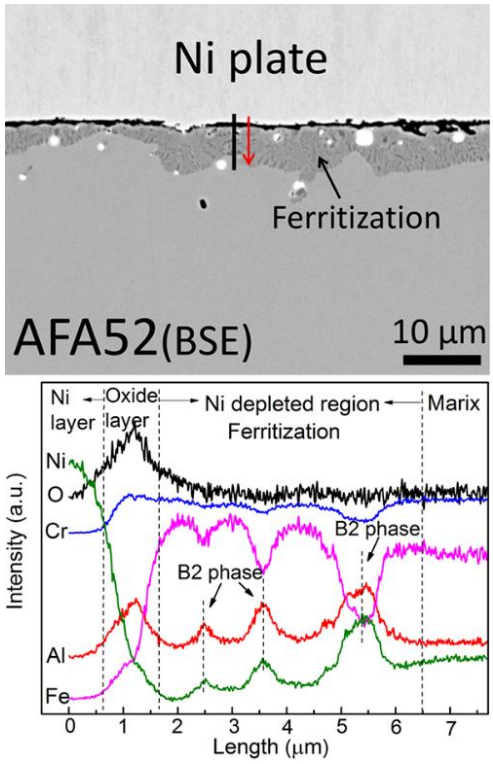

Fig. 5-3 EDS line scan of the cross section of AFA52 after 1000 h exposure to 10^{-6} wt.% oxygen containing molten Pb at 600 °C (The direction of the measurement is indicated by the arrow).

Fig. 5-4 shows the XRD pattern examples of some of the alloys displaying dissolution attack: AFA48 (550 °C), AFA47 (600 °C) and AFA52 (600 °C). According to the analysis, strong intensities from BCC have been identified in all three samples. Corroborated with cross section analysis shown in Fig. 5-1, the gray regions have transformed from FCC to BCC phase due to the depletion of austenitic stabilizer Ni. All samples show no or low intensity peaks belonging to the FCC phase due to the high thickness of the ferrite layer. Besides, the Al-, Ni-rich precipitations, which are observed in the dark-gray layer (see Fig. 5-1), are identified by XRD as the B2-NiAl compound.

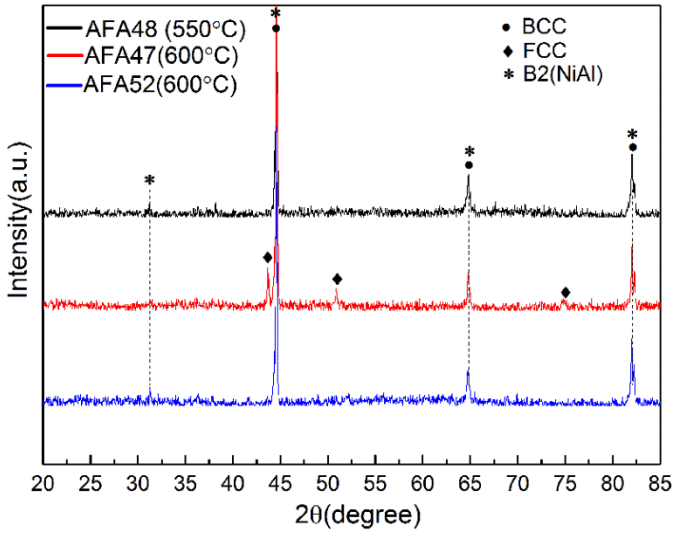

Fig. 5-4 Representative XRD patterns of samples displaying dissolution attack after 1000 h exposure to 10^{-6} wt.% oxygen containing molten Pb at 550 °C and 600 °C: AFA48 (Fe-12.2Cr-4Al-21.3Ni), AFA47(Fe-16.6Cr-2.7Al-21.7 Ni) and AFA52 (Fe-14.3Cr-4.3Al-23.4Ni).

5.1.2 Corrosion resistance of AFA alloys at 550 °C

Alloy surface characterization

Eight samples AFA45, AFA46, AFA47, AFA50, AFA53, AFA54, AFA55 and AFA56 have formed protective oxide scales after 1000 h exposure in low-oxygen containing molten Pb at 550 °C. Fig. 5-5 shows the representative surface morphologies of alloys with 14 wt.% Cr (AFA45), 15 wt.% Cr (AFA56) and 16 wt.% Cr (AFA53). No dissolution attack can be observed. The oxide scales formed on the alloy surfaces are dense and uniform. Besides, Fe-rich oxide protrusions (magnetite, < 2% surface area) have been observed on the surfaces of AFA45, AFA46, AFA53 and AFA56.

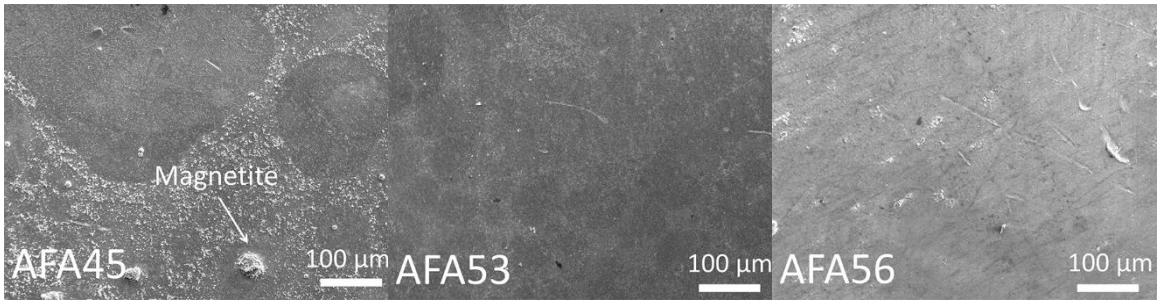

Fig. 5-5 Representative surface morphologies of AFA-1st generation samples after 1000 h exposure to 10^{-6} wt.% oxygen containing molten Pb at 550 °C: AFA45 (Fe-14.4Cr-2.8Al-19.5Ni), AFA53 (Fe-16.5Cr-3.2Al-23.3Ni) and AFA56 (Fe-15.2Cr-3.8Al-28.5Ni).

Cross section analysis

Fig. 5-6 shows the cross sections of passivated AFA-1st generation samples. Cross sectional analysis confirms the formation of a continuous and thin oxide layer on the alloy surfaces. No dissolution attack or Pb penetration has been observed in the alloy matrix. The magnetite protuberances (Fe_3O_4) observed on the surface are parts of thick oxide spots, as shown in the cross

section of AFA46. The evaluation of EDS line-scanning and mapping indicates that the oxide scale mainly consists of Al- and Cr-oxides, as shown in Fig. 5-7 and Fig. 5-8. The oxygen signal maximum observed in the EDS line-scans (Fig. 5-7) coincides the maxima of the Al and Cr signals. Furthermore, the signal maxima of aluminum and chromium are either coincided or slightly shifted, where the Cr peak appears closer to the surface. The thickness of the oxide scale is around 100 to 200 nm according to the full width at half maximum (FWHM) measured from EDS line scanning. Another phenomenon observed in all of these samples is the quasi-continuous transitional layer beneath the oxide scale, with bright aspect in Fig. 5-6. EDS line scanning indicates that the transitional layer is enriched in Fe and Ni, and depleted in Al and Cr. The thickness of the transitional layer varies between 1 and 3 µm and decreases with increasing of the Ni content. Additionally, small precipitates (shown in dark contrast) are distributed among the transitional layer, as it is visible in Fig. 5-7 (AFA54) and Fig. 5-8. According to the EDS measurements, the precipitates are enriched in Al and Ni, e.g. AFA 54 in Fig. 5-7, most probably being B2-NiAl compound. At the interface between the transitional layer and the oxide scale and/or in the surrounding volume of the NiAl-rich precipitates, Cr-enrichment is observed in some spots in all samples. Information about these precipitates is obtained from EDS line-scans and elemental mapping as exemplified in Fig. 5-7 (AFA54) and Fig. 5-8 (AFA47).

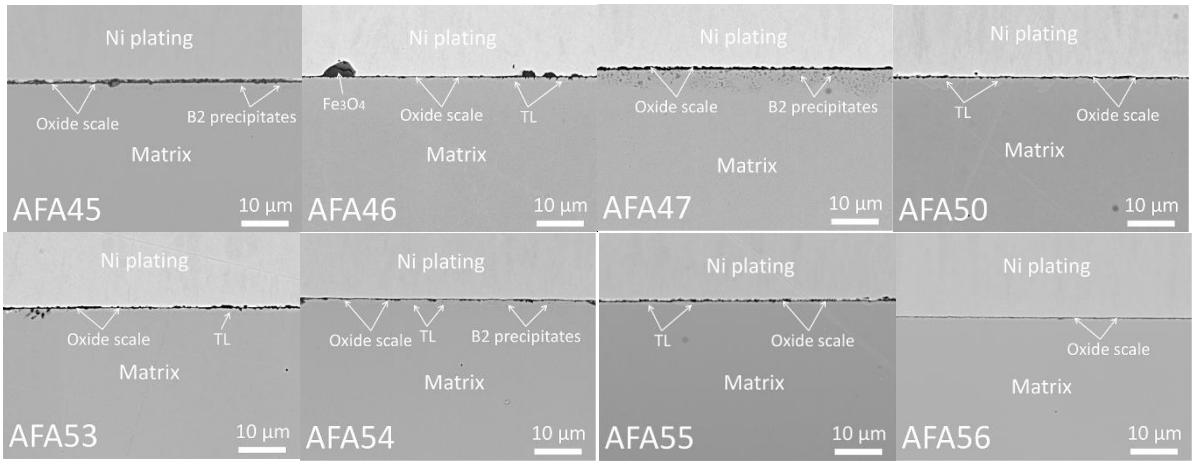

Fig. 5-6 Cross section images of AFA-1st generation samples after 1000 h exposure to 10^{-6} wt.% oxygen containing molten Pb at 550 °C: AFA45 (Fe-14.4Cr-2.8Al-19.5Ni), AFA46 (Fe-16.6Cr-2.3Al-19.6Ni), AFA47 (Fe-16.6Cr-2.7Al-21.7Ni), AFA50 (Fe-16.5Cr-2.5Al-21.4Ni), AFA53 (Fe-16.5Cr-3.2Al-23.3Ni), AFA54 (Fe-16.3Cr-4.3Al-23.4Ni), AFA55 (Fe-15.4Cr-2.5Al-28.3Ni) and AFA56 (Fe-15.2Cr-3.8Al-28.5Ni), TL: transitional layer.

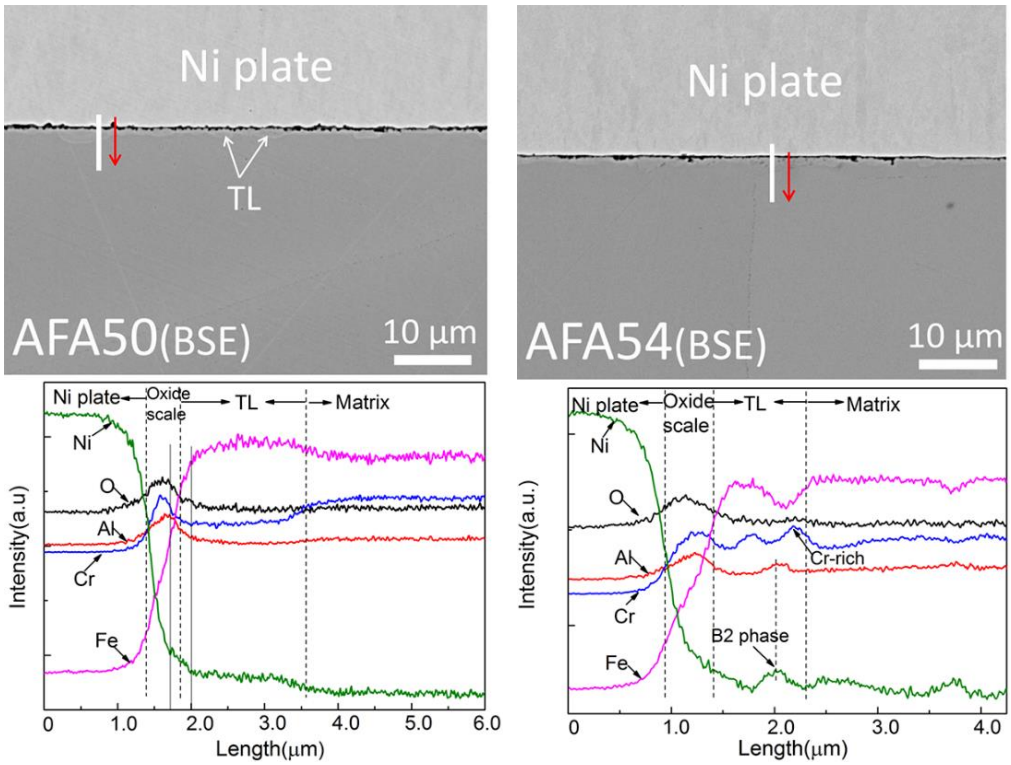

Fig. 5-7 EDS line scans of the cross sections of AFA-1st generation samples after 1000 h exposure to 10^{-6} wt.% oxygen containing molten Pb at 550 °C: AFA50 (Fe-16.5Cr-2.5Al-21.4Ni) and AFA54 (Fe-16.3Cr-4.3Al-23.4Ni), (The direction of the measurement is indicated by the arrow).

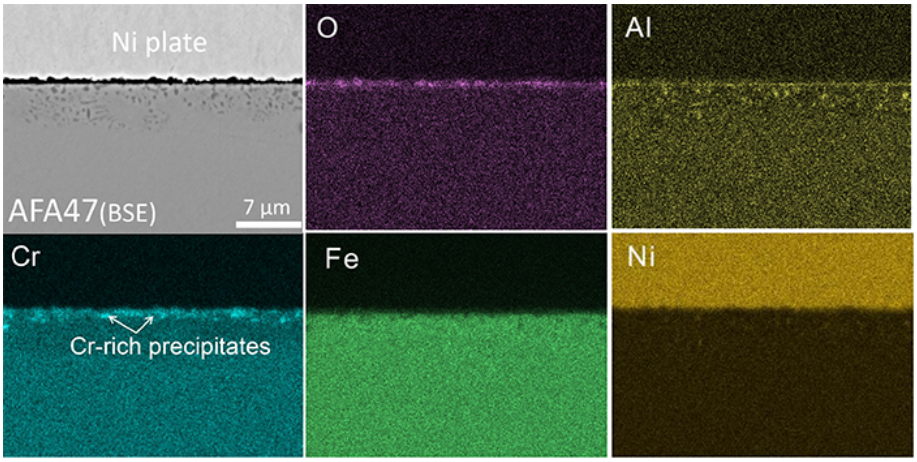

Fig. 5-8 EDS mapping of the cross section of AFA47 sample (Fe-16.6Cr-2.7Al-21.7Ni) after 1000 h exposure to 10^{-6} wt.% oxygen containing molten Pb at 550 °C.

X-ray diffraction pattern

X-ray diffraction analysis has been performed on exposed samples to identify the phase compositions. Since the types of oxides are mainly influenced by the Al and Cr content, samples with different concentrations of Al and Cr are selected to represent the XRD patterns in Fig. 5-9, namely AFA45 (Fe-14.4Cr-2.8Al-19.5Ni), AFA46 (Fe-16.6Cr-2.3Al-19.6Ni), AFA54 (Fe-16.3Cr-4.3Al-23.4Ni),

AFA56 (Fe-15.2Cr-3.8Al-28.5Ni). According to the XRD analysis, the phases identified on each sample are the followings: AFA45: FCC, B2, Fe_3O_4 (strong), Cr_2O_3 and (Al,Cr) $_2O_3$, AFA46: FCC, B2, Fe_3O_4, Cr_2O_3 and $(Al,Cr)_2O_3$; AFA54: FCC, B2 (weak), Cr_2O_3 and $(Al,Cr)_2O_3$ (weak), and AFA56: FCC, BCC, B2 (strong), Cr_2O_3 and $(Al,Cr)_2O_3$ (weak). The X-ray diffraction patterns obtained from the oxide scale are weak due to the small thickness and probably disordered structure of the oxide scale components. However, based on the current results, two corundum-type crystalline structures (rhombohedral lattice system) are identified as the main constituent phases of the oxide scales, one being Cr_2O_3 and the other Al_2O_3-Cr_2O_3 solid solution.

The 100% intensity peak of Cr_2O_3, corresponding to (104) lattice plane, is located at 2θ=33,61°±0.02°, while the 100% intensity peak of the Al_2O_3-Cr_2O_3 solid solution, corresponding to the same lattice plane, is located in the range between 34.44° and 34.65°. Regarding the observed Fe-rich oxide protrusions on some samples' surfaces, magnetite (Fe_3O_4) is identified in the XRD patterns. Moreover, the intensity of magnetite decreases as the Ni and the Al content increase: XRD patterns of the samples AFA54 and AFA56 do not show the peaks from magnetite. As for the phase compositions of the alloy substrate, austenite as the matrix plus B2-NiAl (PDF Nr: 44-1188) are identified from the XRD. Combining with cross section analysis (shown in Fig. 5-7), the Al- and Ni-rich precipitates observed in the transitional layer are B2-NiAl. In addition, AFA56 has shown more intense peaks at 2θ=44.44°, 64.73° and 81.99°, which indicate the presence of a BCC structure (other than B2-NiAl compound) which, after taking into consideration the SEM/EDS results, is a FeCr solid solution formed in the Cr-enriched spots of the transitional layer.

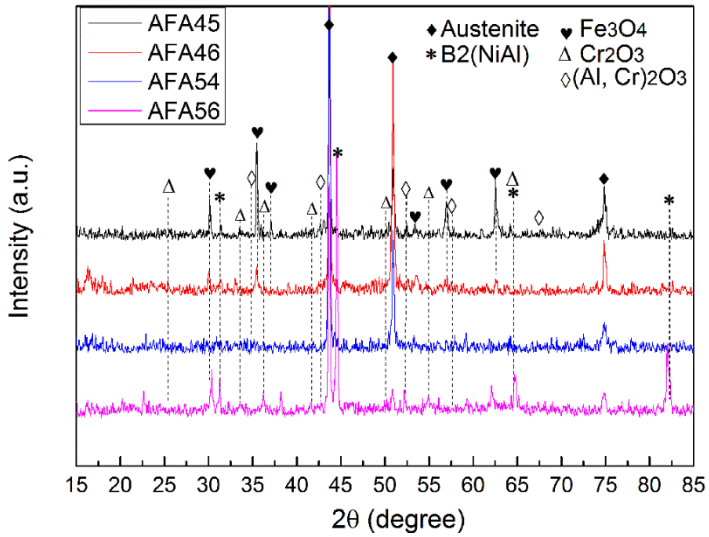

Fig. 5-9 Representative XRD patterns measured on AFA-1st generation samples after 1000 h exposure to 10^{-6} wt.% oxygen containing molten Pb at 550 °C: AFA45 (Fe-14.4Cr-2.8Al-19.5Ni), AFA46 (Fe-16.6Cr-2.3Al-19.6Ni), AFA54 (Fe-16.3Cr-4.3Al-23.4Ni) and AFA56 (Fe-15.2Cr-3.8Al-28.5Ni).

5.1.3 Corrosion resistance of AFA alloys at 600 °C

Alloy surface characterization

Six samples alloyed with 15 wt.% Cr (AFA55, AFA56) and 16 wt.% Cr (AFA46, AFA50, AFA53, AFA54) succeeded to passivate based on an oxide scale formed during 1000 h exposure to low-oxygen containing molten Pb at 600 °C. All samples (having Al concentration between 2.5 and 4 wt.%) formed a dense and continuous Al- and Cr- rich oxide scale. Fig. 5-10 shows the representative surface morphologies of protective samples with different content of Al, Cr and Ni, namely AFA46 (Fe-16Cr-2.5Al-20Ni), AFA50 (Fe-16Cr-2.5Al-22Ni) and AFA55 (Fe-15Cr-2.5Al-29Ni).

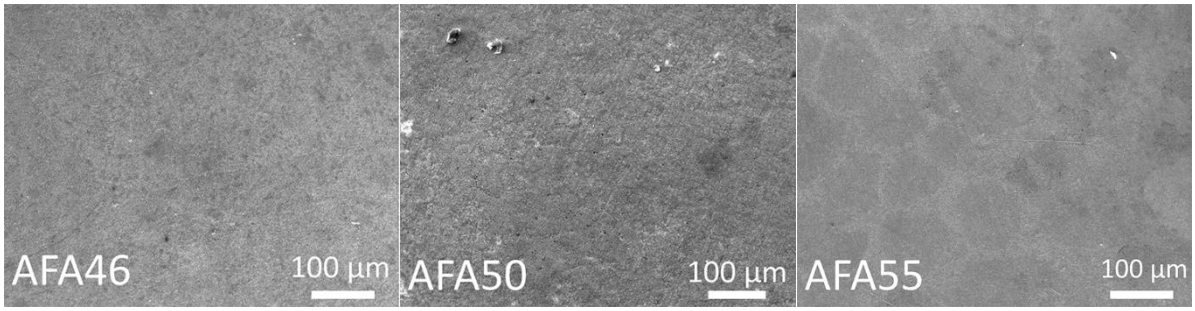

Fig. 5-10 Representative surface morphologies of AFA-1st generation samples after 1000 h exposure to 10^{-6} wt.% oxygen containing molten Pb at 600 °C (AFA46, AFA50, AFA55).

Cross section analysis

The SEM images in Fig. 5-11 show the cross sections of AFA samples forming a protective oxide scale. A continuous oxide scale, based on Al- and Cr- rich oxides, protects the samples from corrosion attack. The thickness of the oxide scale varies from 50 to 200 nm, according to the FWHM measured in EDS line scanning (examples shown in Fig. 5-12). Further EDS line scans of the oxide scale indicate that the signal maximum of chromium coincides with that of aluminum, as depicted in Fig. 5-12. Both signal maxima coincide with the maximum of the oxygen signal which indicates the formation of oxide scale on alloy surface. A bright-gray metallic transitional layer (TL), which is underneath the oxide scale, has been observed in all passivated samples. The thickness of this layer varies between 1 and 3 µm. As the Ni content increases, the transitional layer becomes less pronounced, as in case of the samples passivated during exposure at 550 °C. Moreover, the precipitates observed in the transitional layer mainly consist of Al and Ni, while some Cr-rich spots are also found as shown in the EDS mapping analysis, see Fig. 5-13.

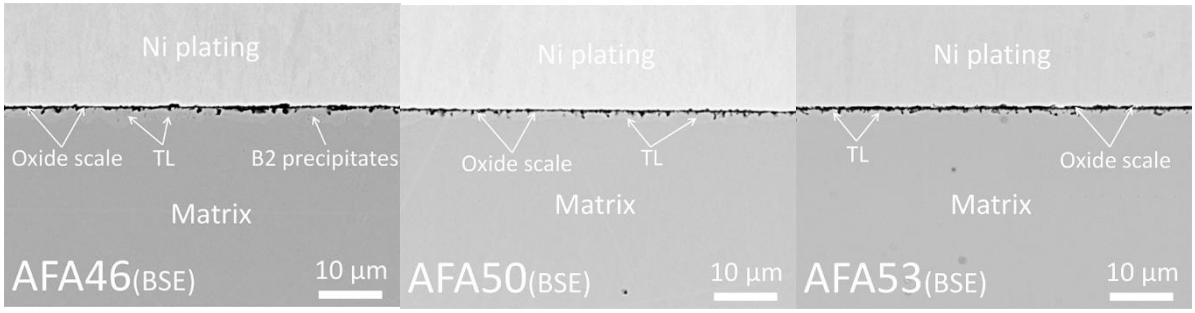

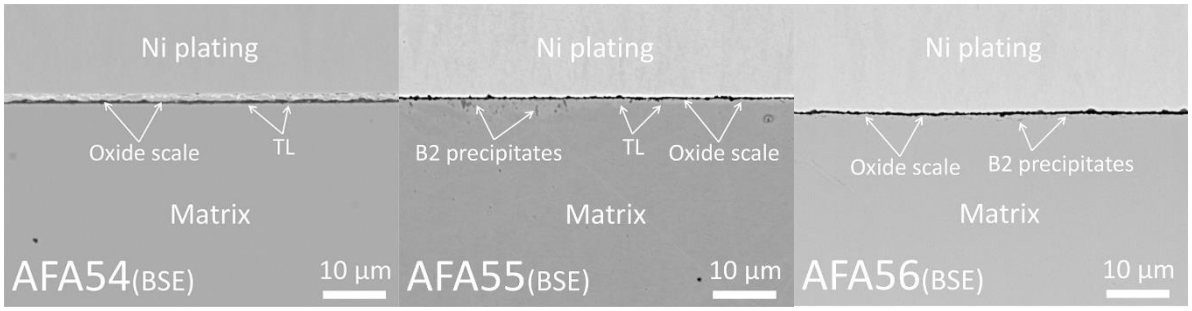

Fig. 5-11 Representative cross section images of AFA-1st generation samples after 1000 h exposure to 10^{-6} wt.% oxygen containing molten Pb at 600 °C: AFA46 (Fe-16.6Cr-2.3Al-19.6Ni), AFA50 (Fe-16.5Cr-2.5Al-21.4Ni), AFA53 (Fe-16.5Cr-3.2Al-23.3Ni), AFA54 (Fe-16.3Cr-4.3Al-23.4Ni), AFA55 (Fe-15.4Cr-2.5Al-28.3Ni) and AFA56 (Fe-15.2Cr-3.8Al-28.5Ni); TL: transitional layer.

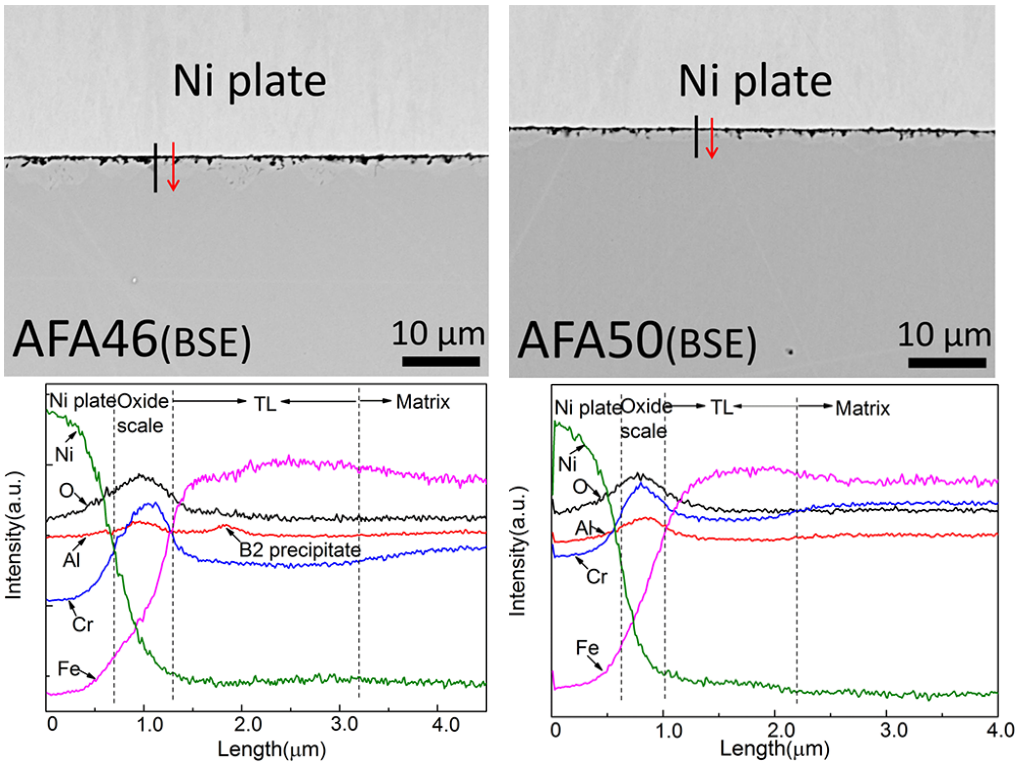

Fig. 5-12 Representative EDS line scans of the cross section of AFA-1st generation samples after 1000 h exposure to 10^{-6} wt.% oxygen containing molten Pb at 600 °C: AFA46 (Fe-16.6Cr-2.3Al-19.6Ni) and AFA50 (Fe-16.5Cr-2.5Al-21.4Ni), TL: transitional layer, (The direction of the measurement is indicated by the arrow).

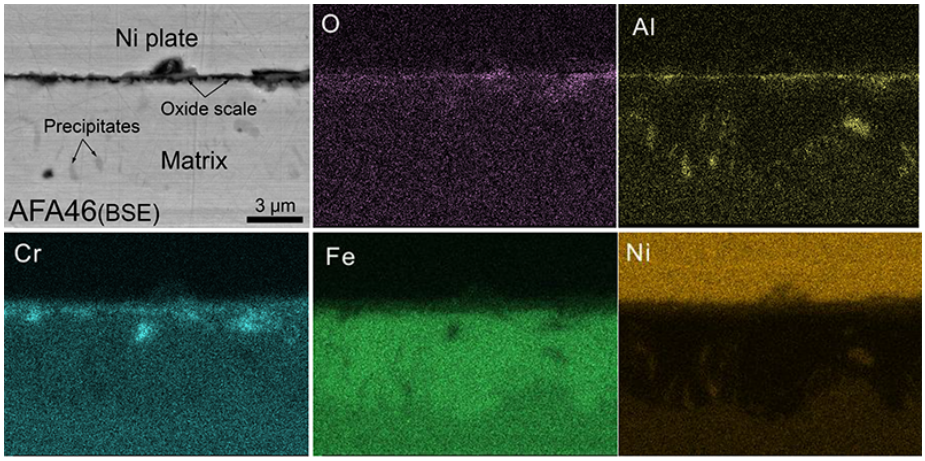

Fig. 5-13 EDS mapping of the cross section of AFA46 (Fe-16.6Cr-2.3Al-19.6Ni) after 1000 h exposure to 10^{-6} wt.% oxygen containing molten Pb at 600 °C.

X-ray diffraction pattern

Fig. 5-14 shows the representative XRD results of AFA-1st alloys after 1000 h exposure at 600 °C. Only Cr_2O_3 and Al_2O_3-Cr_2O_3 solid solution are recognized in the oxide scale. The intensities from the oxides are weak due to the small thickness of the oxide layer. The identified diffraction peak of Cr_2O_3 is at the position of 2θ=33.61°± 0.02°, while the position of Al_2O_3-Cr_2O_3 solid solution is in the range of 34.50°-34.73°. In addition, B2 phase is also identified, which is related to the Al-, Ni- rich precipitates in the transitional layer. Compared with passivated AFA samples exposed at 550 °C, the XRD pattern shows a slightly higher intensity of the diffraction peak at 2θ=31.01°, which indicates the increase of B2-NiAl phase fraction. Likewise, the peaks located at 2θ=44.44°, 64.73° and 81.99° show higher intensities due to extension of the volume occupied by the Cr-rich FeCr solid solution with BCC structure observed in the proximity of the oxide scale and in the surrounding of the B2-NiAl phase precipitates. As for the phase in the alloy matrix, the austenite is conserved after exposure at 600 °C in oxygen-containing molten Pb for 1000 h.

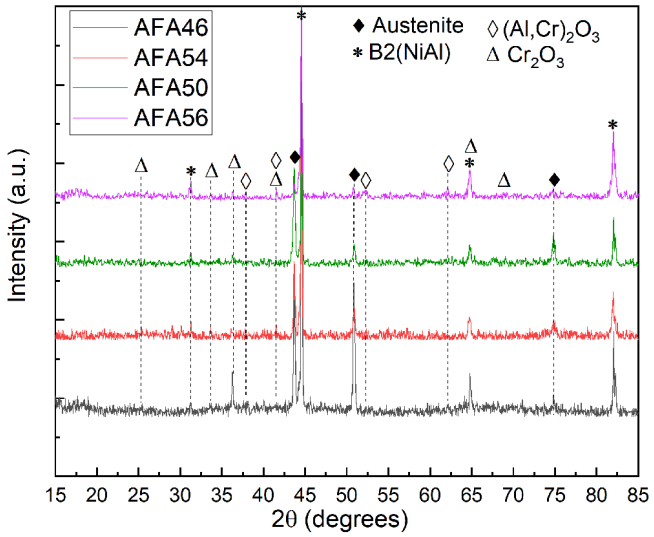

Fig. 5-14 Representative XRD patterns measured on AFA-1st generation samples after 1000 h exposure to 10^{-6} wt.% oxygen containing molten Pb at 600 °C: AFA46 (Fe-16.6Cr-2.3Al-19.6Ni), AFA50 (Fe-16.5Cr-2.5Al-21.4Ni), AFA54 (Fe-16.3Cr-4.3Al-23.4Ni) and AFA56 (Fe-15.2Cr-3.8Al-28.5Ni).

5.2 Corrosion behavior of AFA-1st generation at 600 °C for 2000 h

SEM/EDS, XRD characterization

Two high Al containing samples AFA54 (4 wt.% Al) and AFA56 (3.5 wt.% Al) corresponding to high Ni content AFA54 (24 wt.% Ni) and AFA56 (29 wt.% Ni) have been exposed to 10^{-6} wt.% oxygen containing molten Pb at 600 °C for 2000 h. Fig. 5-15 shows the surface morphologies after the corrosion test. No dissolution attack is observed on both samples. The surface of AFA54 is covered by a smooth and continuous scale based on Al- and Cr- oxides, except a few magnetite (Fe_3O_4) spots (< 1% surface area). In addition, some spots shown in dark-gray contrast (10-15% surface area) have been observed in BSE mode images, e.g. AFA54 (BSE) in Fig. 5-15. The EDS measurements in these dark spots indicate an increase of the Al and O concentration compared with the rest of the surface. The surface of AFA56 is covered by a continuous oxide scale. EDS measurements indicate that the oxide scale is rich in Al, Cr and O. Besides, magnetite spots accounting for 5-10% surface area are also visible. Dark Al and O rich spots are also observed on the scale surface, but have a lower fraction (< 2% surface area) compared with AFA54.

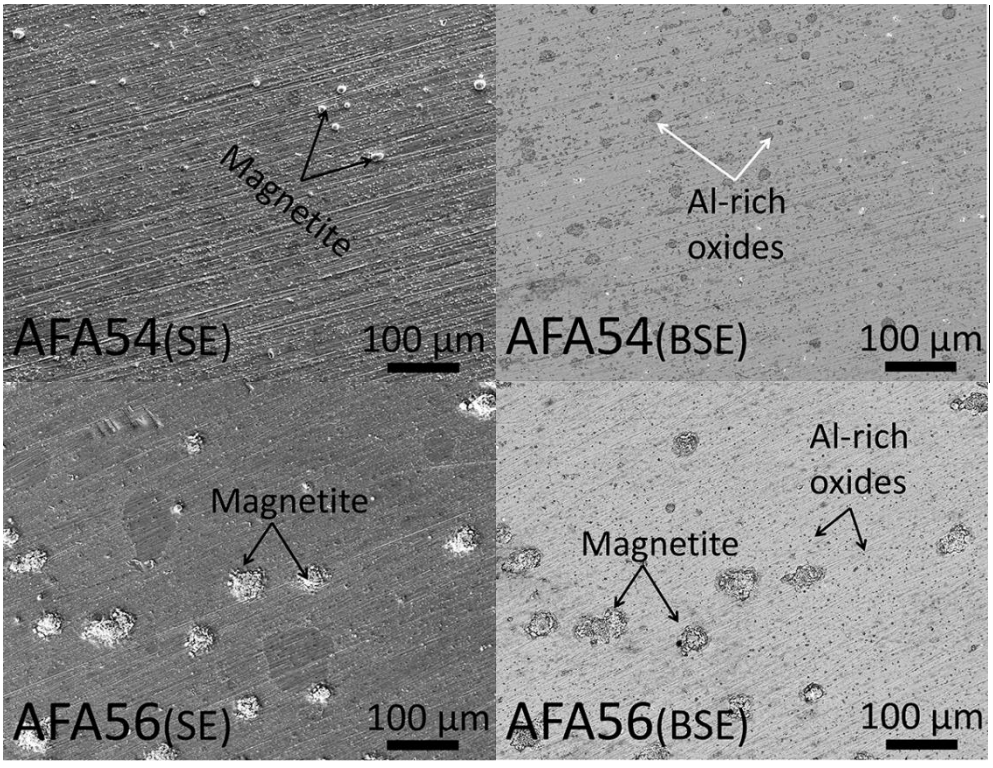

Fig. 5-15 Surface morphologies of AFA54 (SE, BSE) and AFA56 (SE, BSE) after 2000 h exposure to 10^{-6} wt.% oxygen containing molten Pb at 600 °C.

Fig. 5-16 shows as example the cross section image of AFA54. The alloy surface is covered by a thin oxide scale (<100 nm). No dissolution attack or Pb penetration into the matrix has been found. EDS line scanning of the oxide scale indicates that the signal maximum from O coincides with the maxima of the Cr and Al signals, meaning the formation of an Al-, Cr-based oxide scale. The dark Al-, O-rich spots observed on the surface are with thicker oxide layer (≈200 nm). Below the oxide scale, a bright transitional layer, enriched in Fe and Ni, is observed. The thickness varies from 0.5 to 2 µm. In addition, some dark precipitates are also observed in the transitional layer. As evidenced by EDS mapping, the precipitates consist of Al-, Ni-rich spots and some Cr-rich spots located near the oxide scale or/and in vicinity of the NiAl-based precipitates, as shown in Fig. 5-17. Moreover, the mapping of the cross section also shows a distribution of Al and Cr in the oxide layer, with more Al in the thicker parts and more Cr in the thinner ones (Fig. 5-17).

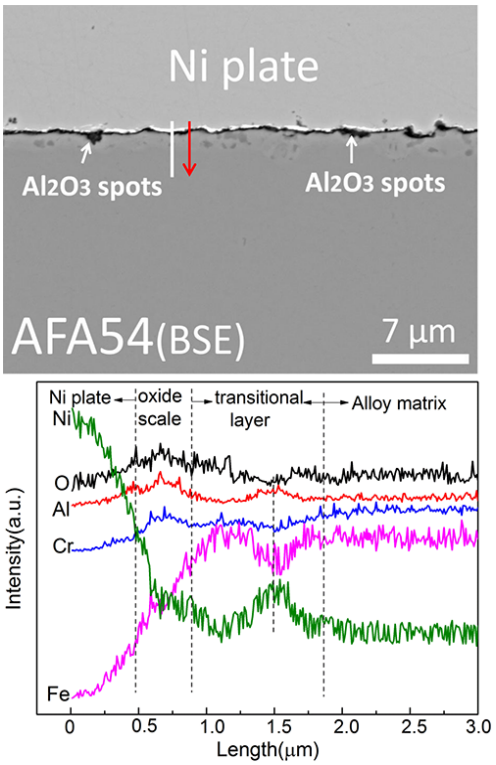

Fig. 5-16 Line scanning of the cross section of AFA54 after 2000 h exposure to 10^{-6} wt.% oxygen containing molten Pb at 600 °C, (The direction of the measurement is indicated by the arrow).

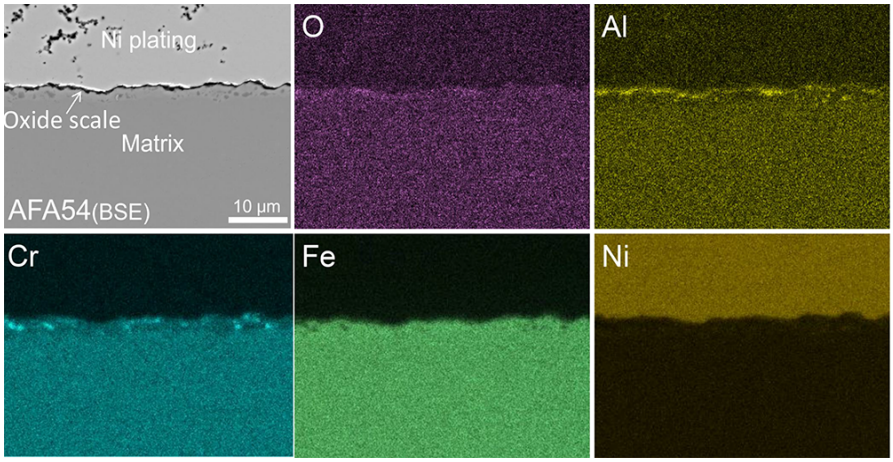

Fig. 5-17 EDS mapping of the cross section of AFA54 sample after 2000 h exposure to 10^{-6} wt.% oxygen containing molten Pb at 600 °C.

Corroborating the SEM/EDS and XRD analysis, protective oxide scales are formed on AFA54 and AFA56 consisting of $(Al_{0.9}Cr_{0.1})_2O_3$, (2θ=34.95-35°, corresponding to (104) lattice plane) and Cr_2O_3 (Fig. 5-18). Peaks of magnetite are also present. In addition, FCC, B2-NiAl and a small fraction of a FeCr solid solution with BCC structure (PDF Nr: 65-7775) phases have been identified in the XRD patterns. The B2-NiAl and FeCr solid solution (BCC) phases are from the transitional layer, while the FCC solid solution is from the alloy matrix.

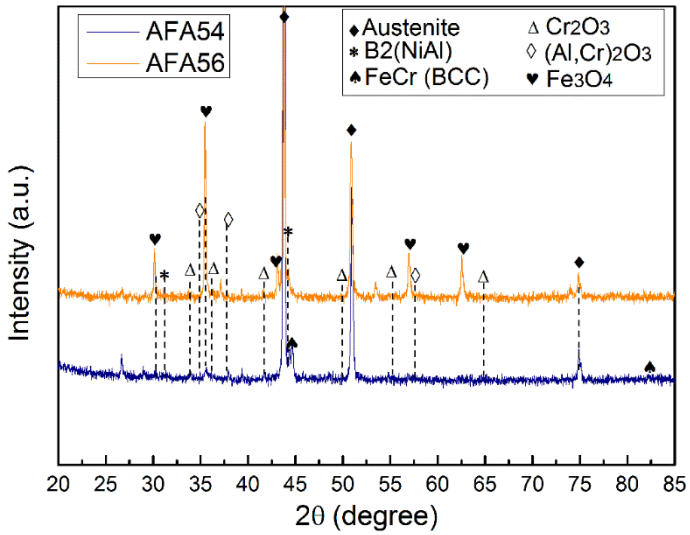

Fig. 5-18 XRD patterns measured on AFA54 (Fe-16.3Cr-4.3Al-23.4Ni) and AFA56 (Fe-15.2Cr-3.8Al-28.5Ni) after 2000 h exposure to 10^{-6} wt.% oxygen containing molten Pb at 600 °C.

TEM evaluation

For further evaluation of the oxide scale and transitional layer, the sample AFA54 (Fe-16Cr-4Al-24Ni) with less magnetite spots after 2000 h exposure in oxygen containing molten Pb at 600 °C is selected and characterized by different TEM techniques.

Fig. 5-19 shows the TEM results of the sample in bright field (BF) mode combined with selected area electron diffraction (SAED) analysis. The SAED performed on bulk material reveals FCC crystalline structure (PDF Nr.33-397) of the alloy matrix, although the sample is not tilted accurately into an appropriate zone axis. The zone axis parallel to the electron beam is close to [001]. The highlighted spots can be attributed to (-200), (200), and (-220), respectively. As for the oxides formed on the surface, the ring patterns on one hand indicate the polycrystalline structure of the oxides. On the other hand, it reflects the nano-sized grains formed in the scale. This is also reflected by the high-resolution TEM image, shown in Fig. 5-19 (e). Here, small grains and lattice fringes with a spacing of 0.19nm are visible. They can be attributed to (202) planes of corundum. The thickness of the oxide scale is around 50 nm. Based on the measured spacing, the ring pattern belongs to corundum $(Al_xCr_{1-x})_2O_3$, with x=0.85-0.9. This is in agreement with the result obtained by the XRD.

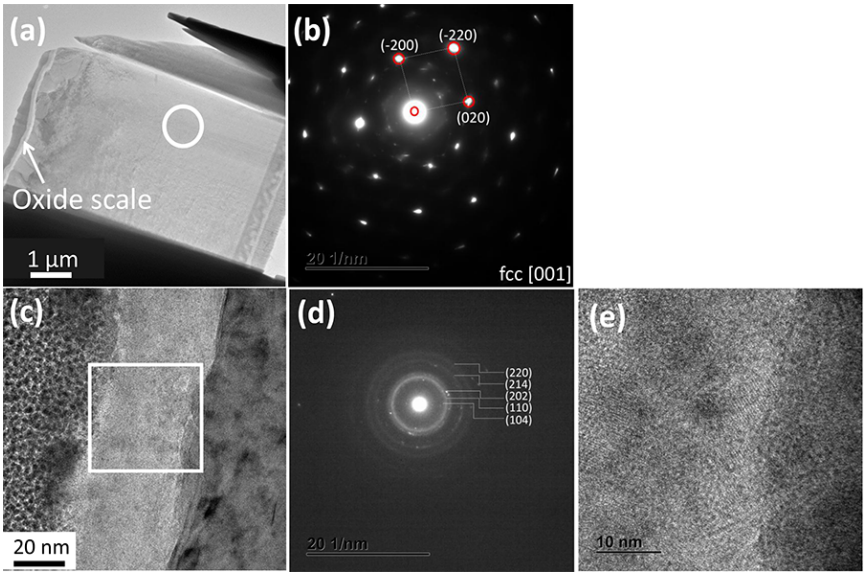

Fig. 5-19 TEM-BF images of AFA54 (Fe-16.3Cr-4.3Al-23.4Ni) and the corresponding SAED obtained on bulk alloy (a, b); the oxide scale (c, d); high resolution image (e).

Fig. 5-20 shows the STEM image and the EDS line profile along the red line, which starts from the middle part of the oxide scale and extends into the alloy matrix. The oxygen signal was not evaluated. In the oxide scale part, Al has a strong intensity while it reduces gradually in the matrix part, which indicates the formation of Al_2O_3-based oxide scale. In contrast, Fe, Cr and Ni show relatively low intensities in the oxide scale. The yellow square is the reference area for drift correction during acquisition.

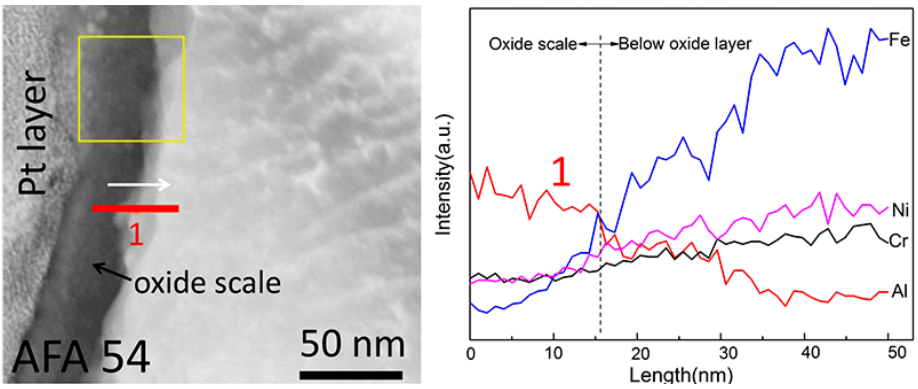

Fig. 5-20 STEM-image (left) and STEM-EDS line profiles (right) of the cross section of the oxide scale formed on AFA54 after 2000 h exposure to 10^{-6} wt.% oxygen containing molten Pb at 600 °C.

Moreover, EDS area analysis has been performed within the oxide scale region, as shown in Fig. 5-21. Table 5-2 shows the standardless quantitative results of the chemical compositions in area 1 and area 2, respectively, evaluated with absorption correction for a 50 nm thin Al_2O_3 film. Based on the measurement, the fraction of Cr_2O_3 is 20.82 wt.% in area 1, and 16.22 wt.% in area 2, being consistent with the Cr_2O_3 content in $(Al_{0.9}Cr_{0.1})_2O_3$ solid solution (θ=34.95-35°, corresponding to (104) lattice plane), identified in the X-ray diffraction patterns (Fig. 5-18)

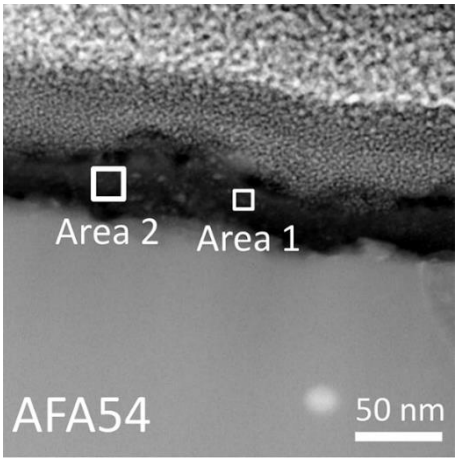

Fig. 5-21 STEM-image showing the areas for EDS analyses of the oxide scale formed on AFA54 after 2000 h exposure to 10^{-6} wt.% oxygen-containing molten Pb at 600 °C.

Table 5-2 EDS standardless quantitative measurements of chemical compositions of areas in oxide scale (wt.%).

Region	O(K)	Al(K)	Cr(K)	Fe(K)	Ni(K)
Area 1	46.91	39.03	13.15	0.88	0.00
Area 2	53.58	36.40	9.08	0.93	0.00

STEM-EDS qualitative area scans have been acquired in the transitional layer and alloy matrix. Compared with the alloy matrix (shown in area 3 in Fig. 5-22), the transitional layer is enriched in Fe

and Ni, and depleted in Al, see area 1 in Fig. 5-22. In addition, the measurement of area 2, which is located at the upper part of the transitional layer, shows the strong intensities from Cr, which confirms the formation of a Cr-rich phase. The observed signal of Cu stems from the Cu-lift-out grid.

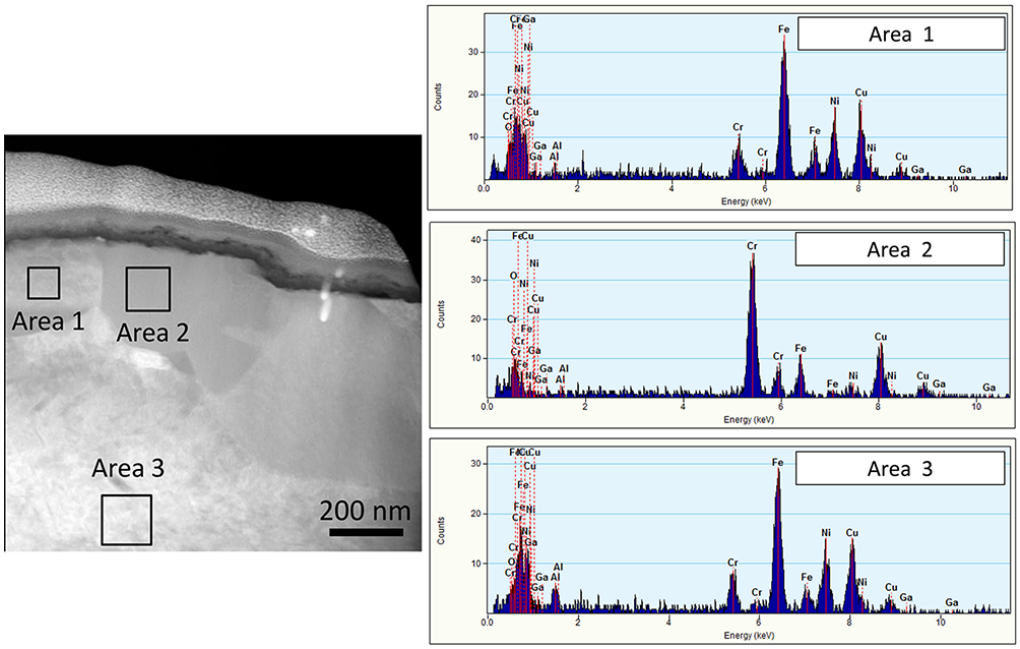

Fig. 5-22 STEM image (left) and STEM-EDS area spectra (right) of the alloy matrix of AFA54 after 2000 h exposure to 10^{-6} wt.% oxygen containing molten Pb at 600 °C.

5.3 Corrosion behavior of AFA-2nd generation at 600 °C

Six AFA-2nd generation alloys have been exposed to 10^{-6} wt.% oxygen containing molten Pb at 600 °C for 1000 h and 2000 h. The surface status of each sample has been checked by SEM/EDS. Table 5-3 summarizes the performance of AFA-2nd generation samples after the corrosion tests.

Table 5-3 Corrosion performance of AFA-2nd generation alloys in molten Pb conditions.

Code	Chemical compositions (wt.%)	1000 h	2000 h
AFA70	Fe-14.7Cr-2.7Al-17.9Ni-0.4Y	🙂	🙂
AFA71	Fe-15.4Cr-2.5Al-19.9Ni-0.5Y	🙂	🙂
AFA72	Fe-15.4Cr-2.5Al-21.8Ni-0.5Y	😐	🙂
AFA73	Fe-15.4Cr-2.1Al-22Ni-0.5Y-1.3Nb	🙂	🙂
AFA74	Fe-15.5Cr-4.3Al-27.9Ni-0.5Y-1.1Nb	🙂	🙂
AFA75	Fe-15.7Cr-3.1Al-24.1Ni-0.7Y-1.68Nb	🙂	🙂

🙂: Corrosion resistance; 😐: Oxide scale spallation (no corrosion attack).

5.3.1 Corrosion test at 600 °C for 1000 h

Alloy surface characterization

Fig. 5-23 shows the surface view of AFA-2nd generation samples after the corrosion tests. The surface morphologies of the samples made from four different alloys are displayed as examples, due to their differences in the Al and Cr concentrations, Nb addition and scale spallation: AFA70 (Fe-14.7Cr-2.7Al-17.9Ni-0.4Y), AFA71 (Fe-15.4Cr-2.5Al-19.9Ni-0.5Y), AFA72 (Fe-15.4Cr-2.5Al-21.8Ni-0.5Y) and AFA73 (Fe-15.4Cr-2.1Al-22Ni-0.5Y-1.3Nb), respectively. All of the samples have been protected by the dense and continuous oxide scale grown during exposure. No corrosion attack is observed. The still visible scratches from the grinding process may indicate that the passivating oxide scales are very thin. As evidenced by quantitative EDS measurements, the oxides formed on the alloys' surfaces are based on Al and Cr. In addition, a few protrusions of Fe-, Cr- rich oxide (magnetite) are observed on all samples. These protrusions are formed at the surface of the regions surrounding YNiAl-rich spots, which are depleted in Al and Ni and hence are rich in Fe and Cr. Regarding AFA72, some regions totalizing between 20% and 30% surface area show the evidence of oxide scale spallation or scale cracks.

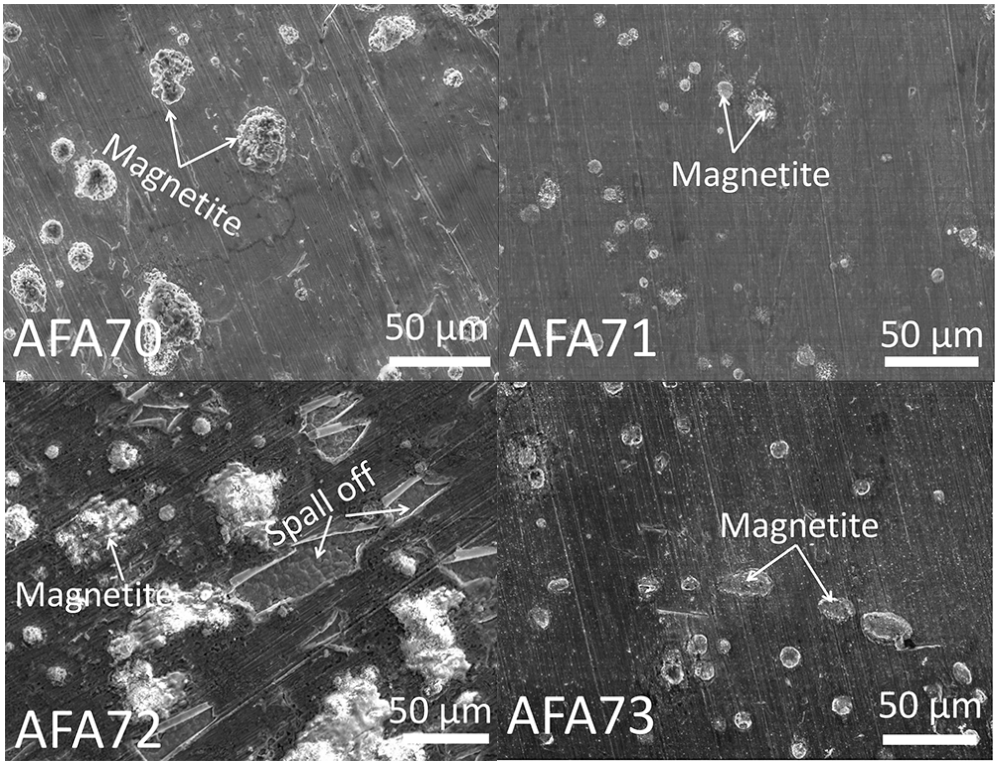

Fig. 5-23 Representative surface morphologies of AFA-2nd generation alloys after 1000 h exposure to 10^{-6} wt.% oxygen containing molten Pb at 600 °C: AFA70 (Fe-14.7Cr-2.7Al-17.9Ni-0.4Y), AFA71(Fe-15.4Cr-2.5Al-19.9Ni-0.5Y), AFA72 (Fe-15.4Cr-2.5Al-21.8Ni-0.5Y) and AFA73 (Fe-15.4Cr-2.1Al-22Ni-0.5Y-1.3Nb).

Cross section analysis

Samples containing different concentrations of Al and Cr and two samples containing Nb are selected to exemplify the cross section analysis in Fig. 5-24. These samples are AFA70 (Fe-14.7Cr-2.7Al-17.9Ni-0.4Y), AFA71 (Fe-15.4Cr-2.5Al-19.9Ni-0.5Y), AFA73 (Fe-15.4Cr-2.1Al-22Ni-

0.5Y-1.3Nb), AFA74 (Fe-15.5Cr-4.3Al-27.9Ni-0.5Y-1.1Nb). No dissolution attack has been observed. A thin oxide scale with a thickness less than 200 nm has been observed on all exposed samples. The EDS line scans of the oxide scales of all AFA-2nd generation alloys show a protective scale consisting of O, Al and Cr, where the Cr peak appears either in front of the peak of Al or overlapped, as shown in the examples displayed in Fig. 5-25. Below the oxide scale, a transitional layer, which is depleted in Al and Cr but enriched in Fe and Ni, is identified by EDS line scanning. Some dark spots enriched in Al and Ni have been observed in the transitional layer (Fig. 5-25, AFA70). The elemental mapping of the oxide scales (an example depicted in Fig. 5-26) shows a uniform distribution of O, Cr and Al in the oxide layer. The intensity of Cr in the scale region is lower in all second generation AFA alloys compared with AFA-1st generation samples exposed to the same conditions. Moreover, the presence of Cr-enriched regions is not observed in some samples (e.g. AFA73).

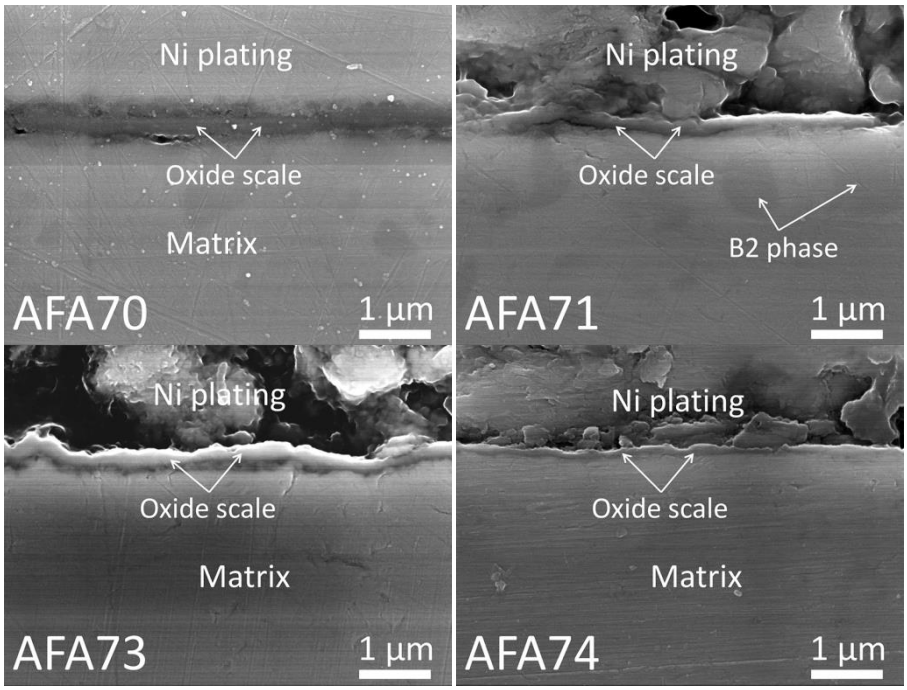

Fig. 5-24 Representative cross section images of AFA-2nd generation alloys after 1000 h exposure to 10^{-6} wt.% oxygen containing molten Pb at 600 °C: AFA70 (Fe-14.7Cr-2.7Al-17.9Ni-0.4Y), AFA71 (Fe-15.4Cr-2.5Al-19.9Ni-0.5Y), AFA73 (Fe-15.4Cr-2.1Al-22Ni-0.5Y-1.3Nb) and AFA74 (Fe-15.5Cr-4.3Al-27.9Ni-0.5Y-1.1Nb).

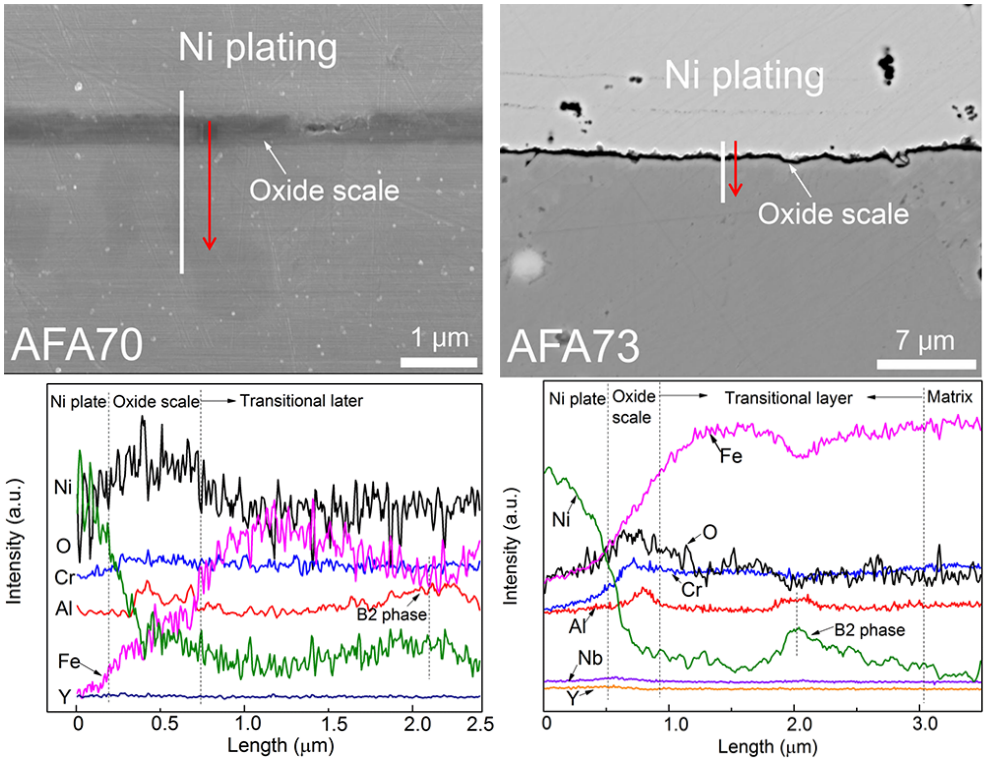

Fig. 5-25 EDS line scanning across the cross section of AFA-2nd generation alloys after 1000 h exposure to 10^{-6} wt.% oxygen containing molten Pb at 600 °C: AFA71 (Fe-15.4Cr-2.5Al-19.9Ni-0.5Y) and AFA73 (Fe-15.4Cr-2.1Al-22Ni-0.5Y-1.3Nb), (The direction of the measurement is indicated by the arrow).

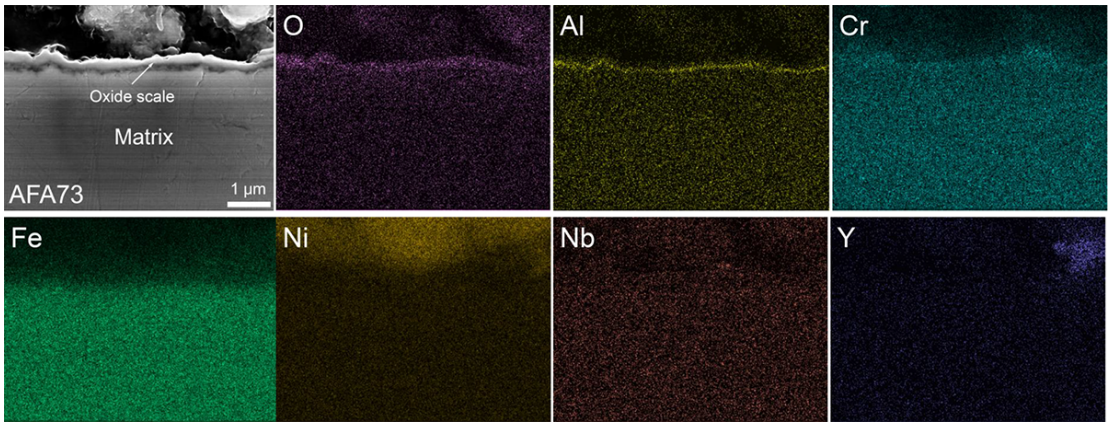

Fig. 5-26 EDS mapping of the cross section of AFA73 alloy after 1000 h exposure to 10^{-6} wt.% oxygen containing molten Pb at 600 °C.

XRD characterization

According to the identified phases shown in the Fig. 5-27, the oxides mainly formed after 1000 h exposure are magnetite (Fe_3O_4), Cr_2O_3 (PDF card Nr: 74-326), and Al_2O_3-Cr_2O_3 solid solution. The identified oxides formed on different samples are as follows: AFA70: Fe_3O_4, Cr_2O_3 (weak); AFA71: Fe_3O_4, Cr_2O_3, $(Al_{0.9}Cr_{0.1})_2O_3$ (weak); AFA72: Fe_3O_4, Cr_2O_3; AFA73: Fe_3O_4, Cr_2O_3, $(Al_{0.9}Cr_{0.1})_2O_3$; AFA74: Fe_3O_4, Cr_2O_3, $(Al_{0.9}Cr_{0.1})_2O_3$; AFA75: Fe_3O_4, Cr_2O_3, $(Al_{0.9}Cr_{0.1})_2O_3$ (weak). The weak signals from oxides are due to the small thickness of the scale (<200 nm). The formed magnetite peaks are from the

protrusions grown on the regions surrounding YNiAl-rich precipitates reaching the sample surface, which are depleted in Al and Ni. Besides, austenite and B2 phases are observed in all the samples. The peaks located at 2θ=44.44°, 64.73° and 81.99° (BCC structure), where the peaks of the B2 phase and FeCr solid solution overlap, are weak, indicating a low concentration of both phases.

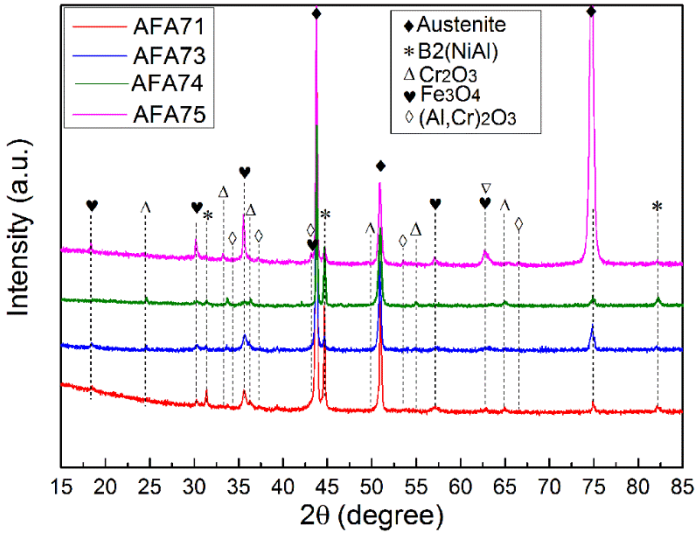

Fig. 5-27 Representative XRD patterns performed on AFA-2nd generation samples after 1000 h exposure in 10^{-6} wt.% oxygen containing molten Pb at 600 °C (sample AFA71, AFA73, AFA74 and AFA75).

5.3.2 Corrosion test at 600 °C for 2000 h

Alloy surface characterization

Fig. 5-28 shows the representative surface view of protective AFA-2nd generation samples after 2000 h exposure. Samples made of AFA70 and AFA71 with different content of Al and Cr and AFA75 containing 1.5 wt.% Nb are selected to be used as examples of the morphologies observed on the exposed sample surfaces. The passivating oxide scales are dense and continuous. No corrosion attack is evident after the corrosion test. Based on the EDS point measurements, the oxide scales are enriched in Al and Cr. In addition, some Fe-, Cr-rich protrusions are observed on the surface of all AFA-2nd generation alloys in the regions (depleted in Al and Ni) surrounding the YNiAl-precipitates reaching the surface.

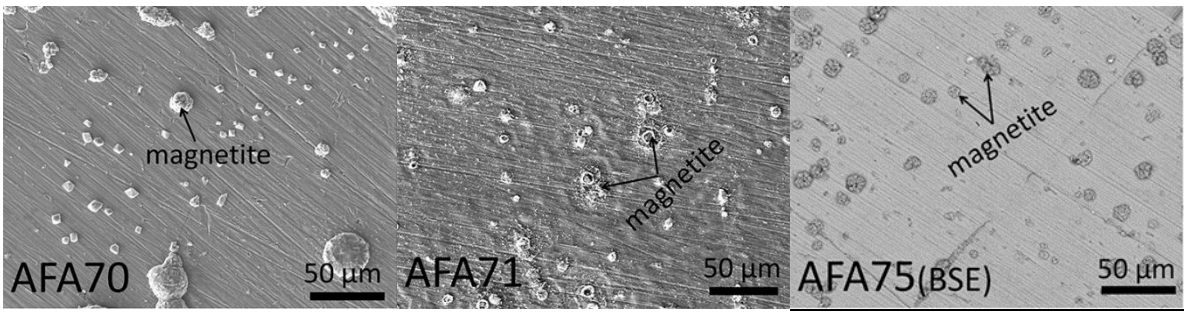

Fig. 5-28 Representative surface morphologies of AFA-2nd generation samples after 2000 h exposure to 10^{-6} wt.% oxygen containing molten Pb at 600 °C (sample AFA70, AFA71 and AFA75).

Cross section analysis

Fig. 5-29 shows representative SEM cross section images: AFA70 (Fe-14.7Cr-2.7Al-17.9Ni-0.4Y), AFA73 (Fe-15.4Cr-2.1Al-22Ni-0.5Y-1.3Nb) and AFA75 (Fe-15.7Cr-3.1Al-24.1Ni-0.7Y-1.68Nb). No corrosion attack is observed in the alloy matrix. The alloy surface is covered by a thin and continuous oxide layer. Selected EDS line scans indicating that the oxide scale is enriched in Al and Cr, are shown in Fig. 5-30. The maximum of the Al signal is either below that of the Cr signal or they are coincided. Below the oxide scale, a bright transitional layer with dark precipitates is visible in the SEM-BSE images (see AFA70 in Fig. 5-29). Based on the EDS line scanning measurements, Al and Cr are depleted while Fe is enriched in the transitional layer (see Fig. 5-30). The thickness of this layer varies from 0.5 to 2 µm, keeping almost the same ranges of values observed in case of the samples exposed for 1000 h to molten Pb. For example, AFA75 has formed a transitional layer, ranging from 0.5 to 1 µm. The transitional layer shows a decrease of Al. Moreover, some bright particles, which are coherent with B2 precipitates, have been observed in the transitional layer, see Fig. 5-30. Based on the EDS measurements, they are Fe-Nb-rich phase. The Cr-rich regions were not observed in the transitional layer.

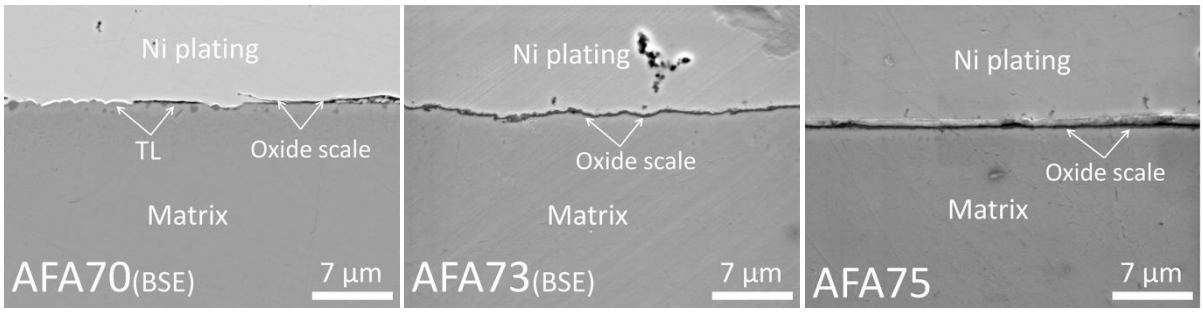

Fig. 5-29 Representative cross section images of AFA-2nd generation samples after 2000 h exposure to 10^{-6} wt.% oxygen containing molten Pb at 600 °C (sample AFA70, AFA73 and AFA75).

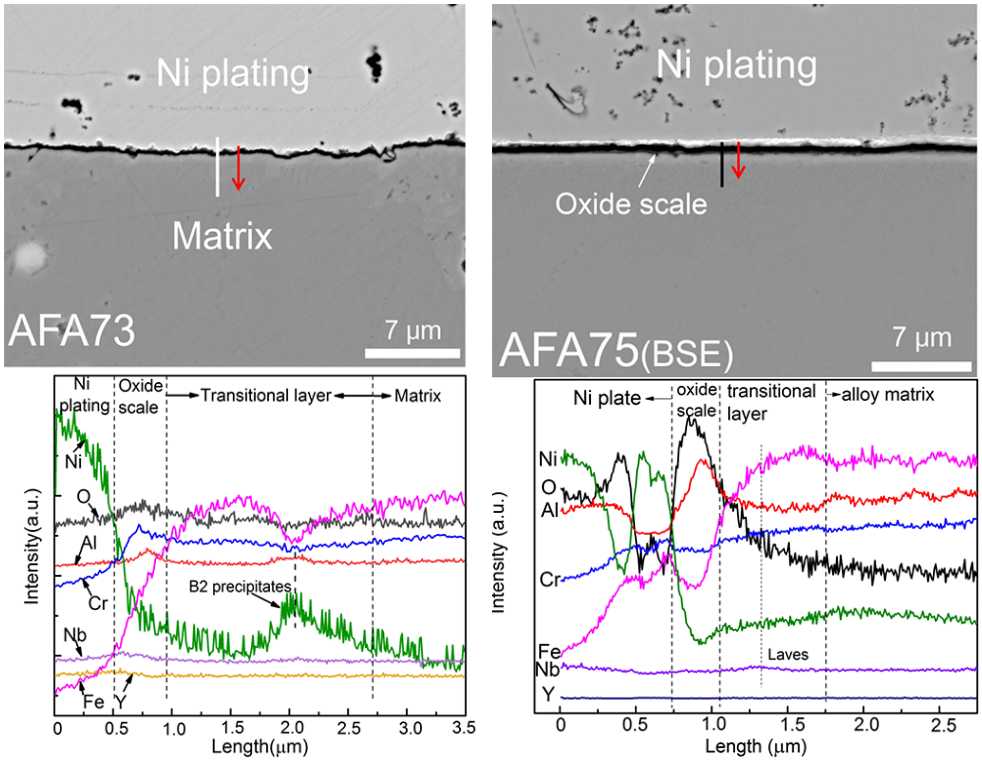

Fig. 5-30 EDS line scans of the cross section of AFA-2nd generation samples after 2000 h exposure to 10^{-6} wt.% oxygen containing molten Pb at 600 °C (sample AFA73 and AFA75), (The direction of the measurement is indicated by the arrow).

The oxides formed on AFA-2nd generation after 2000 h exposure in 10^{-6} wt.% oxygen-containing molten Pb is the same as that found after 1000 h exposure at 600 °C. The detailed XRD analysis results can be found in appendix A.

TEM evaluation

After 2000 h exposure to 10^{-6} wt.% oxygen containing molten Pb at 600 °C, sample AFA75 (Fe-15.7Cr-3.1Al-24.1Ni-0.7Y-1.68Nb) with uniform oxide scale has been selected for further TEM evaluation. The TEM foil is cut from the magnetite-free region in the oxide scale by FIB. Fig. 5-31 shows the SAED results obtained from the alloy matrix (a) and oxide scale region (c). The sample was not tilted accurately to a low indexed zone axis. According to Fig. 5-31 (b), austenite (FCC, PDF Nr.33-397) oriented in <013> zone axis parallel to the electron beam is identified in the bulk material. The SAED ring pattern obtained from the oxide scale indicates the poly- and nano-crystalline morphology of the oxides in the scale. The phase shown in the SAED can be identified as corundum type $(Al_{0.77}Cr_{0.23})_2O_3$ phase (shown in Fig. 5-31 (d)).

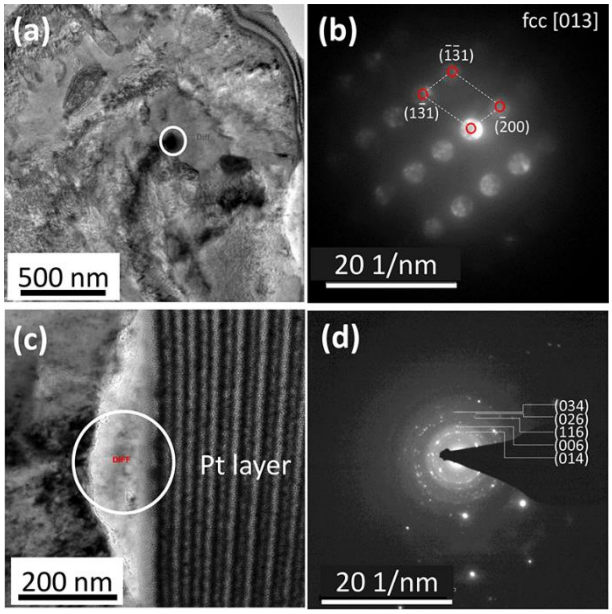

Fig. 5-31 TEM-BF images of the cross section of AFA75 (Fe-15.7Cr-3.1Al-24.1Ni-0.7Y-1.68Nb) and corresponding nano diffraction of the highlighted particle in alloy matrix (a) (b), and oxide scale (c), with the corresponding SAED (d).

Fig. 5-32 displays the STEM-EDS line profiles of the oxide scale. Here, the oxygen signal was not evaluated. At the outer part of the oxide scale below the Pt-layer, the intensities of Cr and Al are identical, and the signal of Fe is low. The thickness of this part is around 50 nm. Following the outer part layer, an inner part with strong signal from Al and reduced Cr intensity is observed. The thickness of this part is also around 50 nm. Below the oxide scale, some Fe-, Nb-rich precipitates can be found, and additionally Al-, Ni-rich B2 phase precipitates, which are also observed by SEM. The yellow square is the reference area for drift correction during acquisition.

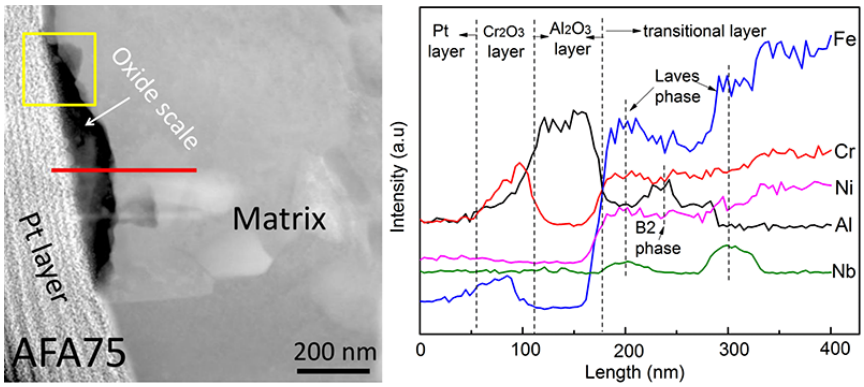

Fig. 5-32 STEM-image (left) and STEM-EDS line profile (right) of the cross section of the oxide scale formed on AFA75 after 2000 h exposure to 10^{-6} wt.% oxygen containing molten Pb at 600 °C.

Fig. 5-33 shows the EDS mapping employed to analyze the phase compositions of the small square marked in the bulk of AFA75. It clearly shows that Al and Ni enrich while Cr depletes at some

large spots (300-500 nm), indicating the formation of B2-NiAl phase. Small precipitates (<50 nm) rich in Nb and Fe may indicate the formation of Laves phase. The yellow square is the reference area for drift correction during acquisition.

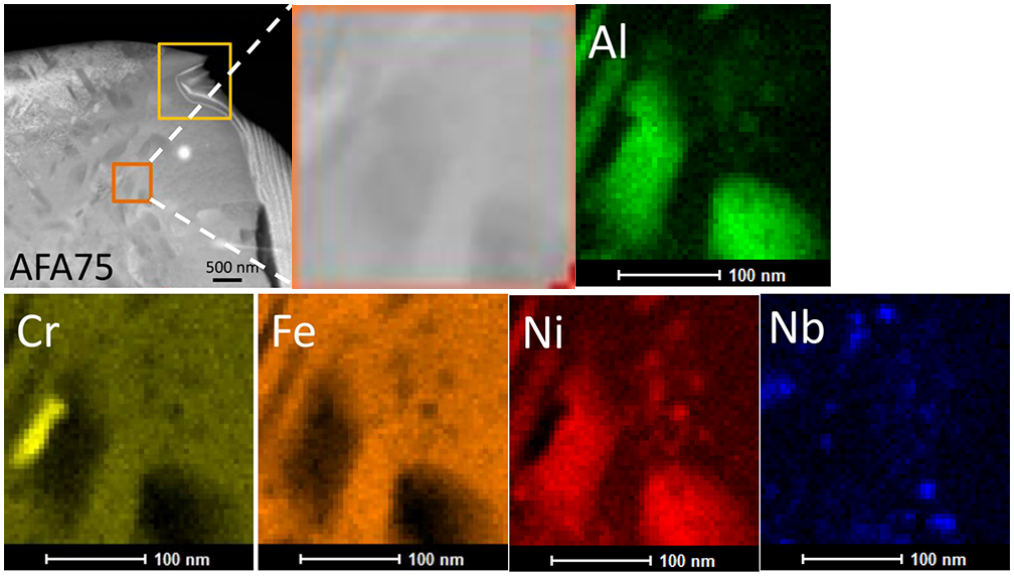

Fig. 5-33 STEM-image (upper left), detail of STEM-image (upper middle) and STEM-EDS mapping of alloy matrix of AFA75 after 2000 h exposure to 10^{-6} wt.% oxygen containing molten Pb at 600 °C.

Further chemical characterization has been performed by STEM-EDS line profiles, shown in Fig. 5-34. Two types of nano-precipitates, shown in dark and bright contrast, are observed. According to the EDS line profiles across the particles, the bright particles, which are rich in Nb and Fe, indicate the formation of laves phase particles. The dark precipitates enriched in Al and Ni belong to the B2 phases. The yellow square is the reference area for drift correction during acquisition.

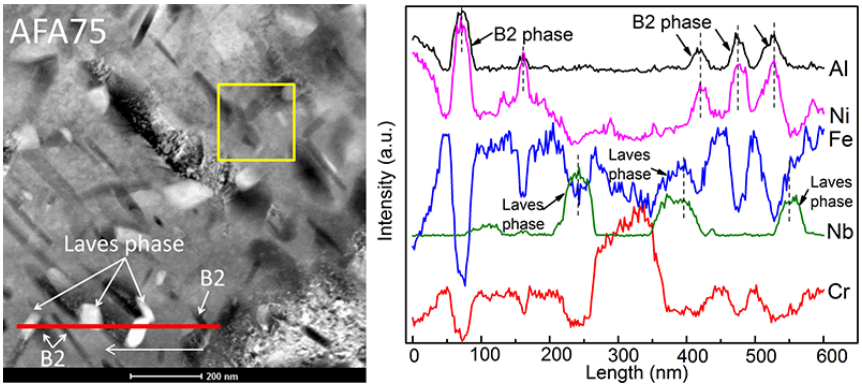

Fig. 5-34 STEM-image (left) and STEM-EDS line profiles (right) of the matrix of AFA75 after 2000 h exposure to 10^{-6} wt.% oxygen containing molten Pb at 600 °C.

5.4 Microstructure stability characterization

Three AFA samples AFA46(20 wt.% Ni), AFA54(24 wt.% Ni) and AFA56(29 wt.% Ni) are selected to characterize their microstructural stabilities after 1000 h exposure to 10^{-6} wt. % oxygen containing

molten Pb at 600 °C, shown in Fig. 5-35. The surface oxide layer has been removed by grinding the metal surface with a depth of 20 µm. Then the samples matrix were analysed by SEM/EDS and XRD.

Fig.5-35 shows the representative SEM morphologies of exposed AFA46 and AFA56 after removal of the surface scale. A few nano size black dots, mainly distributed in the matrix, are identified at high magnification (4000x). Then the EDS point measurements show a slight enrichment of Al and Ni at these spots.

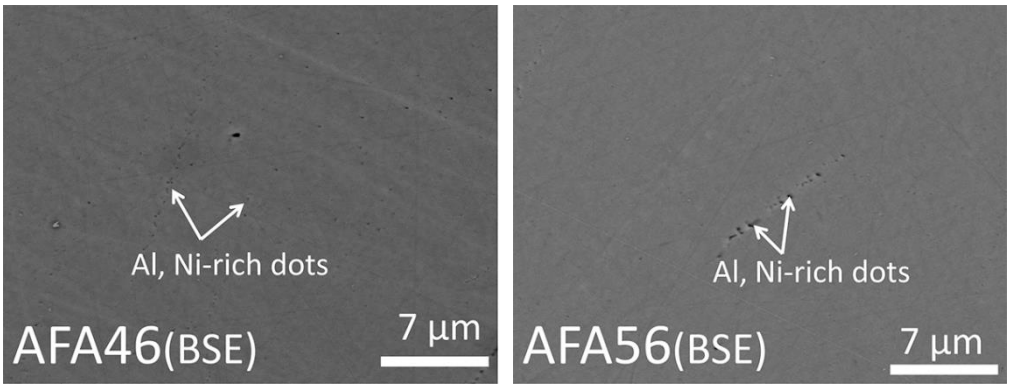

Fig. 5-35 SEM microstructures of samples matrix after removing the surface oxide layer, AFA46 and AFA56 after 1000 h exposure to 10^{-6} wt. % oxygen containing molten Pb at 600 °C.

Further analysis by XRD indicates that the matrix conserves the austenite phase, see Fig. 5-36. In addition, the secondary phase precipitates, intermetallic compound $Ni_3(Al,Fe)$, are also identified in all three samples, shown in Fig. 5-36.

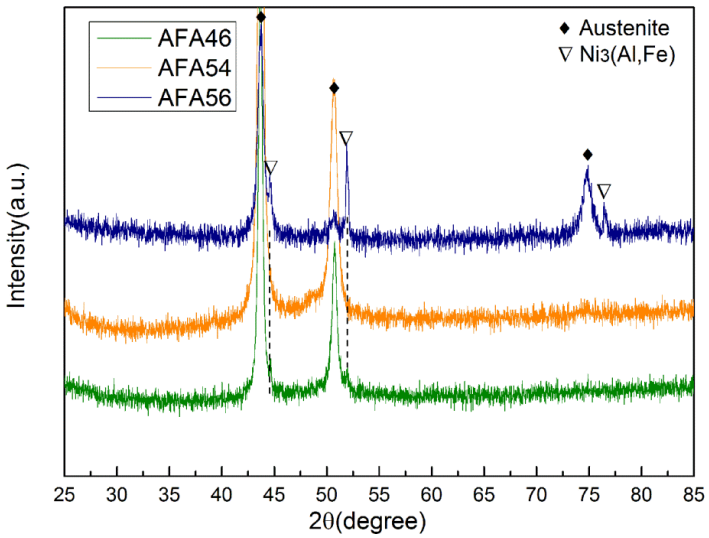

Fig. 5-36 XRD patterns of the AFA46, AFA54 and AFA56 alloys after remove the surface oxide scale, samples exposed to molten Pb with 10^{-6} wt.% oxygen at 600 °C for 1000 h. The microstructure of the exposed alloys consists of austenite (γ) and γ'-$Ni_3(Al,Fe)$ phases.

5.5 Analysis and recommendations for corrosion resistant AFA model alloys

The main goal of this chapter is to define the critical concentrations of Al, Cr and Ni, at which the quaternary Fe-Cr-Al-Ni model alloys (AFA-1st generation) are able to form stable protective oxide scales while preserving an austenite matrix during exposure to 10^{-6} wt.% oxygen containing molten Pb at 550 °C and 600 °C. Additionally, the influence of minor additions of the reactive element yttrium on the protective scale quality (adherence) and of niobium on the mechanical properties at high temperature is explored (AFA-2nd generation).

Twelve AFA-1st generation model alloys have been exposed to 10^{-6} wt.% oxygen containing molten Pb at 550 °C and 600 °C for 1000 h. The corrosion performance of AFA-1st generation alloys have been summarized and shown in Table 5-1. Eight alloys with Cr content above 14 wt.% (AFA45, AFA46, AFA47, AFA50, AFA53, AFA54, AFA55 and AFA56) have formed protective oxide scale at 550 °C. The oxide scale with a thickness of 100-200 nm is based on Cr_2O_3 (outer layer) and Cr_2O_3-Al_2O_3 solid solution (inner layer). Some magnetite protrusions (<2%) are observed on the sample surfaces after the corrosion tests. A quasi-continuous transitional layer with FCC structure and B2-NiAl and BCC solid solution precipitates is found beneath the oxide scale. The thickness of the transitional layer varies from 1 to 3 µm and decreases in thickness with the increase of the Ni content.

From the eight alloys that have shown corrosion resistance at 550 °C, only six AFA-1st generation alloys (AFA46, AFA50, AFA53, AFA54, AFA55, and AFA56) were passivated during 1000 h exposure to oxygen containing molten Pb at 600 °C. The oxide scale and transitional layers formed at the higher temperature are comparable with those formed at 550 °C. The concentration of the precipitates in the transitional layer is slightly higher compared with the same samples exposed at 550 °C.

Two high Ni containing AFA-1st generation alloys AFA54 (24 wt.% Ni) and AFA 56 (29 wt.% Ni) have formed protective oxide scale based on an outer Cr_2O_3 layer and an inner $(Al,Cr)_2O_3$ solid solution layer after 2000 h exposure in 10^{-6} wt.% oxygen containing molten Pb at 600 °C. TEM evaluation of the oxide scale formed on AFA54 indicates the formation of poly- and nano-crystalline oxides in the scale. The thickness of the oxide scale is around 50 nm. A bright transitional layer, with thickness in the range 0.5-2 µm, has been observed below the oxide scale. Some dark precipitates of B2-NiAl and Fe-, Cr-rich ferrite spots have been found in the transitional layer.

In case of the corrosion attacks at 550 °C and 600 °C, both the dissolution of alloying elements (mainly Ni) and oxide scale spallation have been observed. The dissolution of Ni leads to the formation of a ferrite (BCC) layer with a thickness around 15-50 µm. The regions of the alloy matrix

contaminated by Pb show poor adherence of the adjacent oxide scale and corresponding oxide scale spallation. In addition, B2-NiAl precipitates are observed in the ferrite layer.

The AFA-2nd generation alloys have shown their corrosion resistance to low-oxygen containing molten Pb at 600 °C after 1000 h and 2000 h exposure, except AFA72, which shows oxide scale spallation after 1000 h exposure test, shown in Table 5-3. The oxide scale with a thickness less than 200 nm is based on Cr_2O_3 and Cr_2O_3-Al_2O_3 solid solution. By adding yttrium, the distributions of Al and Cr in the oxide scale become more uniform in thickness and distribution of Al and Cr in oxide scale compared with AFA-1st generation alloys exposed at the same condition. In addition, magnetite protrusions are also observed due to the oxidation of regions surrounding YNiAl-rich spots, which are depleted in Al and Ni.

Below the oxide scale, a Fe-, Ni-rich transitional layer, with a thickness of 0.5 to 2 µm has formed during the corrosion tests. Besides, some B2-NiAl and Fe-, Cr-rich precipitates have been observed in the transitional layer of all samples. Moreover, the X-ray peaks of the BCC phase (from B2 and Fe-, Cr-rich precipitates) become less visible compared with the first generation AFA alloys. In case of Nb containing samples, the bright Laves particles coherent with B2 precipitates are also observed in the transitional layer.

TEM evaluation of AFA75 has indicated the formation of poly- and nano-crystalline oxides in the scale after 2000 h corrosion test in oxygen containing molten Pb. The thickness of the oxide scale is 100 nm. TEM-EDS mapping and line scanning of the alloy matrix have shown the formation of small size B2-NiAl (300-500 nm) and Laves (< 50 nm) phases in addition to the austenitic matrix.

The microstructure analysis of bulk alloys of AFA-1st generation after 1000 h corrosion test in 10^{-6} wt.% oxygen containing molten Pb at 600 °C reveal the FCC structure of the matrix with γ'-Ni_3(Al,Fe) phase.

Both Al and Cr play an important role in the corrosion behavior. Minimum amounts of Al and Cr are critical for the formation of protective alumina-based scales on Fe/Ni-based alloys when exposed to oxygen containing environments. According to the experimental results of AFA-1st generation, the Al concentration for the formation of passive oxide scale at the temperature range of 550 to 600 °C varies in the range of 2.3 to 4.3 wt.%. The minimum value of this range corresponds to the Al-solubility limit in austenite. At concentrations above this value the precipitation of a secondary phase B2-NiAl is observed, which is considered as an Al reservoir during the formation and growth of the alumina scale and also as reinforcement phase of the austenite matrix [147, 258].

In alloys designed for applications in oxygen-containing environments, Cr is added in order to reduce the critical Al concentration by forming the Cr_2O_3 scale as the first protective layer, which inhibits the Fe external oxidation and, having a corundum-type structure, acts as support for the nucleation of α–Al_2O_3 (so called "third element effect" [146, 158, 159]. In this thesis it is found that Cr concentrations in the quaternary AFA alloys showing corrosion resistance at 550 °C and 600 °C is in the range of 15.2-16.6 wt.%. In case of Cr content lower than 12 wt.% at 550 °C and 14 wt.% at 600 °C, the alloys are unable to form a protective alumina scale. The major corrosion phenomena observed in the low Cr containing alloys are related to Ni depletion with subsequent ferritization of the Ni-dissolution layer and the concomitant penetration of lead.

Both Al and Cr are elements that stabilize the ferrite phase relative to the austenite phase in steels. For maintaining a single-phase FCC structure (austenite) of the alloys' matrix, the Ni concentration has been selected in the range between 20 and 29 wt.% in order to counterbalance the destabilizing effects of Al and Cr. This work demonstrates that Ni and Al form a B2-NiAl compound in the transitional layer just below the scale, which acts as Al-reservoir for the protective scale formation growth and long-term stability. Moreover, it is presumed that Ni positively supports the formation of the protective scale since higher Ni content may decrease the oxygen solubility/diffusivity in the alloy, favouring external alumina formation, and may increase the Cr activity [259].

The effect of the yttrium addition is observed in AFA-2nd generation alloys, as expected, in the uniformity of the scale thickness and in the Al and Cr distribution in the scale, since this reactive element promotes an increase of Al and Cr selective oxidation and accelerates the development of the protective scale. As consequence, since the scale becomes compact earlier and it suppresses the inward oxygen/outward cation diffusion in Al_2O_3 scale [260], the thickness of the transitional layer as well as the number of the B2-NiAl and adjacent BCC solid solution precipitates are lower compared to AFA-1st generation alloys.

Nb has a beneficial effect on the high-temperature mechanical properties due to the precipitation of Fe_2Nb Laves phases. AFA-2nd generation alloys with 1.5 wt.% Nb exhibit promising corrosion resistance to low-oxygen containing molten Pb. It is found that nano-size precipitates of Fe_2Nb Laves phase are distributed within the alloy after exposure at 600 °C for 2000 h without affecting the formation of the protective alumina-based scale.

The oxides grown on AFA alloys are based on Cr_2O_3 and Al_2O_3 at the temperature range of 550-600 °C. The high resolution TEM indicates a two-layer structure of the oxide scale: an outer layer

of Cr_2O_3 and an inner layer of Al_2O_3. The mechanism of oxide scale growth can be described as follows. At the early exposure stage, a continuous Cr_2O_3 grows on the alloy surface and protects it from corrosion attack. This is due to the higher content of Cr relative to the Al content in austenite matrix and the faster growth rate of Cr_2O_3 compared with Al_2O_3. Then, the oxygen partial pressure at the scale-matrix interface drops to a low level, which favors the selective oxidation of Al and the predominantly inward growth of Al-based oxide. Therefore, the Cr_2O_3 scale serves as a first protective layer and as oxidation retardant, and the corundum-type structure of Cr_2O_3 acts as nucleation sites for the α-Al_2O_3 formation. The relatively thin oxide scale (<200 nm) and the presence of Al_2O_3-Cr_2O_3 solid solutions indicate a slow oxidation kinetics. The reasons for this phenomenon may reside in the low oxygen solubility/diffusivity and sluggish aluminum diffusion in the austenite phase [261].

Based on the detected (104) peak position of the XRD patterns and EDS measurements of the scale chemical composition, the average amount of Cr_2O_3 in the Al_2O_3-Cr_2O_3 solid solution is different as exposure time and temperature change. According to the X-ray diffraction patterns of Al_2O_3-Cr_2O_3 (corresponding to (104) lattice plane), the fraction of Cr_2O_3 in solid solution can be estimated, as shown in Fig. 5-37 [262]. Considering the diffraction angle of the (104) peak, the fraction of Cr_2O_3 in the Al_2O_3-Cr_2O_3 solid solution accounts for ≈40 wt.% at 550 °C for 1000 h exposure, ≈35 wt.% at 600 °C for 1000 h exposure, ≈16-21 wt.% at 600 °C for 2000 h exposure. As the exposure time increases, the alumina scale becomes more pure and in consequence more stable and protective.

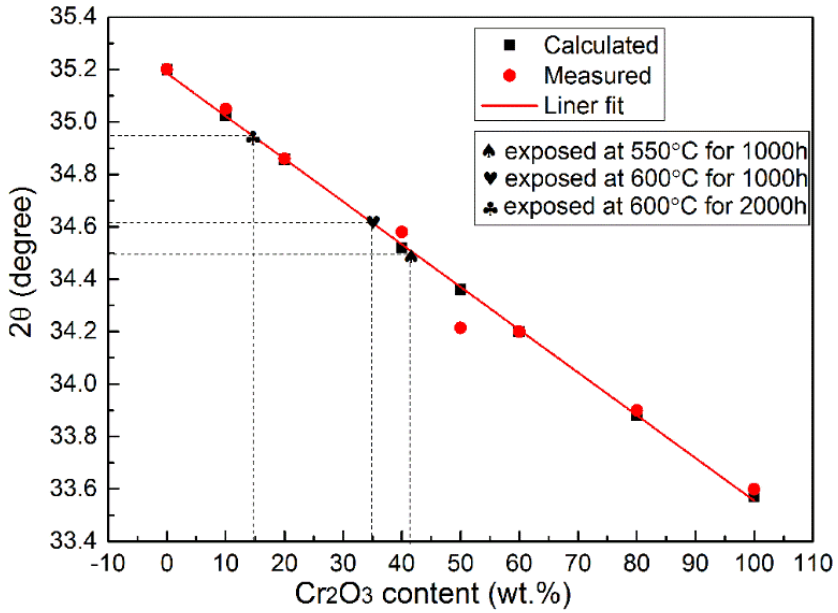

Fig. 5-37 Plot of the relationship between the diffraction angle of Al_2O_3-Cr_2O_3 (corresponding to (104)) and Cr_2O_3 content (wt.%) [262].

A transitional metallic layer below the protective oxide scale has been observed on both AFA-1st and AFA-2nd generation alloys. The enrichment of Ni and Fe in the transitional layer is due to the outer diffusion of Cr and Al towards the oxide scale. Likewise, the enrichment of Ni and Fe also underlines the efficiency of the formed oxide scale as a diffusion barrier for these two elements. However, a decrease of the Al concentration in the region underneath the oxide scale to values below its solubility limit in austenite may limit or hinder the healing process in case of an accidental scale loss. The presence of the B2-NiAl in the transitional layer is due to the faster diffusion of Cr atoms towards the surface during the transient stage of the oxidation, the concentration of Al may locally exceed the solubility limit in austenite (around 2.5 wt.%) leading to the precipitation of the intermetallic B2-NiAl phase. The local enrichment of Cr at the regions surrounding the B2 precipitates leads to the formation of coexisting FeCr ferrite solid solution precipitates.

Regarding the structural stability, the AFA model alloys of 1st and 2nd generation with a minimum Ni amount of 20 wt.% maintained the austenitic matrix even after 2000 h exposure to 10^{-6} wt.% oxygen at 600 °C. At the same time, the precipitates of $L1_2$-ordered $Ni_3(Al,Fe)$ phase with FCC structure is also observed. This secondary phase, known as γ′ phase and found in various Fe-based alloys, is reported to improve the high temperature mechanical properties of alloys [147, 179, 185, 258, 263, 264].

The goal of the corrosion investigation of Fe-Cr-Ni-Al model alloys, exposed to low-oxygen containing molten Pb conditions, is to select the appropriate concentration ranges of the alloying elements, where a protective oxide scale will form on the alloy surface and the austenitic matrix will be maintained at the same time. In case of the maximum temperature of 600 °C and specific corrosion issues related to molten Pb environments, the design of compatible alumina-forming austenitic steels should be based on the following formula: Fe-(20-29)Ni-(15.2-16.5)Cr-(2.3-4.3)Al (wt.%).

At the temperature below 550 °C, the Cr content may decrease to 14.4 wt.%. Based on the backbone of this formula, minor addition of other elements can be considered, for instance: elements C, Cu and Mn stabilize the austenite matrix; element Y improves the scale adherence; elements Nb and Ti promote the precipitates (e.g. Laves, γ′ phase); elements strengthen the austenite (W and Mo) and grain boundaries (B). The concentration of minor elements needs to be correlated with the maximum temperature of the envisaged technological application in order to satisfy the requirements regarding the properties and economics at the same time.

6. Corrosion behavior of HEA model alloys

6.1 Corrosion behavior of HEA at 550 °C and 600 °C

Nine HEA model alloys were exposed to 10^{-6} wt.% oxygen containing molten Pb at 550 °C and 600 °C for 1000 h. Table 6-1 summarizes the corrosion performance of HEA alloys in molten Pb conditions. Eight alloys, HEA1, HEA2, HEA3, HEA4, HEA5, HEA6, HEA7 and HEA8, have formed protective oxide scale during exposure in oxygen containing molten Pb conditions at 550 °C and 600 °C. HEA9 alloyed with Cu shows the features of oxide scale spallation.

Table 6-1 Corrosion performance of HEA alloys after 1000 h exposure to 10^{-6} wt.% oxygen containing molten Pb at 550 °C and 600 °C.

Code	Nominal composition	550 °C	600 °C
HEA1	$Al_{9.76}Cr_{30.28}Fe_{32.95}Ni_{26.91}$	🙂	🙂
HEA2	$Al_{9.85}Cr_{22.50}Fe_{34.50}Ni_{33.15}$	🙂	🙂
HEA3	$Al_{8.91}Cr_{23.13}Fe_{33.68}Ni_{34.28}$	🙂	🙂
HEA4	$Al_{11.69}Cr_{22.40}Fe_{32.62}Ni_{33.29}$	🙂	🙂
HEA5	$Al_{6.02}Cr_{25.01}Fe_{33.99}Ni_{34.98}$	🙂	🙂
HEA6	$Al_{7.96}Cr_{23.23}Fe_{34.06}Ni_{34.75}$	🙂	🙂
HEA7	$Al_{8.24}Cr_{21.37}Fe_{30.29}Ni_{35.02}Nb_{5.08}$	🙂	🙂
HEA8	$Al_{7.90}Cr_{22.04}Fe_{31.91}Ni_{33.14}Ti_{5.01}$	🙂	🙂
HEA9	$Al_{8.01}Cr_{22.01}Fe_{31.96}Ni_{33.01}Cu_{5.00}$	😐	😐

🙂: Corrosion resistance; 😐: Oxide scale spallation (no corrosion attack).

6.1.1 Corrosion resistance of HEA alloys at 550 °C

Alloy surface characterization

After 1000 h exposure to oxygen containing molten Pb at 550 °C, eight samples have formed protective oxide scales. They are HEA1, HEA2, HEA3, HEA4, HEA5, HEA6, HEA7 and HEA8. Fig. 6-1 shows the selected surface view of quaternary alloys with dendrites (HEA1, HEA4), quaternary alloys with single phase (HEA5), and quinary alloys (HEA7, HEA8, HEA9). The surface layer formed on HEA1 displays circular morphologies. The oxide scale inside the "circle" parts are thinner than the "surrounding" regions. No dissolution attack is evident. The oxide scale formed on HEA2, HEA3, HEA4, HEA5 and HEA6 are dense and uniform without dissolution attack. In case of the quinary alloys HEA7 and HEA8, the passive layer shows a pattern similar with the dendrite morphologies of the alloy matrix. The bright inter-dendrites of HEA7 and HEA8 reflect the Laves phase in HEA7 and γ´ phase in HEA8, respectively. No corrosion attack is observed on both samples. HEA9 with Cu addition shows the evidences of oxide layer exfoliation. The spallation area accounts for around 50% of the

surface area. No corrosion attack is observed at the scale exfoliation regions, meaning that this phenomenon happened after extracted from the molten lead (during the cooling process).

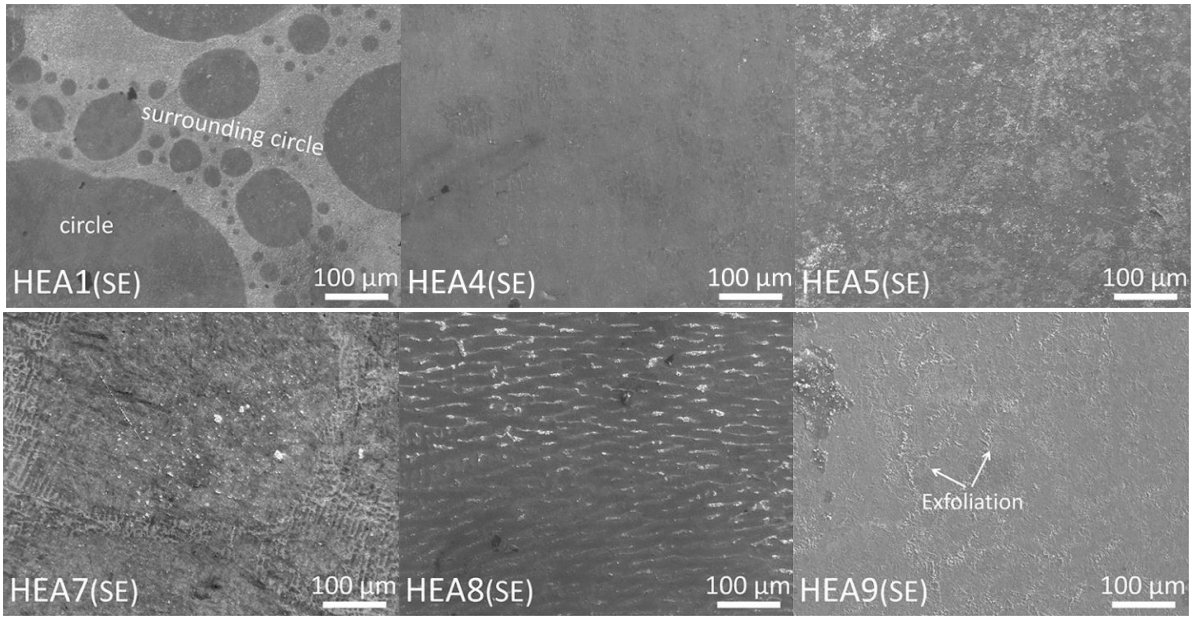

Fig. 6-1 Representative surface morphologies of HEA samples after 1000 h exposure to 10^{-6} wt.% oxygen containing molten Pb at 550 °C.

Cross section and XRD characterization

According to the number of alloying elements and phase composition of as cast samples, the investigated alloys can be classified as quaternary alloys with dual-phase, quaternary alloys with single-phase, and quinary alloys. The cross section and XRD characterization of HEA samples is structured according to this classification, based on the phase composition of the alloys, as following:

(1) HEA1, HEA2, HEA3 and HEA4-quaternary alloys with dual-phase microstructure

Fig. 6-2 and Fig. 6-3 show the EDS cross-sectional line scans of HEA1, HEA2, HEA3 and HEA4. The samples matrix is protected by a thin oxide scale. No dissolution or Pb penetration is visible. According to the EDS line scanning, HEA1 shows the oxygen signal maximum coincides with the maxima of the signals of Al and Cr. No transitional layer is visible between the surface scale and the alloy matrix. According to the full width at half maximum (FWHM) measured from EDS line scanning, the thickness of the oxide scale is around 400 nm. In case of HEA2, HEA3 and HEA4, the oxides formed on the surface mainly consist of O, Al and Cr, where the Cr signal maximum either is in front of the Al signal maximum or coincides, and both are coincided with the O signal maximum, as shown in Fig. 6-2, Fig. 6-3, Fig. 6-4 and Fig. 6-5. Below the oxide scale, a transitional layer with dark precipitates embedded, is visible on all three samples. The thickness of this layer varies from 0.5-2 µm. According to the EDS line scanning and mapping (see HEA2 in Fig. 6-2 and Fig. 6-4), the precipitates observed in the transitional layer are Al- Ni-rich precipitates and Cr-rich spots.

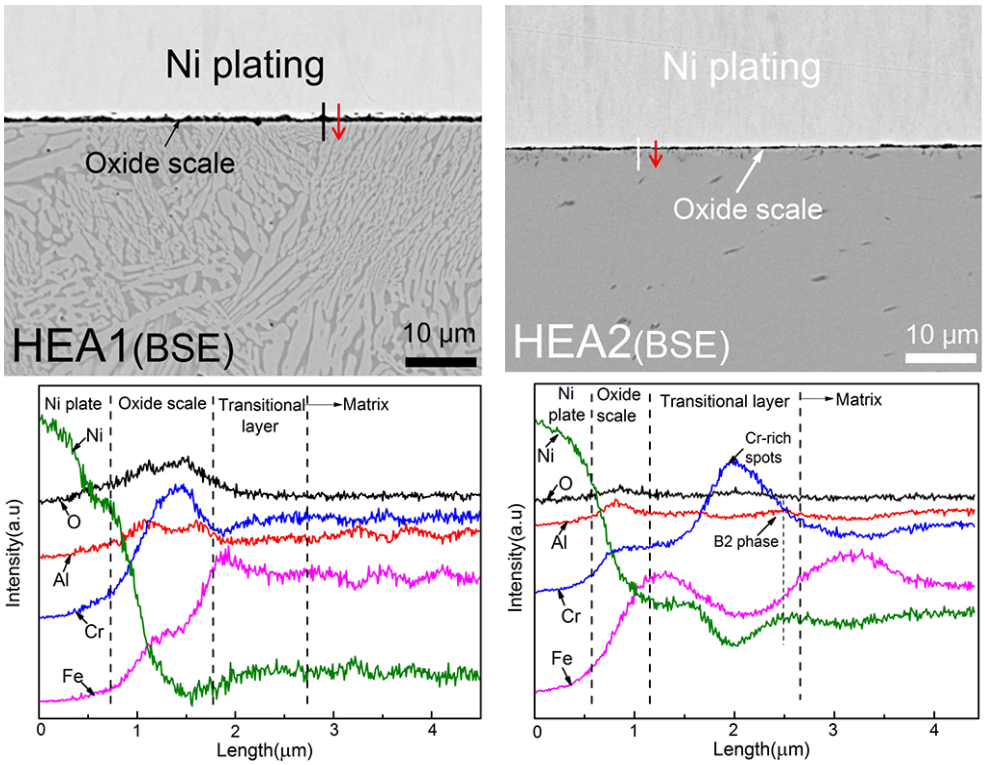

Fig. 6-2 EDS line scans of the cross sections of HEA1 and HEA2 after 1000 h exposure to 10^{-6} wt.% oxygen containing molten Pb at 550 °C (The direction of the measurement is indicated by the arrow).

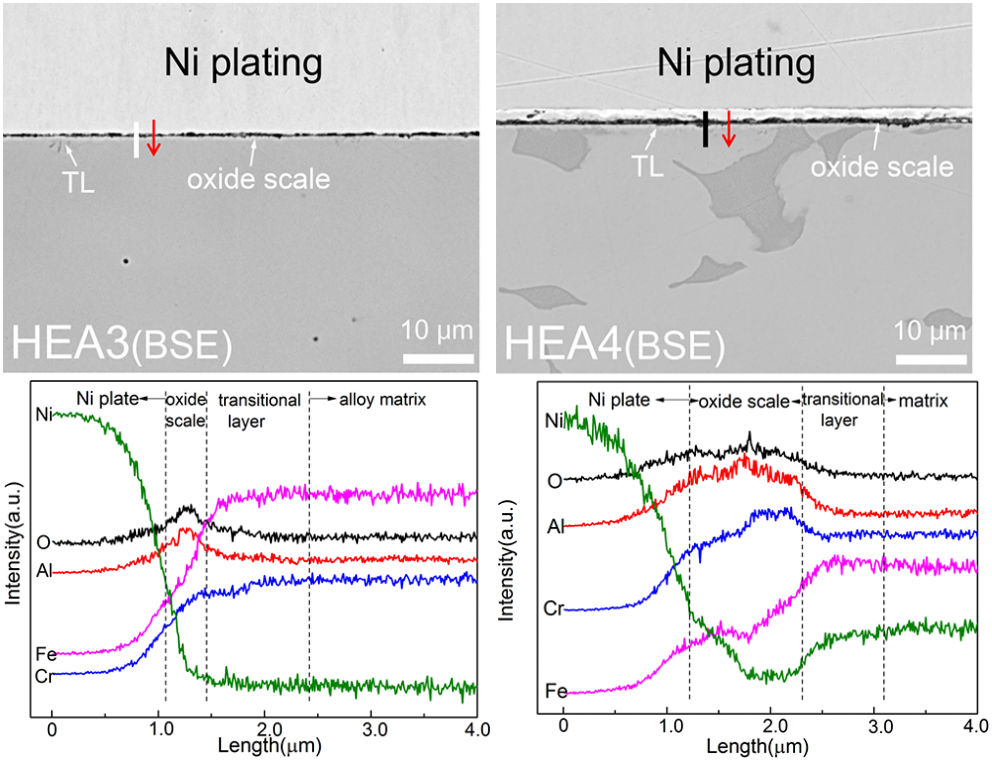

Fig. 6-3 EDS line scans of the cross sections of HEA3 and HEA4 after 1000 h exposure to 10^{-6} wt.% oxygen containing molten Pb at 550 °C (The direction of the measurement is indicated by the arrow).

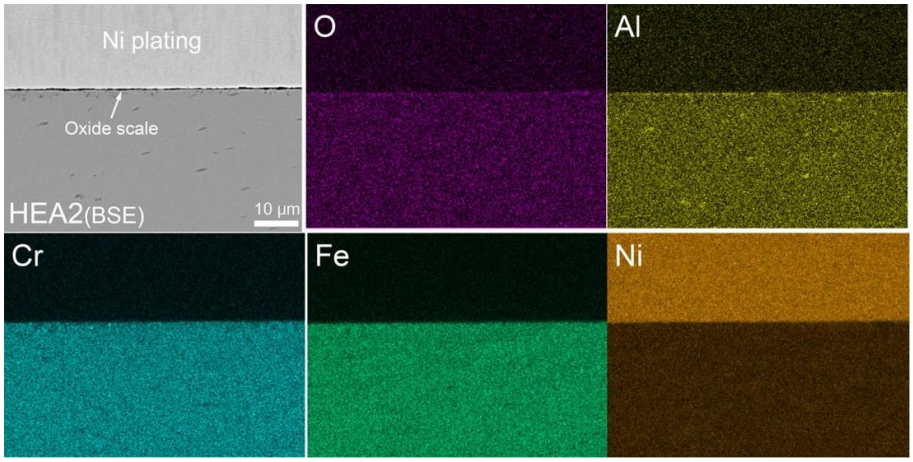

Fig. 6-4 EDS mapping of the cross section of HEA2 after 1000 h exposure to 10^{-6} wt.% oxygen containing molten Pb at 550 °C.

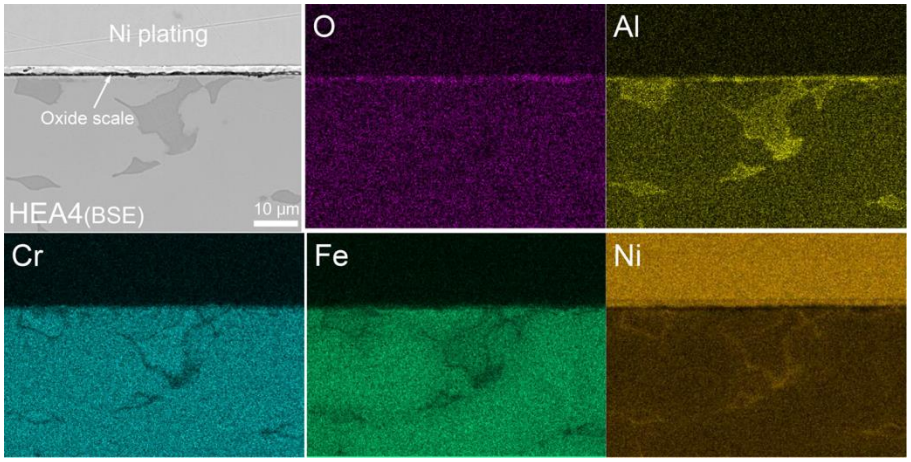

Fig. 6-5 EDS mapping of the cross section of HEA4 after 1000 h exposure to 10^{-6} wt.% oxygen containing molten Pb at 550 °C.

Fig. 6-6 shows the XRD characterization of HEA1, HEA2, HEA3 and HEA4 after the corrosion test. The signals from the oxides are weak in all samples. According to the results, HEA1 has formed $(Fe,Cr)_3O_4$, Cr_2O_3 and $(Al,Cr)_2O_3$ (weak) in the oxide scale. In the alloy matrix, the signals from FCC and B2 phase (overlapping with the BCC phase) have been identified. As for oxide scale formed on HEA2, HEA3 and HEA4, the oxides identified by XRD are mainly Cr_2O_3 and $(Al,Cr)_2O_3$. In the alloy matrix, FCC plus B2 phases are obtained in all three samples.

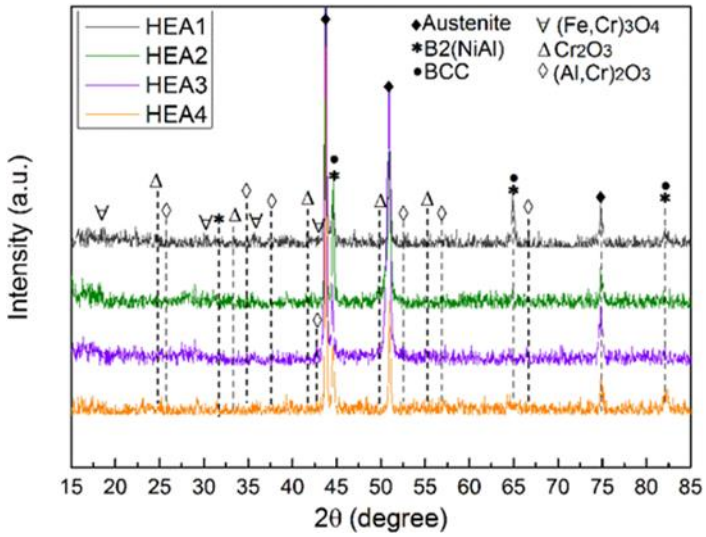

Fig. 6-6 XRD patterns measured after 1000 h exposure to 10^{-6} wt.% oxygen containing molten Pb at 550 °C (HEA1, HEA2, HEA3, HEA4).

(2) HEA5 and HEA6-quaternary alloys with single phase

Fig. 6-7 shows the cross section and EDS line scans of HEA5 and HEA6. The alloys' surfaces are covered by thin and uniform oxide scales. No corrosion attack is visible on both samples. As evidenced by EDS line scanning, the oxide scales show the oxygen signal maxima overlapping with Al and Cr maxima, where the maximum Al signal either coincides with the Cr signal maximum or is in front of it. The thickness of oxide scale is less than 200 nm according to FWHM measured from EDS line scanning. Below the oxide scale, a continuous transitional layer, shown in bright contrast, is observed on both samples. Moreover, the transitional layer is non-uniform, varying in thickness from 0.5 to 5 μm (see HEA5 in Fig. 6-7). As observed by EDS line scanning (Fig. 6-7), Al and Cr are depleted while Ni and Fe are enriched in the transitional layer compared to the matrix. In addition, some dark precipitates, which are rich in Cr, have been observed at the thick parts of the transitional layer, see Fig. 6-8.

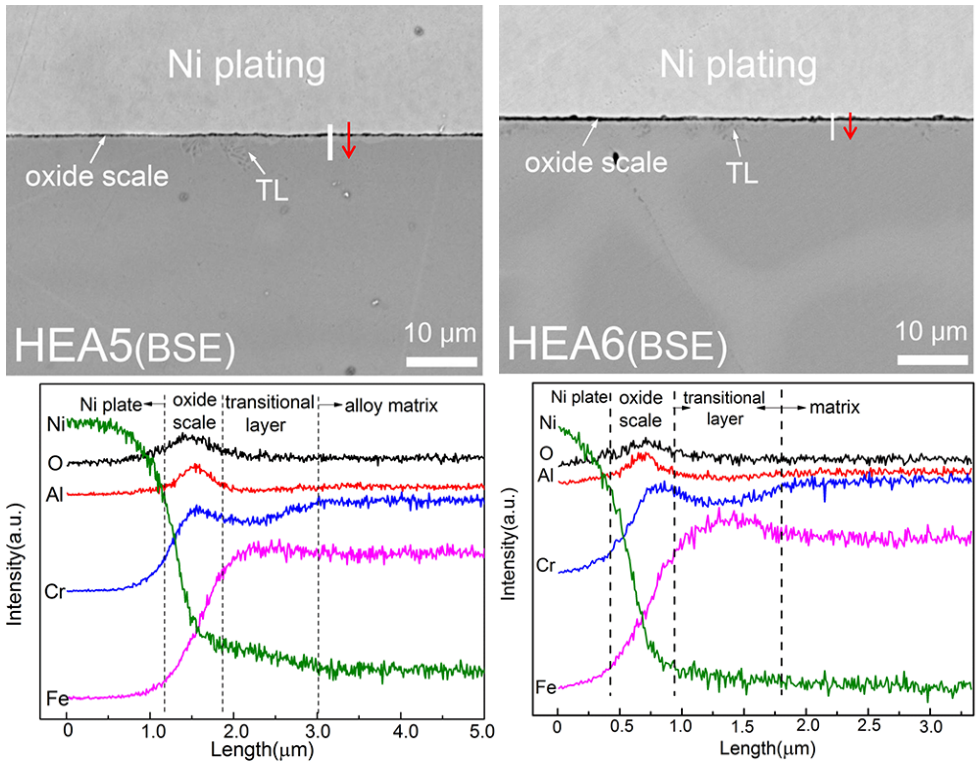

Fig. 6-7 EDS line scans of the cross sections of HEA5 and HEA6 samples after 1000 h exposure to 10^{-6} wt.% oxygen containing molten Pb at 550 °C (The direction of the measurement is indicated by the arrow).

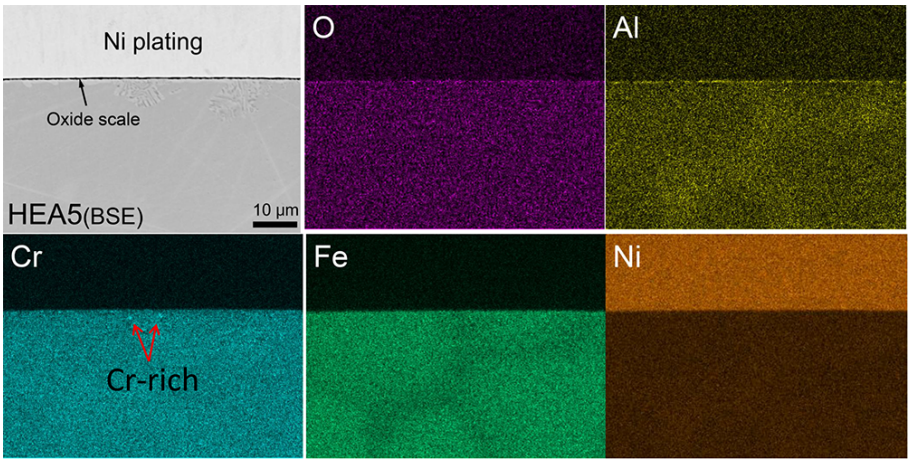

Fig. 6-8 EDS mapping of the cross section of HEA5 after 1000 h exposure to 10^{-6} wt.% oxygen containing molten Pb at 550 °C.

Fig. 6-9 shows the obtained XRD results of HEA5 and HEA6 after the corrosion test. The oxides formed on HEA5 and HEA6 are Cr_2O_3 and $(Al,Cr)_2O_3$ (weak). FCC matrix plus B2-NiAl phases have been identified as the main phases in the alloy matrix of both samples. Combined with cross section analysis, it can be concluded that the B2 phases are precipitates in the transitional layer.

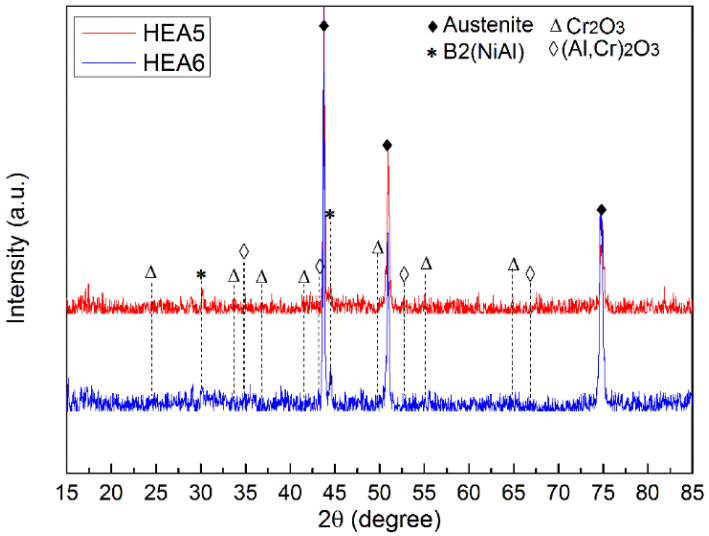

Fig. 6-9 XRD patterns measured on HEA samples after 1000 h exposure to 10^{-6} wt.% oxygen containing molten Pb at 550 °C (HEA5, HEA6).

(3) HEA7 and HEA8-quinary alloys

Fig. 6-10 shows the cross section analysis of HEA7 and HEA8. Both samples are protected by a continuous oxide scale. Moreover, the secondary phases in the bulk alloys are also covered by the oxide scale, e.g. Laves phases, as shown in Fig. 6-10 and Fig. 6-11. No corrosion attack is observed below the oxide scale. Combining the EDS line scanning (Fig. 6-10) and mapping (Fig. 6-11), the oxide scale formed on HEA7 mainly consists of O, Al and Cr, where the maximum of the Cr signal is in front of the Al maximum signal and both coincide with the maximum of the O signal. The thickness of the oxide scale is around 200 nm according to FWHM measured from EDS line scanning. Below the oxide scale, the enrichment of Fe indicates that the oxide scale can effectively inhibit the elements diffusion. Moreover, a dis-continuous transitional layer with some dark precipitates is observed underneath the oxide scale, but only visible at the Laves free regions, see Fig. 6-10 and Fig. 6-11. Besides, the EDS mapping of HEA7 shows the evidence of Al in the Laves phase, see Fig. 6-11. Regarding the oxide layer formed on HEA8, EDS line scanning shows the oxygen signal maximum overlapping with the maxima of the signals from Al, Ti and Cr, where the Cr maximum is closer to the surface than those of Al and Ti, see Fig. 6-10. No transitional layer can be uniquely identified underneath the scale. However, according to the EDS mapping shown in Fig. 6-12, Cr and Fe are enriched underneath the Al-rich oxide scale.

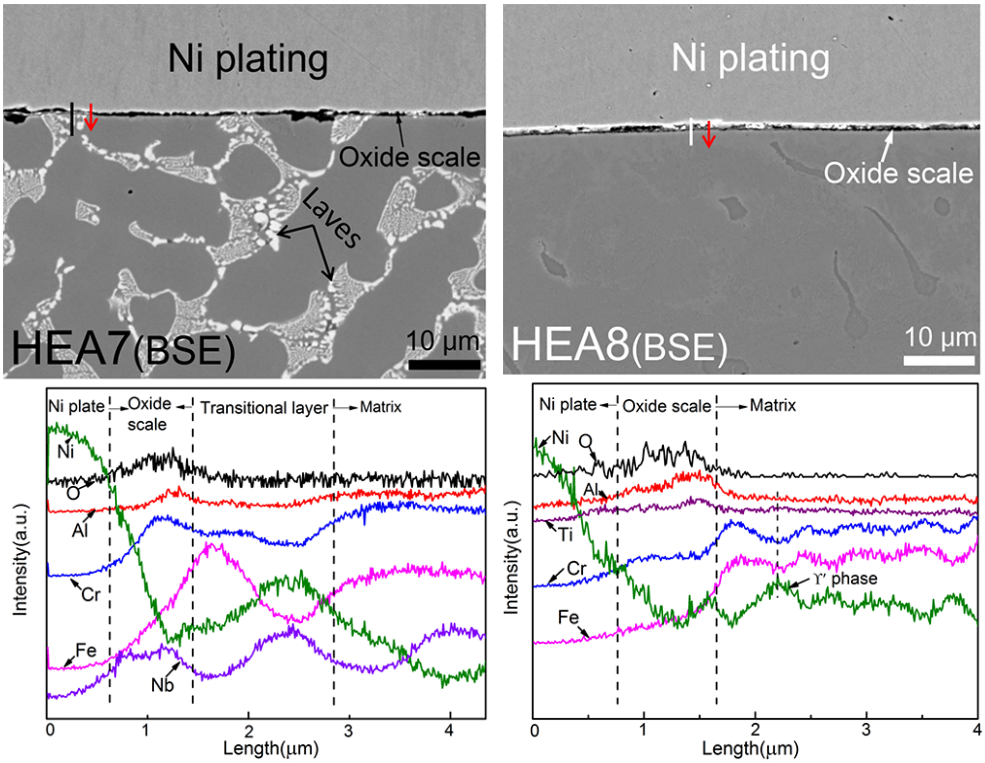

Fig. 6-10 EDS line scans of the cross sections of HEA7 and HEA8 samples after 1000 h exposure to 10^{-6} wt.% oxygen containing molten Pb at 550 °C (The direction of the measurement is indicated by the arrow).

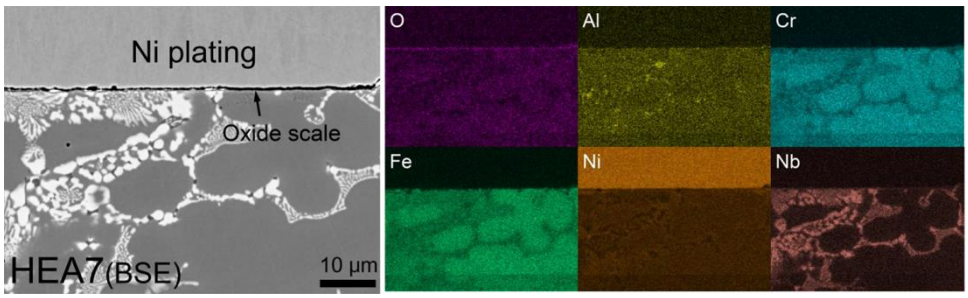

Fig. 6-11 EDS mapping of the cross section of HEA7 after 1000 h exposure to 10^{-6} wt.% oxygen containing molten Pb at 550 °C.

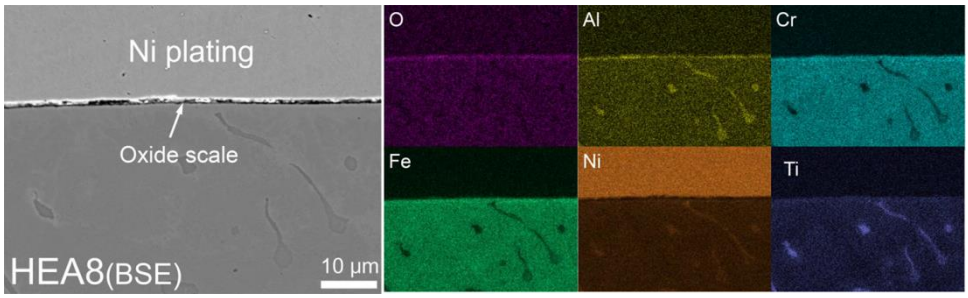

Fig. 6-12 EDS mapping of the cross section of HEA8 after 1000 h exposure to 10^{-6} wt.% oxygen containing molten Pb at 550 °C.

Fig. 6-13 shows the obtained XRD results from exposed HEA7 and HEA8. In case of HEA7 with Nb addition, the oxides formed on the surface are Cr_2O_3 and corundum-Al_2O_3. Besides, FCC, Laves

and B2-NiAl phases are obtained from the alloy matrix. The B2-NiAl phase is assigned to the precipitates observed in the transitional layer. In HEA8, Cr_2O_3, TiO_2 and $(Al,Cr)_2O_3$ (weak) can be identified as the main oxides. Regarding the phases in the alloy matrix, FCC, σ-phase (FeCr) and γ'-phase ($Ni_3(Al, Ti)$) have been obtained after 1000 h exposure at 550 °C.

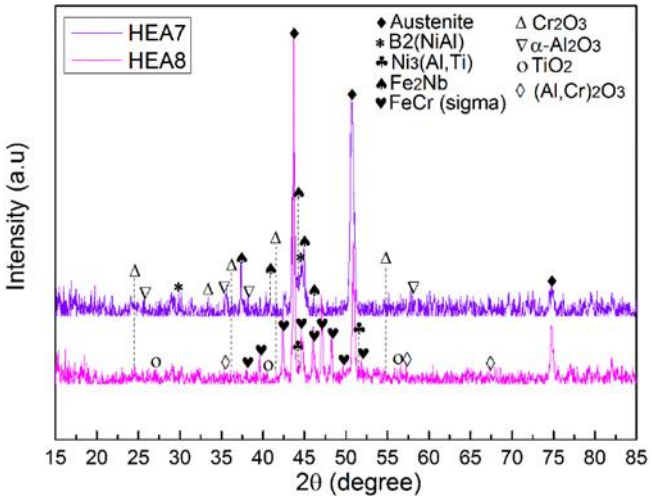

Fig. 6-13 XRD patterns measured on samples after 1000 h exposure to 10^{-6} wt.% oxygen containing molten Pb at 550 °C (HEA7, HEA8).

6.1.2 Corrosion resistance of HEA alloys at 600 °C

Alloy surface characterization

Fig. 6-14 shows selected SEM surface views of quaternary alloys with dendrites (HEA1, HEA4), quaternary alloys with single phase (HEA5), and quinary alloys (HEA7, HEA8, HEA9) after corrosion tests in 10^{-6} wt.% oxygen containing molten Pb at 600 °C. After 1000 h exposure, the surface layer formed on HEA1 presents circular morphologies, which corresponds to the same features the sample had after exposure at 550 °C. The bright parts are due to the still adherent Pb. The oxide scales formed on HEA2, HEA3, HEA4, HEA5 and HEA6 are thin, dense and uniform. No corrosion attack is visible by the surface analysis. In case of samples HEA7 and HEA8, the oxide scale shows different aspects depending on the constituent phases in the alloy matrix. For instance, the bright inter-dendrites of HEA7 are structure information obtained from Laves phases in the alloy matrix. The dark inter-dendrites shown in HEA8 are structures based on the γ' phase in the alloy matrix. Sample HEA9 with Cu addition shows features of oxide scale exfoliation of nearly 90% of surface area. No corrosion attack is present at the oxide scale exfoliation sites.

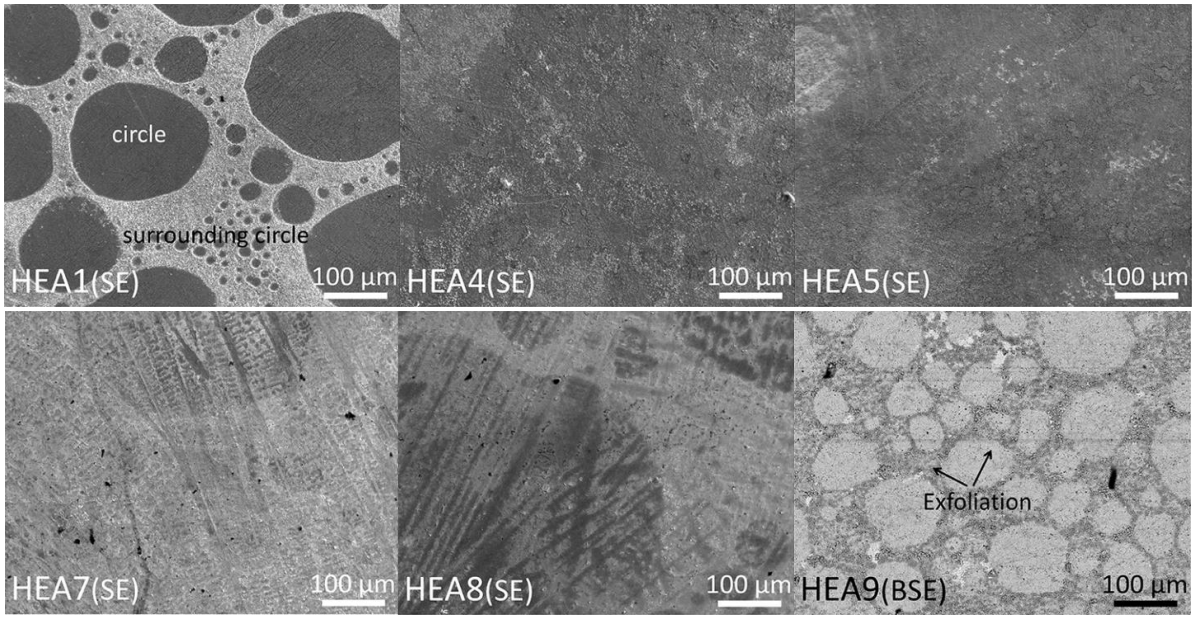

Fig. 6-14 Representative surface morphologies of HEA samples after 1000 h exposure to 10^{-6} wt.% oxygen containing molten Pb at 600 °C.

Cross section and XRD characterization

(1) HEA1, HEA2, HEA3 and HEA4-quaternary alloys with dual-phase

Fig. 6-15 and Fig. 6-16 show the EDS cross sectional mapping and line scan of HEA1. According to the EDS mapping analysis, the bulk alloy surface is covered by a continuous oxide scale enriched in O and Al. The thickness of this layer is less than 200 nm. At some parts of the surface, a thick layer has formed above the Al-rich thin layer. EDS line scanning has been performed on the thick part of the oxide layer, see Fig. 6-16. The slight increase of the Pb signal directly at the outer surface of the oxide layer indicates the attached Pb on alloy surface. At the oxide scale region, a coincidence of signal maxima of O with Cr and Fe has been observed on the top of the scale (Fig. 6-15, Fig. 6-16). Underneath the overlapping signals from O and Al represents the previously described thin continuous oxide scale that is covering the bulk alloy. The overall thickness of this thick part layer varies from 400 to 700 nm. In addition, some pores and Cr-depleted layer are also observed underneath the thick oxide scale. Below the oxide scale, the overlapping signals from Al and Ni indicate the formation of B2-NiAl phases.

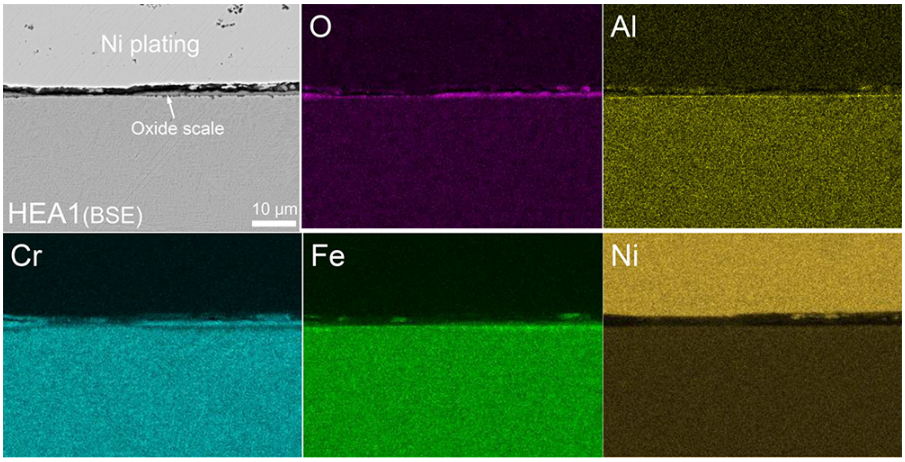

Fig. 6-15 EDS mapping of the cross section of HEA1 after 1000 h exposure to 10^{-6} wt.% oxygen containing molten Pb at 600 °C.

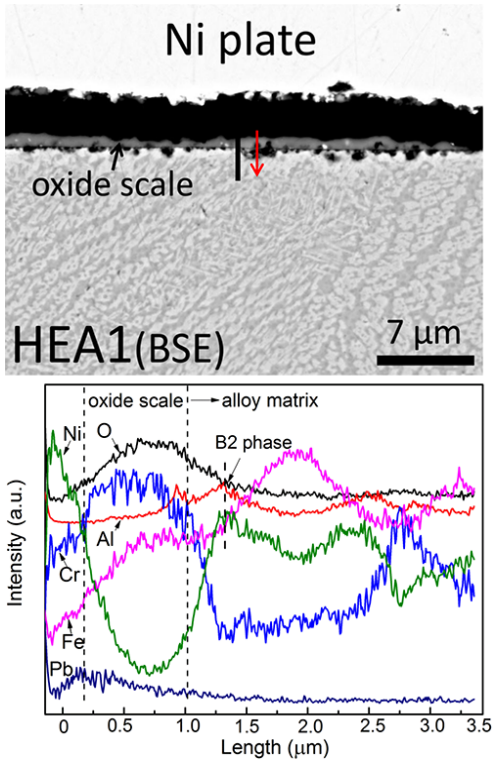

Fig. 6-16 EDS line scan of the cross section of HEA1 after 1000 h exposure to 10^{-6} wt. % oxygen containing molten Pb at 600 °C (The direction of the measurement is indicated by the arrow).

HEA2, HEA3 and HEA4 have formed oxide scales with similar features. Fig. 6-17 and Fig. 6-18 show the selected cross section and EDS mapping of HEA2 and HEA4. No corrosion attack is observed below the oxide scale. According to the mapping results, O and Cr are enriched at the upper part of the oxide layer. Below the Cr-rich layer, a thin layer with uniformly distributed O and Al is visible, see Fig. 6-18. Further EDS line scanning of HEA2 and HEA4 shows the overlapped signal maxima of O with Al and Cr, while the Cr signal maxima are in front of Al signal maxima, see Fig. 6-19. The thickness of oxide scale formed on HEA2 and HEA3 is less than 200 nm, while HEA4 has formed

an oxide scale with a thickness around 400 nm according to FWHM of EDS line scan measurement. Below the oxide scale, no transitional layer is observed. The enrichment of Fe and Ni has been observed underneath the oxide scale, shown in Fig. 6-19.

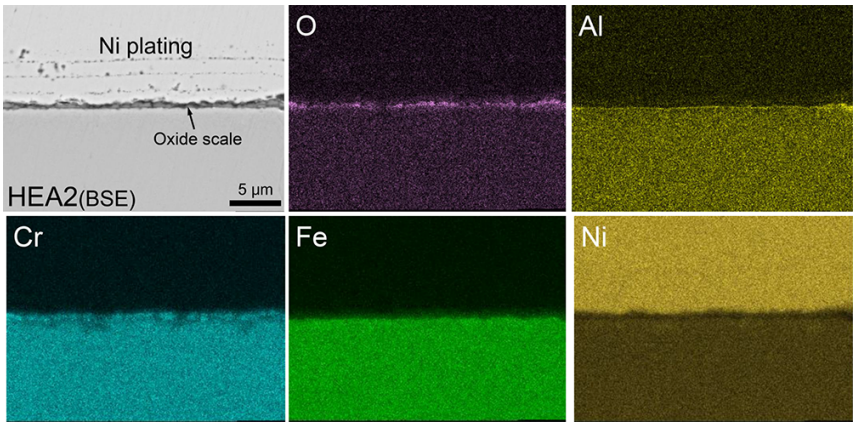

Fig. 6-17 EDS mapping of the cross section of HEA2 after 1000 h exposure to 10^{-6} wt.% oxygen containing molten Pb at 600 °C.

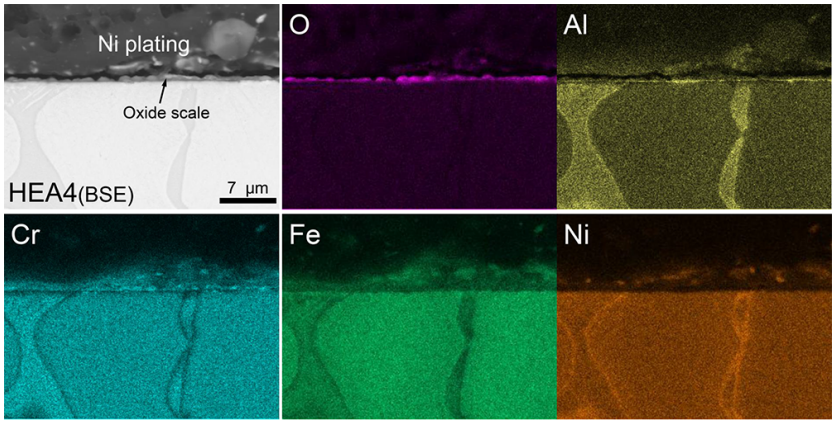

Fig. 6-18 EDS mapping of the cross section of HEA4 after 1000 h exposure to 10^{-6} wt.% oxygen containing molten Pb at 600 °C.

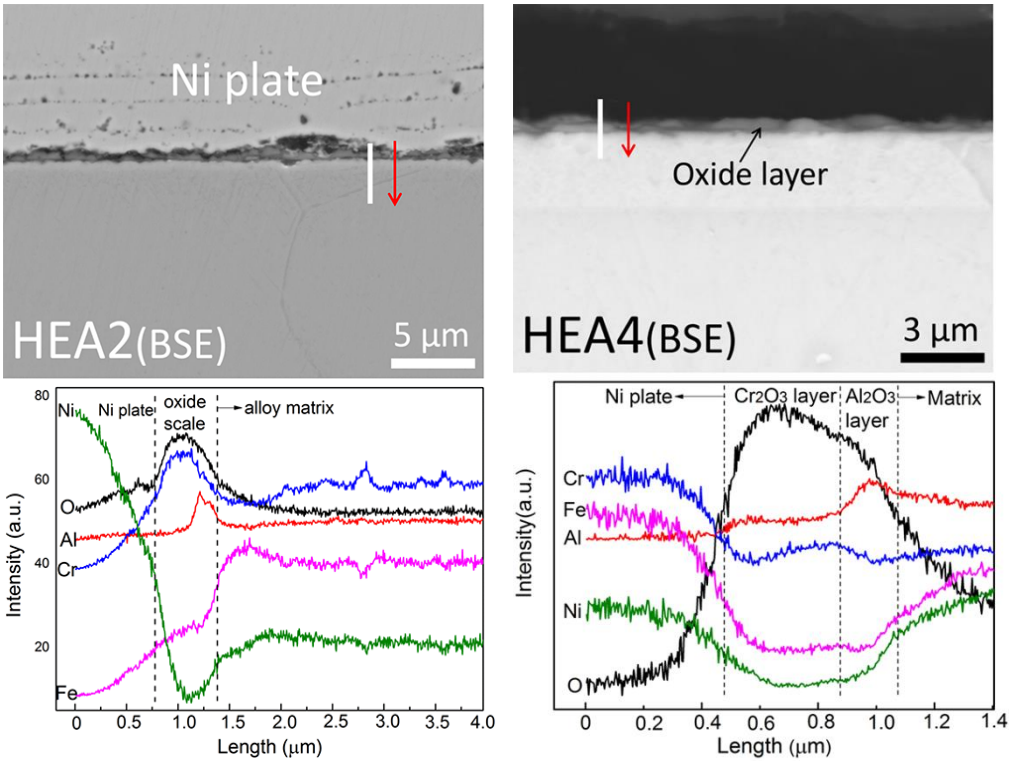

Fig. 6-19 EDS line scans of the cross sections of HEA2 and HEA4 after 1000 h exposure to 10^{-6} wt.% oxygen containing molten Pb at 600 °C (The direction of the measurement is indicated by the arrow).

Fig. 6-20 shows the XRD characterization of HEA1, HEA2, HEA3 and HEA4 after 1000 h exposure at 600 °C. Combining with cross section analysis, the oxides formed on HEA1 are $(Fe,Cr)_3O_4$, Cr_2O_3 and $(Al,Cr)_2O_3$ (weak). In the alloy matrix, FCC, BCC and B2 (weak) phases are identified. The oxides identified from X-ray diffraction patterns of HEA2, HEA3 and HEA4 are Cr_2O_3 and $(Al,Cr)_2O_3$. In the alloy matrix, FCC and B2-NiAl phases are obtained.

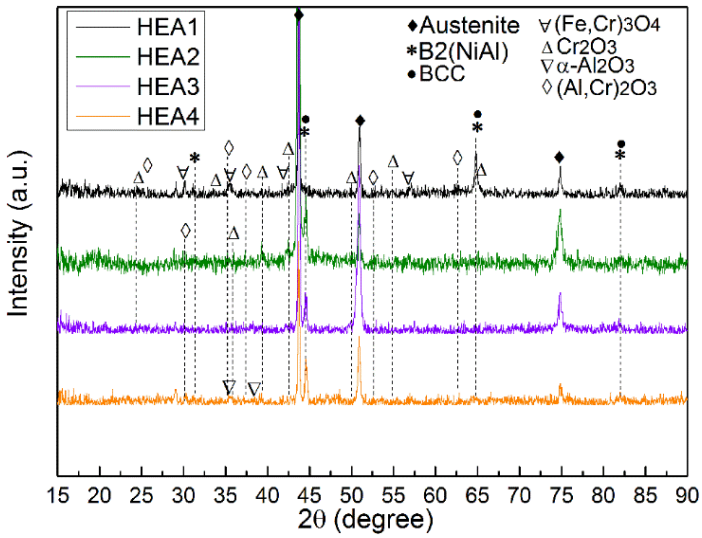

Fig. 6-20 Representative XRD patterns measured on samples after 1000 h exposure to 10^{-6} wt.% oxygen containing molten Pb at 600 °C (HEA1, HEA2, HEA3, HEA4).

(2) HEA5 and HEA6-quaternary alloys with single phase

The cross section analysis of HEA5 and HEA6 is shown in Fig. 6-21 and Fig. 6-22. EDS mapping of the cross sections show the overlapping signal maxima of O with Cr and Al, while the Cr peak is in front of the Al peak, shown the example of HEA6 in Fig. 6-21 and line scans in Fig. 6-22. Below the oxide scale, a transitional layer with some dark precipitates, enriched either in Al or in Cr, is observed at some regions. The thickness of oxide scale formed on both samples is around 400 nm according to FWHM of EDS line scans.

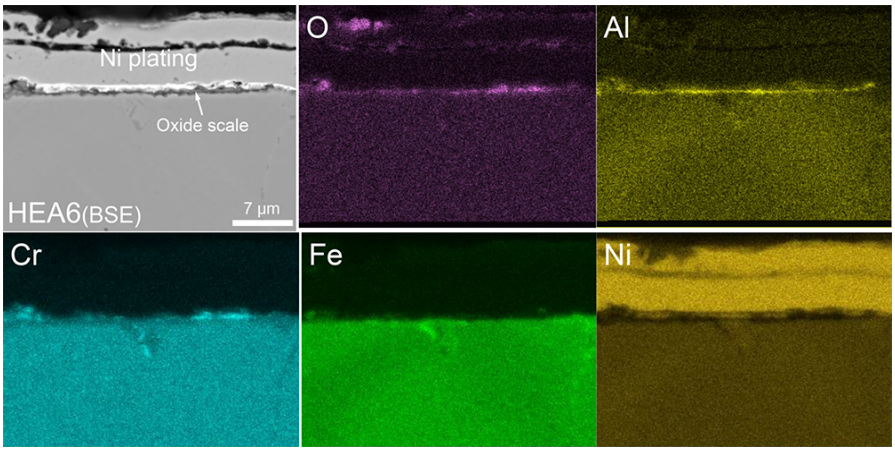

Fig. 6-21 EDS mapping of the cross section of HEA6 after 1000 h exposure to 10^{-6} wt.% oxygen containing molten Pb at 600 °C.

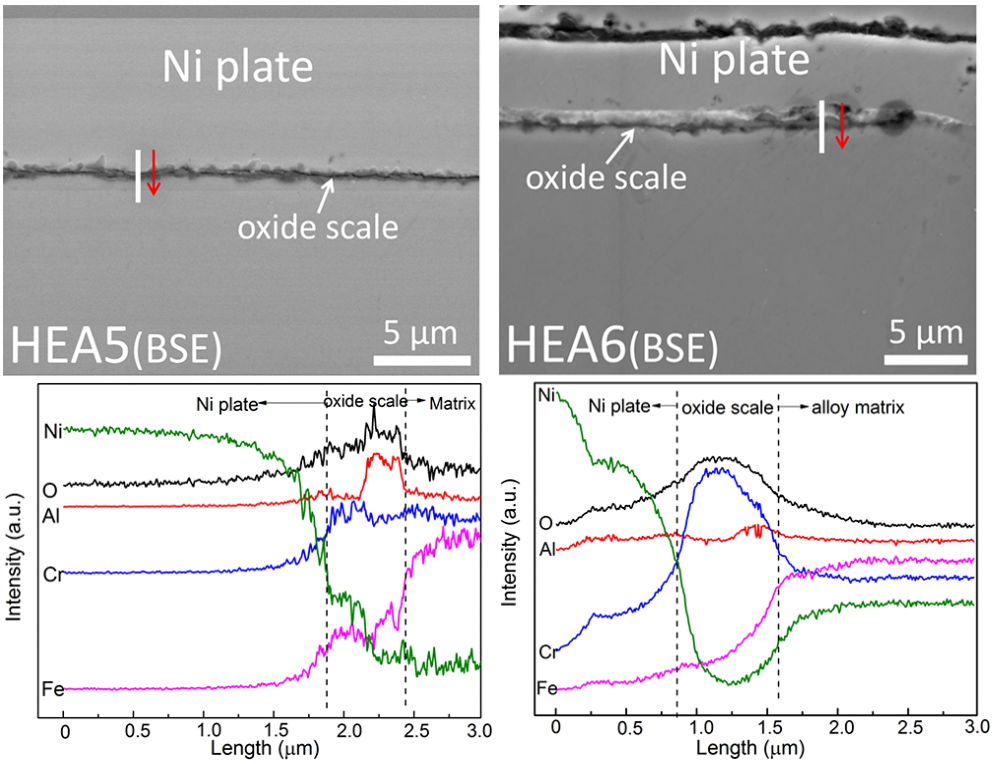

Fig. 6-22 EDS line scans of the cross sections of HEA5 and HEA6 after 1000 h exposure to 10^{-6} wt.% oxygen containing molten Pb at 600 °C (The direction of the measurement is indicated by the arrow).

XRD characterization of HEA5 and HEA6 is shown in Fig. 6-23. According to the results, Cr_2O_3 and $(Al,Cr)_2O_3$ have been identified as the main oxides formed on surface layer of HEA5 and HEA6. In the alloy matrix, FCC and B2 (weak) phases have been identified. Combining with cross section analysis, the B2 phase corresponds to the precipitates observed in the transitional layer, see Fig. 6-22.

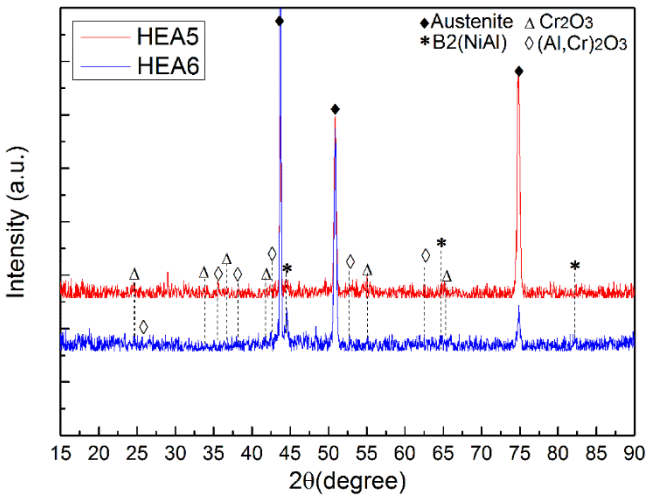

Fig. 6-23 Representative XRD patterns measured on samples after 1000 h exposure to 10^{-6} wt.% oxygen containing molten Pb at 600 °C (HEA5 and HEA6).

(3) HEA7 and HEA8-quinary alloys

The cross sectional EDS mapping analysis of HEA7 and HEA8 is shown in Fig. 6-24 and Fig. 6-25. No evidence of corrosion attack is visible on both samples. According to the analyzed results, HEA7 has formed a uniform oxide layer, which mainly consists of O and Al. The signals from Cr are less visible compared with the signals from Al. The Al-rich scale also covers the surface of the Laves phases. EDS mapping of HEA8 shows the signals from O, Al, Cr and Ti, see Fig. 6-25. The signal from Al is stronger than that of Cr and Ti. Below the oxide scale, no transitional layer is observed on both samples. In alloy matrix, some precipitates enriched in Ti, Al and Ni are visible.

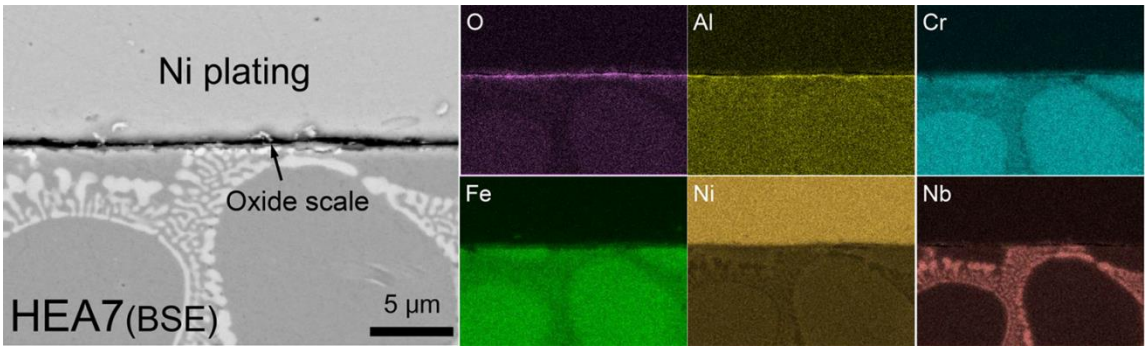

Fig. 6-24 EDS mapping of the cross section of HEA7 after 1000 h exposure to 10^{-6} wt.% oxygen containing molten Pb at 600 °C.

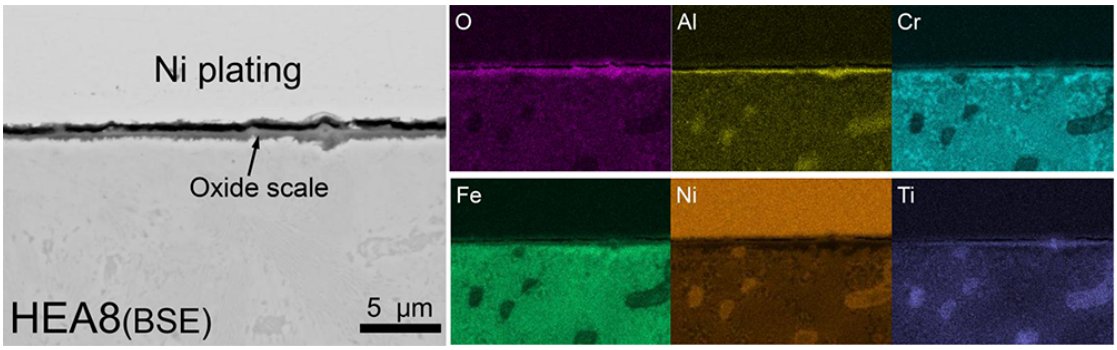

Fig. 6-25 EDS mapping of the cross section of HEA8 after 1000 h exposure to 10^{-6} wt.% oxygen containing molten Pb at 600 °C.

Further EDS line scanning of the cross section of HEA7 shows the overlapping signal maxima of O with Al in the oxide scale, see Fig. 6-26. The thickness of the oxide scale is around 150 nm. Below the oxide scale, the enrichment of Fe at the scale-matrix interface indicates that the oxide scale can effectively inhibit the elements diffusion. Another EDS line scan performed on HEA8 is also shown in Fig. 6-26. The signal maximum from O coincides with the signal maxima from Cr, and the signals from Ti and Fe monotonically falls while Al signals rises across the oxide scale are detected, while the signal maxima from Cr, Fe and Ti are in front of the signal maximum of Al. Below the oxide scale, an enrichment of Fe and Cr is observed.

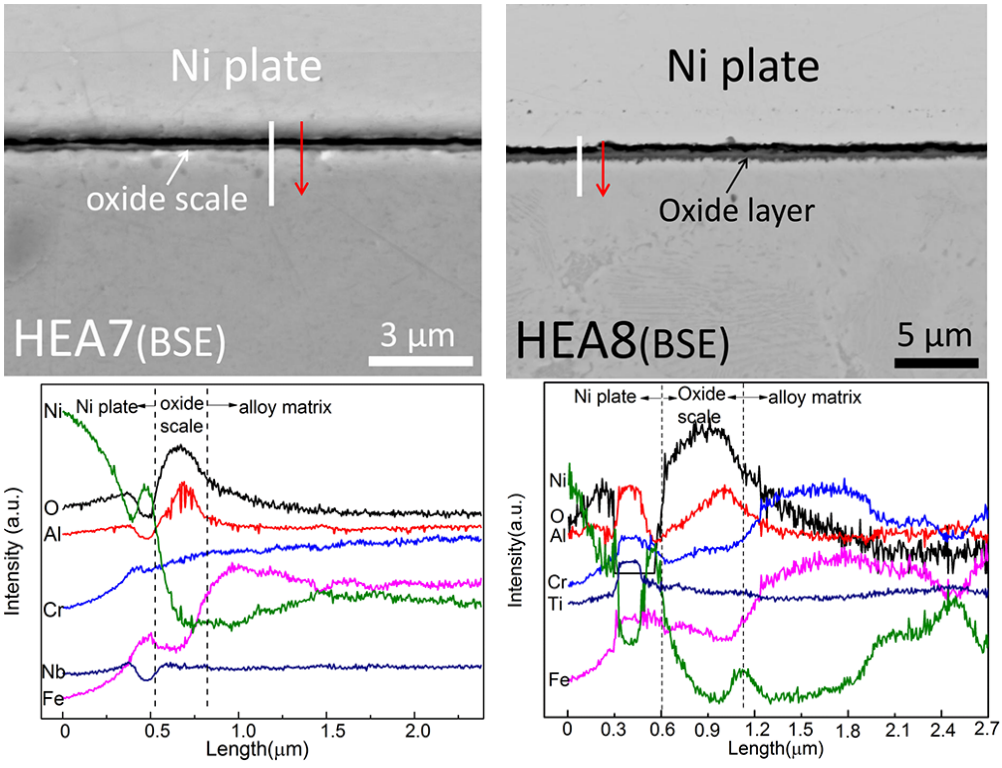

Fig. 6-26 EDS line scans of the cross sections of HEA7 and HEA8 after 1000 h exposure to 10^{-6} wt.% oxygen containing molten Pb at 600 °C (The direction of the measurement is indicated by the arrow).

XRD characterization

Fig. 6-27 shows the XRD characterization of HEA7 and HEA8 after 1000 h exposure to oxygen containing molten Pb at 600 °C. Only corundum-Al_2O_3 is identified from the oxide scale of HEA7. In the alloy matrix, FCC, Laves and B2 phases are identified. The B2 phase can be assigned to the precipitates in the transitional layer. In case of HEA8, the formed oxides include Cr_2O_3 (weak), TiO_2 and $(Al,Cr)_2O_3$. In the alloy matrix, FCC, sigma phase and $Ni_3(Al,Ti)$ have been identified.

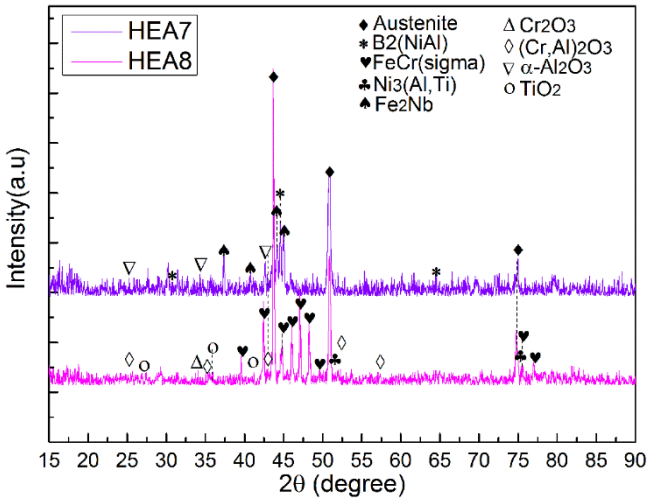

Fig. 6-27 Representative XRD patterns measured on samples after 1000 h exposure to 10^{-6} wt.% oxygen containing molten Pb at 600 °C (HEA7 and HEA8).

6.1.3 TEM evaluation

In order to further characterize the oxidation behavior of HEA alloys, two samples, one sample with duplex phases (HEA1) and another sample with dendrites (HEA4) have been selected for 2000 h exposure test in 10^{-6} wt.% oxygen containing molten Pb at 600 °C. Moreover, a TEM analysis has been employed to characterize the structure of the oxide scale.

Fig. 6-28 shows the surface plan view of both samples after 2000 h exposure. Both samples are protected by the oxide scale without any corrosion attack. The surface of HEA1 depicts the circular morphologies which is same to HEA1 sample exposed to 10^{-6} wt.% oxygen containing molten Pb for 1000 h at 550 °C and 600 °C. The bright and thick parts are due to the still adherent Pb. In case of HEA4, the surface scale is thin and uniform.

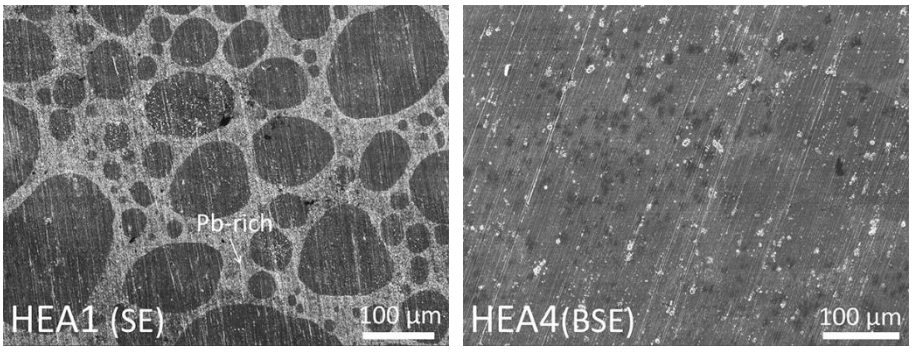

Fig. 6-28 Surface profile of HEA1 and HEA4 after 2000 h exposure to 10^{-6} wt.% oxygen containing molten Pb at 600 °C.

Then the samples have been characterized by XRD, shown in Fig. 6-29. According to the results, the oxides formed on HEA1 are Cr_2O_3 and $(Al,Cr)_2O_3$ (weak). In alloy matrix, X-ray diffraction patterns from FCC, B2 and BCC have been identified. In case of HEA4, the oxides identified are mainly Cr_2O_3 (weak) and $(Al,Cr)_2O_3$ (weak). In the alloy matrix, FCC and B2 phases are identified.

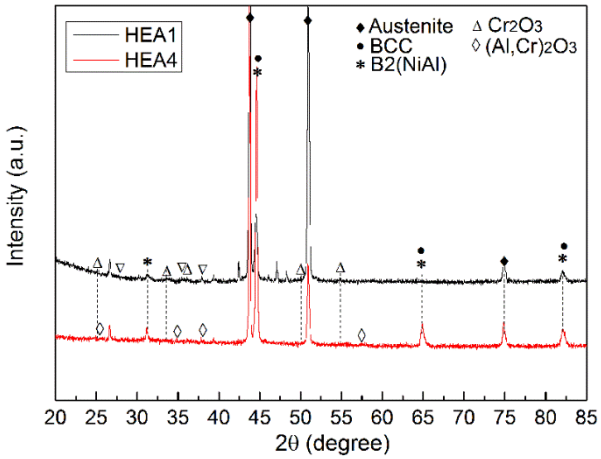

Fig. 6-29 XRD patterns performed on samples after 2000 h exposure to 10^{-6} wt.% oxygen containing molten Pb at 600 °C (HEA1 and HEA4).

Both samples are further characterized by high resolution TEM. Since the oxide scale formed on HEA1 is non-uniform, the TEM foil is cut from the thin part shown in dark contrast in Fig. 6-28. Fig. 6-30 shows the SAED of bulk alloy and oxide scale of HEA1. The sample has not been tilted into a low-indexed zone axis. According to the diffraction pattern of HEA1, two main phases can be identified in the alloy matrix. One phase is an FCC phase (PDF Nr.33-397), orientated in <112> zone axis, the second phase is a BCC phase (PDF Nr.34-396), orientated in <113> zone axis. The phases identified by SAED are in agreement with the XRD measurement. As for the oxides formed in the surface layer, the ring pattern indicates the formation of poly- and nano-crystalline oxides. Based on the evaluated results, the pattern can be attributed to corundum $(Al_xCr_{1-x})_2O_3$, with x= 0.9, which is also identified by the XRD.

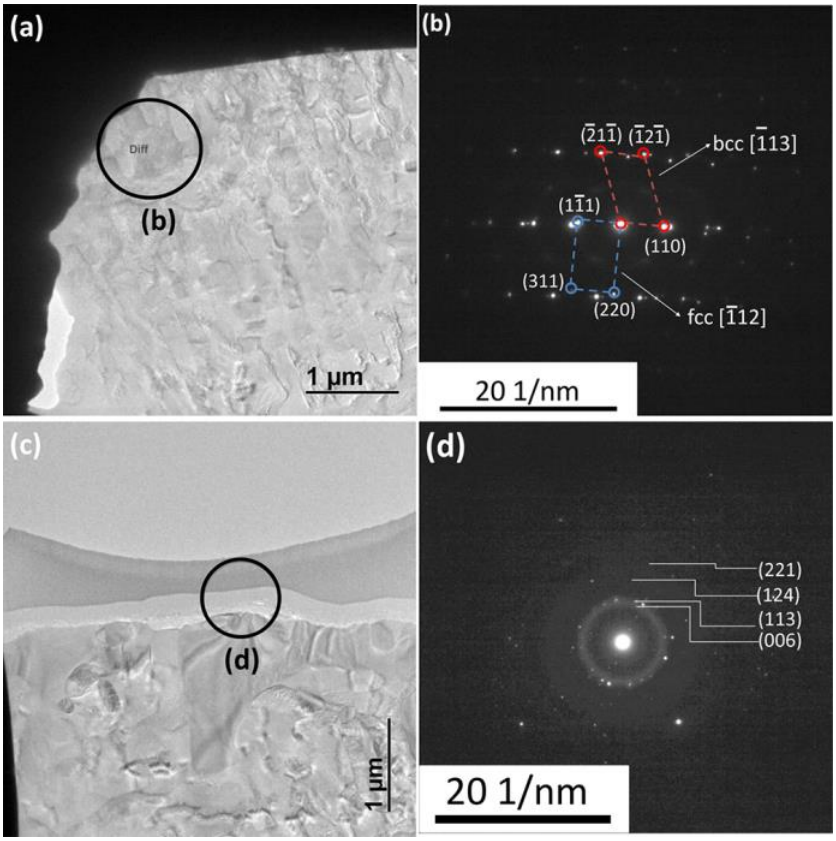

Fig. 6-30 TEM-BF images of the cross section of HEA1 ($Al_{9.76}Cr_{30.28}Fe_{32.95}Ni_{26.91}$) and corresponding SAED in alloy matrix (a, b), FCC <112> zone orientation and BCC <113> zone orientation and oxide scale (d) marked on (c), $(Al_{0.9}Cr_{0.1})_2O_3$.

To identify the oxides formed in the passive layer, a Fast Fourier Transformation (FFT) has been applied to the selected high-resolution transmission electron microscopy images. Two types of oxides based on Cr and based on Al are identified according to the lattice plane distances. Fig. 6-31 (a) shows the regions (P1) where Cr_2O_3 (PDF Nr.84-1616) has been identified. The measured lattice plane distances match the (012) and (104) planes, respectively. In addition to the oxide $(Al_{0.9}Cr_{0.1})_2O_3$ detected by XRD and SAED, α-Al_2O_3 (PDF Nr.75-788) and κ-Al_2O_3 (PDF Nr.73-1199) have been recorded in the regions shown in Fig. 6-31 (b). In case of α-Al_2O_3, the lattice planes of (113) and (202) match the measured lattice plane distance. As for the κ-Al_2O_3, the lattice plane of (002), (101), (110) and (203) match the measured values shown in Fig. 6-31.

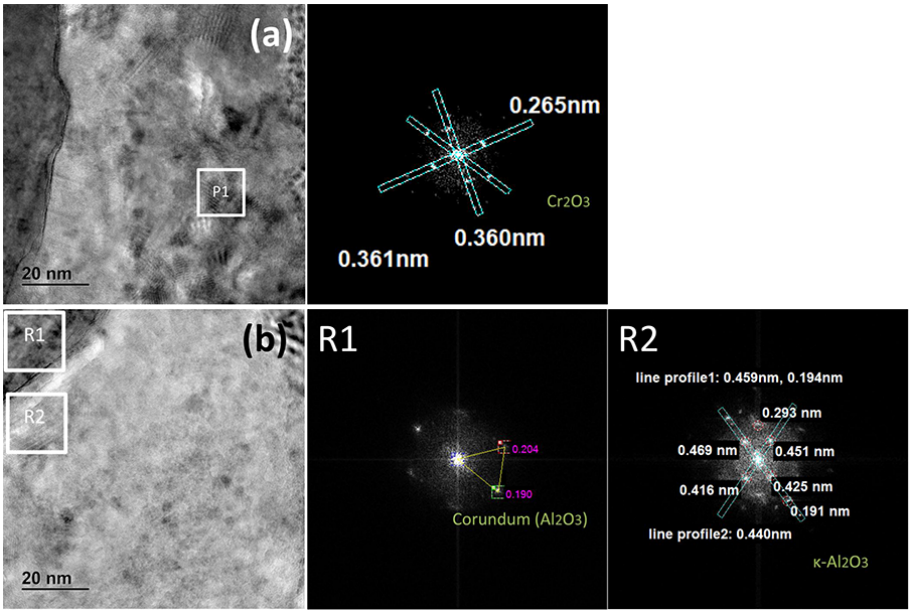

Fig. 6-31 HR-TEM image of oxide scale region (a) and related FFT image of the whole image of HEA1; HR-TEM image of oxide scale region (b) and related FFT images (P1: Cr_2O_3; R1: α Al_2O_3; R2: κ-Al_2O_3).

EDS line profiles across the oxide scale are shown in Fig. 6-32. The oxide layer consists of two parts. The upper part, which shows a strong intensity from Cr, indicates the formation of a Cr_2O_3 layer. The thickness varies from 60 to 80 nm. Below the upper layer, a dark thin layer exhibits a maximum intensity from Al, indicating the formation of Al_2O_3 layer. The thickness varies from 20 to 80 nm. The total thickness of the oxide scale is 80 to 150 nm. The Pt stems from the FIB-sample preparation process (protective coating). The yellow square is the reference area for drift correction during acquisition.

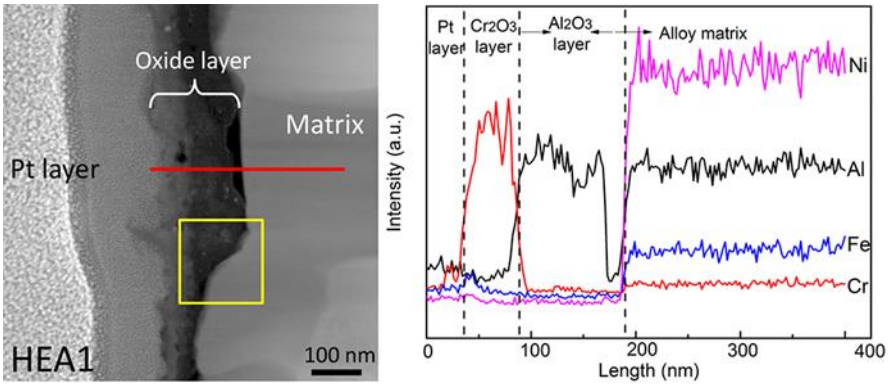

Fig. 6-32 STEM-image (left) and STEM-EDS line profiles of the cross section of the oxide scale formed on HEA1 after 2000 h exposure to 10^{-6} wt.% oxygen containing molten Pb at 600 °C.

Fig. 6-33 shows the SAED of the HEA 4 alloy matrix and oxide scale regions. According to the diffraction pattern, FCC phase with <103> zone axis, which is parallel to the electron beam, has been identified for the alloy matrix. The SAED of the oxide scale shows a ring pattern, indicating the

formation of poly- and nano-crystalline oxides. The measured diameters of the diffraction rings match the oxide $(Al_xCr_{1-x})_2O_3$, x=0.9, which is also detected by XRD.

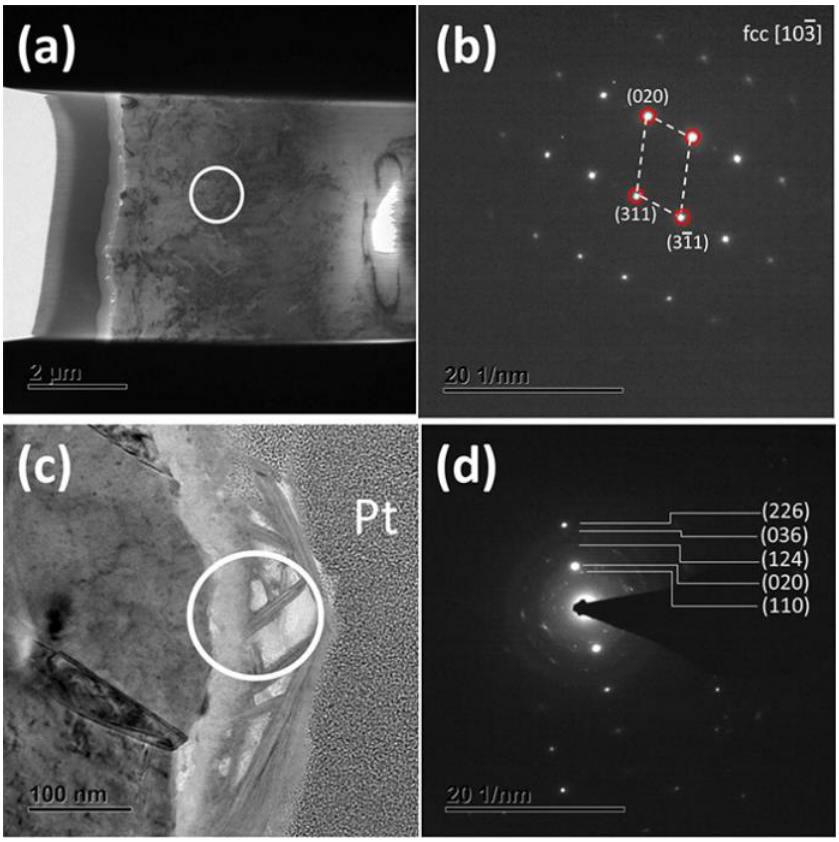

Fig. 6-33 TEM-BF images of the cross section of HEA4 ($Al_{11.69}Cr_{22.40}Fe_{32.62}Ni_{33.29}$) and corresponding SAED in alloy matrix (a, b), FCC <103> zone orientation, and oxide scale (c, d), $(Al_{0.9}Cr_{0.1})_2O_3$.

EDS line profiles across the oxide scale of HEA4 are shown in Fig. 6-34. The oxygen signal has not been evaluated in this measurement. The intensity signals from Cr and Al are both visible in the oxide layer. Therefore, these results indicate the formation of Al-, Cr-rich oxides in the passive surface layer. In the matrix, the signals from Cr, Fe, and Ni are detected, whereas the intensity of the Al signal is significantly reduced. The yellow square is the reference area for drift correction during acquisition.

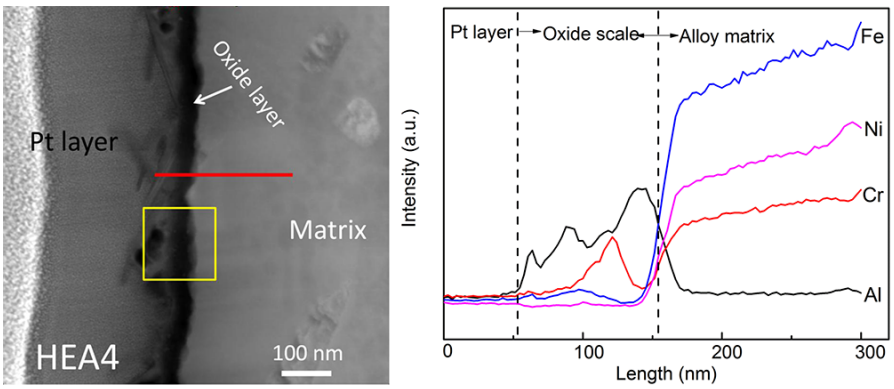

Fig. 6-34 STEM-image (left) and STEM-EDS line profiles of the cross section of the oxide scale formed on HEA41 after 2000 h exposure to 10^{-6} wt.% oxygen containing molten Pb at 600 °C.

6.2 Structural stability analysis

In addition to the corrosion behavior, the structural stability of the investigated samples is also evaluated after the exposure tests. Samples HEA3, HEA5, HEA6, and HEA8 shown either second phase formation or phase transformation have been evaluated. HEA1, HEA2, HEA4 and HEA7 have shown the phase stability during exposure test. The results are shown in appendix B.

Fig. 6-35 shows the microstructure of HEA3 in as-cast state and after 1000 h exposure at 550-600 °C. Before exposure, there are some B2 precipitates distributed among the matrix. After 1000 h exposure at 550 °C, the matrix shows bright Al- and Ni-rich regions instead of dark precipitates. After 1000 h exposure at 600 °C, dark precipitates have formed within the bright network regions. The bright regions can be due to the composition fluctuations during exposure test. The XRD measurement indicates the formation of FCC and B2 phases in the alloy matrix after exposure at 550 °C and 600 °C, shown in Fig. 6-6 and Fig. 6-20. Based on these results, it can be concluded that the sample experienced microstructure reconstruction when exposed at 550 °C and 600 °C.

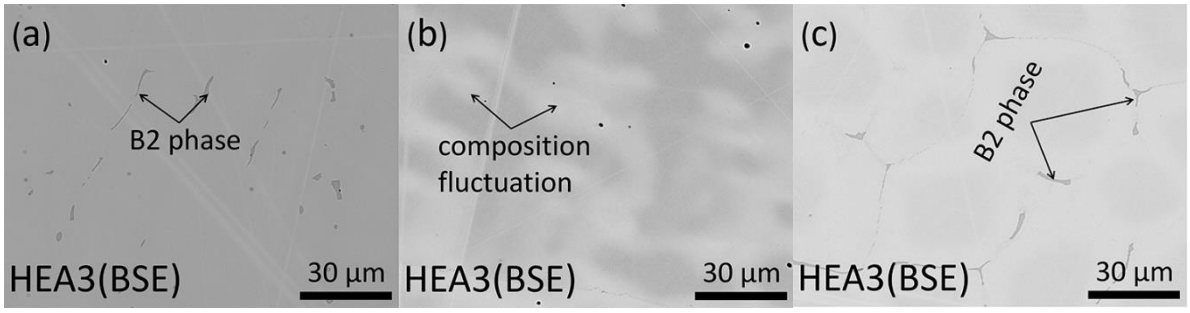

Fig. 6-35 SEM microstructure analysis of HEA3, (a): in as-cast state; (b) and (c): after 1000 h exposure at 10^{-6} wt.% oxygen containing molten Pb at 550 °C (b) and 600 °C (c).

The structure analysis of HEA5 is shown in Fig. 6-36. Before exposure, only a single phase has been detected in the alloy matrix. After 1000 h exposure at 550 °C and 600 °C, some dark precipitates have formed at the grain boundaries. According to the XRD analysis, FCC and B2-NiAl phases have been identified at both temperatures, shown in Fig. 6-9 and Fig. 6-23. The alloy matrix conserves the FCC phase after 1000 h exposure at both temperatures.

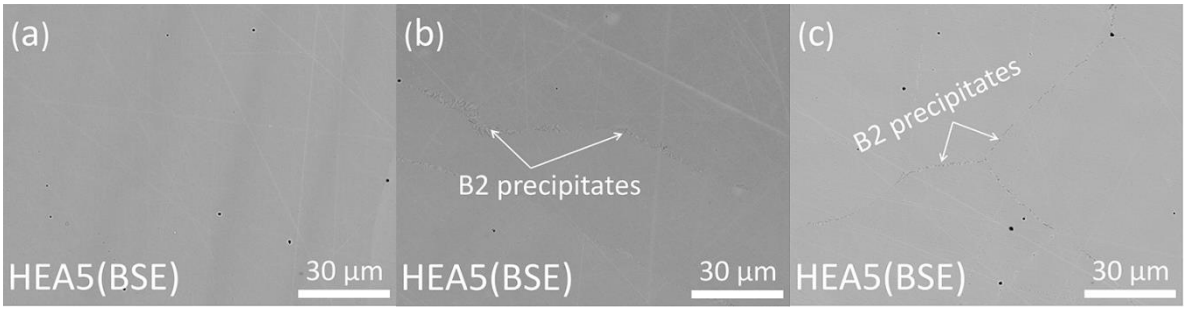

Fig. 6-36 SEM microstructure analysis of HEA5, (a): in as-cast state; (b) and (c): after 1000 h exposure at 10^{-6} wt.% oxygen containing molten Pb at 550 °C (b) and 600 °C (c).

Fig. 6-37 shows the microstructures of HEA6 in as-cast and exposed states. Before exposure, only the single FCC phase has been identified in the alloy matrix. After 1000 h exposure at 550 °C, the alloy matrix exhibits a bright network structures. When the sample was exposed at 600 °C, some dark precipitates are observed at the grain boundaries in addition to the bright network structures. XRD analysis of the exposed sample indicates the formation of FCC and B2-NiAl phase in the alloy matrix, shown in Fig. 6-9 and Fig. 6-23.

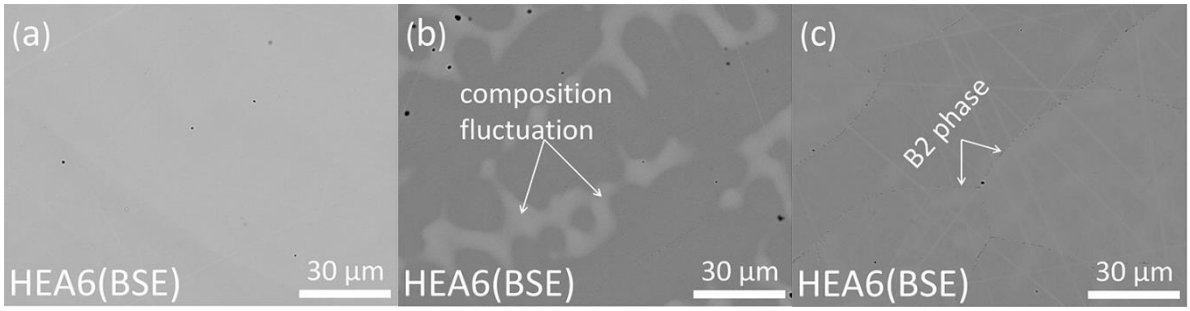

Fig. 6-37 SEM microstructure analysis of HEA6, (a): in as-cast state; (b) and (c): after 1000 h exposure at 10^{-6} wt.% oxygen containing molten Pb at 550 °C (b) and 600 °C (c).

Fig. 6-38 shows the SEM microstructure analysis of as-cast and exposed HEA8. Before exposure, the alloy matrix consists of FCC and γ′ phases. After 1000 h exposure at 550-600 °C, the strip-type morphologies at the dendrite regions have been observed. Based on the XRD analysis, the sample has formed FCC, γ′-phase ($Ni_3(Al,Ti)$), σ-phase (FeCr) and η-phase (Ni_3Ti) in the alloy matrix after 1000 h exposure at 550-600 °C, shown in Fig. 6-13 and Fig. 6-27. The η-phase corresponds to the γ′→η phase transformation at the exposed temperatures. These results indicate structural instability of HEA8 at the investigated temperature range.

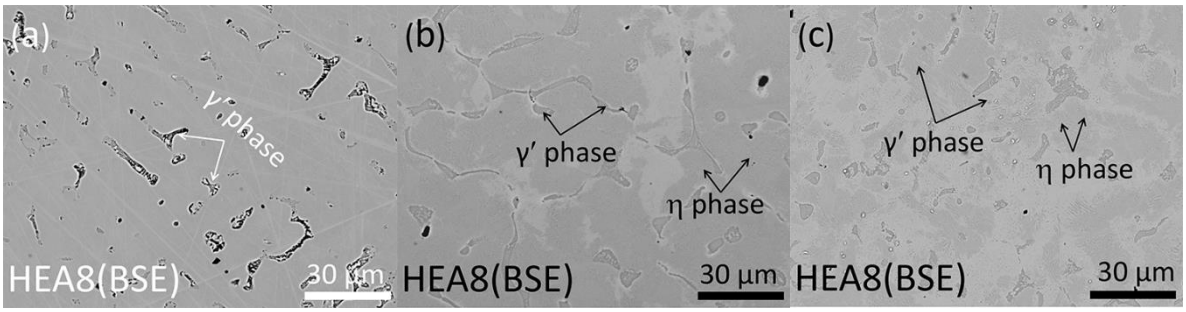

Fig. 6-38 SEM microstructure analysis of HEA8, (a): in as-cast state; (b) and (c): after 1000 h exposure at 10^{-6} wt.% oxygen containing molten Pb at 550 °C (b) and 600 °C (c).

6.3 Performance and recommendations for corrosion resistant HEA model alloys

The high entropy alloys, based on the elements of Fe, Cr, Ni, Al, Nb, Cu and Ti, have been designed on the basis of criteria including -15 kJ/mol < ΔH_{mix} < 5 kJ/mol, 1% < δr < 6.6%, Ω > 1.1 and *VEC*>7.5. Nine samples, six based on quaternary Fe-Cr-Ni-Al and three based on quinary Fe-Cr-Ni-Al-Nb/Cu/Ti have been prepared, cf. Table 6-1. In spite of forming single solid solutions, the dual phases HEA (FCC plus B2 or Laves or γ′ phases) are also designed to improve the high temperature performance of candidate alloys. After 1000-2000 h exposure in 10^{-6} wt.% oxygen containing molten Pb at 550-600 °C, eight alloys, except the sample HEA9 with Cu addition, show excellent corrosion resistance by forming protective oxide scale.

After 1000 h exposure to oxygen containing molten Pb at 550 °C, HEA1 has formed an oxide scale with thick and thin parts, depending on the phase compositions in the alloy matrix. The thick oxide scale part (400-700 nm) is based on an outer layer of $(Fe,Cr)_3O_4$ and an inner layer of $(Al,Cr)_2O_3$, while the thin part (200 nm) is based on an outer Cr_2O_3 layer and an inner $(Al,Cr)_2O_3$ layer. The oxide scales formed after 1000 h at 600 °C have shown the same structure and oxide compositions. Since HEA1 has formed a duplex structure (FCC+BCC phases) in the bulk alloy, the Fe, Cr-rich BCC phases (shown in table 4-9) lead to the formation of a $(Fe,Cr)_3O_4$ layer as a first barrier, while the FCC matrix promotes the formation of Cr_2O_3 as a first barrier. After 2000 h exposure in oxygen containing molten Pb at 600 °C, an oxide scale based on an outer layer of Cr_2O_3 and an inner layer of Al_2O_3 (e.g. α-Al_2O_3, κ-Al_2O_3) and Al_2O_3-Cr_2O_3 solid solutions have been identified in the thinner part of the oxide scale. The formation of transient alumina at this temperature range (500-600 °C) has been also observed in the other corrosion tests of alumina forming ferritic alloys (Fe-(12-16) Cr-(6-8) Al, wt.%) in oxygen containing molten Pb [85, 138]. Due to the exposure temperature lower than 900 °C, aluminum is prone to be oxidized to form transient alumina (e.g. κ-Al_2O_3, γ-Al_2O_3). As oxidation temperature or exposure time increase, the transient alumina is able to transform to stable α-Al_2O_3 [141].

The dual phase HEAs (HEA2, HEA3, HEA4) and single FCC phase HEAs (HEA5, HEA6) have formed an oxide scale based on an outer Cr_2O_3 layer and an inner $(Al,Cr)_2O_3$ layer after 1000 h exposure in oxygen containing molten Pb at 550 °C and 600 °C. As the exposure temperature increases to 600 °C, the signals from Al_2O_3 become more pronounced in some of the samples (e.g. HEA4) compared with the samples exposed to 550 °C. This result confirms that increasing the exposure temperature promotes the formation of alumina scale.

At the selected oxygen containing molten Pb conditions, the mechanisms of passivating Cr_2O_3 and Al_2O_3 based oxide scale on quaternary HEA alloys are similar to that of corrosion resistant AFA alloys. During the early exposure stage, chromium in the alloy is prone to be oxidized due to its high fraction in the alloy matrix and low oxygen decomposition partial pressure of Cr_2O_3. The formation of a continuous and thin Cr_2O_3 scale will slow down the dissolution of alloying elements, e.g. Ni, Fe, Al. Then the oxidation is mainly controlled by the inward oxygen diffusion. The low oxygen partial pressure at the scale-matrix interface mainly allows the selective oxidation of Al due to the lower oxygen decomposition pressure of Al_2O_3, as described in Fig. 2-2. Moreover, the corundum structure of Cr_2O_3 acts as a nucleation site for α-Al_2O_3. As the exposure time increases from 1000 h to 2000 h, more aluminum at the inner part of the scale are oxidized to form pure alumina layer.

When the fifth element Nb, Ti or Cu is added, the quinary alloys (HEA7, HEA8, HEA9) show different corrosion behavior. Sample HEA7 with Nb addition has formed an oxide scale which is based on Cr_2O_3 and α-Al_2O_3 at 550 °C and only α-Al_2O_3 scale at 600 °C when exposed to 10^{-6} wt.% oxygen containing molten Pb for 1000 h. The oxide scale formed at 600 °C (150 nm) is thinner than that formed at 550 °C (200 nm), which might be due to the increased Al-activity when temperature increases. Recent studies show that Nb addition in alumina-forming alloys increases the Cr content in austenite, and may also reduce the oxygen solubility in the alloy matrix, which are favorable for external alumina scale formation [147, 179]. Moreover, the high solubility of Al (up to 50 at.%) in Fe_2Nb Laves phase is also beneficial to the formation of alumina [265]. By adding Ti in sample HEA8, the designed alloy forms an oxide scale which consists of TiO_2, Cr_2O_3 and $(Al,Cr)_2O_3$. The formation of TiO_2 is attributed to the relatively low oxygen decomposition pressure of TiO_2, as shown in Fig. 2-2. However, the formation of a TiO_2 layer is unable to effectively inhibit the inward diffusion of oxygen, which will allow the Al and Cr to be selectively oxidized at a lower level of oxygen partial pressure. As for the HEA9 with Cu addition, the passivated oxide layer shows the evidence of spallation during the cooling, after the extraction of the sample from molten Pb at the end of the corrosion tests. The addition of Cu in HEA alloys (e.g. $AlCoCrCu_xFeNi$, x=0, 0.5, 1) was reported to degrade the scale adherence of α-Al_2O_3 which has formed in air at 1000 °C [266].

In addition to the oxide scale, a transitional metallic layer has been observed in some of the exposed HEA alloys mainly exposed at 550 °C, as summarized in Table 6-2. The enrichment of Fe and Ni in the transitional layer indicates that the passivated oxide scale can effectively inhibit their diffusions. Moreover, B2-NiAl precipitates and a few Cr-rich spots are also visible in the transitional layer. This can be due to the fast diffusion of Cr atoms towards the surface during the transient oxidation stage. The concentration of Al may locally exceed the solubility limit in austenite (2-2.5 wt.%) which leads to B2 precipitations [147]. On the other hand, the local enrichment of Cr at the regions surrounding the B2 precipitates leads to the formation of coexisting Fe-Cr-based ferrite precipitates.

Table 6-2 Summarized results of transitional layer formed on HEA alloys after 1000 h exposure to 10^{-6} wt.% oxygen containing molten Pb at 550-600 °C.

Sample code	Transitional layer	
	550 °C	600 °C
HEA1	N	N
HEA2	Y (dis-continuous)	N
HEA3	Y (dis-continuous)	N
HEA4	Y(dis-continuous)	N
HEA5	Y	Y
HEA6	Y	Y
HEA7	Y(Laves free parts)	Y(Laves free parts)
HEA8	N	N

N: no transitional layer; Y: formation of transitional layer.

The alloys matrix of all samples after the 1000 h exposure tests at 550 °C and 600 °C have been analyzed in comparison with the as-cast samples. Two main points are considered in investigating the structural stability after the exposure tests: (i) phase transformation; (ii) second phase coarsening/precipitates formation. Table 6-3 summarizes the phase evaluation of HEA alloys after 1000 h corrosion tests in 10^{-6} wt.% oxygen containing molten Pb at 550 °C and 600 °C. HEA1 with duplex structure (FCC+BCC) and HEA2, HEA4 with high fraction of B2 inter-dendrites (FCC+B2), and HEA7 with FCC plus Laves in alloy matrix show microstructure stability during exposure at 550 °C and 600 °C. The stability of microstructure and phase compositions in alloys matrix may attribute to the relative high thermal stability of B2 and Laves up to 900 °C [82, 185, 267]. HEA3 and HEA6 have closed chemical compositions in spite of forming B2 precipitates in the alloy matrix of HEA3, see table 4-9. Both samples show the similar structure evolution during the exposure tests at 550 °C and 600 °C, namely composition fluctuations (enrichment of Al and Ni at 550 °C) and B2-NiAl precipitates at the grain boundaries (at 600 °C). Such kind of B2-NiAl precipitates are also observed in the other Al-containing alloys/steels (e.g. AFA steels, AlNiCoCrFe) during the aging at temperature range of

550-800 °C [155, 268, 271], which also fall into the temperature range of B2 phase formation predicted by the Thermo-Calc for Al10Ni22.5Cr22.5Co22.5Fe22.5 (at.%) [155]. However, the mechanical properties of alloys do not degrade up to 700 °C due to the B2 precipitates formation, e.g. the tensile stress of AFA (Fe-3Al-14Cr-32Ni-base, wt.%) is still above 500 MPa with a maxima strain of 0.3 at 700 °C [269]. HEA5 with single FCC phase has formed the B2 precipitates at the grain boundaries after exposure at both 550 °C and 600 °C, which are same to that of HEA6 exposed to 600 °C. By adding Ti in the Fe-Ni or Ni-based alloys, the alloys can form strengthening γ′ phases, which can hinder the grain boundary migration during thermal aging, improve the mechanical behavior at elevated temperature [185, 207], e.g. the creep life of AFA (Fe-14Cr-32Ni-(3-4)Al-(1-3)Ti-base wt.%) alloys is 20 times longer when compared with Fe-based super alloy A286 (Fe–14.5Cr–2.1Ti–0.15Al–25Ni) at 750 °C and 100 MPa [185]. However, the metastable γ′-phase has the tendency to transform to brittle η-phase at high temperature, which is observed in HEA8 after 1000 h exposure test in low-oxygen containing molten Pb at 550 °C and 600 °C. Research of AlxCo1.5CrFeNi1.5Tiy (x+y=0.5) has indicated that increasing the Al content up to 5.5 at.% can suppress the γ′→η phase transformation up to 900 °C [207]. Another research work of AFA alloys (Fe-14Cr-32Ni-(3-4)Al-(1-3)Ti-base, wt.%) indicates that the addition of small amount of Zr (around 0.3 wt.%) can help stabilize the γ′ phase up to 750 °C [185].

Table 6-3 Phase evaluation of HEA samples after 1000 h exposure in 10^{-6} wt.% oxygen containing molten Pb at 550 °C and 600 °C.

Code	Phase transformation	Second phase coarsening or precipitates
HEA1	N	N
HEA2	N	N
HEA3	N	Y (at 600 °C)
HEA4	N	N
HEA5	N	Y
HEA6	N	Y (at 600 °C)
HEA7	N	N
HEA8	Y	Y

N: No; Y: Yes.

According to the experimental results of thermo-physical properties, corrosion behavior and phase stability of HEA alloys, a general formula of corrosion resistant HEA alloys in low-oxygen containing molten Pb at 550-600 °C, based on the backbone compositions of Fe-Ni-Cr-Al, is defined as follows: (30.29-34.50)Fe-(33.15-35.02)Ni-(21.37-25.01)Cr-(6.02-11.69)Al(at.%). In addition, a minimum amount of 5 at.% Nb can be considered having positive influence on the mechanical properties due

to formation of strengthening Laves phase in bulk alloy and on alumina scale formation as well due to the high solubility of Al in the Laves phase [265].

7. Oxidation behavior of AFA and HEA model alloys in steam

Three AFA alloys, AFA71 (Fe-15.4Cr-2.5Al-19.9Ni-0.5Y), AFA72 (Fe-15.4Cr-2.5Al-21.8Ni-0.5Y) and AFA75 (Fe-15.7Cr-3.1Al-24.1Ni-0.7Y-1.68Nb), and four HEA alloys, HEA3 ($Al_{8.91}Cr_{23.13}Fe_{33.68}Ni_{34.28}$), HEA6 ($Al_{7.96}Cr_{23.23}Fe_{34.06}Ni_{34.75}$), HEA7 ($Al_{8.24}Cr_{21.37}Fe_{30.29}Ni_{35.02}Nb_{5.08}$) and HEA8 ($Al_{7.90}Cr_{22.04}Fe_{31.91}Ni_{33.14}Ti_{5.01}$), have been selected and exposed to steam environments at 1200 °C in order to investigate their corrosion behavior at extreme steam conditions, as they may occur in nuclear accidents, as exhaust in fossil fired turbines, or pure hydrogen fired systems.

7.1 Oxidation behavior of AFA alloys

7.1.1 Hydrogen release

During the steam exposure test, the oxidation of metal elements leads to the decomposition of water in the steam and generation of H_2. The following reaction describes the general oxidation process:

$$xM(s)+yH_2O(g)\rightarrow M_xO_y(s)+yH_2(g); \quad (7.1)$$

M: metal element.

The hydrogen release during experiments is used as a probe of the oxidation process of the selected alloys. Fig. 7-1 shows the hydrogen release rate of AFA alloys (Fig. 7-1(a)) and hydrogen production per square meter (Fig. 7-1(b)) in steam at 1200 °C. AFA71 and AFA72 show the same temporal evaluation of hydrogen release. At the initial 150 s exposure, both samples show a sharp increase of hydrogen release rate. Then, the hydrogen release rate decreases to 0.0025 g/s/m^2 at 600 s and stays constant during later exposure, see Fig. 7-1(a). AFA75 exhibits the highest hydrogen release rate during the oxidation test. At the beginning of the exposure, the hydrogen release rate increases rapidly to 0.053 g/s/m^2. Then the release rate drops to 0.0067 g/s/m^2 and stays constant during later exposure.

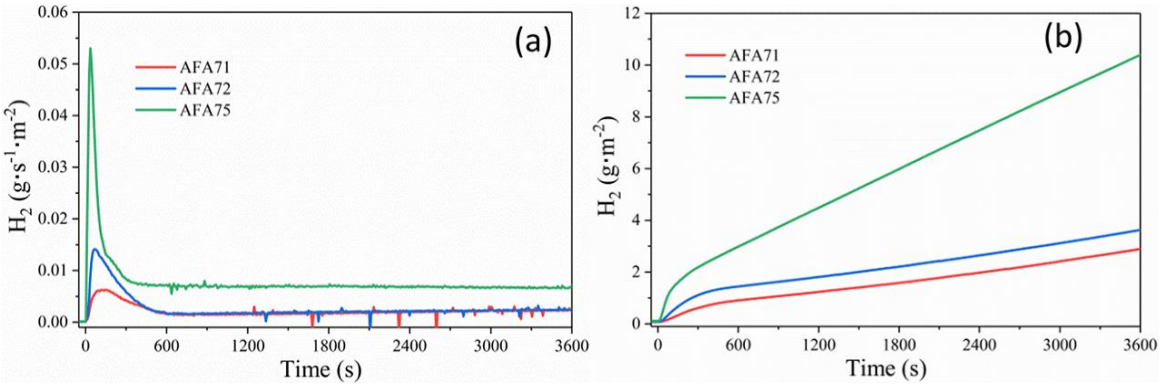

Fig. 7-1 Hydrogen release of AFA samples exposed to steam at 1200 °C for 1 h; (a): hydrogen release rate; (b): hydrogen production per square meter.

7.1.2 Surface and cross section analysis

Fig. 7-2 shows the typical surface view of AFA alloys after 1 h exposure to steam at 1200 °C. The oxide scales formed on AFA71 and AFA72 exhibit wrinkle morphologies. No spallation is evident on both samples. EDS point measurements of the scale show that it mainly consists of O and Al, indicating the formation of an alumina scale. In addition, protrusions are observed on the surface of AFA72, at around 20% of the surface area. As evidenced by EDS point measurements, the protrusions are rich in O, Cr and Fe. These protrusions are due to oxidation of the regions surrounding the YNiAl-rich spots, which are depleted in Al and Ni. AFA75 shows the surface scale with evidence of exfoliation. The oxide scale formed on the surface is non-uniform. Based on the semi-quantitative EDS analysis, the oxide scales mainly consists of O and Fe (>90% of the surface area). Parts of the Fe-rich thick oxide layer spalled off. Only a small surface area (<10% of the surface area) is covered by Al-rich oxide scale.

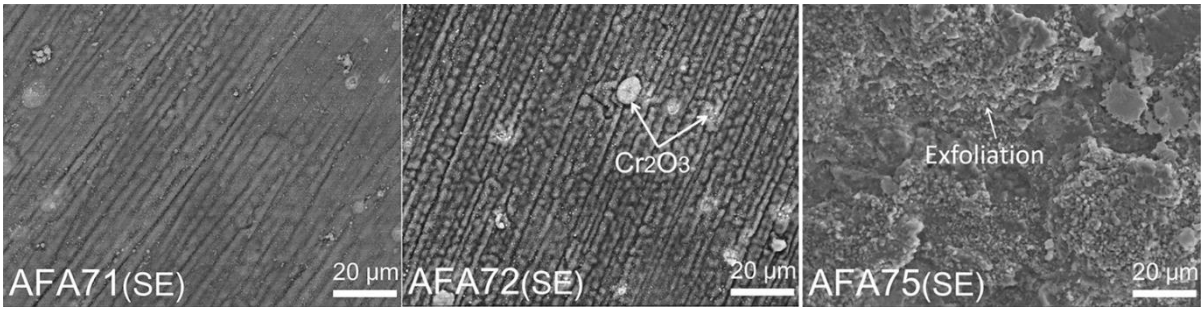

Fig. 7-2 Surface morphologies of AFA samples (AFA71, AFA72, AFA75) after 1 h exposure to steam at 1200 °C.

Further cross section analyses of the tested samples are illustrated in Fig. 7-3. The oxide scales formed on the surfaces of AFA71 and AFA72 are continuous and uniform, as the upper two left figures depict. No spallation or internal oxidation is observed on both samples. Based on the EDS line scanning and mapping, the oxide scale consists of O and Al, as shown in Fig. 7-3 and Fig. 7-4. The thickness of the oxide scale is around 1.2 µm. No second phase or phase transition is observed below the oxide scale. In contrast, AFA75 has formed a thick oxide layer, see Fig. 7-3 top right. According to the cross sectional EDS line scanning, the oxide scale mainly consists of three consecutive layers: at the interface a porous outer layer enriched in O and Fe with a thickness of about 15 µm followed by a middle dense layer enriched in O and Cr of around 7 µm width and, finally, a dis-continuous internal aluminum oxidized layer (6-10 µm). The total thickness of the oxide scale is around 30 µm.

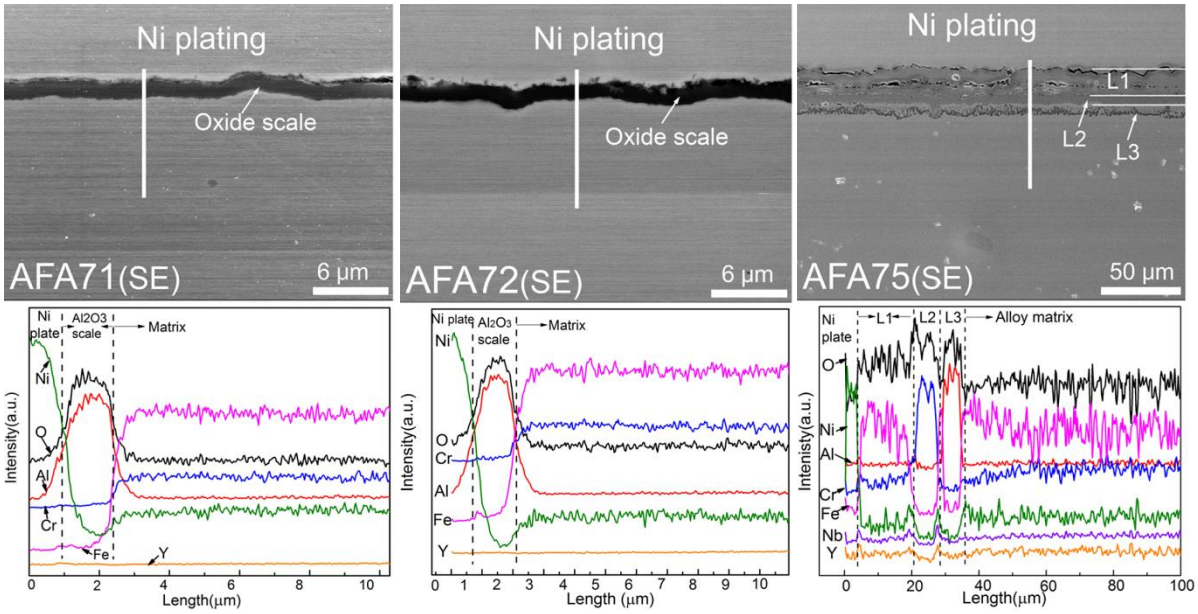

Fig. 7-3 EDS line scans of the cross sections of AFA samples (AFA71, AFA72, AFA75) after 1 h exposure in steam environments at 1200 °C (AFA75, L1:magnetite layer; L2:chromia layer; L3: Al-internal oxidation layer).

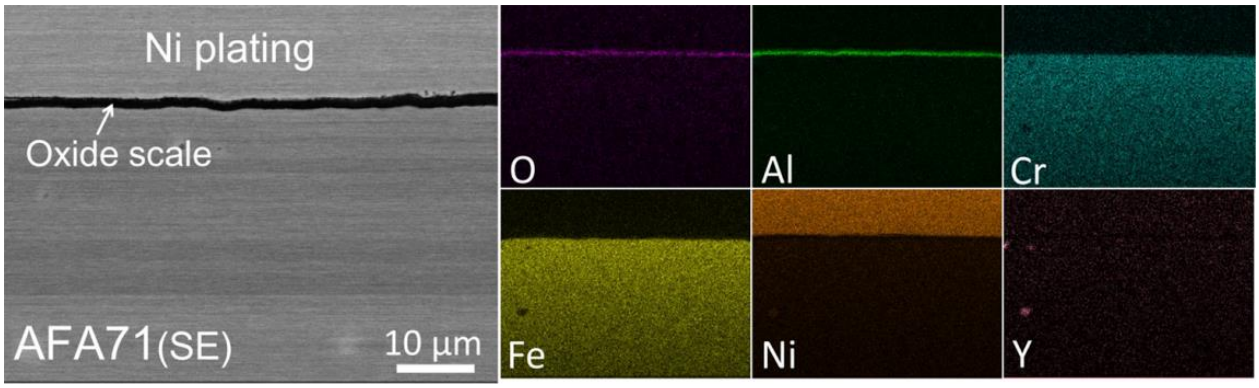

Fig. 7-4 EDS mapping of the cross section of AFA71 after 1 h exposure to steam environments at 1200 °C.

7.1.3 XRD characterization

XRD phase analysis confirms the formation of α-Al_2O_3 (PDF Nr. 46-1212), Cr_2O_3 (PDF Nr. 84-1616) and $(Fe,Cr)_3O_4$ (chromite, PDF Nr. 34-140) in the oxide scale of AFA71 and AFA72, as shown in Fig. 7-5. Both samples have shown the strong intensities of α-Al_2O_3. Compared with AFA71, the intensities of Cr_2O_3 and $(Fe,Cr)_3O_4$ are higher in AFA72. As for the alloy matrix, only FCC phase is identified in AFA71 and AFA72. Sample AFA75 shows different X-ray diffraction pattern, as indicated in Fig. 7-5. The formed oxides are $(Fe,Cr)_3O_4$ (strong) and Cr_2O_3 (weak) according to the X-ray diffraction patterns. In the matrix, FCC (austenite), B2-NiAl and Fe_2Nb (Laves, weak) are identified.

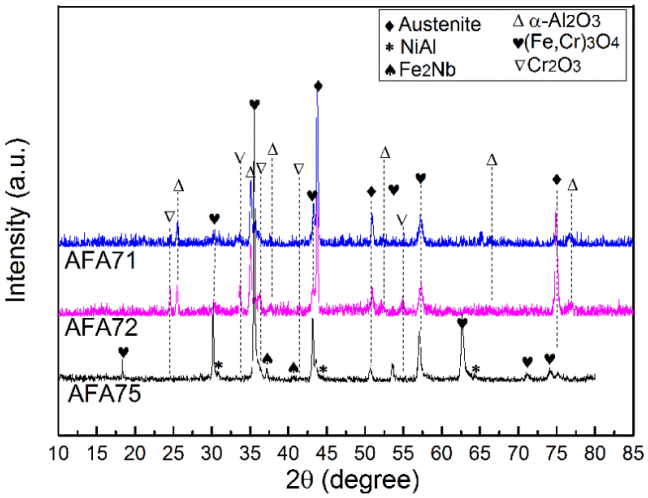

Fig. 7-5 XRD patterns obtained from the AFA samples after 1 h exposure to steam at 1200 °C.

7.2 Oxidation behavior of HEA alloys

7.2.1 Hydrogen release

Fig. 7-6 shows the hydrogen release of HEA alloys in steam at 1200 °C. Both HEA3 and HEA6 show a hydrogen release rate lower than 0.003 g/s/m^2, see Fig. 7-6(a). The hydrogen production per square meter of HEA3 is lower than that of HEA6, as shown in Fig. 7-6(b). Both samples show a slight increase of the hydrogen release rate with the increasing exposure time. HEA7 displays a different temporal behavior of the hydrogen release rate. During the initial 200 s, HEA7 shows a small peak of the hydrogen release rate, with a value of nearly 0.002 g/s/m^2. Then, it deceases rapidly to less than 0.001 g/s/m^2 during the steady oxidation stage, which is less than half of the release rate of HEA3 and HEA6. HEA7 shows the lowest overall hydrogen production after 1 h at 1200 °C in steam among the HEA alloys, see Fig. 7-6(b). In contrast, the hydrogen release rate of HEA8 increases rapidly to 0.0126 g/s/m^2 at the beginning of the exposure, indicating a fast oxidation process before the formation of a continuous oxide scale, also called transitional stage. Then, it decreases to a relatively low value of 0.001 g/s/m^2. The hydrogen production per square meter of HEA8 has the highest value of all tested HEA samples up to 3000 s. The hydrogen production after 300 s oxidation test follows a liner law.

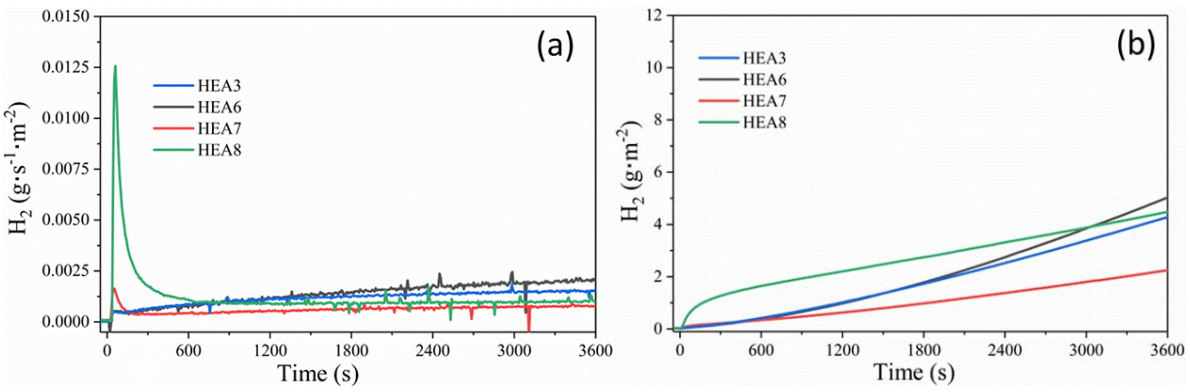

Fig. 7-6 Hydrogen release of HEA samples after 1 h exposure to steam at 1200 °C; (a): hydrogen release rate; (b): hydrogen production per square meter.

7.2.2 Surface & cross section analysis

Fig. 7-7 shows the typical surface view of HEA alloys after exposure to steam at 1200 °C. HEA3 has formed a surface scale with wrinkle morphologies, indicating the formation of α-Al_2O_3 [272]. Parts of the oxide scale (10-15% surface area), shown in bright aspect, spalled off during cooling. The surface of HEA6 is covered by an oxide scale with oxide nodules (< 2% surface area). Parts of the surface regions (20-25% surface area) show the evidence of oxide scale spallation, shown in bright contrast in Fig. 7-7. The qualitative EDS measurements of the remaining scale show the enrichment of O and Al, while the protrusions spots consist of O and Cr. A thin oxide scale is observed on the surface of HEA7. Only some spots, around 5% of the surface area, suffer from cracks or spallation during the cooling. EDS point measurements of the scale show the enrichment of O and Al in surface scale. HEA8 alloyed with 5 wt.% Ti shows a different aspect of the scale morphology. Parts of the oxide scale spalled off. The remaining layer on the surface, measured by EDS, mainly consists of O, Ti and Fe. At the spalled regions, another oxide layer without spallation has been observed. EDS measurements of the layer show the enrichment of O, Cr and Fe.

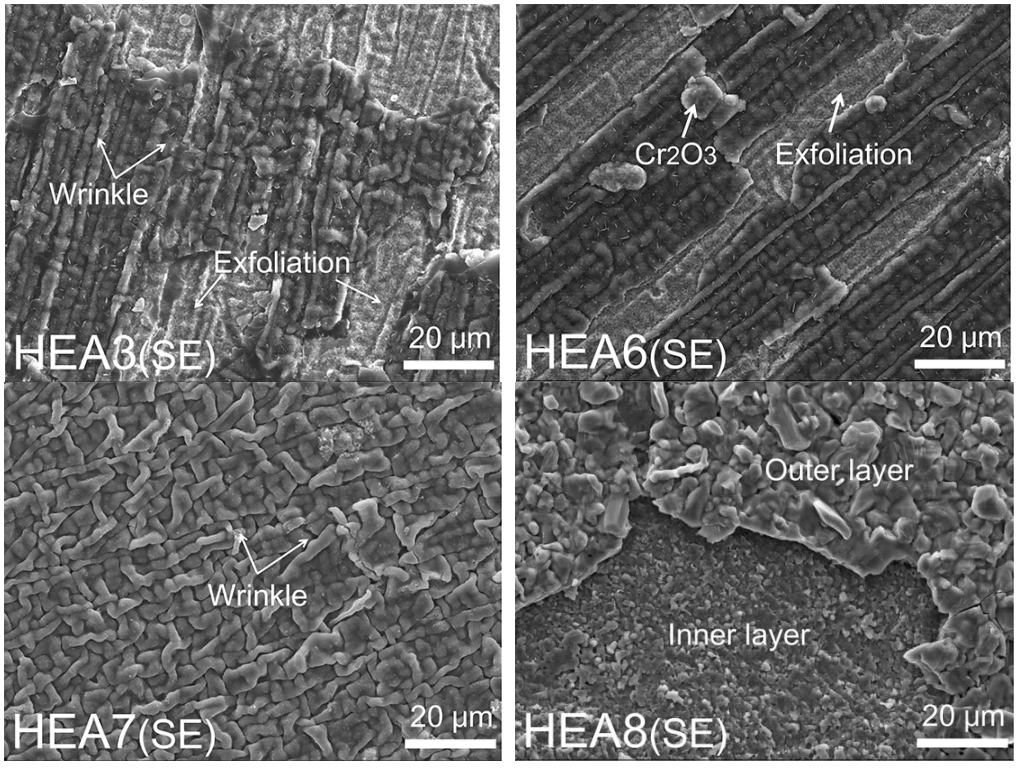

Fig. 7-7 Surface morphologies of HEA samples after 1 h exposure to steam at 1200 °C.

Fig. 7-8 shows the remaining parts of the oxide scale formed on HEA3 and HEA6. A thin and uniform oxide scale is observed on both samples. Based on the EDS line scanning, the oxide scale formed on both samples consists of O and Al, see Fig. 7-8. Besides, the B2 phases observed in alloy

matrix of HEA3 before exposure are invisible below the oxide layer up to a depth of 20 µm, see HEA3 in Fig. 7-8. No second phase has been observed in alloy matrix of HEA6 after the oxidation test in steam.

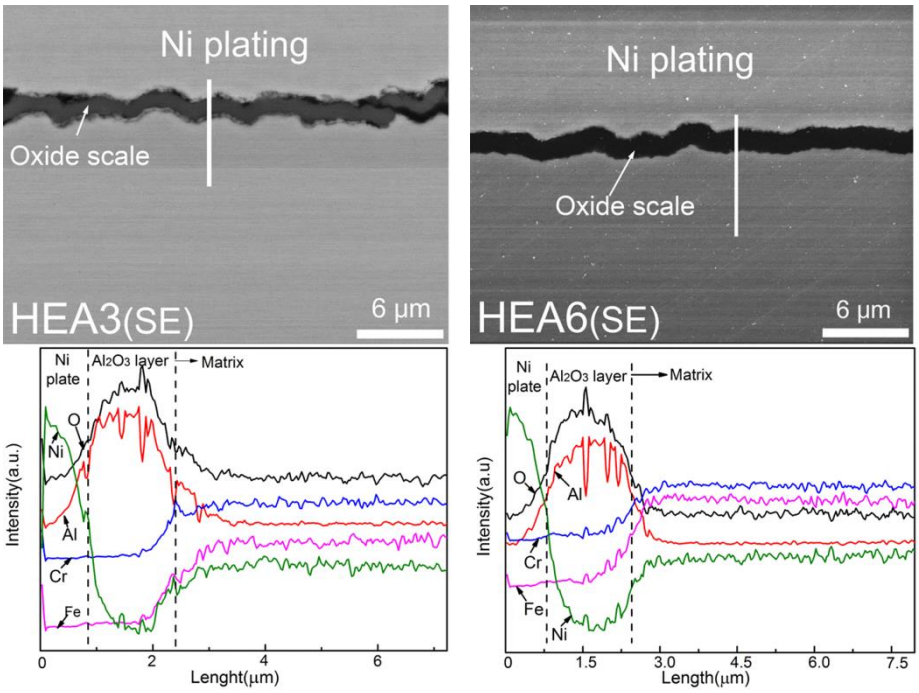

Fig. 7-8 EDS line scans of the cross sections of HEA samples after 1 h exposure to steam environments at 1200 °C (sample HEA3, HEA6).

The cross section analysis of HEA7 and HEA8 is shown in Fig. 7-9 and Fig. 7-10. HEA7 has formed a compact and corrugated oxide scale after the oxidation test in steam. Compared with the oxide scale formed on HEA3 and HEA6, the oxide scale formed on HEA7 shows a larger deformation (more wrinkles) as shown in Fig. 7-9. Based on the EDS line scan and mapping shown in Fig. 7-9 and Fig. 7-10, the scale mainly consists of Al and O. Moreover, the Laves phase grains are also protected by the Al-rich oxide scale. In the bulk alloy of HEA7, the dendrite structures are still visible after the oxidation test. Regarding the oxide scale formed on HEA8, a three-layer structure is identified from the cross section, as shown in Fig. 7-9. The outer layer accompanied by spallation consists of O and Ti. In the middle, a Cr-rich layer, probably chromia, is observed. The total thickness of the oxide scale is around 50 µm. Besides, the internal oxidation roots, which are mainly aluminum being oxidized, have formed underneath the Cr-rich layer. Below the internal oxidation layer, a depletion of dendrites, up to 30 µm, is observed.

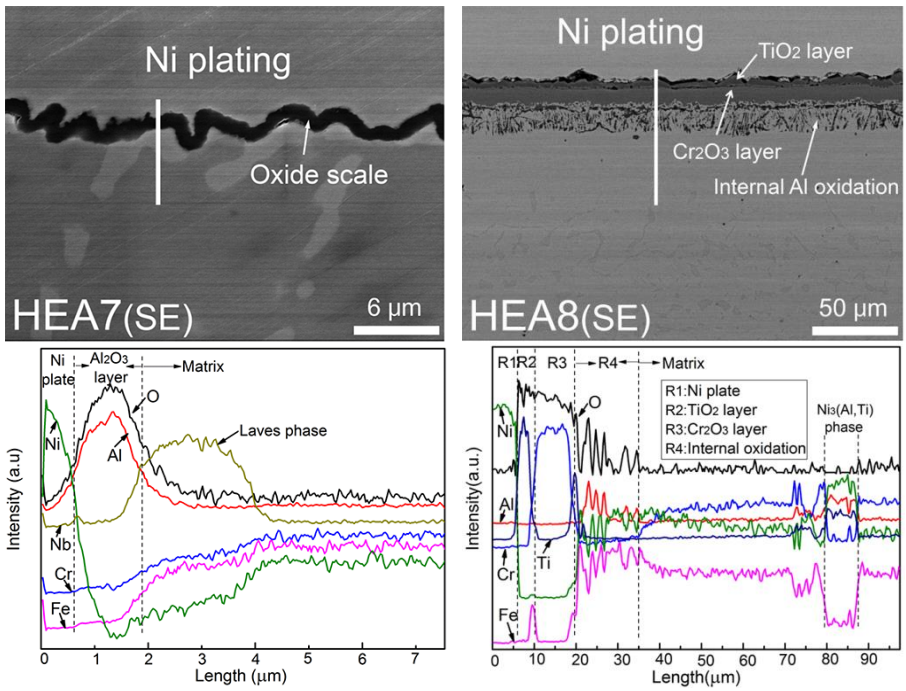

Fig. 7-9 EDS line scans of the cross sections of HEA samples after 1 h exposure to steam environments at 1200 °C (sample HEA7, HEA8).

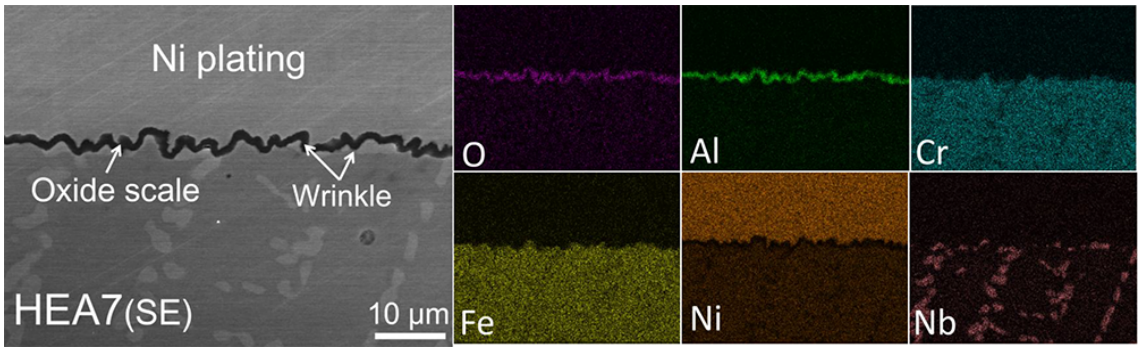

Fig. 7-10 EDS mapping of the cross section of HEA7 after 1 h exposure to steam environments at 1200 °C.

7.2.3 XRD characterization

The X-ray diffraction patterns (XRD) of HEA alloys (HEA3, HEA6, HEA7 and HEA8) after oxidation in steam are shown in Fig. 7-11. Here, only α-Al_2O_3 is identified from HEA3. In the alloy matrix, austenite plus B2 phases are identified. HEA6 has formed α-Al_2O_3 and Cr_2O_3 in the oxide scale. Only austenite is identified in the alloy matrix. HEA7 shows the signals of α-Al_2O_3 in the oxide scale. In the matrix, FCC and Laves phase (Fe_2Nb) are identified after the oxidation test. The oxide phases formed on HEA8 mainly consist of Cr_2O_3, $(Fe, Cr)_3O_4$ (PDF, Nr: 34-140) and TiO_2 (PDF, Nr: 4-551). In addition to the FCC in the matrix, $Ni_3(Al,Ti)$ (PDF, Nr:18-872) phases are also identified after the oxidation test.

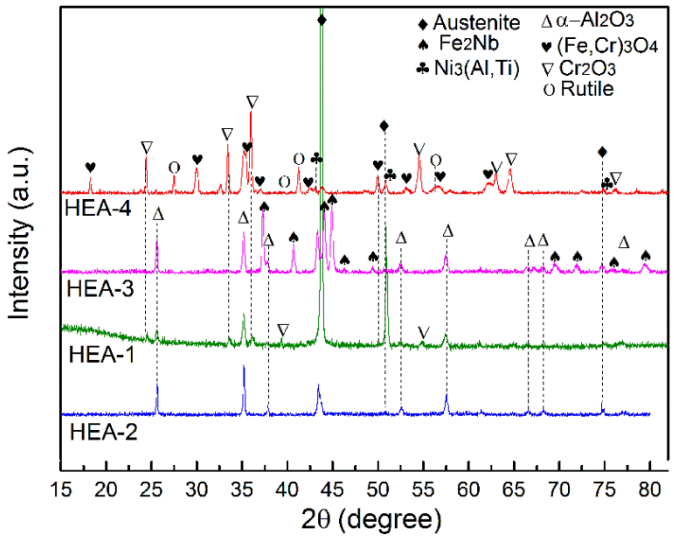

Fig.7-11 XRD patterns obtained from the HEA samples after 1 h exposure to steam at 1200 °C.

7.3 Analysis and recommendations for oxidation behavior of AFA and HEA alloys in steam

Hydrogen release measurements have been applied in this chapter to record the real time oxidation of alloys in steam environments. The measured hydrogen release rate and hydrogen production (per square meter) of test samples are consistent with the surface and cross section analysis results. In the first 300 s of the oxidation tests, all the AFA alloys have shown intensified hydrogen release peaks. The highest hydrogen release peak of AFA75 is due to the fast growing of Cr_2O_3 and $(Fe,Cr)_3O_4$. AFA72 has a hydrogen release rate larger than that of AFA71 because of the formation of higher amounts of Cr_2O_3 and $(Fe,Cr)_3O_4$. After 600 s exposure, the relatively low oxidation rates of AFA71 and AFA72 are attributed to the formation of protective α-Al_2O_3 scale. HEA3 and HEA6 show a similar trend of the hydrogen release rate. The relatively low rate at the beginning of the exposure may indicate the formation of thin Al_2O_3 rich scale, which effectively inhibits the inward diffusion of oxygen and outward diffusion of metal elements. Then HEA6 shows an increased hydrogen release rate during later exposure because of the formation of Cr_2O_3 spots. HEA7 shows a similar hydrogen release trend as AFA71 and AFA72. The small hydrogen release peaks at the initial 300 s may indicate the formation of multiple oxides, which usually has a higher oxidation rate compared with Al_2O_3. HEA8 shows a relatively high hydrogen release rate at the initial 300 s. Based on the EDS surface and cross section analysis, it is due to the fast oxidation of Fe and Ti. Then the dense Cr_2O_3 layer formed below the TiO_2 layer significantly retards the oxidation process.

In pure steam environment, the oxygen consumed during oxidation is provided by H_2O decomposition [273-274]. Only if the oxygen partial pressure is higher than the dissociation partial pressure of the oxide, the metal will be consumed to form stable oxides [54]. Based on reference data [54, 142, 275, 276], the oxygen partial pressure generated by steam dissociation and

dissociation oxygen partial pressure of selected oxides have been calculated within this research work. According to the calculated results, the following Fig.7-12 has been drawn to describe the relationship between the oxygen pressure for formation of selected oxides and steam dissociation as a function of temperature. In the temperature range of 900-1300 °C, metal elements including Fe, Cr, Nb, Ti and Al will be oxidized in 0.5 bar steam since the oxygen dissociation partial pressures of their oxides are lower than that of steam. However, when the oxygen pressure drops to a critical level, for instance at the scale-bulk alloy interface, only the elements with lower oxygen partial pressure will be selectively oxidized, e.g. Al.

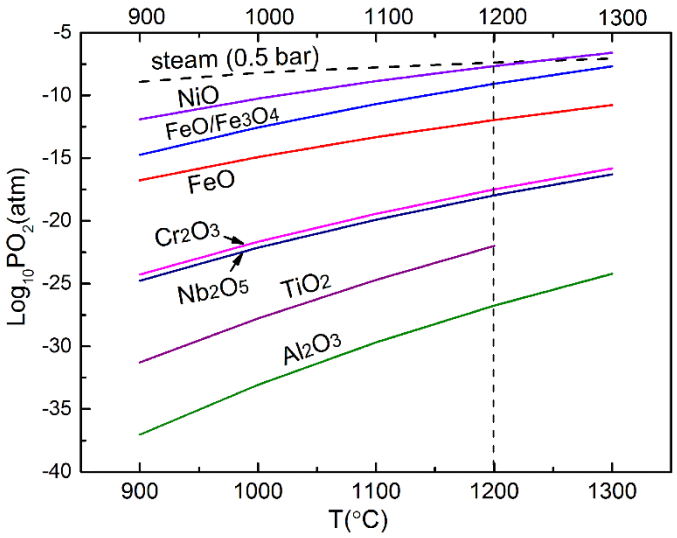

Fig. 7-12 Equilibrium oxygen partial pressures of selected oxides and dissociation pressure of steam as a function of temperature.

In addition, α-Al_2O_3 scale exfoliation has been observed on the yttrium-free samples HEA3, HEA6 and HEA7. This is assumed to have happened during the cooling process because no further oxidation or degradation of the bulk materials occurred at the spalled regions. Another interesting phenomenon is the observation of wrinkle/ridge morphologies of α-Al_2O_3 scale formed on HEA3, HEA6 and HEA7. These samples have formed high quantities of ridges in accompany with large deformations in the oxide scale.

Fig. 7-13 clarifies the process of α-Al_2O_3 scale formation and later spallation (during cooling) in Y-free alumina-forming alloys. At the initial exposure, all the metal elements will be oxidized to form an initial thin oxide scale. Then the oxygen partial pressure will be significantly reduced at the scale-matrix interface. The oxidation rate is mainly controlled by inward diffusion of oxygen species through the initial layer [54]. Alloys with sufficient Al addition have the ability to form an external Al_2O_3 scale due to the lowest dissociation oxygen partial pressure of Al_2O_3, as shown in Fig. 7-13. During this isothermal oxidation stage, the constraint from the bulk material limits the expansion of the oxide scale and causes compression in the scale. Finally, during the cooling process, the

mismatch of the thermal expansion between the base material and the oxide scale facilitates the exfoliation or cracks of the alumina scale. According to the measurements of the linear thermal expansion of HEA alloys (see Fig. 4-23), the thermal expansion coefficient of HEA samples is in the range of $25*10^{-6}$ K^{-1} at 25-1000 °C, while the thermal expansion coefficient of α-Al_2O_3 is between $6*10^{-6}$ and $10*10^{-6}$ K^{-1} [277]. The mismatch of thermal expansion between the alloy matrix and the oxide scale results in the deformation and even scale exfoliation during the cooling.

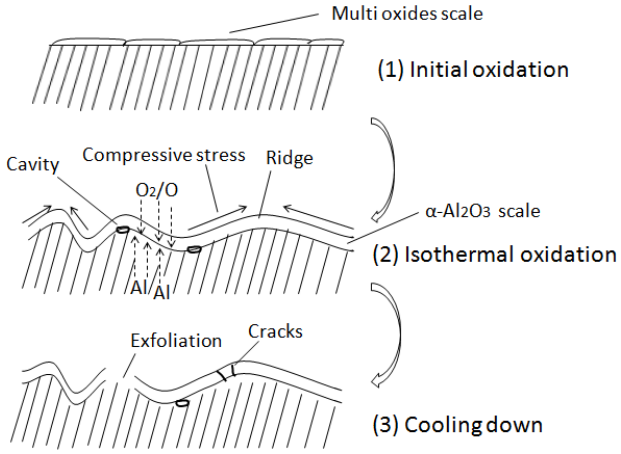

Fig. 7-13 Schematic process of α-Al_2O_3 scale formation and scale degradation of alumina forming alloys exposed to steam environments at 1200 °C.

Adding yttrium not only improves the scale adherence of α-Al_2O_3 scale but also inhibits the wrinkle formations, which are also reported in other literatures [165, 167, 278]. Possible explanations including that yttrium reduces the growth stress, prevents the creep of the scale or retards the lateral growth of the oxide scale seem reasonable. Moreover, the Y-containing alloys are also free of cavities underneath the oxide scale. It is assumed that the yttrium impedes the outward diffusion of cations during oxidation [156, 165]. Sample HEA7 with Nb addition shows a larger deformation of the α-Al_2O_3 scale compared with HEA3 and HEA6, see Fig. 7-8 and Fig. 7-9. This may be related to Laves phases which are thermodynamically stable up to 1600 °C [82]. However, the thin and protective oxide scale with less spallation formed on HEA7 indicates that Nb helps improve the scale adherence and oxidation resistance. Recent studies show that Nb addition in alumina-forming alloys increases the Cr content in austenite and may also reduce the oxygen solubility in the alloy matrix, which is favorable for external alumina scale formation [179, 279].

The duplex structure alloy HEA3, containing the second B2 phase/precipitates, displayed the depletion of B2 phase underneath the oxide scale to a depth of around 15-20 μm. HEA8 alloyed with Ti, which precipitates γ'-Ni_3(Al,Ti) phase in the matrix, shows the depletion of γ'-Ni_3(Al,Ti) phase with a thickness of 30 μm. These results indicate that both B2 and γ'-Ni_3(Al,Ti) phases act as an Al reservoir and aid the formation of alumina scale. However, γ'-Ni_3(Al,Ti) phase not only contains Al but also provides equivalent amount of Ti. The relatively low oxygen partial pressures of Ti oxide

formation, as illustrated by Fig. 2-2, promotes the formation of a TiO_2 oxide layer on the surface of HEA8. Then, the formed TiO_2 scales are less effective to inhibit inward diffusion of oxygen species. The oxygen pressure at the inner part of the TiO_2 layer, which is higher than the oxygen partial pressure of Cr oxide formation, will allow the Cr to be oxidized. Then, the further decreased oxygen partial pressure by the dense Cr_2O_3 scale only allows Al to be internally oxidized. Therefore, at a certain degree, Ti addition degrades the oxidation resistance of the alloys in steam environments.

To conclude, it is recommended to avoid alloying elements as Ti and Mn that competes with Al during the oxidation process in order to promote the formation of external Al_2O_3 scale. The addition of Y and Nb are recommended to improve the adherence of the alumina scale and to mitigate the scale exfoliation, beside the positive effects on the mechanical properties (Nb).

8. Conclusions and outlook

The aim of this thesis was to develop advanced structural materials compatible with liquid Pb and steam at high temperature. Hereby, compatibility comprises two main aspects, (i) corrosion resistance via formation of a protective alumina rich scale in oxygen containing environment and (ii) a FCC alloy matrix stable during exposure to avoid liquid metal embrittlement. The approach taken to achieve these goals is to design alumina-forming model alloys based on two different alloy concepts, austenitic alloys and high entropy alloys, and on the backbone composition of Fe-Ni-Cr-Al. The alumina forming austenitic (AFA) alloys are designed based on the equilibrium phase diagram calculated by Thermo-Calc at 600 °C and Schaeffler diagram at room temperature. The high entropy alloys are designed according to the empirical parameters, namely 15 kJ/mol < ΔH_{mix} < 5 kJ/mol, 1% < δr < 6.6%, Ω >1.1 and VEC >7.5. Both of the design approaches are successfully to predict the phase compositions in AFA and HEA alloys, namely single FCC matrix (AFA, HEA) or FCC matrix plus a second phase (in case of HEA). The annealed AFA and as-cast HEA alloys have shown comparable thermo-physical properties (compared with SS316 steel), excellent corrosion resistance to aggressive environments (e.g. molten Pb, steam), and structural stability after exposure tests at elevated temperature. The designed alloys with the general formula" AFA: Fe-(20-29)Ni-(15.2-16.5)Cr-(2.3-4.3)Al (wt.%); HEA: (30-36)Fe-(30-38)Ni-(20-30)Cr-(3-6)Al-8.5Nb/-4.5 Ti (wt.%)" are able to form a protective oxide scale based on an outer layer of Cr_2O_3 and an inner layer of Cr_2O_3-Al_2O_3 solid solution at the temperature range of 550-600 °C (in oxygen containing Pb), and an external α-Al_2O_3 scale at the temperature of 1200 °C (in steam).

Based on the exposure results of AFA and HEA in oxygen containing molten Pb, a composition map is plotted to show the regions where corrosion resistant alumina-forming alloys (at 550-600 °C), with an austenitic matrix, can be obtained, see Fig. 8-1. Since Ni and Fe have less influence on the oxidation behavior compared with Al and Cr, the composition map is drawn with axes on Al, Cr and (Fe+Ni) concentrations (at.%). The range of Al content of suitable alloys varies from 4-16 at.%, the Cr content varies in 19-30 at.%. Moreover, some of the alloys (AFA, HEA) within the composition map have shown the excellent oxidation resistance to steam at 1200 °C by forming external α-Al_2O_3 scale.

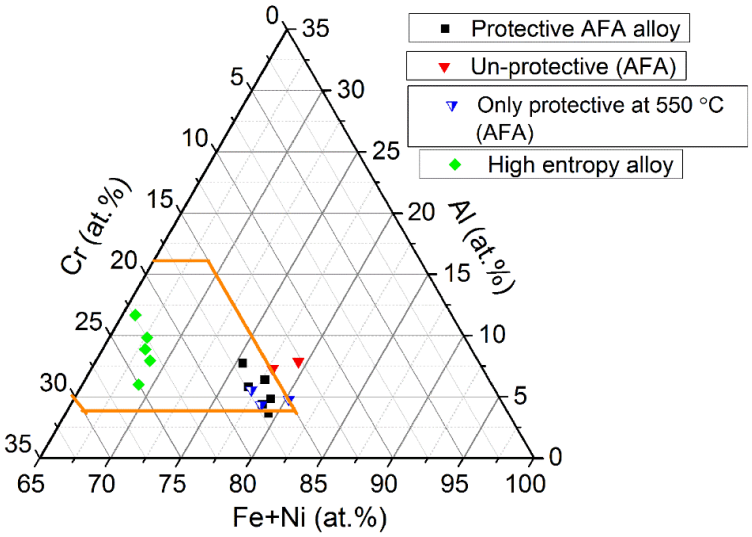

Fig. 8-1 Composition map of corrosion resistant alumina-forming alloys in aggressive environments (10^{-6} wt.% oxygen containing molten Pb at 550-600 °C).

The passivation of the oxide scale on alumina-forming alloys in oxygen containing conditions (molten Pb, steam) is mainly controlled by the oxygen diffusion into the alloy matrix. The mechanism can be explained as the follows: an initial thin oxide scale based on different oxides (e.g. Cr_2O_3, $(Fe,Cr)_3O_4$, TiO_2) forms as a first barrier at the early exposure stage. Then, the diffusion of metallic elements to the alloy surface and the oxygen inward diffusion will be decreased. The oxidation process is mainly controlled by the inward diffusion of oxygen. Due to the reduced oxygen partial pressure at the scale-alloy matrix interface, the alloying elements with low oxygen decompositions partial pressure of their oxides will be selectively oxidized, as e.g. Al. The formation of a dense and continuous alumina-rich oxide scale does significantly mitigate the corrosion/oxidation process by retarding the elemental diffusion process.

Alloying elements like Nb, Ti or Cu are added to act as second strengthening phase formation elements (e.g. Laves, γ' phase) and FCC structure stabilizer (Cu). The addition of different levels of Nb in AFA (1.5 wt.%) and HEA (8.5 wt.%), and Ti (4.5 wt.%) in HEA, have confirmed the formation of Laves and γ' phase in the alloy matrix, which is expected to improve the mechanical performance of candidate alumina-forming alloys. Moreover, the alloys with Nb addition have shown comparable thermo-physical properties with SS316 steel and improved corrosion resistance of HEA alloys in different environments (molten Pb, steam) by promoting the formation of alumina and improving the adherence of α-Al_2O_3 scale (in steam). In case of adding Ti, the HEA alloy has shown the comparable thermo-physical properties, but with degraded oxidation behavior in terms of formation of less protective TiO_2 (compared with alumina) or the structural instability after 1000 h corrosion tests at 550-600 °C. The addition of Cu in HEA stabilizes the FCC matrix by forming single solid solution of the quinary Fe-Ni-Cr-Al-Cu alloy. However, Cu addition negatively impacts the corrosion

behavior by degrading the adherence of the alumina scale to the matrix. The minor addition of yttrium has shown positive effects on the oxide scale adherence, the uniformity of the scale thickness and of the Al and Cr distribution within the oxide scale, when exposed to different oxidizing environments (molten Pb, steam).

During the corrosion tests in molten Pb and steam, a metallic transitional layer have been observed both for AFA and HEA alloys (except HEA1, HEA7, HEA8) after 1000-2000 h exposure to molten Pb at 550-600 °C. A depletion of second phase (e.g. B2, γ' phase) has been observed in some HEA alloys after oxidation test in steam. This is due to the consumption of alloying elements (e.g. Al, Cr, Ti) during the oxidation process. As for the alloy matrix, the designed AFA alloys have shown their promising high temperature phase stability both at the low temperature range of 550-600 °C and at the high temperature of 1200 °C. In case of HEA alloys, the samples with high fraction of B2 or Laves phases (HEA1, HEA2, HEA4, HEA7) show the structural stability during exposure test in low-oxygen containing Pb at 550-600 °C. Samples with low fraction of B2 precipitates or single FCC solid solutions (HEA3, HEA5, HEA6) show precipitates of B2-NiAl phase at the grain boundaries when exposed to low-oxygen containing molten Pb at 550-600 °C, and maintain the structural stability in steam at 1200 °C. The sample HEA8 alloyed with Ti shows phase transformation of FCC phase to brittle sigma phase and γ′ phase to brittle η phase during exposure in low-oxygen containing molten Pb at 550-600 °C.

The model alloys of both AFA and the HEA concept designed within the compositions map (displayed in Fig. 8-1) have shown promising thermo-physical properties, corrosion resistance to different aggressive environments, and short-term structural stability at elevated temperatures. These experimental results represent the first step in the development of advanced alumina forming austenitic steels and high entropy alloys suitable for applications in the temperature range up to 600 °C in Pb and up to 1200 °C in steam. Such conditions are foreseen in Gen IV nuclear reactors, concentrated solar power, and steam reforming.

For further improvement of these alloys, small amounts of additional elements need to be added to the base formula of AFA alloys to further optimize the properties, like stabilizing the austenitic structure (C, Mn, Cu), and improving the mechanical properties (Nb, Ti, W, Mo, B), and increasing the scale adherence (Y). Long-term (>2000 h) corrosion tests of optimized AFA alloys in stagnant and flowing molten Pb conditions have to be performed to investigate the alumina scale durability in extreme conditions. The mechanical properties (e.g. creep resistance, fatigue, strength-ductility) have to be tested in order to understand their high temperature behavior in aggressive conditions. Additionally, the irradiation behavior of AFA alloys is also essential to be

known in case of nuclear applications. First generation AFA alloys will be irradiated in Petten reactor in the frame of the H2020 project GEMMA.

HEA alloys have shown the excellent high temperature corrosion resistance in aggressive environments (molten Pb, steam) and are considered for energy related applications such as GenIV nuclear reactors (cladding tubes and heat exchanger), concentrated solar power (pipes, receiver), methane cracking (vessel), liquid metal batteries (electrode), etc. However, further investigations are suggested in following aspects. The chemical compositions of HEA alloys have to be optimized to improve the mechanical properties, structural stability and corrosion behavior. Mechanical tests of alumina-forming HEA alloys at high temperature are also important. For the structure evaluation, calculations (equilibrium phase diagram or simulation) and high temperature annealing test are to be considered to improve the long-term structural stability. Moreover, the microstructural characterization applying high resolution methods should be considered to better understand the structure-behavior relationship.

References

[1] Global energy statistical yearbook 2019. https://yearbook.enerdata.net/electricity/electricity-domestic-consumption-data.html (retrieved on 15/10/2019).

[2] BP Energy Outlook 2019 edition. https://www.bp.com/content/dam/bp/business-sites/en/global/corporate/pdfs/energy-economics/energy-outlook/bp-energy-outlook-2019.pdf (retrieved on 16/10/2019).

[3] Full report-BP Statistical Review of World Energy 2019. https://www.bp.com/content/dam/bp/business-sites/en/global/corporate/pdfs/energy-econom ics/statistical-review/bp-stats-review-2019-full-report.pdf (retrieved on 16/10/2019).

[4] Wikipedia-renewable energy, https://en.wikipedia.org/wiki/Renewable_energy (retrieved on 3/10/2019).

[5] Eco Friendly Energy, http://www.eco-friendly-emporium.com/eco-friendly-energy.html (retrieved on 16/10/2019)

[6] Abolhosseini, S., Heshmati, A., Altmann, J., A review of renewable energy supply and energy efficiency technologies. Institute for the Study of Labor, Bonn, Discussion Paper, IZA DP No. 8145. 2014.

[7] Pimentel, D., Herz, M., Glickstein, M., Zimmerman, M., Allen, R., Becker, K., Evans, J., Hussain,B. Sarsfeld, R., Grosfeld, A., Seidel, T., Renewable Energy: Current and Potential Issues Renewable energy technologies could, if developed and implemented, provide nearly 50% of US energy needs; this would require about 17% of US land resources, Bioscience. 52 (2002)1111-1120. https://doi.org/10.1641/0006-3568(2002)052[1111:RECAPI]2.0.CO;2

[8] Lund, H., Renewable energy strategies for sustainable development, Energy. 32 (2007) 912-919. https://doi.org/10.1016/j.energy.2006.10.017

[9] Zhang, H., Sun, Y., Wu, L., Zhang, X., Xiang, Y., Tracking mechanism and cosine effect study of Module-Heliostat Solar Collector, In 2016 4th International Conference on Machinery, Materials and Information Technology Applications. Atlantis Press, 2017, published in Advances in Computer Science Research (71), 469-474. https://doi.org/10.2991/icmmita-16.2016.87

[10] Sen, S., Ganguly, S., Opportunities, barriers and issues with renewable energy development–A discussion, Renewable and Sustainable Energy Reviews. 69 (2017) 1170-1181. https://doi.org/10.1016/j.rser.2016.09.137

[11] Chu, S., Majumdar, A., Opportunities and challenges for a sustainable energy future, Nature. 488 (2012) 294. https://doi.org/10.1038/nature11475

[12] Barlev, D., Vidu, R. and Stroeve, P., Innovation in concentrated solar power, Solar Energy Materials and Solar Cells. 95 (2011) 2703-2725. https://doi.org/10.1016/j.solmat.2011.05.020

[13] Zhang, H.L., Baeyens, J., Degrève, J. and Cacères, G., Concentrated solar power plants: Review and design methodology, Renewable and sustainable energy reviews. 22 (2013) 466-481.

https://doi.org/10.1016/j.rser.2013.01.032

[14] Wikipedia-Concentrated solar power. https://en.wikipedia.org/wiki/Concentrated_solar_power (retrieved on 16/10/2019).

[15] Tian, Y., Zhao, C.Y., A review of solar collectors and thermal energy storage in solar thermal applications, Applied Energy. 104 (2013) 538-553. https://doi.org/10.1016/j.apenergy.2012.11.051

[16] Henry, A., Prasher, R., The prospect of high temperature solid state energy conversion to reduce the cost of concentrated solar power, Energy & Environmental Science. 7 (2014) 1819-1828. 10.1039/C4EE00288A

[17] Myers Jr, P.D., Goswami, D.Y., Thermal energy storage using chloride salts and their eutectics, Applied Thermal Engineering. 109 (2016) 889-900. https://doi.org/10.1016/j.applthermaleng.2016.07.046

[18] 2014 SunShot Initiative Portfolio Book (Solar Energy Technologies Office, U.S. Department of Energy),https://www.energy.gov/sites/prod/files/2014/08/f18/2014_SunShot_Initiative_Portfolio8.13.14.pdf (retrieved on 16/10/2019).

[19] Friedman, S.M., Three Mile Island, Chernobyl, and Fukushima: An analysis of traditional and new media coverage of nuclear accidents and radiation, Bulletin of the atomic scientists. 67 (2011) 55-65. https://doi.org/10.1177/0096340211421587

[20] IAEA, Accident Tolerant Fuel Concepts for Light Water Reactors, Proceedings of a Technical Meeting held at Oak Ridge National Laboratories, United States of America. 2014, Vienna, IAEA TECDOC No. 1797, ISBN 978-92-0-105216-2.

[21] Zinkle, S.J., Ghoniem, N.M., Prospects for accelerated development of high performance structural materials, Journal of Nuclear Materials. 417(2011) 2-8. https://doi.org/10.1016/j.jnucmat.2011.05.021

[22] Terrani, K.A., Zinkle, S.J., Snead, L.L., Advanced oxidation-resistant iron-based alloys for LWR fuel cladding, Journal of Nuclear Materials. 448(2014) 420-435. https://doi.org/10.1016/j.jnucmat.2013.06.041

[23] Overview of Generation IV (Gen IV) Reactor Designs, Safety and Radiological Protection considerations, 2012, IRSN 2012/158. https://www.irsn.fr/EN/Research/publications-documentation/Scientific-books/Documents/GENIV_texte_VA_241012a.pdf (retrieved on 16/10/2019).

[24] Locatelli, G., Mancini, M., Todeschini, N., Generation IV nuclear reactors: Current status and future prospects, Energy Policy. 61 (2013) 1503-1520. https://doi.org/10.1016/j.enpol.2013.06.101

[25] Yildiz, B., Kazimi, M.S., Efficiency of hydrogen production systems using alternative nuclear energy technologies, International Journal of Hydrogen Energy. 31(2006) 77-92. https://doi.org/10.1016/j.ijhydene.2005.02.009

[26] Verfondern, K. ed., Nuclear energy for hydrogen production, ForschungszentrumJülich, Energy Technology. Vol. 58, 2007, ISBN 978-3-89336-468-8.

[27] Su'ud, Z., Sekimoto, H., Design and safety aspect of lead and lead-bismuth cooled long-life small safe fast reactors for various fore configurations, Journal of Nuclear Science and Technology. 32 (1995) 834-845. https://doi.org/10.1080/18811248.1995.9731785

[28] US DoE nuclear energy research advisory committee, A technology roadmap for generation IV nuclear energy systems. 2002, Report No GIF-002-00. https://www.gen-4.org/gif/upload/docs/application/pdf/2013-09/genivroadmap2002.pdf (retrieved on 15/10/2019).

[29] Fazio, C., Sobolev, V.P., Aerts, A., Gavrilov, S., Lambrinou, K., Schuurmans, P., Gessi, A., Agostini, P., Ciampichetti, A., Martinelli, L., Gosse, S., Handbook on lead-bismuth eutectic alloy and lead properties, materials compatibility, thermal-hydraulics and technologies-2015 edition (No. NEA--7268). Organisation for Economic Co-Operation and Development. 2015.

[30] Kim, H., Boysen, D.A., Newhouse, J.M., Spatocco, B.L., Chung, B., Burke, P.J., Bradwell, D.J., Jiang, K., Tomaszowska, A.A., Wang, K., Wei, W., Liquid metal batteries: past, present, and future, Chemical reviews. 113 (2012) 2075-2099. https://doi.org/10.1021/cr300205k

[31] Mansani, L., Artioli, C., Schikorr, M., Rimpault, G., Angulo, C. and Bruyn, D.D., The European Lead-Cooled EFIT Plant: An Industrial-Scale Accelerator-Driven System for Minor Actinide Transmutation—I, Nuclear Technology. 180 (2012) 241-263.https://doi.org/10.13182/NT11-96

[32] Walczak, M., Pineda, F., Fernández, Á.G., Mata-Torres, C., Escobar, R.A., Materials corrosion for thermal energy storage systems in concentrated solar power plants, Renewable and Sustainable Energy Reviews. 86 (2018) 22-44. https://doi.org/10.1016/j.rser.2018.01.010

[33] Sarvghad, M., Maher, S.D., Collard, D., Tassan, M., Will, G., Steinberg, T.A., Materials compatibility for the next generation of Concentrated Solar Power plants, Energy Storage Materials. 14 (2018) 179-198. https://doi.org/10.1016/j.ensm.2018.02.023

[34] J.D. Osorio, R. Hovsapian, J.C. Ordonez, Effect of multi-tank thermal energy storage, recuperator effectiveness, and solar receiver conductance on the performance of a concentrated solar supercritical CO_2-based power plant operating under different seasonal conditions, Energy. 115 (2016) 353–368. https://doi.org/10.1016/j.energy.2016.08.074

[35] Dongke Zhang, Ultra-Supercritical Coal Power Plants, Materials, Technologies and Optimisation, Woodhead Publishing Series in Energy. 2013 ISBN 978-0-85709-116-1.

[36] F. Roelofs, B. de Jager, A. Class, H. Jeanmart, P. Schuurmans, A. Ciampichetti, G. Gerbeth, R. Stieglitz, C. Fazio, European research on HLM thermal hydraulics for ADS applications, Journal of Nuclear Materials. 376 (2008) 401–404. https://doi.org/10.1016/j.jnucmat.2008.02.014

[37] L. Mansani, C. Artioli, M. Schikorr, G. Rimpault, C. Angulo, D. De Bruyn, The European Lead-Cooled EFIT Plant: An Industrial-Scale Accelerator-Driven System for Minor Actinide Transmutation, Nuclear Technology. 180 (2012) 241-263, ISSN 0029-5450.

[38] C. D. Bowman, E.D. Arthur, P.W. Lisowski, G.P. Lawrence, et al.: Nuclear energy generation and waste transmutation using an accelerator-driven intense thermal neutron source, Nuclear Instruments and Methods A. 320 (1992) 336–367. https://doi.org/10.1016/0168-9002(92)90795-6

[39] V. Coen, Lithium-lead eutectic as breeding material in fusion reactors, Journal of Nuclear Materials. 133-134, (1995) 46-51. https://doi.org/10.1016/0022-3115(85)90110-2

[40] D. Frazer, E. Stergar, C. Cionea, P Hosemann, Liquid metal as heat transport fluid for thermal solar power applications, Energy Procedia. 49 (2014) 627-636. https://doi.org/10.1016/j.egypro.2014.03.068

[41] J. Pacio, T. Wetzel, Assessment of liquid metal technology status and research paths for their use as efficient heat transfer fluids in solar central receiver systems, Solar Energy. 93 (2013) 11–22. https://doi.org/10.1016/j.solener.2013.03.025

[42] M. Serban, M. A. Lewis, Ch. L. Marshall, R. D. Doctor, Hydrogen production by direct contact pyrolysis of natural gas, Energy&Fuels. 17 (2003) 705-713.https://doi.org/10.1021/ef020271q

[43] A. Abánades, R. K. Rathnam, T. Geissler, A. Heinzel, K. Mehravaran, G. Müller, M. Plevan, C. Rubbia, D. Salmieri, L. Stoppel, S. Stückrad, A. Weisenburger, H. Wenninger, T. Wetzel, Development of methane decarbonisation based on liquid metal technology for CO_2-free production of hydrogen, International Journal of Hydrogen Energy. 41 (2016) 8159–8167. https://doi.org/10.1016/j.ijhydene.2015.11.164

[44] Murty, K.L., Charit, I., Structural materials for Gen-IV nuclear reactors: Challenges and opportunities, Journal of Nuclear Materials. 383 (2008) 189-195. ttps://doi.org/10.1016/j.jnucmat.2008.08.044

[45] Vignarooban, K., Xu, X., Arvay, A., Hsu, K., Kannan, A.M., Heat transfer fluids for concentrating solar power systems–a review, Applied Energy. 146 (2015) 383-396. https://doi.org/10.1016/j.apenergy.2015.01.125

[46] Bonk, A., Sau, S., Uranga, N., Hernaiz, M., Bauer, T., Advanced heat transfer fluids for direct molten salt line-focusing CSP plants, Progress in Energy and Combustion Science. 67 (2018) 69-87. https://doi.org/10.1016/j.pecs.2018.02.002

[47] González-Roubaud, E., Pérez-Osorio, D., Prieto, C., Review of commercial thermal energy storage in concentrated solar power plants: Steam vs. molten salts, Renewable and Sustainable Energy Reviews. 80 (2017) 133-148. https://doi.org/10.1016/j.rser.2017.05.084

[48] Ahn, Y., Bae, S.J., Kim, M., Cho, S.K., Baik, S., Lee, J.I., Cha, J.E., Review of supercritical CO2 power cycle technology and current status of research and development, Nuclear Engineering and Technology. 47 (2015) 647-661. https://doi.org/10.1016/j.net.2015.06.009

[49] Heinzel, A., Hering, W., Konys, J., Marocco, L., Litfin, K., Müller, G., Pacio, J., Schroer, C., Stieglitz, R., Stoppel, L., Weisenburger, A., Liquid Metals as Efficient High-Temperature Heat-Transport Fluids, Energy Technology. 5 (2017) 1026-1036. https://doi.org/10.1002/ente.201600721

[50] Herring, J.S., O'Brien, J.E., Stoots, C.M., Hawkes, G.L., Hartvigsen, J.J., Shahnam, M., Progress in high-temperature electrolysis for hydrogen production using planar SOFC technology, International Journal of Hydrogen Energy. 32 (2007) 440-450. https://doi.org/10.1016/j.ijhydene.2006.06.061

[51] Gunarathne, D.S., Mellin, P., Yang, W., Pettersson, M., Ljunggren, R., Performance of an effectively integrated biomass multi-stage gasification system and a steel industry heat treatment furnace, Applied Energy. 170 (2016) 353-361. ttps://doi.org/10.1016/j.apenergy.2016.03.003

[52] Nipattummakul, N., Ahmed, I., Kerdsuwan, S., Gupta, A.K., High temperature steam gasification of wastewater sludge, Applied Energy. 87 (2010) 3729-3734. https://doi.org/10.1016/j.apenergy.2010.07.001

[53] Bruni, G., Rizzello, C., Santucci, A., Alique, D., Incelli, M., Tosti, S., On the energy efficiency of hydrogen production processes via steam reforming using membrane reactors, International Journal of Hydrogen Energy. 44 (2019) 988-999. https://doi.org/10.1016/j.ijhydene.2018.11.095

[54] Wright, I.G., Dooley, R.B., A review of the oxidation behavior of structural alloys in steam, International Materials Reviews. 55(2010) 129-167. https://doi.org/10.1179/095066010X12646898728165

[55] Solar thermal power plants to become practice. http://www.bine.info/fileadmin/content/Publikationen/Englische_Infos/projekt_0708_engl_Internetx.pdf (retrieved on 14/8/2019).

[56] Specific heat Capacities of Air. https://www.ohio.edu/mechanical/thermo/property_tables/air/air_cp_cv.html (retrieved on 14/8/2019)

[57] Fujikawa, S., Hayashi, H., Nakazawa, T., Kawasaki, K., Iyoku, T., Nakagawa, S., Sakaba, N., Achievement of reactor-outlet coolant temperature of 950° C in HTTR, Journal of Nuclear Science and Technology. 41 (2004) 1245-1254. https://doi.org/10.1080/18811248.2004.9726354

[58] Petersen, H., The properties of helium: density, specific heat capacitys, viscosity, and thermal conductivity at pressures from 1 to 100 bar and from room temperature to about 1800 K. 1970. Roskilde, Denmark: Risø National Laboratory. Denmark. Forskningscenter Risoe. Risoe-R, No. 224.

[59] Methnani, M., Stanculescu, A., Status of high temperature gas-cooled reactor technology, In First Information Exchange Meeting on Basic Studies in the Field of High Temperature Engineering, IAEA Gas-Cooled Reactor Technical Working Group, 1999, Paris. https://www.oecd-nea.org/science/docs/pubs/hightemp.pdf (retrieved on 16/10/2019).

[60] Beiser, Arthur. Applied physics, Schaum's outline series, 2004, McGraw-Hill, ISBN 9780071426114, United States.

[61] Shell thermia B, Shell Heat Transfer Oil S2, Technical data sheet, August 2010, Classified as ISO 6743-12 Family Q. http://epoxyoil.com/downloads/shell_heat-transfer-oil.pdf (retrieved on 15/10/2019).

[62] Thurnay, Kalman. Thermophysical properties of sodium in the liquid and gaseous states. No. KFK—2863, 1981, Kernforschungszentrum Karlsruhe GmbH, Germany.

[63] Sobolev, V., Database of thermophysical properties of liquid metal coolants for GEN-IV, 2011, scientific Report SCIENTIFIC REPORT SCK•CEN-BLG-1069, Mol Belgium, ISSN 1379-2407.

[64] Sobolev, V.P., Schuurmans, P., Benamati, G., Thermodynamic properties and equation of state of liquid lead and lead–bismuth eutectic, Journal of Nuclear Materials. 376 (2008) 358-362. https://doi.org/10.1016/j.jnucmat.2008.02.030

[65] Liu, M., Saman, W., Bruno, F., Review on storage materials and thermal performance enhancement techniques for high temperature phase change thermal storage systems, Renewable and Sustainable Energy Reviews. 16 (2012) 2118-2132. https://doi.org/10.1016/j.rser.2012.01.020

[66] Ding, W., Shi, H., Xiu, Y., Bonk, A., Weisenburger, A., Jianu, A., Bauer, T., Hot corrosion behavior of commercial alloys in thermal energy storage material of molten MgCl2/KCl/NaCl under inert atmosphere, Solar Energy Materials and Solar Cells. 184 (2018) 22-30. https://doi.org/10.1016/j.solmat.2018.04.025

[67] Asher, R.C., Davies, D., Beetham, S.A., Some observations on the compatibility of structural materials with molten lead, Corrosion Science. 17 (1977) 545-557. https://doi.org/10.1016/S0010-938X(77)80001-2

[68] Jianu, A., Müller, G., Weisenburger, A., Heinzel, A., Fazio, C., Markov, V.G., Kashtanov, A.D., Creep-to-rupture tests of T91 steel in flowing Pb–Bi eutectic melt at 550 C, Journal of Nuclear Materials. 394 (2009) 102-108. https://doi.org/10.1016/j.jnucmat.2009.08.013

[69] Weisenburger, A., Schroer, C., Jianu, A., Heinzel, A., Konys, J., Steiner, H., Müller, G., Fazio, C., Gessi, A., Babayan, S., Kobzova, A., Long term corrosion on T91 and AISI1 316L steel in flowing lead alloy and corrosion protection barrier development: Experiments and models, Journal of Nuclear Materials. 415 (2011) 260-269. https://doi.org/10.1016/j.jnucmat.2011.04.028

[70] Shi, H., Jianu, A., Weisenburger A., Tang C.C., Fetzer R., Heinzel A., Lang F., Stieglitz R., Mueller G., Corrosion resistance and microstructural stability of austenitic Fe-Cr-Al-Ni model alloys exposed to oxygen-containing molten lead, Journal of Nuclear Materials. 524 (2019) 177-190. https://doi.org/10.1016/j.jnucmat.2019.06.043

[71] Weeks, J. R. Corrosion of steam generator tubing in operating pressurized water reactors (No. BNL-19158; CONF-741013-2), 1974, USAEC Directorate of Licensing, Washington, DC.

[72] Müller, G., Schumacher, G., Zimmermann, F., Investigation on oxygen controlled liquid lead corrosion of surface treated steels, Journal of Nuclear Materials. 278 (2000) 85-95. https://doi.org/10.1016/S0022-3115(99)00211-1

[73] Bischoff, J., Motta, A.T., Eichfeld, C., Comstock, R.J., Cao, G., Allen, T.R., Corrosion of ferritic–martensitic steels in steam and supercritical water, Journal of Nuclear Materials. 441 (2013) 604-611. https://doi.org/10.1016/j.jnucmat.2012.09.037

[74] Wallwork, G.R., The oxidation of alloys, Reports on Progress in Physics. 39 (1976) 401. https://doi.org/10.1088/0034-4885/39/5/001

[75] Brumm, M.W., Grabke, H.J., The oxidation behavior of NiAl-I. Phase transformations in the alumina scale during oxidation of NiAl and NiAl-Cr alloys, Corrosion Science. 33 (1992) 1677-1690. https://doi.org/10.1016/0010-938X(92)90002-K

[76] Quadakkers, W.J., Bennett, M.J., Oxidation induced lifetime limits of thin walled, iron based, alumina forming, oxide dispersion strengthened alloy components, Materials Science and Technology. 10 (1994) 126-131. https://doi.org/10.1179/mst.1994.10.2.126

[77] Yang, Z.G., Paxton, D.M., Weil, K.S., Stevenson, J.W., Singh, P., Materials properties database for selection of high-temperature alloys and concepts of alloy design for SOFC applications (No. PNNL-14116), Pacific Northwest National Lab. (PNNL), Richland, WA (United States). 2002. 10.2172/15010553

[78] Grabke, H.J., Oxidation of NiAl and FeAl, Intermetallics. 7 (1999) 1153-1158. https://doi.org/10.1016/S0966-9795(99)00037-0

[79] Stallybrass, C., Sauthoff, G., Ferritic Fe–Al–Ni–Cr alloys with coherent precipitates for high-temperature applications, Materials Science and Engineering: A. 387 (2004) 985-990. https://doi.org/10.1016/j.msea.2004.01.108

[80] Stallybrass, C., Schneider, A., Sauthoff, G., The strengthening effect of (Ni, Fe) Al precipitates on the mechanical properties at high temperatures of ferritic Fe–Al–Ni–Cr alloys, Intermetallics. 13 (2005) 1263-1268. https://doi.org/10.1016/j.intermet.2004.07.048

[81] Yamamoto, Y., Brady, M. P., Lu, Z. P., Maziasz, P. J., Liu, C. T., Pint, B. A., More, K.L., Meyer, H.M., Payzant, E. A, Creep-resistant, Al2O3-forming austenitic stainless steels, Science. 316 (2007) 433-436. https://doi.org/10.1126/science.1137711

[82] Yamamoto, Y., Brady, M.P., Lu, Z.P., Liu, C.T., Takeyama, M., Maziasz, P.J., Pint, B.A., Alumina-forming austenitic stainless steels strengthened by laves phase and MC carbide precipitates, Metallurgical and Materials Transactions A. 38 (2007) 2737-2746. https://doi.org/10.1007/s11661-010-0295-2

[83] Deodeshmukh, V.P., Matthews, S.J., Klarstrom, D.L., High-temperature oxidation performance of a new alumina-forming Ni–Fe–Cr–Al alloy in flowing air, International Journal of Hydrogen Energy. 36 (2011) 4580-4587. https://doi.org/10.1016/j.ijhydene.2010.04.099

[84] Pint, B.A., The future of alumina-forming alloys: challenges and applications for power generation, In Materials Science Forum, Trans Tech Publications. 696 (2011) 57-62. https://doi.org/10.4028/www.scientific.net/MSF.696.57

[85] Weisenburger, A., Jianu, A., Doyle, S., Bruns, M., Fetzer, R., Heinzel, A., DelGiacco, M., An, W., Müller, G., Oxide scales formed on Fe–Cr–Al-based model alloys exposed to oxygen containing

molten lead, Journal of Nuclear Materials. 437 (2013) 282-292. https://doi.org/10.1016/j.jnucmat.2013.02.044

[86] Pint, B. A., Unocic, K. A., Terrani, K. A, Effect of steam on high temperature oxidation behavior of alumina-forming alloys, Materials at High Temperatures. 32 (2015) 28-35. https://doi.org/10.1179/0960340914Z.00000000058

[87] Chyrkin, A., Pillai, R., Galiullin, T., Wessel, E., Grüner, D., Quadakkers, W.J., External α-Al2O3 scale on Ni-base alloy 602 CA.–Part I: Formation and long-term stability, Corrosion Science. 124 (2017) 138-149. https://doi.org/10.1016/j.corsci.2017.05.017

[88] Rebak, R. B., Gupta, V. K., Larsen, M., Oxidation Characteristics of Two FeCrAl Alloys in Air and Steam from 800° C to 1300° C, The Journal of The Minerals, Metals & Materials Society (TMS). 70 (2018) 1484-1492. https://doi.org/10.1007/s11837-018-2979-9

[89] Warke, W.R., Johnson, K.L., Breyer, N.N., Liquid metal embrittlement of steel by lead and lead alloys, In Corrosion by Liquid Metals. Springer, Boston, MA. 1970. 417-439. https://doi.org/10.1007/978-1-4684-1845-3_23

[90] Van den Bosch, J., Bosch, R.W., Sapundjiev, D., Almazouzi, A., Liquid metal embrittlement susceptibility of ferritic–martensitic steel in liquid lead alloys, Journal of Nuclear Materials. 376 (2008) 322-329. https://doi.org/10.1016/j.jnucmat.2008.02.008

[91] Kobayashi, S., Takasugi, T., Mapping of 475 C embrittlement in ferritic Fe–Cr–Al alloys, Scripta Materialia. 63 (2010) 1104-1107. https://doi.org/10.1016/j.scriptamat.2010.08.015

[92]Yeh, J.W., Chen, S.K., Lin, S.J., Gan, J.Y., Chin, T.S., Shun, T.T., Tsau, C.H., Chang, S.Y., Nanostructured high-entropy alloys with multiple principal elements: novel alloy design concepts and outcomes, Advanced Engineering Materials. 6 (2004) 299-303. https://doi.org/10.1002/adem.200300567

[93] Cantor, B., Chang, I.T.H., Knight, P., Vincent, A.J.B., Microstructural development in equiatomic multicomponent alloys, Materials Science and Engineering: A. 375 (2004) 213-218. https://doi.org/10.1016/j.msea.2003.10.257

[94] Otto, F., Dlouhý, A., Somsen, C., Bei, H., Eggeler, G., George, E.P., The influences of temperature and microstructure on the tensile properties of a CoCrFeMnNi high-entropy alloy, Acta Materialia. 61 (2013) 5743-5755. https://doi.org/10.1016/j.actamat.2013.06.018

[95] Gludovatz, B., Hohenwarter, A., Catoor, D., Chang, E.H., George, E.P., Ritchie, R.O., A fracture-resistant high-entropy alloy for cryogenic applications, Science. 345 (2014) 1153-1158. https://doi.org/10.1126/science.1254581

[96] Xia, S., Gao, M.C., Yang, T., Liaw, P.K. and Zhang, Y., Phase stability and microstructures of high entropy alloys ion irradiated to high doses. Journal of Nuclear Materials, 480 (2016) 100-108. https://doi.org/10.1016/j.jnucmat.2016.08.017

[97] Miracle, D. B. Critical assessment 14: High entropy alloys and their development as structural materials, Materials Science and Technology. 31 (2015) 1142-1147. https://doi.org/10.1179/1743284714Y.0000000749

[98] Li, Z., Pradeep, K.G., Deng, Y., Raabe, D., Tasan, C.C., Metastable high-entropy dual-phase alloys overcome the strength-ductility trade-off, Nature. 534 (2016) 227. https://doi.org/10.1038/nature17981

[99] Praveen, S., Kim, H.S., High-Entropy Alloys: Potential Candidates for High-Temperature Applications-An Overview, Advanced Engineering Materials. 20 (2018) 1700645. https://doi.org/10.1002/adem.201700645

[100] Ilinčev, G., Research results on the corrosion effects of liquid heavy metals Pb, Bi and Pb–Bi on structural materials with and without corrosion inhibitors, Nuclear Engineering and Design. 217 (2002) 167-177. https://doi.org/10.1016/S0029-5493(02)00158-9

[101] Weeks, J.R., LEAD, BISMUTH, TIN, AND THEIR ALLOYS AS NUCLEAR COOLANTS, Brookhaven National Lab., Upton, NY. 1971. https://doi.org/10.1016/0029-5493(71)90075-6

[102] O.Madelung (Ed.), Landolt–Bornstein New Series IV, 5 (1995), Springer, Berlin.

[103] Ballinger, R.G., Lim, J., An overview of corrosion issues for the design and operation of high-temperature lead-and lead-bismuth-cooled reactor systems, Nuclear Technology. 147 (2004) 418-435. https://doi.org/10.13182/NT04-A3540

[104] Zhang, J., Li, N., Review of the studies on fundamental issues in LBE corrosion, Journal of Nuclear Materials. 373 (2008) 351-377. https://doi.org/10.1016/j.jnucmat.2007.06.019

[105] Hojna, A., Di Gabriele, F., Klecka, J., Characteristics and Liquid Metal Embrittlement of the steel T91 in contact with Lead–Bismuth Eutectic, Journal of Nuclear Materials. 472 (2016) 163-170. https://doi.org/10.1016/j.jnucmat.2015.08.048

[106] Weisenburger, A., Heinzel, A., Müller, G., Muscher, H., Rousanov, A., T91 cladding tubes with and without modified FeCrAlY coatings exposed in LBE at different flow, stress and temperature conditions, Journal of Nuclear Materials. 376 (2008) 274-281. ttps://doi.org/10.1016/j.jnucmat.2008.02.026

[107] Kondo, M., Takahashi, M., Suzuki, T., Ishikawa, K., Hata, K., Qiu, S., Sekimoto, H., Metallurgical study on erosion and corrosion behaviors of steels exposed to liquid lead–bismuth flow, Journal of Nuclear materials. 343 (2005) 349-359. https://doi.org/10.1016/j.jnucmat.2004.08.037

[108] Kondo, M., Takahashi, M., Sawada, N. and Hata, K., Corrosion of steels in lead-bismuth flow, Journal of Nuclear Science and Technology. 43 (2006) 107-116.

[109] Müller, G., Heinzel, A., Konys, J., Schumacher, G., Weisenburger, A., Zimmermann, F., Engelko, V., Rusanov, A., Markov, V., Behavior of steels in flowing liquid PbBi eutectic alloy at 420–600 C after 4000–7200 h, Journal of Nuclear Materials. 335 (2004) 163-168. https://doi.org/10.1016/j.jnucmat.2004.07.010

[110] Müller, G., Heinzel, A., Schumacher, G., Weisenburger, A., Control of oxygen concentration in liquid lead and lead–bismuth, Journal of Nuclear Materials. 321 (2003) 256-262. https://doi.org/10.1016/S0022-3115(03)00250-2

[111] Li, N., Active control of oxygen in molten lead–bismuth eutectic systems to prevent steel corrosion and coolant contamination, Journal of Nuclear Materials. 300 (2002) 73-81. https://doi.org/10.1016/S0022-3115(01)00713-9

[112] Martinelli, L., Dufrenoy, T., Jaakou, K., Rusanov, A., Balbaud-Célérier, F., High temperature oxidation of Fe–9Cr–1Mo steel in stagnant liquid lead–bismuth at several temperatures and for different lead contents in the liquid alloy, Journal of Nuclear Materials. 376 (2008) 282-288. https://doi.org/10.1016/j.jnucmat.2008.02.006

[113] Kikuchi, K., Kamata, K., Ono, M., Kitano, T., Hayashi, K., Oigawa, H., Corrosion rate of parent and weld materials of F82H and JPCA steels under LBE flow with active oxygen control at 450 and 500° C, Journal of Nuclear Materials. 377 (2008) 232-242. https://doi.org/10.1016/j.jnucmat.2008.02.047

[114] Martinelli, L., Balbaud-Célérier, F., Modelling of the oxide scale formation on Fe-Cr steel during exposure in liquid lead-bismuth eutectic in the 450–600 °C temperature range, Materials and Corrosion. 62 (2011) 531-542. https://doi.org/10.1002/maco.201005871

[115] Roy, M., Martinelli, L., Ginestar, K., Favergeon, J., Moulin, G., Dissolution and oxidation behavior of various austenitic steels and Ni rich alloys in lead-bismuth eutectic at 520 °C, Journal of Nuclear Materials. 468 (2016) 153-163. https://doi.org/10.1016/j.jnucmat.2015.11.005

[116] Schroer, C., Wedemeyer, O., Novotny, J., Skrypnik, A., Konys, J., Selective leaching of nickel and chromium from Type 316 austenitic steel in oxygen-containing lead–bismuth eutectic (LBE), Corrosion Science. 84 (2014) 113-124. https://doi.org/10.1016/j.corsci.2014.03.016

[117] Tsisar, V., Schroer, C., Wedemeyer, O., Skrypnik, A., Konys, J., Long-term corrosion of austenitic steels in flowing LBE at 400 °C and 10^{-7} mass% dissolved oxygen in comparison with 450 and 550 °C, Journal of Nuclear Materials. 468 (2016) 305-312. https://doi.org/10.1016/j.jnucmat.2015.09.027

[118] Schroer, C., Voß, Z., Wedemeyer, O., Novotny, J., Konys, J., Oxidation of steel T91 in flowing lead–bismuth eutectic (LBE) at 550 °C, Journal of Nuclear Materials. 356 (2006) 189-197. https://doi.org/10.1016/j.jnucmat.2006.05.009

[119] Birks, N., Meier, G.H., Pettit, F.S., Introduction to the high temperature oxidation of metals, 2006, Cambridge University Press. 2nd edition, ISBN- 9780521480420.

[120] Purgert, R., Phillips, J., Hendrix, H., Shingledecker, J., & Tanzosh, J. Materials for Advanced Ultra-supercritical (A-USC) Steam Turbines–A-USC Component Demonstration, 2016, Energy Industries Of Ohio Inc., Independence, OH (United States), DOI: 10.2172/1332274.

[121] Dudziak, T, Steam Oxidation of Fe-Based Materials, In High Temperature Corrosion. IntechOpen, 2016, Online ISBN 978-953-51-2508-2. http://dx.doi.org/10.5772 /62935

[122] Quadakkers, W.J., Ennis, P.J., Zurek, J., Michalik, M., Steam oxidation of ferritic steels–laboratory test kinetic data, Materials at high temperatures. 22 (2005) 47-60. https://doi.org/10.1179/mht.2005.006

[123] Wright, I.G., Howe, J.Y., Sabau, A.S., Morphological evolution of oxide scales grown on ferritic steels in steam, Materials at High Temperatures. 26 (2009) 105-111. https://doi.org/10.3184/096034009X464348

[124] Pint, B.A., Terrani, K.A., Brady, M.P., Cheng, T., Keiser, J.R., High temperature oxidation of fuel cladding candidate materials in steam–hydrogen environments, Journal of Nuclear Materials. 440 (2013) 420-427. https://doi.org/10.1016/j.jnucmat.2013.05.047

[125] Jiang, D., Xu, H., Deng, B., Li, M., Xiao, Z., Zhang, N., Effect of oxygenated treatment on corrosion of the whole steam–water system in supercritical power plant, Applied Thermal Engineering. 93 (2016) 1248-1253. https://doi.org/10.1016/j.applthermaleng.2015.10.098

[126] Garcia-Fresnillo, L., Chyrkin, A., Böhme, C., Barnikel, J., Schmitz, F., Quadakkers, W.J., Oxidation behavior and microstructural stability of alloy 625 during long-term exposure in steam, Journal of Materials Science. 49 (2014) 6127-6142. https://doi.org/10.1007/s10853-014-8344-7

[127] Yamamoto, Y., Pint, B.A., Terrani, K.A., Field, K.G., Yang, Y., Snead, L.L., Development and property evaluation of nuclear grade wrought FeCrAl fuel cladding for light water reactors, Journal of Nuclear Materials. 467 (2015) 703-716. https://doi.org/10.1016/j.jnucmat.2015.10.019

[128] Pint, B. A., Unocic, K. A., Terrani, K. A, Effect of steam on high temperature oxidation behavior of alumina-forming alloys, Materials at High Temperatures. 32 (2015) 28-35. https://doi.org/10.1179/0960340914Z.00000000058

[129] Rebak, R. B., Gupta, V. K., Larsen, M. Oxidation Characteristics of Two FeCrAl Alloys in Air and Steam from 800 °C to 1300 °C, The Journal of The Minerals, Metals & Materials Society (TMS). 70 (2018) 1484-1492. https://doi.org/10.1007/s11837-018-2979-9

[130] Tang, C., Jianu, A., Steinbrueck, M., Grosse, M., Weisenburger, A., Seifert, H.J., Influence of composition and heating schedules on compatibility of FeCrAl alloys with high-temperature steam, Journal of Nuclear Materials. 511 (2018) 496-507. https://doi.org/10.1016/j.jnucmat.2018.09.026

[131] Terrani, K.A., Pint, B.A., Kim, Y.J., Unocic, K.A., Yang, Y., Silva, C.M., Meyer III, H.M., Rebak, R.B., Uniform corrosion of FeCrAl alloys in LWR coolant environments, Journal of Nuclear Materials. 479 (2016) 36-47. https://doi.org/10.1016/j.jnucmat.2016.06.047

[132] Pint, B.A., Steam Oxidation Testing in the Severe Accident Test Station (No. RNL/LTR-2017/368). Oak Ridge National Lab (ORNL), Oak Ridge, TN (United States). 2017. DOI: 10.2172/1324197

[133] Moon, J., Kim, S., Park, W.D., Kim, T.Y., McAlpine, S.W., Short, M.P., Kim, J.H., Bahn, C.B., Initial oxidation behavior of Fe-Cr-Si alloys in 1200 °C steam, Journal of Nuclear Materials. 513 (2019) 297-308. https://doi.org/10.1016/j.jnucmat.2018.10.010

[134] A. Zahs, M. Spiegel, H. J. Grabke, Chloridation and oxidation of iron, chromium, nickel and their alloys in chloridizing and oxidizing atmospheres at 400–700 °C, Corrosion Science. 42 (2000) 1093-1122. https://doi.org/10.1016/S0010-938X(99)00142-0

[135] Fry, A., Osgerby, S., Wright, M. Oxidation of alloys in steam environments: A review. NPL Report MATC (A) 90, ISSN 1473-2734, 2002.

[136] Y. S. Li, Y. Niu, M. Spiegel, High temperature interaction of Al/Si-modified Fe–Cr alloys with KCl, Corrosion Science. 49 (2007) 1799-1815. https://doi.org/10.1016/j.corsci.2006.10.019

[137] He, L. F., Roman, P., Leng, B., Sridharan, K., Anderson, M., Allen, T. R., Corrosion behavior of an alumina forming austenitic steel exposed to supercritical carbon dioxide, Corrosion Science. 82 (2014) 67-76. https://doi.org/10.1016/j.corsci.2013.12.023

[138] Jianu, A., Fetzer, R., Weisenburger, A., Doyle, S., Bruns, M., Heinzel, A., Hosemann, P., Mueller, G., Stability domain of alumina thermally grown on Fe–Cr–Al-based model alloys and modified surface layers exposed to oxygen-containing molten Pb, Journal of Nuclear Materials. 470 (2016) 68-75. https://doi.org/10.1016/j.jnucmat.2015.12.009

[139] J. C. Gomez-Vidal, A. G. Fernandez, R. Tirawat, C. Turchi and W. Huddleston, Corrosion resistance of alumina-forming alloys against molten chlorides for energy production. I: Pre-oxidation treatment and isothermal corrosion tests, Solar Energy Materials and Solar Cells. 166 (2017) 222-233. https://doi.org/10.1016/j.solmat.2017.02.019

[140] Kim, H., Jang, H., Subramanian, G. O., Kim, C., Jang, C., Development of alumina-forming duplex stainless steels as accident-tolerant fuel cladding materials for light water reactors, Journal of Nuclear Materials. 507 (2018) 1-14. https://doi.org/10.1016/j.jnucmat.2018.04.027

[141] Naumenko, D., Effects of metallurgical chemistry and service conditions on the oxidation limited life time of FeCrAl-based components (PhD Dissertation), Fakultät für Maschinenwesen, Rheinisch-Westfälischen Technischen Hochschule Aachen, Germany, 2001.

[142] Kochubey, V., Effect of Ti, Hf and Zr additions and impurity elements on the oxidation limited lifetime of thick-and thin-walled FeCrAlY-components (PhD Dissertation), Fakultät für Maschinenbau, Ruhr-Universität Bochum, Germany 2006.

[143] Brady, M.P., Yamamoto, Y., Santella, M.L., Maziasz, P.J., Pint, B.A., Liu, C.T., Lu, Z.P., Bei, H., The development of alumina-forming austenitic stainless steels for high-temperature structural use, The Journal of The Minerals, Metals & Materials Society (TMS). 60 (2008) 12. https://doi.org/10.1007/s11837-008-0083-2

[144] Canovic, S., Engkvist, J., Liu, F., Lai, H., Götlind, H., Hellström, K., Svensson, J.E., Johansson, L.G., Olsson, M., Halvarsson, M., Microstructural investigation of the initial oxidation of the FeCrAlRE alloy Kanthal AF in dry and wet O2 at 600 and 800° C, Journal of The Electrochemical Society. 157 (2010) C223-C230. doi: 10.1149/1.3391447

[145] Kitaoka, S., Kuroyama, T., Matsumoto, M., Kitazawa, R., Kagawa, Y., Control of polymorphism in Al_2O_3 scale formed by oxidation of alumina-forming alloys, Corrosion Science. 52 (2010) 429-434. https://doi.org/10.1016/j.corsci.2009.09.031

[146] Tomaszewicz, P., Wallwork, G.R., The oxidation of high-purity iron-chromium-aluminum alloys at 800° C, Oxidation of Metals. 20 (1983) 75-109. https://doi.org/10.1007/BF00662042

[147] Brady, M. P., Yamamoto, Y., Santella, M. L., Walker, L. R. Composition, microstructure, and water vapor effects on internal/external oxidation of alumina-forming austenitic stainless steels, Oxidation of Metals. 72 (2009) 311. https://doi.org/10.1007/s11085-009-9161-2

[148] Tsai, M.H., Yeh, J.W., High-entropy alloys: a critical review, Materials Research Letters. 2 (2014) 107-123. https://doi.org/10.1080/21663831.2014.912690

[149] Miracle, D.B., Senkov, O.N., A critical review of high entropy alloys and related concepts, Acta Materialia. 122 (2017) 448-511. https://doi.org/10.1016/j.actamat.2016.08.081

[150] Li, Z., Pradeep, K. G., Deng, Y., Raabe, D., Tasan, C. C., Metastable high-entropy dual-phase alloys overcome the strength–ductility trade-off, Nature. 534 (2016) 227. https://doi.org/10.1038/nature17981

[151] King, D. J. M., Investigation of high-entropy alloys for use in advanced nuclear applications (Doctoral dissertation), University of Technology Sydney, Australia, 2016.

[152] Shi, Y., Yang, B., Liaw, P. Corrosion-resistant high-entropy alloys: A review, Metals. 7 (2017) 43. https://doi.org/10.3390/met7020043

[153] Senkov, O. N., Miracle, D. B., Chaput, K. J., Couzinie, J. P., Development and exploration of refractory high entropy alloys—A review, Journal of Materials Research. 33 (2018) 3092-3128. https://doi.org/10.1557/jmr.2018.153

[154] Tsao, T.K., Yeh, A.C., Kuo, C.M., Murakami, H., High temperature oxidation and corrosion properties of high entropy superalloys, Entropy. 18 (2016) 62. https://doi.org/10.3390/e18020062

[155] Butler, T.M., Weaver, M.L., Investigation of the phase stabilities in AlNiCoCrFe high entropy alloys, Journal of Alloys and Compounds. 691 (2017) 119-129. https://doi.org/10.1016/j.jallcom.2016.08.121

[156] Mortazavi, N., Geers, C., Esmaily, M., Babic, V., Sattari, M., Lindgren, K., Malmberg, P., Jönsson, B., Halvarsson, M., Svensson, J.E., Panas, I., Interplay of water and reactive elements in oxidation of alumina-forming alloys, Nature Materials. 17 (2018) 610. https://doi.org/10.1038/s41563-018-0105-6

[157] Zinkle, S.J., Terrani, K.A., Gehin, J.C., Ott, L.J., Snead, L.L., Accident tolerant fuels for LWRs: A perspective, Journal of Nuclear Materials. 448 (2014) 374-379. https://doi.org/10.1016/j.jnucmat.2013.12.005

[158] Niu, Y., Wang, S., Gao, F., Zhang, Z.G., Gesmundo, F., The nature of the third-element effect in the oxidation of Fe–xCr–3 at.% Al alloys in 1 atm O_2 at 1000 °C, Corrosion Science. 50 (2008) 345-356. https://doi.org/10.1016/j.corsci.2007.06.019

[159] Zhang, Z.G., Zhang, X.L., Sheng, L., Teng, X., The effect of the third element Cr on oxidation behavior of Fe-xCr-10Al (at.%) alloys at 900 °C, The Open Corrosion Journal. 2 (2009) 37-44. DOI:10.2174/1876503300902010037

[160] Wagner, C., Passivity and inhibition during the oxidation of metals at elevated temperatures, Corrosion Science. 5 (1965) 751-764. https://doi.org/10.1016/S0010-938X(65)80003-8

[161] Götlind, H., Liu, F., Svensson, J.E., Halvarsson, M., Johansson, L.G., The effect of water vapor on the initial stages of oxidation of the FeCrAl alloy Kanthal AF at 900 °C, Oxidation of Metals. 67 (2007) 251-266. https://doi.org/10.1007/s11085-007-9055-0

[162] Messaoudi, K., Huntz, A. M., Lesage, B., Diffusion and growth mechanism of Al_2O_3 scales on ferritic Fe-Cr-Al alloys, Materials Science and Engineering: A. 247 (1998) 248-262. https://doi.org/10.1016/S0921-5093(97)00711-9

[163] Mennicke, C., Schumann, E., Ruhle, M., Hussey, R.J., Sproule, G.I., Graham, M.J., The effect of yttrium on the growth process and microstructure of α-Al_2O_3 on FeCrAl, Oxidation of Metals. 49 (1998) 455-466. https://doi.org/10.1023/A:101880311309

[164] Pint, B.A., Optimization of reactive-element additions to improve oxidation performance of alumina-forming alloys, Journal of the American Ceramic Society. 86 (2003) 686-95. https://doi.org/10.1111/j.1151-2916.2003.tb03358.x

[165] Amano, T., Takezawa, Y., Shiino, A., Shishido, T., Surface morphology of scale on FeCrAl (Pd, Pt, Y) alloys, Journal of alloys and Compounds. 452 (2008) 16-22. https://doi.org/10.1016/j.jallcom.2007.01.170

[166] Cueff, R., Buscail, H., Caudron, E., Issartel, C., Riffard, F., Oxidation of alumina formers at 1173 K: effect of yttrium ion implantation and yttrium alloying addition, Corrosion Science. 45 (2003) 1815-1831. https://doi.org/10.1016/S0010-938X(02)00254-8

[167] Cueff, R., Buscail, H., Caudron, E., Riffard, F., Issartel, C., El Messki, S., Effect of reactive element oxide coating on the high temperature oxidation behavior of FeCrAl alloys, Applied Surface Science. 229 (2004) 233-241. https://doi.org/10.1016/j.apsusc.2004.01.072

[168] Pint, B.A., Experimental observations in support of the dynamic-segregation theory to explain the reactive-element effect, Oxidation of Metals. 45 (1996) 1-37. https://doi.org/10.1007/BF01046818

[169] Israelsson, N., Engkvist, J., Hellström, K., Halvarsson, M., Svensson, J.E., Johansson, L.G., KCl-Induced Corrosion of an FeCrAl Alloy at 600 °C in O_2+ H_2O Environment: The Effect of Pre-oxidation, Oxidation of Metals. 83 (2015) 29-53. https://doi.org/10.1007/s11085-014-9507-2

[170] Miner, R.G., Nagarajan, V., The morphology of oxidation of alumina-forming iron-base alloys containing chromium and aluminum, Oxidation of Metals. 16 (1981) 313-325. https://doi.org/10.1007/BF00603839

[171] Zhang, Z.G., Gesmundo, F., Hou, P.Y., Niu, Y., Criteria for the formation of protective Al_2O_3 scales on Fe–Al and Fe–Cr–Al alloys, Corrosion Science. 48 (2006) 741-765. https://doi.org/10.1016/j.corsci.2005.01.012

[172] Fetzer, R., Weisenburger, A., Jianu, A., Müller, G., Oxide scale formation of modified FeCrAl coatings exposed to liquid lead, Corrosion Science. 55 (2012) 213-218. https://doi.org/10.1016/j.corsci.2011.10.019

[173] Auger, T., Lorang, G., Liquid metal embrittlement susceptibility of T91 steel by lead–bismuth, Scripta Materialia. 52 (2005) 1323-1328. https://doi.org/10.1016/j.scriptamat.2005.02.027

[174] Ersoy, F., Gavrilov, S., Verbeken, K., Investigating liquid-metal embrittlement of T91 steel by fracture toughness tests, Journal of Nuclear Materials. 472 (2016) 171-177. https://doi.org/10.1016/j.jnucmat.2015.12.019

[175] Marshall, P., Austenitic stainless steels: microstructure and mechanical properties, Springer Science & Business Media, 1984, ISBN 978-0-85334-277-9, Netherlands.

[176] Maziasz, P. J., Developing an austenitic stainless steel for improved performance in advanced fossil power facilities, The Journal of The Minerals, Metals & Materials Society (TMS). 41 (1989) 14-20. https://doi.org/10.1007/BF03220265

[177] Maziasz, P. J., McGreevy, T., Pollard, M. J., Siebenaler, C. W., Swindeman, R. W., U.S. Patent No. 7,153,373. Washington, DC: U.S. Patent and Trademark Office. 2006.

[178] McGuire, M.F., Stainless steels for design engineers, ASM International. 2008, ISBN: 978-0-87170-717-8, Materials Park, Ohio 44073-0002, United States.

[179] Yamamoto, Y., Brady, M. P., Santella, M. L., Bei, H., Maziasz, P. J., Pint, B. A., Overview of strategies for high-temperature creep and oxidation resistance of alumina-forming austenitic stainless steels, Metallurgical and Materials Transactions A. 42 (2011) 922-931. https://doi.org/10.1007/s11661-010-0295-2

[180] Brady, M. P., Magee, J., Yamamoto, Y., Helmick, D., Wang, L., Co-optimization of wrought alumina-forming austenitic stainless steel composition ranges for high-temperature creep and oxidation/corrosion resistance, Materials Science and Engineering: A. 590 (2014) 101-115. https://doi.org/10.1016/j.msea.2013.10.014

[181] Ejenstam, J., Szakálos, P., Long term corrosion resistance of alumina forming austenitic stainless steels in liquid lead, Journal of Nuclear Materials. 461 (2015) 164-170. https://doi.org/10.1016/j.jnucmat.2015.03.011

[182] Brady, M. P., Pint, B. A., Liu, C. T., Maziasz, P. J., Yamamoto, Y., Lu, Z. P., Oxidation resistant high creep strength austenitic stainless steel, U.S. Patent No. 7,744,813, Washington, DC: U.S. Patent and Trademark Office. 2010.

[183] Brady, M. P., Santella, M. L., Yamamoto, Y., Liu, C. T., High Nb, Ta, and Al creep-and oxidation-resistant austenitic stainless steel, U.S. Patent No. 7,754,144. Washington, DC: U.S. Patent and Trademark Office. 2010.

[184] Yan, Y. F., Xu, X. Q., Zhou, D. Q., Wang, H., Wu, Y., Liu, X. J., Lu, Z. P. Hot corrosion behavior and its mechanism of a new alumina-forming austenitic stainless steel in molten sodium sulphate, Corrosion Science. 77 (2013) 202-209. https://doi.org/10.1016/j.corsci.2013.08.003

[185] Yamamoto, Y., Muralidharan, G., Brady, M. P., Development of $L1_2$-ordered Ni_3(Al, Ti)-strengthened alumina-forming austenitic stainless steel alloys, Scripta Materialia. 69 (2013) 816-819. https://doi.org/10.1016/j.scriptamat.2013.09.005

[186] Brady, M. P., Muralidharan, G., Yamamoto, Y., Pint, B. A., Development of 1100 °C capable alumina-forming austenitic alloys, Oxidation of Metals. 87 (2017) 1-10. https://doi.org/10.1007/s11085-016-9667-3

[187] Pint, B.A., Brady, M.P., Yamamoto, Y., Santella, M.L., Howe, J.Y., Trejo, R., Maziasz, P.J., Development of alumina-forming austenitic alloys for advanced recuperators. In ASME Turbo Expo 2009: Power for Land, Sea, and Air, American Society of Mechanical Engineers. 2009 271-280. https://doi.org/10.1115/GT2009-60197

[188] Yamamoto, Y., Takeyama, M., Lu, Z. P., Liu, C. T., Evans, N. D., Maziasz, P. J., Brady, M. P., Alloying effects on creep and oxidation resistance of austenitic stainless steel alloys employing intermetallic precipitates, Intermetallics. 16 (2008) 453-462. https://doi.org/10.1016/j.intermet.2007.12.005

[189] Guo, X., Chen, K., Gao, W., Shen, Z., Zhang, L., Corrosion behavior of alumina-forming and oxide dispersion strengthened austenitic 316 stainless steel in supercritical water, Corrosion Science. 138 (2018) 297-306. https://doi.org/10.1016/j.corsci.2018.04.026

[190] Put, A. R. V., Unocic, K. A., Brady, M. P., Pint, B. A., Performance of chromia-and alumina-forming Fe-and Ni-base alloys exposed to metal dusting environments: The effect of water vapor and temperature, Corrosion Science. 92 (2015) 58-68. https://doi.org/10.1016/j.corsci.2014.11.022

[191] Fernández, A. G., Rey, A., Lasanta, I., Mato, S., Brady, M. P., Pérez, F. J., Corrosion of alumina-forming austenitic steel in molten nitrate salts by gravimetric analysis and impedance spectroscopy, Materials and Corrosion. 65 (2014) 267-275. https://doi.org/10.1002/maco.201307422

[192] Brady, M.P., Banta, K., Mizia, J., Lorenz, N., Leonard, D.N., Yamamoto, Y., DeFoort, M., Keiser, J.R., Alloy Corrosion Considerations in Low-Cost, Clean Biomass Cookstoves for the Developing World, Energy for Sustainable Development. 37 (2017) 20-32. https://doi.org/10.1016/j.esd.2016.12.002

[193] Xu, X., Zhang, X., Chen, G., Lu, Z., Improvement of high-temperature oxidation resistance and strength in alumina-forming austenitic stainless steels, Materials Letters. 65 (2011) 3285-3288. https://doi.org/10.1016/j.matlet.2011.07.021

[194] Maziasz, P.J., Development of creep-resistant and oxidation-resistant austenitic stainless steels for high temperature applications, The Journal of The Minerals, Metals & Materials Society (TMS). 70 (2018) 66-75. https://doi.org/10.1007/s11837-017-2642-x

[195] Yeh, J.W., Recent progress in high-entropy alloys. Annales de Chimie, Science des Materiaux (Paris). 31 (2006) 633-648.

[196] Yang, X., Zhang, Y. Prediction of high-entropy stabilized solid-solution in multi-component alloys, Materials Chemistry and Physics. 132 (2012) 233-238. https://doi.org/10.1016/j.matchemphys.2011.11.021

[197] Zhang, Y., Zhou, Y. J., Lin, J. P., Chen, G. L., Liaw, P. K., Solid-solution phase formation rules for multi-component alloys, Advanced Engineering Materials. 10 (2008) 534-538. https://doi.org/10.1002/adem.200700240

[198] Sheng, G. U. O., Liu, C. T., Phase stability in high entropy alloys: formation of solid-solution phase or amorphous phase, Progress in Natural Science: Materials International. 21 (2011) 433-446. https://doi.org/10.1016/S1002-0071(12)60080-X

[199] Zhang, Y., Zuo, T. T., Tang, Z., Gao, M. C., Dahmen, K. A., Liaw, P. K., Lu, Z. P., Microstructures and properties of high-entropy alloys, Progress in Materials Science. 61 (2014) 1-93. https://doi.org/10.1016/j.pmatsci.2013.10.001

[200] Guo, S., Ng, C., Lu, J., Liu, C. T., Effect of valence electron concentration on stability of fcc or bcc phase in high entropy alloys, Journal of Applied Physics. 109 (2011) 103505. https://doi.org/10.1063/1.3587228

[201] Gao, M., Alman, D., Searching for next single-phase high-entropy alloy compositions, Entropy. 15 (2013) 4504-4519. https://doi.org/10.3390/e15104504

[202] Senkov, O. N., Miller, J. D., Miracle, D. B., Woodward, C., Accelerated exploration of multi-principal element alloys with solid solution phases, Nature Communications. 6 (2015) 6529. https://doi.org/10.1038/ncomms7529

[203] Gurao, N. P., Biswas, K., In the quest of single phase multi-component multi-principal high entropy alloys, Journal of Alloys and Compounds. 697 (2017) 434-442. https://doi.org/10.1016/j.jallcom.2016.11.383

[204] Miracle, D., Miller, J., Senkov, O., Woodward, C., Uchic, M., Tiley, J., Exploration and development of high entropy alloys for structural applications, Entropy. 16 (2014) 494-525. https://doi.org/10.3390/e16010494

[205] Wang, W. R., Wang, W. L., Wang, S. C., Tsai, Y. C., Lai, C. H., Yeh, J. W., Effects of Al addition on the microstructure and mechanical property of AlxCoCrFeNi high-entropy alloys, Intermetallics. 26 (2012) 44-51. https://doi.org/10.1016/j.intermet.2012.03.005

[206] Lu, Y., Dong, Y., Guo, S., Jiang, L., Kang, H., Wang, T., Wen, B., Wang, Z., Jie, J., Cao, Z., Ruan, H., A promising new class of high-temperature alloys: eutectic high-entropy alloys, Scientific Reports. 4 (2014) 6200. https://doi.org/10.1038/srep06200

[207] Chang, Y. J., Yeh, A. C., The evolution of microstructures and high temperature properties of $AlxCo_{1.5}CrFeNi_{1.5}Ti_y$ high entropy alloys, Journal of Alloys and Compounds. 653 (2015) 379-385. https://doi.org/10.1016/j.jallcom.2015.09.042

[208] K.R. Lim, K.S. Lee, J.S. Lee, J.Y. Kim, H.J. Chang, Dual phase high-entropy alloys for high-temperature structural applications, Journal of Alloys and Compounds. 728 (2017) 1235-1238. https://doi.org/10.1016/j.jallcom.2017.09.089

[209] Lu, Y., Dong, Y., Guo, S., Jiang, L., Kang, H., Wang, T., Wen, B., Wang, Z., Jie, J., Cao, Z., Ruan, H., A promising new class of high-temperature alloys: eutectic high-entropy alloys, Scientific Reports. 4 (2014) 6200. https://doi.org/10.1038/srep06200

[210] Song, R., Wei, L., Yang, C., Wu, S., Phase formation and strengthening mechanisms in a dual-phase nanocrystalline CrMnFeVTi high-entropy alloy with ultrahigh hardness, Journal of Alloys and Compounds. 744 (2018) 552-560. https://doi.org/10.1016/j.jallcom.2018.02.029

[211] Hsu, C.Y., Juan, C.C., Wang, W.R., Sheu, T.S., Yeh, J.W., Chen, S.K., On the superior hot hardness and softening resistance of $AlCoCrxFeMo_{0.5}Ni$ high-entropy alloys, Materials Science and Engineering: A. 528 (2011) 3581-3588. https://doi.org/10.1016/j.msea.2011.01.072

[212] Hemphill, M.A., Yuan, T., Wang, G.Y., Yeh, J.W., Tsai, C.W., Chuang, A., Liaw, P.K., Fatigue behavior of $Al_{0.5}CoCrCuFeNi$ high entropy alloys, Acta Materialia. 60 (2012) 5723-5734. https://doi.org/10.1016/j.actamat.2012.06.046

[213] Butler, T. M., Weaver, M. L., Oxidation behavior of arc melted AlCoCrFeNi multi-component high-entropy alloys, Journal of Alloys and Compounds. 674 (2016) 229-244. https://doi.org/10.1016/j.jallcom.2016.02.257

[214] Chen, X., Sui, Y., Qi, J., He, Y., Wei, F., Meng, Q., Sun, Z., Microstructure of $Al_{1.3}CrFeNi$ eutectic high entropy alloy and oxidation behavior at 1000° C, Journal of Materials Research. 32 (2017) 2109-2116. https://doi.org/10.1557/jmr.2017.10

[215] Wang, W. R., Wang, W. L., Yeh, J. W., Phases, microstructure and mechanical properties of $Al_xCoCrFeNi$ high-entropy alloys at elevated temperatures, Journal of Alloys and Compounds. 589 (2014) 143-152. https://doi.org/10.1016/j.jallcom.2013.11.084

[216] Wang, R., Zhang, K., Davies, C., Wu, X. Evolution of microstructure, mechanical and corrosion properties of AlCoCrFeNi high-entropy alloy prepared by direct laser fabrication, Journal of Alloys and Compounds. 694 (2017) 971-981. https://doi.org/10.1016/j.jallcom.2016.10.138

[217] Tung, C. C., Yeh, J. W., Shun, T. T., Chen, S. K., Huang, Y. S., Chen, H. C., On the elemental effect of AlCoCrCuFeNi high-entropy alloy system, Materials Letters. 61 (2007) 1-5. https://doi.org/10.1016/j.matlet.2006.03.140

[218] Zhang, C., Cao, H., Firouzdor, V., Kou, S., Chang, Y. A., Microstructure investigations of directionally solidified Mg-rich alloys containing Al, Ca and Sn, Intermetallics. 18 (2010) 1597-1602. https://doi.org/10.1016/j.intermet.2010.04.017

[219] Hu, Z., Zhan, Y., Zhang, G., She, J., Li, C., Effect of rare earth Y addition on the microstructure and mechanical properties of high entropy AlCoCrCuNiTi alloys, Materials & Design. 31 (2010) 1599-1602. https://doi.org/10.1016/j.matdes.2009.09.016

[220] Chen, M. R., Lin, S. J., Yeh, J. W., Chuang, M. H., Chen, S. K., Huang, Y. S., Effect of vanadium addition on the microstructure, hardness, and wear resistance of $Al_{0.5}CoCrCuFeNi$ high-entropy alloy, Metallurgical and Materials Transactions A. 37 (2006) 1363-1369. https://doi.org/10.1007/s11661-006-0081-3

[221] Ren, B., Zhao, R. F., Liu, Z. X., Guan, S. K., Zhang, H. S., Microstructure and properties of $Al_{0.3}CrFe_{1.5}MnNi_{0.5}Ti_x$ and $Al_{0.3}CrFe_{1.5}MnNi_{0.5}Si_x$ high-entropy alloys, Rare Metals. 33 (2014) 149-154. https://doi.org/10.1007/s12598-014-0224-4

[222] Shun, T. T., Hung, C. H., Lee, C. F., The effects of secondary elemental Mo or Ti addition in $Al_{0.3}CoCrFeNi$ high-entropy alloy on age hardening at 700 °C, Journal of Alloys and Compounds. 495 (2010) 55-58. https://doi.org/10.1016/j.jallcom.2010.02.032

[223] Dong, Y., Lu, Y., Kong, J., Zhang, J., Li, T., Microstructure and mechanical properties of multi-component AlCrFeNiMox high-entropy alloys, Journal of Alloys and Compounds. 573 (2013) 96-101. https://doi.org/10.1016/j.jallcom.2013.03.253

[224] Gwalani, B., Choudhuri, D., Soni, V., Ren, Y., Styles, M., Hwang, J.Y., Nam, S.J., Ryu, H., Hong, S.H., Banerjee, R., Cu assisted stabilization and nucleation of $L1_2$ precipitates in $Al_{0.3}CuFeCrNi_2$ fcc-based high entropy alloy, Acta Materialia. 129 (2017) 170-182. https://doi.org/10.1016/j.actamat.2017.02.053

[225] Ren, B., Liu, Z. X., Li, D. M., Shi, L., Cai, B., Wang, M. X., Effect of elemental interaction on microstructure of CuCrFeNiMn high entropy alloy system, Journal of Alloys and Compounds. 493 (2010) 148-153. https://doi.org/10.1016/j.jallcom.2009.12.183

[226] Ma, S. G., Zhang, Y., Effect of Nb addition on the microstructure and properties of AlCoCrFeNi high-entropy alloy, Materials Science and Engineering: A. 532 (2012) 480-486. https://doi.org/10.1016/j.msea.2011.10.110

[227] Zhu, J. M., Fu, H. M., Zhang, H. F., Wang, A. M., Li, H., Hu, Z. Q., Microstructures and compressive properties of multicomponent AlCoCrFeNiMox alloys, Materials Science and Engineering: A. 527 (2010) 6975-6979. https://doi.org/10.1016/j.msea.2010.07.028

[228] Kai, W., Li, C. C., Cheng, F. P., Chu, K. P., Huang, R. T., Tsay, L. W., Kai, J. J., The oxidation behavior of an equimolar FeCoNiCrMn high-entropy alloy at 950 °C in various oxygen-containing atmospheres, Corrosion Science. 108 (2016) 209-214. https://doi.org/10.1016/j.corsci.2016.03.020

[229] Butler, T. M., Alfano, J. P., Martens, R. L., Weaver, M. L., High-temperature oxidation behavior of Al-Co-Cr-Ni-(Fe or Si) multicomponent high-entropy alloys, The Journal of The Minerals, Metals & Materials Society (TMS). 67 (2015) 246-259. https://doi.org/10.1007/s11837-014-1185-7

[230] Butler, T. M., Phase stability and oxidation behavior of Al-Ni-Co-Cr-Fe based high-entropy alloys, (PhD Dissertation), Department of Metallurgical and Materials Engineering, The University of Alabama, TUSCALOOSA, 2016.

[231] Liu, Y. X., Cheng, C. Q., Shang, J. L., Rui, W. A. N. G., Peng, L. I., Jie, Z. H. A. O., Oxidation behavior of high-entropy alloys AlxCoCrFeNi (x=0.15, 0.4) in supercritical water and comparison with HR3C steel, Transactions of Nonferrous Metals Society of China. 25 (2015) 1341-1351. https://doi.org/10.1016/S1003-6326(15)63733-5

[232] Guinier, A., X-ray diffraction in crystals, imperfect crystals, and amorphous bodies, Dover Publications, 1994, ISBN 9780486680118, New York.

[233] Fultz, B., Howe, J.M., Transmission electron microscopy and diffractometry of materials, Springer Science & Business Media, Heidelberg. 2012, DOI: 10.1007/978-3-642-29761-8

[234] Ul-Hamid, A., A Beginners' Guide to Scanning Electron Microscopy, Springer, Cham, 2018, ISBN: 978-3-319-98482-7. https://doi.org/10.1007/978-3-319-98482-7

[235] Krumeich, F., Properties of electrons, their interactions with matter and applications in electron microscopy, Laboratory of Inorganic Chemistry, ETH Zurich, 2015. https://pdfs.semanticscholar.org/8a69/7a2b32d9401091b913c58d95ce3485133754.pdf (retrieved on 17/10/2019)

[236] Wirth, R., Focused Ion Beam (FIB) combined with SEM and TEM: Advanced analytical tools for studies of chemical composition, microstructure and crystal structure in geomaterials on a nanometre scale, Chemical Geology. 261 (2009) 217-229. https://doi.org/10.1016/j.chemgeo.2008.05.019

[237] Carter, C. B., Williams, D. B. (Eds.), Transmission electron microscopy: Diffraction, imaging, and spectrometry. 2016, Springer International Publishing Switzerland. DOI: 10.1007/978-3-319-26651-0.

[238] Springer. Parker, W.J., Jenkins, R.J., Butler, C.P., Abbott, G.L., Flash method of determining thermal diffusivity, heat capacity, and thermal conductivity, Journal of Applied Physics. 32 (1961) 1679-1684. https://doi.org/10.1063/1.1728417

[239] Thermo-Calc software, https://www.thermocalc.com/ (retrieved 17/10/2019).

[240] Kotecki, D.J. and Siewert, T.A., WRC-1992 constitution diagram for stainless steel weld metals: a modification of the WRC-1988 diagram, Welding Journal. 71(1992), 171-178.

[241] R.H. Espy, Weldability of nitrogen-strengthened stainless steels, Welding Journal. 43 (1982) 149-156.

[242] He, J.Y., Wang, H., Huang, H.L., Xu, X.D., Chen, M.W., Wu, Y., Liu, X.J., Nieh, T.G., An, K., Lu, Z.P., A precipitation-hardened high-entropy alloy with outstanding tensile properties, Acta Materialia. 102 (2016) 187-196. https://doi.org/10.1016/j.actamat.2015.08.076

[243] Wang, Q., Ma, Y., Jiang, B., Li, X., Shi, Y., Dong, C., Liaw, P.K., A cuboidal B2 nanoprecipitation-enhanced body-centered-cubic alloy $Al_{0.7}CoCrFe_2Ni$ with prominent tensile properties, Scripta Materialia. 120 (2016) 85-89. https://doi.org/10.1016/j.scriptamat.2016.04.014

[244] Gwalani, B., Soni, V., Choudhuri, D., Lee, M., Hwang, J.Y., Nam, S.J., Ryu, H., Hong, S.H., Banerjee, R., Stability of ordered $L1_2$ and B2 precipitates in face centered cubic based high entropy alloys-$Al_{0.3}CoFeCrNi$ and $Al_{0.3}CuFeCrNi_2$, Scripta Materialia. 123 (2016) 130-134. https://doi.org/10.1016/j.scriptamat.2016.06.019

[245] Rao, J.C., Diao, H.Y., Ocelík, V., Vainchtein, D., Zhang, C., Kuo, C., Tang, Z., Guo, W., Poplawsky, J.D., Zhou, Y., Liaw, P.K., Secondary phases in AlxCoCrFeNi high-entropy alloys: An in-situ TEM heating study and thermodynamic appraisal, Acta Materialia. 131 (2017) 206-220. https://doi.org/10.1016/j.actamat.2017.03.066

[246] Park, E.S., Oh, H.S., Kim, I.H., Chang, H.J., SangJun, K.I.M., Ryu, C.W., Entropy-controlled bcc alloy having strong resistance to high-temperature neutron radiation damage, U.S. Patent Application No. 15/146,151, U.S. Patent and Trademark Office. 2016.

[247] Senkov, O.N., Wilks, G.B., Scott, J.M., Miracle, D.B., Mechanical properties of $Nb_{25}Mo_{25}Ta_{25}W_{25}$ and $V_{20}Nb_{20}Mo_{20}Ta_{20}W_{20}$ refractory high entropy alloys, Intermetallics. 19 (2011) 698-706. https://doi.org/10.1016/j.intermet.2011.01.004

[248] Senkov, O.N., Scott, J.M., Senkova, S.V., Meisenkothen, F., Miracle, D.B., Woodward, C.F., Microstructure and elevated temperature properties of a refractory TaNbHfZrTi alloy, Journal of Materials Science. 47 (2012) 4062-4074. https://doi.org/10.1007/s10853-012-6260-2

[249] Dong, Y., Jiang, L., Jiang, H., Lu, Y., Wang, T., Li, T., Effects of annealing treatment on microstructure and hardness of bulk $AlCrFeNiMo_{0.2}$ eutectic high-entropy alloy, Materials & Design. 82 (2015) 91-97. https://doi.org/10.1016/j.matdes.2015.05.046

[250] F.R. de Boer, B. Boom, W.C.M. Mattens, A.R. Miedema, A.K. Niessen, Cohesion in Metals: Transition Metal Alloys, Elsevier Science Publishers, Amsterdam, The Netherlands, 1988, ISBN: 0-444-87098-9.

[251] Takeuchi, A. and Inoue, A., Classification of bulk metallic glasses by atomic size difference, heat of mixing and period of constituent elements and its application to characterization of the main alloying element, Materials Transactions. 46 (2005) 2817-2829. https://doi.org/10.2320/matertrans.46.2817

[252] Hume-Rothery, W., Atomic diameters, atomic volumes and solid solubility relations in alloys, Acta Metallurgica. 14 (1966) 17-20. https://doi.org/10.1016/0001-6160(66)90267-7

[253] MacGillavry, C.H., Rieck, G.D., International Tables for X-ray crystallography, Vol 3., The International Union of Crystallography, The Kynoch Press, Birmingham, England, 1968.

[254] Wang, Z., Guo, S., Liu, C.T., Phase selection in high-entropy alloys: from non-equilibrium to equilibrium, The Journal of The Minerals, Metals & Materials Society (TMS). 66 (2014) 1966-1972. https://doi.org/10.1007/s11837-014-0953-8

[255] Zieliñska, M., Yavorska, M., Porêba, M., Sieniawski, J., Thermal properties of cast nickel based superalloys, Archives of Materials Science and Engineering. 44 (2010) 35-38.

[256] Rai, A.K., Trpathy, H., Hajra, R.N., Raju, S., Saroja, S., Thermo-physical properties of Ni based super alloy 617, Journal of Alloys and Compounds. 698 (2017) 442-450. https://doi.org/10.1016/j.jallcom.2016.12.183

[257] Chou, H.P., Chang, Y.S., Chen, S.K., Yeh, J.W., Microstructure, thermo-physical and electrical properties in AlxCoCrFeNi (0≤x≤2) high-entropy alloys, Materials Science and Engineering: B. 163 (2009) 184-189. https://doi.org/10.1016/j.mseb.2009.05.024

[258] Yamamoto, Y., Santella, M.L., Brady, M.P., Bei, H., Maziasz, P.J., Effect of alloying additions on phase equilibria and creep resistance of alumina-forming austenitic stainless steels, Metallurgical and Materials Transactions A. 40 (2009) 1868-1880. https://doi.org/10.1007/s11661-009-9886-1

[259] Peraldi, R., Pint, B.A., Effect of Cr and Ni contents on the oxidation behavior of ferritic and austenitic model alloys in air with water vapor, Oxidation of Metals. 61 (2004) 463-483. https://doi.org/10.1023/B:OXID.0000032334.75463.da

[260] Stott, F.H., Wood, G.C., Stringer, J., The influence of alloying elements on the development and maintenance of protective scales, Oxidation of Metals. 44 (1995) 113-145. https://doi.org/10.1007/BF01046725

[261] Emo, J., Maugis, P., Perlade, A., Austenite growth and stability in medium Mn, medium Al Fe-C-Mn-Al steels, Computational Materials Science. 125 (2016) 206-217. https://doi.org/10.1016/j.commatsci.2016.08.041

[262] Zhao, P., Zhao, H., Yu, J., Zhang, H., Gao, H., Chen, Q., Crystal structure and properties of Al_2O_3-Cr_2O_3 solid solutions with different Cr_2O_3 contents, Ceramics International, 44(2018) 1356-1361. https://doi.org/10.1016/j.ceramint.2017.08.195

[263] Trotter, G., Hu, B., Sun, A.Y., Harder, R., Miller, M.K., Yao, L., Baker, I., Precipitation kinetics during aging of an alumina-forming austenitic stainless steel, Materials Science and Engineering: A. 667 (2016) 147-155. https://doi.org/10.1016/j.msea.2016.04.081

[264] Moon, J., Lee, T.H., Heo, Y.U., Han, Y.S., Kang, J.Y., Ha, H.Y., Suh, D.W., Precipitation sequence and its effect on age hardening of alumina-forming austenitic stainless steel, Materials Science and Engineering: A. 645 (2015) 72-81. https://doi.org/10.1016/j.msea.2015.08.005

[265] Mota, M.A., Coelho, A.A., Bejarano, J.M.Z., Gama, S., Caram, R., Fe–Al–Nb phase diagram investigation and directional growth of the $(Fe, Al)_2Nb$–$(Fe, Al, Nb)_{ss}$ eutectic system, Journal of Alloys and Compounds. 399 (2005) 196-201. https://doi.org/10.1016/j.jallcom.2005.03.038

[266] Dąbrowa, J., Cieślak, G., Stygar, M., Mroczka, K., Berent, K., Kulik, T. and Danielewski, M., Influence of Cu content on high temperature oxidation behavior of $AlCoCrCu_xFeNi$ high entropy alloys (x= 0; 0.5; 1), Intermetallics. 84 (2017) 52-61. https://doi.org/10.1016/j.intermet.2016.12.015

[267] Massalski, T.B., Murray, J.L., Bennett, L.H., Baker, H., Binary alloy phase diagrams, American Society of Metals: Metals Park, OH. 1986, University of Michigan, ISBN 9780871702630.

[268] Bei, H., Yamamoto, Y., Brady, M.P., Santella, M.L., Aging effects on the mechanical properties of alumina-forming austenitic stainless steels, Materials Science and Engineering: A. 527 (2010) 2079-2086. https://doi.org/10.1016/j.msea.2009.11.052

[269] Hu, B., Trotter, G., Wang, Z., Chen, S., Cai, Z., Baker, I., Effect of boron and carbon addition on microstructure and mechanical properties of the aged gamma-prime strengthened alumina-forming austenitic alloys, Intermetallics. 90 (2017) 36-49. https://doi.org/10.1016/j.intermet.2017.06.011

[270] Trotter, G., Hu, B., Sun, A.Y., Harder, R., Miller, M.K., Yao, L., Baker, I., Precipitation kinetics during aging of an alumina-forming austenitic stainless steel, Materials Science and Engineering: A. 667 (2016) 147-155. https://doi.org/10.1016/j.msea.2016.04.081

[271] Hochanadel, P.W., Edwards, G.R., Robino, C.V., Cieslak, M.J., Heat treatment of investment cast PH 13-8 Mo stainless steel: Part I. Mechanical properties and microstructure, Metallurgical and Materials Transactions A. 25 (1994) 789-798. https://doi.org/10.1007/BF02665455

[272] Prescott, R. and Graham, M.J., The formation of aluminum oxide scales on high-temperature alloys, Oxidation of Metals. 38 (1992) 233-254. https://doi.org/10.1007/BF00666913

[273] Fujii, C.T., Meussner, R.A., The Mechanism of the High-Temperature Oxidation of Iron-Chromium Alloys in Water Vapor, Journal of the Electrochemical Society. 111 (1964) 1215-1221. doi: 10.1149/1.2425963

[274] Viswanathan, R., Sarver, J., Tanzosh, J.M., Boiler materials for ultra-supercritical coal power plants-steamside oxidation, Journal of Materials Engineering and Performance. 15 (2006) 255-274. https://doi.org/10.1361/105994906X108756

[275] Kubaschewski, O., Evans, A.L., Alcock, C.B., Metallurgical thermochemistry. 1967, Pergamon Press, ISBN-9780895203564, Oxford, New York.

[276] Young, D.J., High temperature oxidation and corrosion of metals (Vol. 1), 2008, Elsevier, ISBN: 978-0-08-044587-8, Linacre House, Jordan Hill, Oxford OX2 8DP, UK.

[277] Shang, S.L., Zhang, H., Wang, Y., Liu, Z.K., Temperature-dependent elastic stiffness constants of α-and θ-Al2O3 from first-principles calculations, Journal of Physics: Condensed Matter. 22 (2010) 375403. doi:10.1088/0953-8984/22/37/375403.

[278] Tolpygo, V.K., Clarke, D.R., Competition between stress generation and relaxation during oxidation of an Fe-Cr-Al-Y alloy, Oxidation of Metals. 49 (1998) 187-212. https://doi.org/10.1023/A:1018828619028

[279] Brady, M.P., Yamamoto, Y., Santella, M.L., Pint, B.A., Effects of minor alloy additions and oxidation temperature on protective alumina scale formation in creep-resistant austenitic stainless steels, Scripta Materialia. 57 (2007) 1117-1120. https://doi.org/10.1016/j.scriptamat.2007.08.032

Appendix A: XRD results of AFA-2nd generation alloys (600 °C, 2000 h)

The following Fig. 1 shows the XRD results of AFA-2nd generation after 2000 h exposure in 10^{-6} wt.% oxygen- containing molten Pb at 600 °C. The phase composition of the oxide scales is the same as that found after 1000 h exposure. As for the phase in bulk alloys, austenite and B2 phases have been identified in all samples. There is no experimental evidence from SEM/EDS or XRD regarding the formation of FeCr solid solution in the transitional layer.

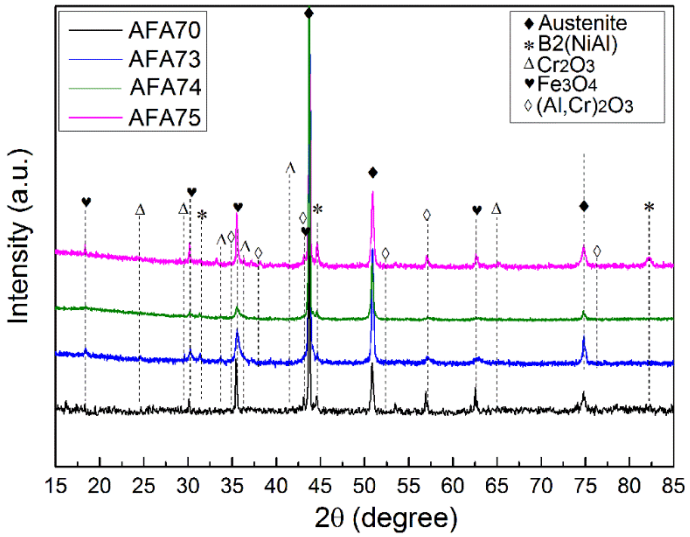

Fig. 1 XRD patterns performed on AFA-2nd generation samples after 2000 h exposure to 10^{-6} wt.% oxygen containing molten Pb at 600 °C (sample AFA70, AFA73, AFA74 and AFA75).

Appendix B: structural stability analysis of HEA alloys

Fig. 2 shows the SEM microstructure analysis of HEA1 in as-cast state and after 1000 h exposure in 10^{-6} wt.% oxygen containing molten Pb at 550 °C and 600 °C. In the as-cast state, the alloy matrix consists of FCC, BCC and B2 phase. The samples after exposure at 550 °C and 600 °C show no difference in microstructures compared with the as-cast sample. Only the number of dark precipitates (B2 phase) increases after corrosion test, see the small precipitates area in Fig. 1 (c). According to the XRD characterization shown in Fig. 6-6 and Fig. 6-20, the phases after exposure at 550 °C and 600 °C consist of FCC, BCC and B2 phase, which are consistent with the as-cast samples, see Fig. 4-17. This result indicates the structure stability of HEA1 at the exposed temperatures.

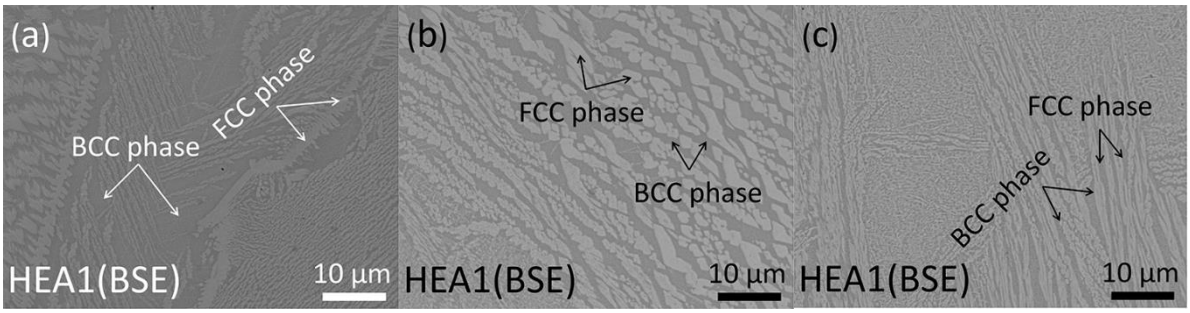

Fig. 2 SEM microstructure analysis of HEA1, (a): in as-cast state; (b) and (c): after 1000 h exposure at 10^{-6} wt.% oxygen containing molten Pb at 550 °C (b) and 600 °C (c).

The SEM microstructure analysis of HEA2 before and after exposure at 550 °C and 600 °C are shown in Fig. 3. After 1000 h exposure at 550 °C, the dendrites show no difference either in size or in morphologies. After the sample was exposed at 600 °C, the inter-dendrites enriched in Al and Ni are still visible in alloy matrix. Further evaluation of the structures by XRD show the formation of FCC and B2 phase before and after exposure tests at 550 °C and 600 °C, shown in Fig. 6-6 and Fig. 6-20.

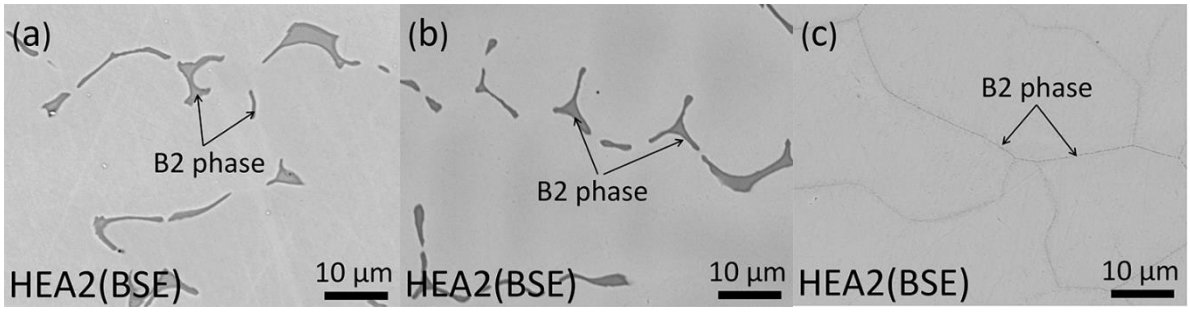

Fig. 3 SEM microstructure analysis of HEA2, (a): in as-cast state; (b) and (c): after 1000 h exposure at 10^{-6} wt.% oxygen containing molten Pb at 550 °C (b) and 600 °C (c).

Fig. 4 shows the microstructures of HEA4 in as-cast and exposed state. The dendrite structures are observed in the alloy matrix before and after exposure. According to XRD analysis of exposed samples, the alloy matrix consists of FCC and B2 phases, as shown in Fig. 6-6 and Fig. 6-20. The microstructures of the alloy matrix remain stable during the exposure at test conditions.

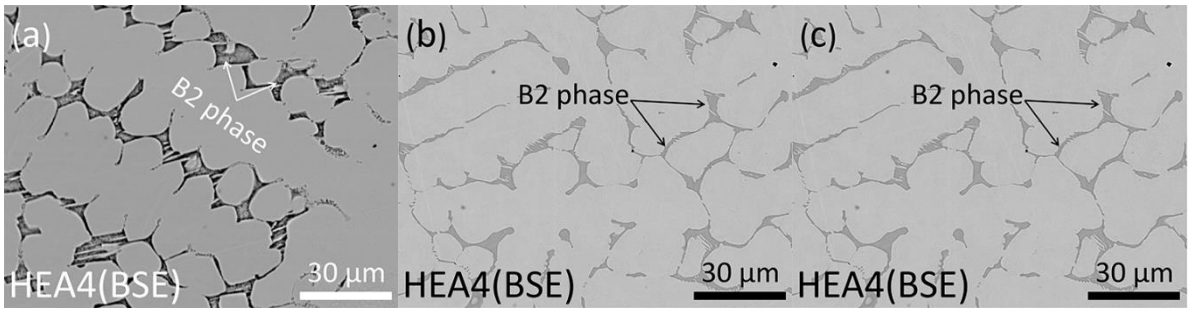

Fig. 4 SEM microstructure analysis of HEA4, (a): in as-cast state; (b) and (c): after 1000 h exposure at 10^{-6} wt.% oxygen containing molten Pb at 550 °C (b) and 600 °C (c).

The SEM microstructure analysis of as-cast and exposed HEA7 is shown in Fig. 5. The morphologies show no difference between the as-cast and exposed samples. According to the XRD and EDS analysis, the bright inter-dendrites are Laves phase, shown in Fig. 6-13 and Fig. 6-27. The alloy matrix is FCC phase.

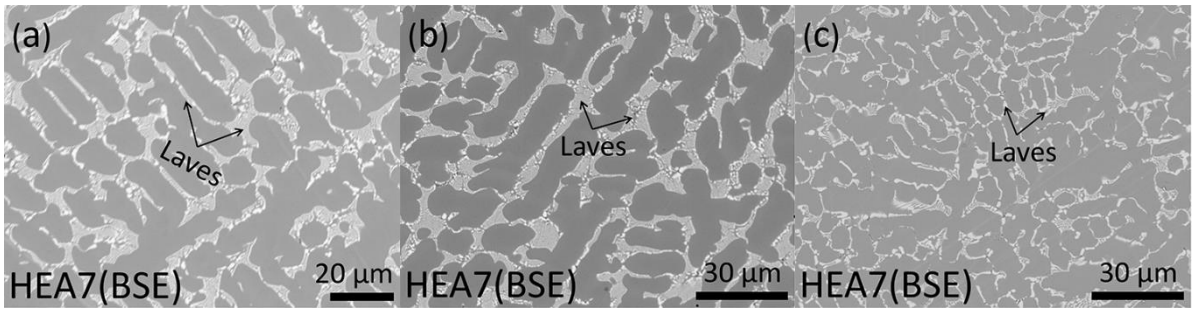

Fig. 5 SEM microstructure analysis of HEA7, (a): in as-cast state; (b) and (c): after 1000 h exposure at 10^{-6} wt.% oxygen containing molten Pb at 550 °C (b) and 600 °C (c).

List of publications

Journal papers (peer-reviewed)

1. Ding, W., **Shi, H.**, Xiu, Y., Bonk, A., Weisenburger, A., Jianu, A., & Bauer, T, Hot corrosion behavior of commercial alloys in thermal energy storage material of molten $MgCl_2$/KCl/NaCl under inert atmosphere. *Solar Energy Materials and Solar Cells*, 184 (2018), 22-30.
2. Ding, W., **Shi, H.**, A., Jianu, A., Xiu, Y., Bonk, A., Weisenburger, A. & Bauer, T, Molten chloride salts for next generation concentrated solar power plants: Mitigation strategies against corrosion of structural materials. *Solar Energy Materials and Solar Cells*. 193 (2019), 298-313.
3. **Shi, H.**, Jianu, A., Weisenburger A., Tang C.C., Fetzer R., Heinzel A., Lang F., Stieglitz R., Mueller G., Corrosion resistance and microstructural stability of austenitic Fe-Cr-Al-Ni model alloys exposed to oxygen-containing molten lead. *Journal of Nuclear Materials*. 524 (2019), 177-190.
4. **Shi, H.**, Chongchong Tang, Adrian Jianu, Weisenburger A., Mueller G., Oxidation and scaling behaviour of alumina-forming austenitic & high entropy alloys in steam environment at 1200°C. (submitted).

Conference papers

1. Alfons Weisenburger*, Adrian Jianu, Annette Heinzel, **Hao Shi** and Georg Müller, Development of alumina forming materials for corrosion mitigation in heavy liquid metal cooled nuclear reactors. IAEA TM on LFR Structural Materials, 15-17 October 2019 in Vienna. (accepted).

Oral presentations

1. **Shi Hao**, Adrian Jianu, Alfons Weisenburger, Annette Heinzel, Georg Mueller, KIT: AFA development and actual status of work, 28-31 November, 2018, KIT Campus Nord, Karlsruhe, Germany.
2. **Shi Hao,** A. Jianu, A. Georg Mueller, Robert Stieglitz**,** Development of alumina-forming(AFA+HEA) alloys for the mitigation of compatibility issues with liquid lead in energy related applications. **"**3th and 4th INR Ph.D. Students Seminar", Bad Herrenalb, Baden-Württemberg, Germany, 2017, 2018.

Poster presentations

1. **Shi Hao,** A. Jianu, A. Weisenburger, et.al, Alumina-forming austenitic steels exposed to oxygen containing molten lead. "EUROMAT", 2017, 15-22 September 2017, Thessaloniki, Greece.
2. Adrian Jianu, **Shi Hao**, Alfons Weisenburger, Annette Heizel, Renate Fetzer, Ionelia Voiculescu, Victor Geanta, Georg Mueller, Corrosion behaviour of high entropy alloys exposed to oxygen containing molten lead. "EUROMAT", 2017, 15-22 September 2017, Thessaloniki, Greece.

3. **H. Shi,** A. Jianu, A. Weisenburger, S. Miran, A. Heinzel, R. Fetzer, L. Fabian, Georg Mueller, Corrosion behaviour and microstructural stability of alumina-forming austenitic model alloys exposed to oxygen-containing molten lead. CIMTEC 2018, 14th International Ceramics Congress and 8th Forum on New Materials, 10-14 June 2018, Perugia, Italy.
4. **H. Shi,** A. Jianu, A. Weisenburger, Sabine Schlabach, Dorothee-Vinga Szabo, Georg Müller, HEAFNA High Entropy Alloys for nuclear applications, the Fifth International Workshop on Structural Materials for Innovative Nuclear Systems (SMINS-5) 8-11 July 2019, Kyoto, Japan.

Acknowledgements

My PhD work has been built upon great support of the colleagues from GESA (Gepulste ElektronenStrahlAnlage) group at the Institute for Pulsed Power and Microwave Technology. This thesis represents the work I have carried over the last four years. It would not be possible without the unlimited support and guidance from a large number of colleges, families and friends.

First and foremost, I would like to express my greatly appreciation to my supervisors Prof. George Mueller, Dr. Adrian Jianu, Dr. Alfons Weisenburger, Dr. Annette Heinzel, Dr. Renate Fetzer and Prof. Robert Stieglitz for guiding through my Ph.D. stage. Prof. George Mueller is very friendly and scholarly boss. He fully support and motivate my PhD work at the Institute for Pulsed Power and Microwave Technology. My very special appreciation to my tutor Dr. Adrian Jianu. He is my enlightening teacher of scientific work. He works very carefully with great knowledge. He teaches me something beyond the PhD work like how to reading, critical thinking and scientific writing. We keep discussion of the scientific issues nearly every working day and make sure the work towards the right direction. Dr. Alfons Weisenburger is an intellectual and excellent leader. He also gave me very important guides during my study. I also want to thank Dr. Annette Heinzel and Dr. Renate Fetzer. Both of them are very friendly colleges. Whenever I need help, they are always enthusiastic. Dr. Annette Heinzel supports my corrosion experimental work and give me useful advice. Dr. Renate Fetzer provides me great help especially when I prepare the thesis and papers. We have nice talk during lunch time every day. Prof. Robert Stiegltz is a knowledgeable scientist. I learned a lot from his tremendous guidance, instructive and expert advices. During the couple of years, we have formed good cooperation with an efficient team. I am also looking forward to our future endeavors.

I gratefully acknowledge Dr. Chongchong Tang (IAM, KIT) for his fruitful cooperation and discussion of the work. My appreciations are for Dr. mont. Dorothée Vinga Szabó (INT, KIT) and Dr. Sabine Schlabach (INT, KIT) for their excellent work of the TEM sample preparation and evaluation, comments and advices on my PhD thesis. I also thanks Dr. Andrei Galatanu and Dr. Magdalena Galatanu from National Institute of Materials Physics in Romania for their cooperation for the measurement of thermo-physical properties of my samples. Dr. Wenjin Ding (DLR) is also appreciated for the successful scientific cooperation and suggestion during my study.

I acknowledge all members of the institute at IHM for them creating a professional, friendly and pleasant working atmosphere: Prof. Jelonnek, John, Prof. Thumm, Manfred, Lang, Fabian, Zhen Wang, Dr. Yi Zhang, Tianru Zhang, An, Wladimir, Bertsch, Gabriela, Dr. Chuanren Wu, Dr. Martin

Hochberg, Dr. Martin Sack. I also take this chance to thanks Dr. Martin Steinbrück (IAM, KIT), Prof. Hans Jürgen Seifert (chairman of my PhD defense), for their support during my study.

In addition, thanks my friends for their help for making my life easier in Karlsruhe. I am very thankful to the friends and colleagues, especially to Dr. Tao Zhang, Xiaozhuang Zhou, Dr. Peng Wang, Dr. Guorui Xiao, Dr. Tao Lei, Kaiju Lu, Prof. Kai Wu, Xiang Zhan, Dongxu Xie, Dr. Jian Dong, Dr. Xiaojuan Yu, Weibin Wu, Jiamin Hu, Prof. Kai Jiang, Prof. Kangli Wang, Prof. Wei Wang, Prof Min Zhou, Dr. Wei Li, Dr. Haomiao Li in Huazhong University of Science and Technology, Prof. Ke Zhang from Shanghai Jiaotong University, Prof. Yaming Wang from Harbin Institute of Technology, Prof. Zhiming Li from Central South University, Prof Yueling Guo from Northwestern Polytechnical University, for their support and encourage of my PhD study.

My sincerely and deeply gratitude gives to my family, my parents, my brother and sister, sister in law and brother in law, for their endless love and great support during these years. Thanks them form understanding my life alone in abroad and always encourage me forward.

Finally, I acknowledge China Scholarship Council (CSC) for providing the financial support during my PhD study.

Hao Shi
Karlsruhe, Jan, 2020